

Theoretical modelling of nano-scaled systems with heavy ions

Dissertation

zur Erlangung des Doktorgrades der Naturwissenschaften
(Dr. rer. nat.)

Kris Holtgrewe



Fachbereich 07
Institut für theoretische Physik

Gießen, Juli 2022

Dem Fachbereich 07 der Justus-Liebig-Universität Gießen
als Dissertation vorgelegt.

Tag der Disputation: 24. Oktober 2022

Erstgutachter: Prof. Dr. Simone Sanna

Zweitgutachter: Prof. Dr. Wolf Gero Schmidt

Equidem beatos puto, quibus deorum munere datum est aut facere scribenda aut scribere legenda, beatissimos vero quibus utrumque.

— *Gaius Plinius Caecilius Secundus (Plinius Minor), Epistulae VI.16*

—

Ich jedenfalls glaube, dass diejenigen glücklich sind, denen als Geschenk der Götter die Gabe zuteil geworden ist, entweder Dinge zu tun, die es Wert sind aufgeschrieben zu werden, oder Dinge zu schreiben, die es Wert sind gelesen zu werden. Die Glücklichsten sind wahrhaftig diejenigen, die beides erfüllen.

—

I, for one, believe that those are blissful who are gifted by the gods either to do things worth writing down, or to write things worth reading. The most blissful, truly, are those who fulfil both.

Abstract

Systems on the nanoscale are a hot topic in science and technology as they may be applied in future concepts for microprocessors, memory storage and sensors. This PhD thesis covers two nano-scaled systems which promise particularly advantageous properties: rare-earth silicide nanowires on silicon surfaces, a quasi-one-dimensional electronic system, and thin antimony layers on bismuth selenide, a two-dimensional system with topologically protected surface states. These systems have in common that their fascinating properties are due to heavy ions incorporated in the structures. This thesis theoretically investigates them by means of density functional theory (DFT). However, DFT encounters problems when describing such materials since the high atomic numbers of the involved elements give rise to exotic phenomena, e.g. strongly correlated electronic subshells (the incomplete 4f shell of the lanthanoids), strong relativistic effects (topologically non-trivial insulators) and high contributions to the electronic long-range correlation (“van der Waals interactions”). These problems are solved by approaches beyond DFT, including LDA+U, spin-orbit coupling and dispersion corrections.

Both systems investigated in this work have higher-dimensional prototype structures, which are explored at first and then scaled down to the final nanostructures. Different structure models are set up and optimised regarding the ionic positions. Their stability is evaluated by means of ab initio thermodynamics and phase diagrams are derived. For the most stable structure models, the electronic properties are calculated, including band structures, Fermi surfaces and simulated scanning tunnelling microscopy. All theoretical findings on the structural and electronic properties are carefully compared with experimental reference. In this way, a conclusive ab initio framework is established for these systems, which permits a deep understanding of the underlying physics. Furthermore, novel and fascinating phenomena are identified. The rare-earth silicide nanowires on Si(557) show a unique dimensional crossover, which gives rise to quasi-one-dimensional, metallic edge states. The thin antimony layers are proven to underlie a complex interplay with the topologically protected surface states of the bismuth selenide surface, which involves an intricate series of topological phase transitions.

Zusammenfassung

Nanoskopische Systeme sind ein heißes Thema in Wissenschaft und Forschung, da sie Anwendung in künftigen Konzepten für Mikroprozessoren, Datenspeicher und Sensoren finden könnten. Diese Dissertation behandelt zwei nanoskopische Systeme, die besonders vorteilhafte Eigenschaften versprechen: Seltenerdsilizidnanodrähte auf Siliziumoberflächen, ein quasi-eindimensionales elektronisches System, und dünne Antimonlagen auf Bismutselenid, ein zweidimensionales System mit topologisch geschützten Oberflächenzuständen. Diesen Systemen ist gemein, dass ihre faszinierenden Eigenschaften auf die Einbindung schwerer Ionen in die Strukturen zurückzuführen sind. Diese Dissertation untersucht sie mittels der Dichtefunktionaltheorie (DFT). Jedoch ist die DFT problematisch in der Beschreibung solcher Materialien, da die hohen Ordnungszahlen der beteiligten Elemente exotische Phänomene verursachen, z.B. stark korrelierte elektronische Unterschalen (die inkomplette 4f-Schale der Lanthanoide), starke relativistische Effekte (topologisch nicht-triviale Isolatoren) und hohe Beiträge zur langreichweitigen elektronischen Korrelation („van-der-Waals-Wechselwirkungen“). Diese Probleme werden durch Methoden jenseits der DFT gelöst, u.a. LDA+U, Spin-Bahn-Kopplung und Dispersionskorrekturen.

Für beide in dieser Arbeit untersuchten Systeme existieren höherdimensionale Strukturprototypen, die zunächst erforscht und danach auf die finalen Nanostrukturen herunter skaliert werden. Verschiedene Strukturmodelle werden aufgesetzt und bezüglich der ionischen Positionen optimiert. Ihre Stabilität wird mittels ab initio-Thermodynamik ausgewertet und Phasendiagramme werden aufgestellt. Für die stabilsten Strukturmodelle werden die elektronischen Eigenschaften berechnet, darunter Bandstrukturen, Fermiflächen und simulierte Rasterelektronenmikroskopie. Alle theoretischen Ergebnisse für die strukturellen und elektronischen Eigenschaften werden sorgfältig mit experimenteller Referenz verglichen. Auf diese Weise wird für diese Systeme ein geschlossenes Rahmenwerk konstruiert, das ein tiefes Verständnis der zugrunde liegenden Physik ermöglicht. Des Weiteren werden neuartige und faszinierende Phänomene identifiziert. In den Seltenerdsilizidnanodrähten wird ein einzigartiger dimensionaler Übergang entdeckt, der quasi-eindimensionale metallische Kantenzustände erzeugt. Den dünnen Antimonlagen wird nachgewiesen, dass sie einem komplexen Zusammenspiel mit den topologisch geschützten Oberflächenzuständen der Bismutselenidoberfläche unterworfen sind, das eine komplizierte Reihe von topologischen Phasenübergängen beinhaltet.

Contents

1	Introduction	1
1.1	The microprocessor	2
1.2	The structure of this work	8
2	Methods	9
2.1	Density functional theory	9
2.1.1	The LDA+U method	12
2.1.2	Spin-orbit coupling in DFT	16
2.1.3	Van der Waals corrections	17
2.2	The Bloch theorem	19
2.2.1	Basis changes	22
I	Rare-earth silicide nanowires on silicon surfaces	25
3	Chemical background	28
3.1	The rare-earth elements	28
3.2	Silicon and silicides	32
4	The rare-earth silicide bulk phases	34
4.1	Structure prototypes	35
4.2	Structure optimisation	41
4.2.1	Methodological details	41
4.2.2	The stoichiometric RESi_2 phases	45
4.2.3	The role of the 4f electrons in RESi_2	47
4.2.4	Vibrational contributions in RESi_2	50
4.2.5	The vacancy-populated RESi_{2-x} phases	52
4.2.6	The CaSi_2 phases	59
4.3	Electronic properties	62
4.4	Discussion and summary	69
5	Monolayer films on silicon(111)	71
5.1	Structure optimisation	72
5.2	Electronic properties	79
5.2.1	Band structures	79
5.2.2	Charge transfer	85
5.2.3	Fermi surfaces	86
5.3	Discussion and summary	88
5.3.1	Strain induced growth?	89

6	Nanowires on silicon(557)	91
6.1	Structure optimisation	92
6.2	Electronic properties	97
6.2.1	Band structures	97
6.2.2	Fermi surfaces	100
6.3	Discussion and summary	103
II	Thin antimony layers on bismuth selenide	105
7	Geometric phases	108
7.1	The Aharonov-Bohm effect	108
7.2	The Berry phase	111
7.3	The electric polarisation in a crystal	113
7.4	Topological transport	116
7.4.1	The integer Hall effect	116
7.4.2	The two-dimensional \mathbb{Z}_2 insulator	120
7.4.3	The three-dimensional \mathbb{Z}_2 insulator	128
8	The bulk phases of bismuth selenide and antimony	131
8.1	Bismuth selenide	132
8.1.1	Structure optimisation	133
8.1.2	Electronic properties	135
8.2	Antimony	137
8.2.1	Structure optimisation	138
8.2.2	Electronic properties	139
8.3	Discussion and summary	142
9	The antimony on bismuth selenide heterostructure	143
9.1	Structure optimisation	144
9.1.1	The stacking sequence of the adlayer	145
9.1.2	The effects from SOC and vdW on the heterostructure	148
9.2	Electronic properties	149
9.2.1	Band structures	149
9.2.2	Simulated STM images	154
9.3	The topological phase transition	156
9.4	Discussion and summary	160
10	Conclusions	162
	Appendix	A1
	Bibliography	A15
	Publication list	A24
	Danksagung	A25

List of Figures

1.1	Performance development of the Top500 list	6
3.1	Atomic radii of the REs.	31
4.1	Overview over the RESi_2 structure prototypes.	36
4.2	Possible configurations of ordered Si vacancies in $\text{RESi}_{1.67}$	36
4.3	Schematic phase diagram of the Tb–Si system.	39
4.4	Murnaghan fits of TbSi_2 , DySi_2 , HoSi_2 and ErSi_2 in the hex- AlB_2 and the tet- ThSi_2 phase.	46
4.5	Vibrational free energies of hex- AlB_2 - TbSi_2 , ort- AlB_2 - TbSi_2 and tet- ThSi_2 - TbSi_2 and the corrected Tb chemical potentials $\mu_{\text{Tb}}(T)$ calculated in different supercells.	52
4.6	Structure models of vacancy-populated TbSi_{2-b}	54
4.7	Linear interpolation of $\Delta\mu_{\text{RE}}$ for TbSi_{2-x} and ErSi_{2-x} between $x = \frac{1}{3}$ and $x = 0$	57
4.8	Models of TbSi_2 in the ort- AlB_2 , tr3- CaSi_2 and tr6- CaSi_2 structures. . .	60
4.9	Band structures of tet- ThSi_2 - TbSi_2 and hex- AlB_2 - TbSi_2	63
4.10	Band structures of hex- AlB_2 - TbSi_2 and ort- AlB_2 - TbSi_2	65
4.11	Band structures of trivalent and f-valent, FMO ort- AlB_2 - RESi_2	67
4.12	Band structures of hex- AlB_2 - TbSi_{2-b} and ort- AlB_2 - TbSi_2	68
4.13	Charge transfer in ort- AlB_2 - TbSi_2 and hex- AlB_2 - RESi_{2-b}	69
5.1	Sketch of the Si(111) slab and the TbSi_2 monolayer structures.	74
5.2	Tb chemical potentials of the monolayer- $\text{Tb@Si}(111)$ structures and decision tree for the energy penalties upon structure variations.	76
5.3	Vertical positions and distances of the atomic layers in the monolayer- $\text{Tb@Si}(111)$ structures.	77
5.4	Band structures of the T_4 -h-B structure and the clean Si(111) surface.	80
5.5	Band structures of the monolayer- $\text{Tb@Si}(111)$ structures.	83
5.6	Band folding of the bulk TbSi_2 structures.	84
5.7	Charge transfer in T_4 -h-B.	86
5.8	Fermi surfaces of the monolayer- $\text{Tb@Si}(111)$ structures.	87
5.9	Energy surfaces of T_4 -h-B at different energy levels.	87
6.1	Sketch of the Si(551) slab and the optimised TbSi_2 nanowire structures.	93
6.2	Band structures of dense and sparse nanowires on Si(557) and the monolayer on Si(111).	98
6.3	Segmentation of the Brillouin zone of the monolayer.	99
6.4	Band structures of the nanowires and projected bands of the monolayer. . .	100
6.5	Fermi surfaces of the $\text{Tb@Si}(hkh)$ systems.	102

7.1	Sketch of the ABE setting.	110
7.2	Path for calculating the electric polarisation as a geometric phase.	115
7.3	Sketch of the directions of the integer Hall effect and path of ξ on the Brillouin torus for calculating the topological transport.	118
7.4	Sketch of the reciprocal space of the T-symmetric Bloch system and flow chart of the connection between the partial polarisations \mathbf{P}^I and \mathbf{P}^{II} , the total polarisation \mathbf{P}^+ and the time-reversal polarisation \mathbf{P}^-	124
7.5	Sketch of the Laughlin-type gedankenexperiment and sketches of possible topologies of T-symmetric edge band structures.	127
7.6	TRIMs Γ_i in a cubic Brillouin zone.	128
8.1	Bulk structure of Bi_2Se_3	133
8.2	Band structure of Bi_2Se_3 for the rhombohedrally centred DFT-D2+SOC structure.	136
8.3	Bulk structure of β -Sb.	138
8.4	Band structure of bulk β -Sb and isolated β -Sb sheets.	140
9.1	Sketch of the BS(0001) slab.	145
9.2	Sb chemical potentials μ_{Sb} and interlayer distances d_1 and d_2 of the structure models for the Sb@BS system optimised with DFT-D2+SOC.	147
9.3	Interlayer distances d_1 and d_2 of 1BL-Sb and 2BL-Sb optimised with different treatments.	149
9.4	Band structures of the clean Bi_2Se_3 surface and the heterostructures 1BL-Sb and 2BL-Sb optimised with DFT-D2+SOC.	150
9.5	Comparison between the theoretical band structures and ARPES images of the heterostructures 1B-Sb and 2BL-Sb.	152
9.6	Spin texture of the clean Bi_2Se_3 surface and the heterostructures 1BL-Sb and 2BL-Sb.	153
9.7	STM images of 1BL-Sb and 2BL-Sb.	155
9.8	Real-space isosurfaces of the wavefunctions at the Dirac points D and D^* of the clean substrate, (b) 1BL-Sb and (c) 2BL-Sb.	156
9.9	Hexagonal Brillouin zone with TRIMs.	157
9.10	Topological phase transitions in the Sb@BS heterostructure.	158
B.1	Band structures of hex- $\text{AlB}_2\text{-TbSi}_2$, hex- $\text{AlB}_2\text{-Si}_2$, ort- $\text{AlB}_2\text{-TbSi}_2$ and ort- $\text{AlB}_2\text{-Si}_2$	A8
B.2	Band structures of trivalent and f-valent tet- $\text{ThSi}_2\text{-TbSi}_2$	A8
C.1	Band structures of 1BL-Sb and 2BL-Sb structure models with different stacking optimised with DFT-D2+SOC.	A13

List of Tables

3.1	Valencies of the lanthanoids occurring in aqueous solution and VEC of the trivalent ions.	30
4.1	Bulk mechanical properties of TbSi ₂ , DySi ₂ , HoSi ₂ and ErSi ₂ in the hex-AlB ₂ and the tet-ThSi ₂ phase.	46
4.2	Lattice parameters and relative RE chemical potentials of TbSi ₂ , DySi ₂ , HoSi ₂ and ErSi ₂ in the hex-AlB ₂ and the tet-ThSi ₂ phase.	46
4.3	Lattice parameters and relative Tb chemical potentials of TbSi ₂ in the AlB ₂ and the ThSi ₂ phase under different f-electron treatments. . . .	48
4.4	Lattice parameters and relative Er chemical potentials of ErSi ₂ in the AlB ₂ and the ThSi ₂ phase under different f-electron treatments. . . .	49
4.5	Lattice parameters and relative Tb chemical potentials of TbSi ₂ in the AlB ₂ and the ThSi ₂ phase in orthorhombic Tb ₄ Si ₈ cells.	51
4.6	Lattice parameters and relative Tb chemical potentials of TbSi _{2-x} in the stoichiometric and the vacancy-populated AlB ₂ and ThSi ₂ phases. . .	55
4.7	Si-Si nearest-neighbour distances in TbSi _{2-x} optimised with PBE. . .	58
4.8	Lattice parameters and relative Tb chemical potentials of stoichiometric TbSi ₂ in the AlB ₂ and CaSi ₂ phases.	61
5.1	Bond distances and angles in the monolayer-Tb@Si(111) structures. .	77
8.1	Lattice parameters of bulk Bi ₂ Se ₃	135
8.2	Lattice parameters of bulk β-Sb.	139
9.1	Sb chemical potentials μ _{Sb} , basal lattice constants <i>a</i> and interlayer distances <i>d</i> of 2D and 3D β-Sb systems.	146
B.1	Lattice parameters and relative Er chemical potentials of ErSi _{2-x} in the stoichiometric and the vacancy-populated AlB ₂ and ThSi ₂ phases. . .	A6
B.2	Si-Si nearest neighbour distances in TbSi _{2-x} optimised with different xc-functionals.	A6
B.3	Si-Si nearest neighbour distances in ErSi _{2-x} optimised with different xc-functionals.	A7
B.4	Lattice parameters and relative RE chemical potentials of TbSi ₂ and ErSi ₂ in the stoichiometric AlB ₂ and CaSi ₂ phases.	A7

Acronyms

ABE Aharonov-Bohm effect	108
AMO antiferromagnetically ordered	48
ARPES angle-resolved photoemission spectroscopy	26
BL bilayer (layers consisting of two atomic sublayers)	138
CB conduction band	82
CBM conduction band minimum	80
CI conventional insulator	107
DFT density functional theory	8
DOS density of states	40
FMO ferromagnetically ordered	48
GGA generalised-gradient approximation	12
HPC high-performace computer	6
IHE integer Hall effect	105
LDA local density approximation	12
LDOS local density of states	154
LEED low-energy electron diffraction	78
MEIS medium-energy ion scattering	78
MOSFET metal-oxide-semiconductor field-effect transistor	2
PAW projector-augmented wave	17
PBE Perdew-Burke-Ernzerhof functional	12
PBEsol Perdew-Burke-Ernzerhof functional revised for solids	12
pBZ prmitive Brillouin zone	97
PDOS partial density of states	62
QE Quantum Espresso (https://www.quantum-espresso.org/)	9
QL quintuple layer (layers consisting of five atomic sublayers)	132
RE rare-earth element	25

sBZ supercell Brillouin zone	97
SKP surface Kramers pair	156
SOC spin-orbit coupling	9
STM scanning tunnelling microscopy	26
STS scanning tunnelling spectroscopy	26
TI topological insulator	106
TRIM time-reversal-invariant momentum	121
TSS topologically protected surface state	107
UHV ultra-high vacuum	146
VASP Vienna Ab initio Simulation Package (https://www.vasp.at/)	9
VB valence band	159
VBM valence band maximum	79
vdW van der Waals	1
VEC valence electron configuration	28
XRD X-ray diffraction	34
ZKB Zintl-Klemm-Busmann concept	33

Erklärung

Ich erkläre: Ich habe die vorgelegte Dissertation selbstständig und ohne unerlaubte fremde Hilfe und nur mit den Hilfen angefertigt, die ich in der Dissertation angegeben habe. Alle Textstellen, die wörtlich oder sinngemäß aus veröffentlichten Schriften entnommen sind, und alle Angaben, die auf mündlichen Auskünften beruhen, sind als solche kenntlich gemacht. Ich stimme einer evtl. Überprüfung meiner Dissertation durch eine Antiplagiat-Software zu. Bei den von mir durchgeführten und in der Dissertation erwähnten Untersuchungen habe ich die Grundsätze guter wissenschaftlicher Praxis, wie sie in der „Satzung der Justus-Liebig-Universität Gießen zur Sicherung guter wissenschaftlicher Praxis“ niedergelegt sind, eingehalten.

Ort, Datum

Unterschrift

1 Introduction

Systems on the nanoscale are one of the most active scientific research fields. They all have in common that they trap particles in less than three spatial dimensions: surfaces (2D), nanowires (1D), quantum dots (0D) and systems with dimensions in between. The reduced dimensionality gives rise to fascinating physical phenomena, some of them are of pure quantum nature. The research efforts in the broad field of nano-scaled systems are driven by two major motives. On the one hand, nano-structured devices may be applied in new technologies, e.g. for processors, memory storage and sensors. On the other hand, nano-scaled systems provide also the opportunity to observe and understand fundamental physical principles which are otherwise predicted by theoretical frameworks.

This PhD thesis investigates two groups of low-dimensional systems. The **rare-earth silicide nanowires on silicon surfaces** are ensembles of few nanometre wide and several 100 nm long RESi_2 strips which grow horizontally on silicon substrates. Since bearing highly anisotropic metallic states, they are promising candidates for quasi-one-dimensional electronic systems. The **thin antimony layers on bismuth selenide** are van der Waals heterostructures consisting of a topologically non-trivial Bi_2Se_3 substrate and a few atomic layers thick Sb adsorbate. Such heterostructures constitute a junction between materials of different dimensions and different topological classes. Therefore, they bear a complex system of two-dimensional metallic surface states, which have a unique spin texture and are protected by topology. Although the two systems seem to be very different at first glance, they have in common that they involve the heaviest non-radioactive elements of the periodic table: the lanthanoids (La–Lu, $Z \in [57, 71]$) and bismuth (Bi, $Z = 83$), both located in the sixth and last stable row. The high atomic numbers of the constituents are responsible for the unique properties of the systems and give rise to exciting phenomena. A further common property of the systems is the practical motivation that they both may play a role in future processor technology. The nanowires are interesting from the point of view of miniaturising the feature sizes. The $\text{Sb@Bi}_2\text{Se}_3$ heterostructures are interesting for spintronics, an alternative concept of circuits based on spin densities.

Before the investigations of the above systems begin, the applicability-related motivation will be elaborated in more detail. In short, it is all about Moore's law approaching its limit. However, solely stating the emergence of general problems would be too superficial to understand the technical and economic challenges impending in the medium-term future. Therefore, a short overview of the microprocessor is given, beginning with the success story of the computer and the silicon-based integrated circuits. It is followed by the problems which the semiconductor and computer industry will encounter in the 2020s. These considerations clarify why so much effort is put into developing concepts for novel electronics.

1.1 The microprocessor

There are probably no technical component which has been affecting humankind more than the microprocessor. Being part of nearly every device, microprocessors are not only present in obviously computer-like devices, e.g. smartphones, laptops and tablets. Also smart devices like watches, TVs, sound systems and kitchen equipments contain small data-processing semiconductor chips, which run more or less elaborate programs to facilitate our life. Since the breakthrough of home automation, formerly simple devices like thermostats, plug sockets and light switches have been upgraded by processing units as well. They can be integrated into a “network of smart things” where they communicate with each other, controlled by a computer-based central control unit. Microprocessors do not only inspire intelligence into individual components. Also the internet, on which every job in every economic sector depends, is based on servers, which are accumulations of microprocessors.

A striking example for how strong technological progress depends on powerful computing units are cars. Despite their seemingly simple purpose to transport passengers or freight, they are equipped with many microcontrollers and processors. The R&D departments of the automotive industry are quite busy with developing computing hardware and software as the abilities of a car become a growingly important sales argument, beside CO₂-neutral vehicle propulsion. Modern cars have an interface which looks rather like a smartphone display than a traditional car interface. The superficial applications like the board info, the navigation system or the smartphone integration are only the visible output from the built-in microprocessors. Moreover, there are advanced driver-assistance systems, such as adaptive cruise control and lane centring, which are driven by processing units: the input from many sensors is converted into output for the steering, braking and acceleration actuators. As Germany licensed autonomous driving this year¹, the future cars will require even more powerful and, in particular, reliable processing units – on boards and off board – to cope with the complexity of traffic.

A historical note

The history of the microprocessor is intricate as several parallel trends lead to those silicon-based microprocessors which keep our modern world running. There were two main threads: the development of the computer, which includes the fundamentals on how to run a program on a machine, and the invention of the metal-oxide-semiconductor field-effect transistor (MOSFET), which permitted miniaturising the chip features. The history can be experienced in respective museums. The world’s largest computer museum is the Heinz-Nixdorf-Forum in Paderborn, Germany, dedicated to Heinz Nixdorf, an important entrepreneur in the German computer industry. It offers many exhibits about mathematics, calculation machines and computers from the past to the present, including original parts of famous computers

¹*Bald fahren autonome Fahrzeuge in Deutschland*, <https://www.faz.net/aktuell/wirtschaft/bald-fahren-autonome-fahrzeuge-auf-deutschen-strassen-17827948.html> (visited on 24/05/2022).

which fundamentally changed the world². The development of the transistor and the microprocessor is comprehensively demonstrated as a timeline by the Computer History Museum near San Jose, California³. The important milestones, which can be found also on the museum websites, are summarised in the following paragraphs.

The development of the computer began with the emergence of relay-based calculators in the 1930s. Konrad Zuse developed the first programmable, program-controlled machines in Germany. The most famous is the Z3 machine (1941), which was a purely binary computer and, thus, capable for floating-point arithmetic. At the same time, several relay-based, decimal machines were developed in the USA. Driven by their participation in World War II, the USA needed fast machines for ballistic calculations and for the development of nuclear weapons. The *Harvard Mark I* machine (1944) by Howard H. Aiken was an early example, which, like the other machines, was slow since based on mechanical relays. J. Presper Eckert and John Mauchly had the idea to replace the slow relays with faster vacuum tubes. They presented the first purely electronic computer at the University of Pennsylvania in 1946: the *Electronic Numerical Integrator and Computer* (ENIAC). Although it was a 1000 times faster than relay-based machines, the ENIAC had the drawback that “programming” consisted in plugging cables, a procedure which could take several days. At that time, John von Neumann, who worked in the atomic bomb projects, was looking for machines capable of doing calculations on detonators and ignition heights. He soon got notice of the ENIAC and joined the ENIAC team to develop a stored-program successor: the *Electronic Discrete Variable Automatic Computer* (EDVAC, 1952). Its design, the *von-Neumann architecture* comprising the arithmetic unit, the control unit, the memory, input and output, is the basic principle for most of our modern computers².

The basic ingredient for all computers is the *transistor*. In its simplest form, it has three contacts: the source, the drain and the gate. In principle, it blocks the current between the source and the drain, until the gate receives a signal. Relays and vacuum tubes were the first “transistors”, which did their job, but could not noteworthily be miniaturised. This inspired researchers to pursue the concept of solid-state transistors, realised at the interface of materials with different carrier chemical potentials. Although early ideas had already been proposed in the 1920s, it was not before 1947, until a working point-contact transistor was invented by William Bradford Shockley, John Bardeen and Walter Houser Brattain at Bell Labs. The fundamentality of their invention was acknowledged with the Nobel Prize in Physics in 1956⁴. Short after the group at Bell Labs, Herbert Mataré and Heinrich Welker independently invented the point-contact transistor in Paris in 1948. In 1951, Gordon Teal and Morgan Sparks from Bell Labs fabricated the first working *npn*-transistor. It soon replaced the vacuum tubes in many products, e.g. radios and clocks, until it dominated the world electronics market less than ten years later. The fast growing transistor market was accompanied by the foundation of several companies, of which some still

²*THE INVENTION OF THE COMPUTER*, <https://www.hnf.de/en/permanent-exhibition/exhibition-areas/the-invention-of-the-computer.html> (visited on 14/04/2022)

³*TIMELINE*, <https://www.computerhistory.org/siliconengine/timeline/> (visited on 15/04/2022)

⁴*All Nobel Prizes in Physics*, <https://www.nobelprize.org/prizes/lists/all-nobel-prizes-in-physics/> (visited on 04/03/2022).

exist today: Intermetall (West Germany, today part of TDK-Micronas), Texas Instruments (USA) and the Tokyo Telecommunications Company (Japan, renamed to Sony in 1958). Of course, computers were upgraded with transistors as well. The first fully transistorised computer was the TRAnsistor DIgital Computer (TRADIC), developed at Bell Labs in 1954 and used by the U.S. Air Force.

In the first half of the 1950s, germanium transistors dominated the market as they are easier to fabricate and can operate at higher frequencies than silicon transistors. However, the operational temperature of germanium devices is limited to a range of 0 °C to 70 °C, whereas silicon devices work in a broader temperature range of –55 °C to 125 °C. This excluded germanium devices in particular from aerospace technology, which required devices operating reliably under extreme conditions. Although Morris Tanenbaum from Bell Labs succeeded in developing a working silicon transistor in Jan. 1954, the laboratory misjudged the importance of his work and decided not to pursue the silicon approach any more. Three months later, in Apr. 1954, Gordon Teal, who had changed from Bell Labs to Texas Instruments by the time, succeeded in the synthesis of a silicon transistor as well – unknowingly about Tanenbaum’s work. After this breakthrough, silicon transistors quickly conquered the market and had replaced the germanium transistors by the end of the decade. The 1950s were also the decade in which important fabrication techniques were developed, including diffusion processes, oxide masking and photolithography. These techniques combined produced the planar integrated circuit, released in 1960. Finally, the MOSFET permitted a fast miniaturisation of the features of integrated circuits. While the first patent for a field-effect transistor was written by Julius Lilienfeld in 1928, the successful fabrication was not achieved before 1960 by Mohammed M. Atalla and Dawon Kahng at Bell Labs. Since 1964, MOSFET-based integrated circuits have been sold and, since the beginning of the 1970s, the central processing components of computers have been integrated into central processing units (CPUs), called microprocessors today^{3 5}.

Moore’s Law

Since their breakthrough, planar integrated circuits had smaller features with each new generation so that more transistors could be assembled on a chip of fixed size. Consequently, they became more and more powerful while their costs of production and the energy demand decreased. In 1965, Gordon Moore stated his famous law in an internal correspondence, telling that the number of transistors per chip grows over time at exponential speed. He estimated the doubling time to 12 months at first and corrected it to two years in 1975. Since then, Moore’s law has been a self-fulfilling prophecy as the semiconductor industry benchmarks its new releases

⁵In the course of technical break-overs, the topography of companies underwent many changes. The most important one was the foundation of the Shockley Semiconductor Laboratory by William Shockley and Arnold Beckman in 1955. They recruited several capable people, among them Gordon Moore and Robert Noyce. After differences between Shockley and his employees, Moore, Noyce and six other colleagues left the company to found the Fairchild Semiconductor Corporation in Palo Alto, California, in 1957. This was the birth of Silicon Valley, named after the breakthroughs based on the silicon transistor. Several startups and spin-offs of Fairchild still exist today, among them Intel (from INTegrated ELectionics, founded by Moore and Noyce) and Advanced Micro Devices (AMD, founded by Jerry Sanders, a sales manager at Fairchild who was singed off).

to compete with Moore's prediction. Although it has been valid for several decades, it encountered problems, of which the first emerged in the 1980s: The growing complexity of the chips required an increasing number of production steps and specialised machines which were distributed over a growing number of companies. This made the costs of developing new chip generations explode. To maintain Moore's law, the US semiconductor industry initiated a board consisting of engineers from several semiconductor companies worldwide. It developed the International Technology Roadmap for Semiconductors in 1998, which, updated every second year, should facilitate the coordination, identify upcoming problems early and find solutions for them so as to maintain the technological progress [1].

The first principal problem arose in the early 2000s, when the transistors became so dense that the heat could not dissipate any more. The temperature problem forced the manufacturers to limit the clock rates, which have not exceeded a few GHz until today. In order to still gain computational power from feature miniaturisation, the processor was divided into cores which each represent a closed processing unit. Provided that a program is parallelisable, i.e. it can be divided into independent chunks which can be distributed over the cores to be run in parallel, the total calculative capability of a processor is proportional to the clock rate multiplied with the number of cores [1]. The multi-core strategy maintained Moore's law until the second principal problem arose. When the feature sizes drop below a few 10 nm, quantum mechanical effects like electron tunnelling produce undesirable leakage currents. The complementary metal-oxide semiconductor (CMOS, a combination of *p*-type and *n*-type MOSFETs) was the last planar processor technology, which hit the physical limits at the 22 nm technology node⁶ in the 2010s. Smaller features were realised with the fin field-effect transistor (FinFET), which exploits the third dimension to a certain extent. In 2020, the most miniaturised processors belonged to the 5 nm technology node with ~100 million transistors per square millimetre. However, the term "5 nm" is misleading as it refers to the minimum feature width instead of the average half pitch, which is in the range of 10 nm⁷. This marketing-driven redefinition of the feature sizes cannot obfuscate that the development of the transistor density clearly begins to deviate from Moore's law⁸. Further miniaturisation might be physically possible and is actually planned. However, the development costs grow faster than the transistor density as each new processor generation requires a new set of more precise production facilities. Therefore, it is likely that Moore's law will cease for economical reasons before it reaches the physical limits [1].

The emergence of high-performance computing

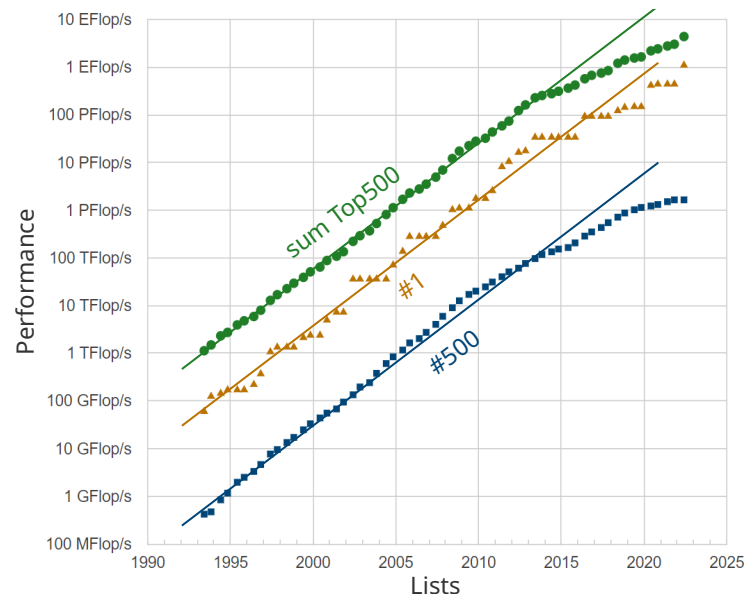
Scientific research and technological progress have become crucially dependent on the internet and on powerful computing facilities. Today's science is based on the solution of complex numerical problems and the evaluation of huge amounts of data,

⁶22 nm refer to the half distance between repeating features, the half pitch; *22 nm process*, https://en.wikipedia.org/wiki/22_nm_process (visited on 18/04/2022)

⁷*5 nm process*, https://en.wikipedia.org/wiki/5_nm_process (visited on 18/04/2022).

⁸*Intel Now Packs 100 Million Transistors in Each Square Millimeter*, <https://spectrum.ieee.org/nanoclast/semiconductors/processors/intel-now-packs-100-million-transistors-in-each-square-millimeter> (visited on 18/04/2022).

Figure 1.1: Performance development of the Top500 list [W10]. Green → sum of the list; Orange → leading machine; Blue → last machine. The lines are guides for the eyes to demonstrate the exponential growth and its recent slowdown.



which both exponentially grow in size. Consequently, the calculative demand of research has exceeded the capability of local computers, which are limited in performance, even if equipped with multicore CPUs. Therefore, the numerics are outsourced to large servers providing thousands of CPUs: the high-performance computers (HPCs) or supercomputers. A very recent example for HPC-aided science is the research related to the SARS-CoV2 pandemic: HPC resources have been supporting the investigations of the interaction between the spike protein of the virus and the human ACE2 receptors, the development of remedies and vaccines, and the analysis of the infection spread⁹. A further example is the large hadron collider (LHC) at CERN: Even after filtering the experimental data, the LHC produces one petabyte (10^6 GB) of data per day¹⁰, which can only be stored and analysed by huge computing facilities. In addition to the numerics based on classical programs, artificial intelligence (AI) has emerged as a tool for analysing scientific data. The growth in demand for HPC facilities is thus expected to remain undiminished.

The fast growth of the world's computing facilities can impressively be demonstrated by the Top500 list of the world's largest supercomputers¹¹. In 1993, right after my birth, the total peak performance of the Top500 amounted to $1.1 \cdot 10^{12}$ floating-point operations per second (FLOPS) or – with the appropriate prefix – 1.1 TFLOPS. To classify this number, consider that a modern smartphone has a peak performance of a few GFLOPS, so the top 500 smartphones in 2022 have more computational power than the Top500 supercomputers in 1993. Today, almost 30 years later, the Top500 peak performance has passed six orders of magnitude – or two prefixes –

⁹Mit Höchstleistungsrechnern und Data Analytics gegen das Coronavirus, <https://www.gesundheitsindustrie-bw.de/fachbeitrag/aktuell/mit-hoechstleistungsrechnern-und-data-analytics-gegen-das-coronavirus> (visited on 13/04/2022).

¹⁰Storage, <https://home.cern/science/computing/storage> (visited on 13/04/2022).

¹¹PERFORMANCE DEVELOPMENT, <https://top500.org/statistics/perfdevel/> (visited on 13/04/2022).

and amounts to 3.0 EFLOPS. It is a matter of time until performance on the exascale is provided by the leading machine on its own. Fig. 1.1 shows that the total performance of the Top500 list grows at exponential speed. From the 1990s to the 2010s, the tenfold-increase time was 4 years. In the last decade, however, the growth has decelerated to a tenfold-increase time of approximately 8 years. Although there is no definite reason for the decline, two points certainly contribute to arising difficulties in setting up more and more powerful supercomputers¹². Firstly, Moore's law, having described the improvement of single processors (single- and multi-core) for decades, approaches its limits. As a consequence, computational power cannot notably improve at the processor level any more. Instead, the number of processors in the HPC facilities grows, which, however, leads to the second problem: Because each processor costs a certain amount of money and consumes a certain amount of electric power, the costs for installing and running a supercomputer inflate with the number of processors. A concrete example for the hugeness of the electric power consumption of modern supercomputers is "Fugaku"¹³ in Japan, the leading supercomputer in 2021 with a peak performance of ~500 PFLOPS. It is supplied with a power of 30 MW, which corresponds to 260 GWh per annum. This equals the electric power demand of 85 000 German average households in 2019¹⁴.

The exploding operating costs put an economic limit on the growth of the world's HPC capacity based on the current technology. In particular, the electricity demand bears a *power-consumption wall* which is already approaching and will become growingly important within the 2020s (see the decline in growth, Fig. 1.1). The power problem even tapers as sustainability policies claim that the significantly growing energy demand of the IT sector must be satisfied by regenerative sources – in addition, to decarbonising all other electric power generation. Thus, the maintenance of the computational progress will certainly be a tough challenge. As the recent chip crisis demonstrates¹⁵, our modern economy is very sensitive towards the availability of more and more capacious computing facilities. A stalling of their growth would entail disruptions in every sector of our everyday life and seriously threaten the progress of science and technology. In order to leave the silicon MOSFET technology, billions of dollars are invested in the exploration of alternative concepts for integrated circuits which permit miniaturising the features, increasing the clock rates and curbing the energy consumption. The two concepts relevant for this work are the field of anisotropic, metallic nanowires, to which the rare-earth silicide nanowires belong, and spintronics, for which the Sb@Bi₂Se₃ heterostructures may be interesting. A break-

¹²TOP500 Meanderings: Sluggish Performance Growth May Portend Slowing HPC Market, <https://www.top500.org/news/top500-meanderings-sluggish-performance-growth-may-portend-slowng-hpc-market/> (visited on 13/04/2022).

¹³TOP 10 Sites for November 2020, <https://top500.org/lists/top500/2020/11/> (visited on 13/04/2022).

¹⁴Stromverbrauch der privaten Haushalte nach Haushaltsgrößenklassen, <https://www.destatis.de/DE/Themen/Gesellschaft-Umwelt/Umwelt/UGR/private-haushalte/Tabellen/stromverbrauch-haushalte.html> (visited on 24/05/2022).

¹⁵Halbleiter-Knappheit – Wie der Chipmangel überwunden werden kann, <https://www.faz.net/aktuell/wirtschaft/digitec/chipmangel-wie-das-problem-ueberwunden-werden-kann-17682182.html> (visited on 24/05/2022), Ende der Chip-Engpässe könnte noch auf sich warten lassen, <https://www.faz.net/agenturmeldungen/dpa/ende-der-chip-engpaesse-koennte-noch-auf-sich-warten-lassen-18027141.html> (visited on 24/05/2022).

through in novel processor technology would end the age of silicon-based MOSFET processors, which have driven the scientific and economic progress for almost 60 years. The replacement of the vacuum tubes by solid-state transistors in the 1950s proves how quick such an adaption can proceed.

1.2 The structure of this work

This thesis is organised in two parts, which are each dedicated to one of the two above-mentioned nano-scaled systems. Both systems are derivable from higher dimensional structure prototypes, which are investigated as well since their properties are necessary for understanding the lower dimensional systems. At the beginning of each part, the respective systems are introduced in a general manner. The first chapter of each part contains preparatory remarks which are necessary for understanding the particular methods employed in that part. The subsequent chapters each treat one system, beginning with an overview over the literature and the formulation of the scientific questions, and concluding with a discussion of the results.

In detail:

Part I treats the rare-earth silicide nanowires in four chapters: the chemical background of the constituents (Chap. 3), the bulk phases of RESi_{2-x} (Chap. 4), the monolayer TbSi_2 film on Si(111) (Chap. 5), and the TbSi_2 nanowires on Si(557) (Chap. 6).

Part II treats the thin antimony layers on Bi_2Se_3 in three chapters: the concept of geometric phases (Chap. 7), the bulk phases of Bi_2Se_3 and Sb (Chap. 8), and the $\text{Sb@Bi}_2\text{Se}_3$ heterostructures (Chap. 9).

The thesis concludes with Chap. 10, where also an outlook on future work is given.

Part of the findings on the nano-scaled systems have already been published. The own and co-authored publications are labelled by a separate indexing system, prefixed by the letter "P". Whenever this thesis addresses those publications, they are referenced accordingly. The full publication list can be found on p. A24. Before the investigations start, the general methods are shortly introduced in Chap. 2, with focus on the density functional theory and its extensions.

2 Methods

The stationary condensed-matter problem consists in solving the eigenvalue equation for the Hamilton operator for N_K nuclei with positions $\{\mathbf{R}_k\}$ and momenta $\{\mathbf{P}_k\}$, and N_e electrons with positions $\{\mathbf{r}_i\}$ and momenta $\{\mathbf{p}_i\}$:

$$H = T_K(\{\mathbf{P}_k\}) + T_e(\{\mathbf{p}_i\}) + V_{e-e}(\{\mathbf{r}_i\}) + V_{K-K}(\{\mathbf{R}_k\}) + V_{e-K}(\{\mathbf{r}_i, \{\mathbf{R}_k\}) \quad (2.1)$$

where $T_K(\{\mathbf{P}_k\})$ are the kinetic energies of the nuclei; $T_e(\{\mathbf{p}_i\})$ are the kinetic energies of the electrons; $V_{e-e}(\{\mathbf{r}_i\})$ are the electron-electron interactions; $V_{K-K}(\{\mathbf{R}_k\})$ are the nucleus-nucleus interactions; $V_{e-K}(\{\mathbf{r}_i, \{\mathbf{R}_k\})$ are the electron-nucleus interactions. Calculating the eigenspace of Eq. (2.1) is a quantum-mechanical “ N -particle problem”, which is insoluble – even within numerics – as $N \sim 10^{24} \approx 1$ mol in typical solid-state systems. Therefore, methods are necessary which simplify the problem.

This chapter presents the main methods employed in this work: the density functional theory (DFT) and the Bloch theorem. While the DFT is quite familiar to most condensed-matter scientists, its extensions might be less known since they are relevant only in special situations. The three approaches relevant for this work are the LDA+U method, spin-orbit coupling (SOC) and van der Waals (vdW) corrections, which are each shortly introduced. Both the DFT and the Bloch theorem are the fundament of many plane-wave codes by means of which the properties of a solid-state system can be calculated. The codes relevant for this work are the Vienna Ab initio Simulation Package (VASP) [2, 3] and Quantum Espresso (QE) [4, 5].

2.1 Density functional theory

The first simplification of the solid-state problem consists in the Born-Oppenheimer approximation. It is based on the assumption that the light electrons follow the movement of the much heavier nuclei instantaneously, hence also called *adiabatic approximation*. Consequently, the electronic subsystem can be separated from the dynamics of the nuclei in that the nuclear positions $\{\mathbf{R}_k\}$ enter the electronic Hamiltonian H_e merely as parameters. The electronic ground state energy $E_e(\{\mathbf{R}_k\})$ in turn determines the potential of the nuclear Hamiltonian H_K [6, pp. 27ff].

$$\begin{aligned} H_e(\{\mathbf{R}_k\}) &= T_e(\{\mathbf{p}_i\}) + V_{e-e}(\{\mathbf{r}_i\}) + V_{e-K}(\{\mathbf{r}_i \mid \{\mathbf{R}_k\}) + V_{K-K}(\{\mathbf{R}_k\}) \\ H_e(\{\mathbf{R}_k\}) \mid \Psi(\{\mathbf{R}_k\}) \rangle &= E_e(\{\mathbf{R}_k\}) \mid \Psi(\{\mathbf{R}_k\}) \rangle \\ H_K &= T_K(\{\mathbf{P}_k\}) + E_e(\{\mathbf{R}_k\}) \end{aligned} \quad (2.2)$$

As the electronic and the nuclear subproblems are disentangled, they can be treated independently. A very common approach is to treat the electronic system quantum-mechanically, while the nuclei (or ions if core electrons are attached) move in their potentials $E_e(\{\mathbf{R}_k\})$ according to classical mechanics. The electronic system can be simplified by exploiting symmetries. Most importantly, the translation symmetry of crystals reduces the infinite number of electrons to a finite one, according to the Bloch theorem (vide infra). Furthermore, the symmetries of the space group remove redundancies in the unit cell. Although the symmetries can reduce the number of interacting electrons to ~ 100 , the computational demand of directly solving the N -particle Schrödinger equation will be still huge. Walter Kohn, who was awarded with the Nobel prize in chemistry for the DFT, impressively demonstrates this in his Nobel prize lecture in 1999 [7, p. 1257]:

For an exemplary accuracy of $O(10^{-2})$ of the total energy, each degree of freedom contributes $3 \leq p \leq 10$ parameters to the Hilbert space of the multi-electron system, resulting in a total number of parameters of

$$M = p^{3N}. \quad (2.3)$$

Even if p is set to the lower boundary, the number of parameters for $N_e = 100$ electrons will exceed any imagination: $M = 3^{3 \cdot 100} \approx 10^{143}$. Kohn states that he “cannot foresee an advance in computer science which can minimize a quantity in a space of 10^{150} dimensions” and referred to Eq. (2.3) as an “exponential wall” [7]. Today, 20 years later, one of the fastest supercomputers in the world is the Hawk machine in Stuttgart, Germany. If its peak performance of $P = 26$ PFLOPS [W16] was used for calculating a quantity like the total energy depending on M parameters, the computation time would be $T = M/P \approx 10^{127}$ s at the minimum. For comparison, the age of the universe amounts to 10^{18} s.

The basic idea of the DFT is that knowing observable quantities of a solid-state system like the total energy E and the ground state electron density $n(\mathbf{r})$ are sufficient for many purposes. The detailed electronic many-particle wavefunction $|\Psi\rangle$ is just a means to an end. The bijective link between these three quantities is ensured by the Hohenberg-Kohn theorem: 1) The electronic ground-state density $n(\mathbf{r})$ is uniquely connected to the external potential $v_{\text{ext}}(\mathbf{r})$ and 2) this ground state density minimises the total energy E of the system [7, 8]. The second part of the theorem leads to the energy functional $E[n(\mathbf{r})]$.

$$E[n(\mathbf{r})] = T_s[n(\mathbf{r})] + V[n(\mathbf{r})] + U[n(\mathbf{r})] + E_{\text{xc}}[n(\mathbf{r})] \quad (2.4)$$

with

$$V[n(\mathbf{r})] = \int d\mathbf{r} n(\mathbf{r})v_{\text{ext}}(\mathbf{r}) \quad \text{and} \quad U[n(\mathbf{r})] = \frac{1}{2} \int d\mathbf{r} \int d\mathbf{r}' \frac{n(\mathbf{r})n(\mathbf{r}')}{|\mathbf{r} - \mathbf{r}'|}$$

The total energy in Eq. (2.4) comprises four terms:

- the single-particle kinetic energy $T_s[n(\mathbf{r})]$ of the electrons
- the interaction between the electrons gas and the external potential $V[n(\mathbf{r})]$

- the classical Coulomb energy of the electron gas $U[n(\mathbf{r})]$ (Hartree term)
- the exchange-correlation functional $E_{\text{xc}}[n(\mathbf{r})]$

The last term, often abbreviated to xc-functional, contains any many-particle effects: the part of the kinetic energy not covered by T_{s} , the exchange energy between electrons with parallel spins and the correlation due to electrostatic repulsion.

Eq. (2.4) can formally be minimised by introducing the Lagrange parameter ε to reflect the boundary condition of particle-number conservation:

$$N_e - \int d\mathbf{r} n(\mathbf{r}) = 0 \quad \Rightarrow \quad 0 = \int d\mathbf{r} \delta n(\mathbf{r}) \cdot \left[\frac{\delta E[n(\mathbf{r})]}{\delta n(\mathbf{r})} - \varepsilon \right] \quad (2.5)$$

Kohn and Sham realised that Eq. (2.5) appears in the self-consistent Hartree scheme. This scheme considers non-interacting electrons which move in an effective potential given by the external potential and their own electron gas. The corresponding energy-density functional comprises $T_{\text{s}}[n(\mathbf{r})]$, $V[n(\mathbf{r})]$ and $U[n(\mathbf{r})]$. Thus, the Hartree scheme can be adapted to the Hohenberg-Kohn functional (Eq. (2.4)) by adding the functional derivative of $E_{\text{xc}}[n(\mathbf{r})]$ to the effective potential [7, 9].

$$n(\mathbf{r}) = \sum_{i=1}^{N_e} f_i |\psi_i(\mathbf{r})|^2 \quad (2.6a)$$

$$\varepsilon_i \psi_i(\mathbf{r}) = \left[-\frac{1}{2} \nabla^2 + v_{\text{ext}}(\mathbf{r}) + v_{\text{H}}(\mathbf{r}) + v_{\text{xc}}(\mathbf{r}) \right] \psi_i(\mathbf{r}) \quad (2.6b)$$

with

$$v_{\text{H}}(\mathbf{r}) = \frac{\delta U[n(\mathbf{r})]}{\delta n(\mathbf{r})} = \int d\mathbf{r}' \frac{n(\mathbf{r}')}{|\mathbf{r} - \mathbf{r}'|} \quad \text{and} \quad v_{\text{xc}}(\mathbf{r}) = \frac{\delta E_{\text{xc}}[n(\mathbf{r})]}{\delta n(\mathbf{r})} \quad (2.6c)$$

The coefficients $f_i \in [0, 1]$ in Eq. (2.6a) are occupation numbers which fill the energetically lowest eigenstates according to a function of choice, e.g. finite-temperature smearing. The *Fermi energy* is defined as the chemical potential of the fermions, coinciding with the highest occupied level if the occupation function is a step function.

Eqs. (2.6), the *Kohn-Sham equations*, define a *self-consistent* scheme for obtaining the electronic ground state:

- 1) Start with a trial charge density $n(\mathbf{r})$ and calculate the potentials $v_{\text{H}}(\mathbf{r})$ and $v_{\text{xc}}(\mathbf{r})$ with Eq. (2.6c).
- 2) Calculate the eigenvalues and eigenstates $\{(\varepsilon_i, \psi_i(\mathbf{r}))_i\}$ of Eq. (2.6b).
- 3) With these states, calculate the new charge density with Eq. (2.6a) and iterate.

The above steps are looped until convergence is reached according to a stop criterion, e.g. the constancy of the total energy $E[n(\mathbf{r})]$ (Eq. (2.4)). The Kohn-Sham scheme maps the many-particle problem of N_e interacting electrons onto an effective system of single-particle differential equations for N_e non-interacting fermions. Therefore, it considerably reduces the computational demand of the solution. The only term which depends on the concrete system is the external potential $v_{\text{ext}}(\mathbf{r})$, while all other

terms depend uniquely and universally on the charge density. Although the Kohn-Sham scheme is formally exact, the unknown xc-functional $E_{xc}[n(\mathbf{r})]$ is a source of uncertainty as it has to be approximated, despite its universality (vide infra).

All density-related quantities are, in principle, observable: the ground state density $n(\mathbf{r})$, the ground state energy $E[n(\mathbf{r})]$ and, hence, all derived quantities, e.g. the ionic forces. On the contrary, the Lagrange parameters ε_i , having the dimension of an energy, and the single particle orbitals $\psi_i(\mathbf{r})$ are mere mathematical artefacts which have no physical meaning a priori. In particular, they are not necessarily observable and can differ considerably from real excitation energies, even if an exact representation of the xc-functional was given.

Several approximations for the xc-functional $E_{xc}[n(\mathbf{r})]$ exist. The best-known is the local density approximation (LDA) which approximates $E_{xc}[n(\mathbf{r})]$ locally by the value for a respective homogeneous electron gas. While systems with slowly varying density can be described well, inhomogeneous systems can incur systematic failures. This can be corrected (and is then likely to be overcorrected) by taking also the gradients of the local density into account, leading to the generalised-gradient approximation (GGA). Perdew et al. proposed a simple implementation of GGA, the Perdew-Burke-Ernzerhof functional (PBE), which avoids several weaknesses of former GGA approaches and in which all parameters are fundamental constants [10]. Although PBE works quite well for atoms and molecules, it overcorrects the overbinding of LDA in solids, so bulk lattice constants are slightly too large by $\sim 1\%$. This issue is addressed by the Perdew-Burke-Ernzerhof functional revised for solids (PBEsol) [11].

The xc-functional is not restricted to scalar electronic densities, but it can be extended to spinorial densities. In this case, the density is a (2×2) matrix $N(\mathbf{r})$. The scalar electron density is then the trace of N and the magnetisation densities are the expectation values of the Pauli matrices $\{\sigma_i\}$:

$$\begin{aligned} n(\mathbf{r}) &= \text{tr}(N(\mathbf{r})) \\ m_i(\mathbf{r}) &= \text{tr}(\sigma_i N(\mathbf{r})) \end{aligned} \tag{2.7}$$

The spinor components couple via the xc-functional, which depends on the scalar electron density $n(\mathbf{r})$ and the total magnetisation density $|\mathbf{m}(\mathbf{r})|$. As the derivatives of the xc-functional yield a (2×2) potential, non-collinear magnetism emerges by this means [12]. Although this approach allows the magnetic moments to assume certain angles to each other, the magnetic structure is still isotropic, i.e. if all magnetic densities are rotated by a rigid angle, the total energy remains the same. Magnetic anisotropy follows from SOC (vide infra).

2.1.1 The LDA+U method

The approximative xc-functionals describe the total-energy-related quantities well if the electrons are delocalised. In some cases, however, DFT fails in finding the correct ground state and yields considerably wrong energies and forces. In particular,

systems with strong electronic correlation are problematic because DFT tends to delocalise electrons and, thus, to weaken correlation effects. An example relevant for this work consists in valence electronic multiplets which populate nearly atomic orbitals. The electronic correlation is then subjected to Hund's rules, which force the electrons into a certain configuration concerning spin and magnetic quantum numbers. In particular, the occupations of the single-particle subshell orbitals $|\varphi_m\rangle$ are integral, ergo 0 or 1. These on-site correlation effects prevail in localised d shells and, even more pronounced, in localised f shells. The LDA+U method, on which Cococcioni wrote a comprehensive discussion [13], addresses this issue.

The approach is based on the orthogonality relations of quantum states, i.e. a localised subshell projects the delocalised electrons forming the chemical bonds out. As a consequence, the intracorrelation of the subshell not covered by DFT is much stronger than the intercorrelation between the subshell and the outer electrons. This permits a selective correction of the former. A suitable ansatz is the Hubbard model, which, being a tight-binding approach, is naturally constructed from a localised basis set. In detail, each localised subshell orbital $|\varphi_m^I\rangle$ with index m and belonging to the atomic site I interacts with each subshell orbital $|\varphi_{m'}^I\rangle$ on the same site. The sum of the pairwise interactions, the Hubbard energy E_{Hub} , is added to the DFT energy functional E_{LDA} . In order to avoid double-counting, the correlation energy E_{dc} which DFT already includes has to be subtracted. It is calculated from the mean-field interaction of the electrons on the respective site, which depends only on their total number.

$$E_{\text{LDA+U}}[n(\mathbf{r})] = E_{\text{LDA}}[n(\mathbf{r})] + E_{\text{Hub}}[\{n_{mm'}^{I\sigma}\}] - E_{\text{dc}}[\{N^{I\sigma}\}] \quad (2.8)$$

where $n(\mathbf{r})$ is the DFT electron density and σ the spin. $n_{mm'}^{I\sigma}$ is the on-site density matrix defined by the projections of the Kohn-Sham eigenfunctions $|\psi_i^\sigma\rangle$ (Eq. (2.6b)) on the localised basis set $\{|\varphi_m^I\rangle\}$ of site I . $\{N^{I\sigma}\}$ is the total number of electrons in the subshell of site I .

$$n_{mm'}^{I\sigma} = \sum_i f_i^\sigma \langle \psi_i^\sigma | \varphi_{m'}^I \rangle \langle \varphi_m^I | \psi_i^\sigma \rangle \quad (2.9a)$$

$$N^{I\sigma} = \sum_m n_{mm}^{I\sigma} \quad (2.9b)$$

where f_i^σ is the occupation function.

In the one-band version of the Hubbard model, each site I can be occupied by two electrons with opposite spin. Only electron pairs on the same site increase the potential energy of the Hamiltonian by the parameter $U > 0$ representing the repulsive Coulomb interaction. In the limit of zero-hopping (total localisation), the Hubbard total energy comprises only the U contributions. If the sites are inequivalent, the parameter U depends on I .

$$E_{\text{Hub},1} = \sum_I U^I n^{I\uparrow} n^{I\downarrow} \quad (2.10)$$

where $n^{I\sigma}$ is the occupation number of site I and spin σ . If two or more orbitals interact on the same site, the total Coulomb interaction equals the sum of two-particle

interactions between all pairs of electrons with different orbital and/or spin quantum numbers on that site. In this case, the total energy comprises not only the Coulomb repulsion between each two electrons, which is modelled by the parameter U . It has also a term describing the attractive exchange interaction between electrons with parallel spin, which is modelled by a second parameter $J > 0$. The Hubbard energy functional $E_{\text{Hub}}[\{n_{mm'}^{I\sigma}\}]$ is then:

$$\begin{aligned}
 E_{\text{Hub}}[\{n_{mm'}^{I\sigma}\}] &= \sum_I \left[\frac{U^I}{2} \sum_{m,\sigma \neq m'\sigma'} n_{mm}^{I\sigma} n_{m'm'}^{I\sigma'} - \frac{J^I}{2} \sum_{m \neq m'} \sum_{\sigma} n_{mm}^{I\sigma} n_{m'm'}^{I\sigma} \right] \\
 &= \sum_{I,\sigma} \left[\frac{U^I}{2} \sum_{m,m'} n_{mm}^{I\sigma} n_{m'm'}^{I(-\sigma)} + \frac{U^I - J^I}{2} \sum_{m \neq m'} n_{mm}^{I\sigma} n_{m'm'}^{I\sigma} \right] \quad (2.11) \\
 &\stackrel{\text{Eq. (2.9b)}}{=} \sum_{I,\sigma} \left[\frac{U^I}{2} N^{I\sigma} N^{I(-\sigma)} + \frac{U^I - J^I}{2} \left(N^{I\sigma} N^{I\sigma} - \sum_m n_{mm}^{I\sigma} n_{mm}^{I\sigma} \right) \right]
 \end{aligned}$$

The double counting term $E_{\text{dc}}[\{N^{I\sigma}\}]$ is approximated by the mean-field interaction of the total number of electrons. If N^\uparrow and N^\downarrow are integers, there are $N^\uparrow \cdot N^\downarrow$ antiparallel spin pairs and $N^\sigma \cdot (N^\sigma - 1)/2$ parallel spin pairs for each spin. The former contribute only repulsive U -terms, the latter repulsive U -terms and attractive J -terms. This can be extrapolated to non-integral $\{N^\sigma\}$.

$$E_{\text{dc}}[\{N^{I\sigma}\}] = \sum_I \left[\sum_{\sigma} \frac{U^I}{2} N^{I\sigma} N^{I(-\sigma)} + \sum_{\sigma} \frac{U^I - J^I}{2} N^{I\sigma} (N^{I\sigma} - 1) \right] \quad (2.12)$$

Inserting Eqs. (2.11) and (2.12) into Eq. (2.8) and using Eq. (2.9b) gives the total correction of the DFT energy functional.

$$\begin{aligned}
 E_{\text{LDA+U}}[n(\mathbf{r})] &= E_{\text{LDA}}[n(\mathbf{r})] + \sum_{I\sigma} \frac{U^I - J^I}{2} \left(N^{I\sigma} - \sum_m n_{mm}^{I\sigma} n_{mm}^{I\sigma} \right) \\
 &\stackrel{(*)}{=} E_{\text{LDA}}[n(\mathbf{r})] + \sum_{I\sigma} \frac{U^I - J^I}{2} \left(\text{tr}(\hat{n}^{I\sigma}) - \text{tr}([\hat{n}^{I\sigma}]^2) \right) \quad (2.13)
 \end{aligned}$$

Step (*) uses that the atomic subshells have a finite and orthonormal basis, the spherical harmonics. Thus, each configuration has an axis along which the density matrices are diagonal. Replacing the them by the density operators $\hat{n}^{I\sigma}$ renders Eq. (2.13) invariant under unitary transformations of the localised basis set [13].

The Hubbard approach to correct the correlation in the DFT is called *LDA+U method* since the U is the most important parameter. It is not restricted to LDA, but it can also be adapted to other functionals like GGA. Eq. (2.13) is the rotationally invariant and simplified LDA+U formulation introduced by Dudarev et al., where the parameters U and J represent the spherically averaged Coulomb integrals [14, 15]. The more general formulation employs explicitly calculated screened Coulomb integrals between

the subshell wavefunctions for E_{Hub} , as proposed by Liechtenstein et al. Nevertheless, the double-counting energy E_{dc} has still to be parametrised by U and J [16]. The simplified formulation in Eq. (2.13) demonstrates important properties of the LDA+U correction. The additive to the DFT functional is always positive if the density matrix is not idempotent¹. Conversely, if \hat{n} is idempotent, i.e. all eigenvalues are 0 or 1, the correction term vanishes. In other words, the LDA+U method penalises fractional occupations and drives the subshell into a state where all orbitals are fully occupied or empty. *Nota bene*, the LDA+U correction in Eq. (2.13) does not explicitly encourage spin polarisation (Hund's second rule) as the effective $(U - J)$ -term does not include a magnetisation-dependent penalty.

An important deficiency of the LDA+U method is the introduction of parameters to the DFT approach, which is otherwise *ab initio* and avoids empirical parameters. The parameters U and J for a particular system are often determined by tuning them so that the materials properties match the experiment (e.g. band gaps, lattice constants). However, this approach opens a gateway for systematic errors because it can overcorrect other, erroneous effects and thus obfuscate weaknesses of the model. A more sophisticated approach is to calculate the parameters self-consistently from linear response, as introduced by Cococcioni. In detail, a small penalty α^I is applied to the Kohn-Sham potential of a certain site I and the effect on the on-site occupations $N^K = N^{K\uparrow} + N^{K\downarrow}$ is measured for sites K . This leads to the susceptibility χ .

$$\chi_{KI} = \frac{dN^K}{d\alpha^I} \quad (2.14)$$

The inverse of χ basically equals the negative Hubbard U , according to the quadratic dependence of the double-counting term on the on-site density N^I (Eq. (2.12)). However, a term from the electronic rehybridisation at constant total density, leading to the susceptibility χ_0 , has to be subtracted [13].

$$U^I = (\chi_0^{-1} - \chi^{-1})_{II} \quad (2.15)$$

The procedure of determining U can be summarised as follows:

- 1) Calculate the self-consistent DFT ground-state density of the system in question.
- 2) Apply an on-site penalty α^I to site I and calculate the respective on-site occupations $N^K(\alpha^I)$ within a non-self-consistent calculation at the fixed ground-state density. This yields χ^0 by Eq. (2.14) and finite differences.
- 3) Repeat 2), but let the charge relax (self-consistent charge density with penalty). This yields χ by Eq. (2.14) and finite differences.
- 4) Calculate U^I with Eq. (2.15).

¹A quadratic matrix \hat{A} is idempotent, if $\hat{A}^2 = \hat{A}$.

Because $\text{tr}(\hat{n}) = 1$ and $\hat{n}^* = \hat{n}$, the Cauchy-Schwarz inequality holds: $\text{tr}(\hat{n}^2) \leq \text{tr}(\hat{n})$.

2.1.2 Spin-orbit coupling in DFT

The steep potentials of nuclei with high atomic numbers give rise to relativistic effects, which must be considered if a material contains elements of the fifth row of the periodic table and beyond. In particular, the elements of the sixth row, the last row containing stable isotopes, are subjected to a considerable relativistic contraction of the atomic shells. As a response to relativistic corrections, the 6s radius shrinks by a few percent for the lighter elements, by $\sim 10\%$ for the heavier ones and by 15% for gold (Au, $Z = 79$), a local extremum [17, pp. 372f].

The fully relativistic version of quantum mechanics is based on the Dirac equation which fulfils the prerequisite of invariance under Lorentz transformations. Being a system of four coupled differential equations, the Dirac equation is demanding, even for a single particle, and contains much redundant information for the purposes of condensed-matter theory. The two approximations to make the relativistics suitable for solid-state systems are the elimination of the small component and a truncated series expansion of the resulting Hamilton operator². The zeroth-order approximation of the correct expansion yields the following Hamilton operator, called CPD Hamiltonian after Chang, Pelissier, and Durand [19, 20]:

$$H_0 = V(\mathbf{r}) + \frac{1}{2m_0}(\boldsymbol{\sigma} \cdot \mathbf{p})\kappa(\mathbf{r})(\boldsymbol{\sigma} \cdot \mathbf{p}) \quad \text{with} \quad \kappa(\mathbf{r}) = \left(1 - \frac{V(\mathbf{r})}{2m_0c^2}\right)^{-1} \quad (2.16)$$

where $V(\mathbf{r})$ is the potential, m_0 the rest mass of the electron, c the speed of light, and \mathbf{r} and \mathbf{p} the canonical variables. As $\boldsymbol{\sigma} = (\sigma_x, \sigma_y, \sigma_z)$ is the vector of Pauli matrices, the Hamilton operator in Eq. (2.16) acts on a 2-spinor. Test calculations on the uranium atom (U, $Z = 92$), in which all core and valence states are affected by relativistics, show that the zeroth order CPD Hamiltonian is quite accurate. It predicts the valence levels very close to those calculated with the full Dirac equation and fails only in predicting the levels of the most inner K and L shells [19].

The commutator relation $[r_i, p_j] = i\hbar\delta_{ij}$ and the algebra of the Pauli matrices lead to the following, more interpretable representation of H_0 :

$$\begin{aligned} (\boldsymbol{\sigma} \cdot \mathbf{a})(\boldsymbol{\sigma} \cdot \mathbf{b}) &= \mathbf{a} \cdot \mathbf{b} + i\boldsymbol{\sigma} \cdot (\mathbf{a} \times \mathbf{b}) & (*) \\ [\mathbf{p}, \kappa(\mathbf{r})] &\stackrel{\text{Eq. (A.93)}}{=} -i\hbar\kappa'(\mathbf{r}) \left(\frac{-\nabla_r V(\mathbf{r})}{2m_0c^2}\right) = \frac{-i\hbar}{2m_0c^2}\kappa^2(\mathbf{r})\nabla_r V(\mathbf{r}) & (**) \\ H_0 &\stackrel{(*)}{=} V(\mathbf{r}) + \frac{1}{2m_0}\mathbf{p} \cdot (\kappa(\mathbf{r})\mathbf{p}) + \frac{i}{2m_0}\boldsymbol{\sigma} \cdot (\mathbf{p} \times (\kappa(\mathbf{r})\mathbf{p})) & (2.17) \\ &\stackrel{(**)}{=} V(\mathbf{r}) + \frac{1}{2m_0}\mathbf{p} \cdot (\kappa(\mathbf{r})\mathbf{p}) + \frac{\hbar}{(2m_0c)^2}\kappa^2(\mathbf{r})\boldsymbol{\sigma} \cdot (\nabla_r V(\mathbf{r}) \times \mathbf{p}) \end{aligned}$$

²An interesting issue of these expansions concerns in the convergence of the series. The traditional expansion in $(E - V)/2m_0c^2$ causes severe problems because electrons have non-zero probability densities near the singularities of a Coulomb potential wherefore the expansion parameter diverges. The expansion in $E/(2m_0c^2 - V)$ leads to a reliable and fast convergence [19].

According to Eq. (2.17), the main relativistic effects can be summarised as two contributions: an alteration in the kinetic energy which, in a simplifying manner, corresponds to the relativistic mass increase and the *spin-orbit coupling* (SOC) term. The name of the latter name becomes obvious after inserting a spherically symmetric potential as in the case of single atoms:

$$H_0^{\text{atom}} = V(\mathbf{r}) + \frac{1}{2m_0} \mathbf{p} \cdot (\kappa(\mathbf{r})\mathbf{p}) + H_{\text{SOC}} \quad (2.18)$$

with $H_{\text{SOC}} = \frac{\hbar}{(2m_0c)^2} \kappa^2(\mathbf{r}) \frac{1}{r} \frac{dV}{dr} \boldsymbol{\sigma} \cdot \mathbf{L}$ and $\mathbf{L} = \mathbf{r} \times \mathbf{p}$

Solving the eigenspace of Eq. (2.18) for solid-states is still demanding wherefore the code package used in this work, VASP, uses a further approximation: As the relativistics is expected to prevail solely in the vicinity of the atomic cores³, the SOC Hamiltonian can be assumed to act solely within the PAW spheres, which are introduced by the projector-augmented wave (PAW) method [21, 22]. As a consequence, H_{SOC} can be expressed solely by means of the PAW projectors which mix the on-site densities of the pseudo-spinor [23]. Moreover, since the PAW projections are still resolved with respect to orbital quantum numbers and spin, it is possible to track the atomic orbitals upon forming chemical bonds even with SOC included.

2.1.3 Van der Waals corrections

Since the correlation part of v_{xc} is local in the charge density or its gradients, DFT bears the general weakness that it describes long-range electronic correlation insufficiently. This is less problematic for systems in which all bonding is covalent or ionic as the atomic overlap lets the xc-functional account for the major part of correlation. However, it can deteriorate the results for materials in which van der Waals interactions dominate the bonding between closed-shell entities.

Van der Waals (vdW) interactions, more precisely the London dispersion effects⁴, arise from fluctuations in charge distributions which polarise the environment. In the demonstrative case of neutral molecules, the temporary dipole moment emerging in one molecule induces dipole moments in the adjacent molecules, which results in a net attractive force. The fundament of such fluctuations consists in the quantum nature of charge, which is the probability density of quantum particles. The mutual dependence of the temporary dipoles leads to their quasi-synchronised occurrence and is thus a type of electronic correlation.

³If the potential vanishes, $\kappa(\mathbf{r})$ is close to unity. Furthermore, the derivative of $V(r)$ vanishes fast for Coulomb-like $1/r$ potentials. Thus, Eq. (2.16) adopts the form of the non-relativistic Hamilton operator $H = V(\mathbf{r}) + \mathbf{p}^2/2m_0$ on domains excluding the neighbourhood of the nuclei.

⁴The original work on interactions between neutral molecules by Johannes Diderik van der Waals included attractive and repulsive forces of differing nature. One of these are the attractive interactions from short-frequency perturbations between polarisable molecules, which were described by Fritz London. He called these interactions the “dispersion effect” as he found that knowledge about the frequency-dependence of the response of the charge densities towards short-frequency perturbations is necessary for correctly calculating the same [24].

The common mistake to avoid when considering vdW interactions consists in the assumption that these interactions are generally small. While this is indeed true for the mutual attraction between isolated atoms, it proves to be completely wrong in dense systems where vdW interactions dominate the intermolecular bonding. For example, the boiling points of hydrogen halides increase with growing halogen atomic numbers, despite the decrease of the static dipole moments. In this case, vdW interactions obviously exceed the interactions between the static dipoles. Not only do vdW interactions influence the intermolecular bonding, but they can also influence the intramolecular bonding. For instance, the alkanes are often employed to demonstrate the positive relation between vdW-related intermolecular attraction and chain length. However, they are also subjected to intramolecular vdW interactions which stabilise branched molecules with respect to the linear ones [25]. Further examples where vdW interactions play an important role are “the structures of DNA and proteins, the packing of crystals, the formation of aggregates, host-guest systems, or the orientation of molecules on surfaces or in molecular films” [26]. Being a dynamic long-range correlation effect, vdW interactions are complicated to describe and numerically expensive. In particular their introduction into DFT is subject of a vivid research activity which tries finding a compromise between numerical feasibility, accuracy and avoiding empirical parameters. The large number of approaches can be classified by their level of sophistication [25]. It is therefore obligatory to test the different vdW schemes in order to find the method which is sufficiently accurate for the respective problem while saving computational resources.

The DFT-D2 method introduced by Grimme will be the most important method in this work. It is a semi-empirical approach which adds the R^{-6} -dependent dipolar dispersion correction for each pair of interacting atoms [26]:

$$E_{\text{disp}}^{\text{DFT-D2}} = -\frac{s_6}{2} \sum_{I \neq J} \frac{C_6^{IJ}}{R_{IJ}^6} f(R_{IJ}) \quad (2.19)$$

where R_{IJ} is the distance between the atoms I and J and s_6 is a universal scaling constant which depends on the xc-functional. The coefficients

$$C_6^{IJ} = \sqrt{C_6^I \cdot C_6^J}$$

are the geometric mean of the C_6 coefficients of the single atoms. These, in turn, are proportional to the respective static dipolar polarisabilities, i.e. they describe how susceptible the atoms are towards vdW interactions. $f(R_{IJ})$ is a damping function limiting the vdW interactions if the atoms are too close to each other. The parameters are fitted to match experimental reference and are considered universal for the employed atomic species [26].

A bit more sophistication provides the DFT-D3 method by Grimme et al. [27]. This method complements the C_6 contributions from the dipole-dipole dispersion by the C_8 contributions from the dipole-quadrupole dispersion. In addition, the coefficients are not fixed any more, but they scale with the fractional coordination number of the respective atoms to partially reflect different chemical environments. Moreover, the

parameter fitting is more *ab initio*. The original DFT-D3 method employs a damping function which scales the dispersion to zero for small atomic distances (zero-damping) [27]. Later, a Becke-Johnson-type damping was introduced, which reduces the dispersion to a finite value instead of zero and enhances short vdW contacts [25, 28]. The last vdW scheme tested in this work is the method introduced by Tkatchenko and Scheffler [29]. It is formally identical to the DFT-D2 method, however the vdW coefficients reflect the variation of the atomic charges with respect to the neutral atoms by means of Hirshfeld partitioning. This procedure explicitly considers the influence of the chemical environment on the polarisabilities in an *ab initio* manner. The original method [29], however, has problems with ionic systems, in which charge transfer alters the atomic reference charges. The solution consists in shifting the reference from the neutral atoms to the atoms in a charged state by means of an iterative Hirshfeld partitioning scheme [30, 31].

The construction of the above semi-empirical methods shows why vdW interactions become growingly important in materials involving elements with high atomic numbers: Since the C coefficients are proportional to atomic polarisabilities, atoms with larger electron shells contribute more dispersion to the total energy. Therefore, in particular the elements of the last rows of the periodic table are expected to have high vdW-related effects on the structures which incorporate them.

2.2 The Bloch theorem

Most solid-states are periodic, i.e. their properties are completely described on a finite, microscopic domain which is replicated into all N spatial directions. Traditional crystals, for example, are periodic in all three spatial dimensions with a small replication unit representing the symmetry of the macroscopic material. Also non-periodic systems can be described with a periodic ansatz. The unit cell has then to be large enough, that the local conditions are well described and the influence from the periodic replica vanishes. The domain of a periodic system is the generalised period length, which can always be chosen as an N -dimensional parallelepiped (a line, a parallelogram and a parallelepiped for $N = 1, 2, 3$, respectively). It contains all information about the macroscopic properties, in particular the potential and the solutions of the corresponding quantum-mechanical eigenvalue equation. Most importantly, the finiteness of the domain ensures the integrability of the Hilbert space.

The wavefunctions of a particle in a periodic potential underlie boundary conditions, which are summarised as Bloch's theorem. It can be derived in several ways like the common one considering the properties of translation operators or the abstract one employing N -dimensional Fourier series. The derivation presented here is based on the properties of the translation group and connects the Bloch theorem with the gauge degree of freedom of the wavefunctions. Furthermore, some identities are listed, which become important when the geometric phases are considered (Chap. 7). In the following paragraphs, a single quantum particle moving in a periodic potential is assumed. Since the solutions of the Kohn-Sham equations fulfil this condition, Bloch's theorem is compatible with the DFT.

The direct lattice. A N -dimensional crystal is defined by a set of N linearly independent (*direct*) basis vectors $\{\mathbf{R}_i, i = 1, \dots, N\}$. The parallelepiped

$$C_{\mathbf{R}} := \left\{ \sum_i r_i \mathbf{R}_i \mid r_i \in [0, 1] \right\} \quad (2.20a)$$

is the (*direct*) unit cell and the set

$$\mathcal{R} := \left\{ \sum_i n_i \mathbf{R}_i \mid n_i \in \mathbb{Z} \right\} \quad (2.20b)$$

is the (*direct*) lattice of the crystal. An alternative unit cell, the *Wigner-Seitz cell*, is defined as the set of points which are closer to $\mathbf{R}_0 = 0$ than to any other $\mathbf{R} \in \mathcal{R}$.

The Bloch theorem as a gauge function

The physics of a charged particle in a crystal is determined by an electrostatic potential $V(\mathbf{x})$ which is periodic on \mathcal{R} . Consequently, the corresponding Hamilton operator H of a non-magnetic system ($\mathbf{A} \equiv 0$) is invariant under translations by a lattice vector $\mathbf{R} \in \mathcal{R}$, which are represented by the unitary translation operator $U_{\mathbf{R}}$.

$$\begin{aligned} U_{\mathbf{R}} &= \exp(-i\frac{1}{\hbar} \mathbf{R} \cdot \mathbf{p}), \quad U_{\mathbf{R}} H(\mathbf{p}, \mathbf{x}) U_{\mathbf{R}}^{-1} = H(\mathbf{p}, \mathbf{x} - \mathbf{R}) = H(\mathbf{p}, \mathbf{x}) \\ \Rightarrow H(\mathbf{p}, \mathbf{x}) |\Psi_n\rangle &= E_n |\Psi_n\rangle \quad \Leftrightarrow \quad H(\mathbf{p}, \mathbf{x}) U_{\mathbf{R}} |\Psi_n\rangle = E_n U_{\mathbf{R}} |\Psi_n\rangle \end{aligned} \quad (2.21)$$

Hence, if $|\Psi_n\rangle$ is an eigenstate with eigenenergy E_n , then $U_{\mathbf{R}} |\Psi_n\rangle$ is also an eigenstate with the same energy. The effect of $U_{\mathbf{R}}$ on $|\Psi_n\rangle$ is thus equivalent to a gauge transformation (Eq. (A.98)).

$$U_{\mathbf{R}} = \exp(-i\chi(\mathbf{x}, \mathbf{R})) \quad (2.22)$$

The gauge function $\chi(\mathbf{x}, \mathbf{R})$ can be derived in two steps. Firstly, the group properties of $U_{\mathbf{R}}$ tell that $\chi(\mathbf{x}, \mathbf{R})$ is linear in \mathbf{R} , so it can be written as a scalar product between \mathbf{R} and a vectorial function $\mathbf{f}(\mathbf{x})$.

$$\chi(\mathbf{x}, \mathbf{R}) + \chi(\mathbf{x}, \mathbf{S}) = \chi(\mathbf{x}, \mathbf{R} + \mathbf{S}), \quad -\chi(\mathbf{x}, \mathbf{R}) = \chi(\mathbf{x}, -\mathbf{R}) \quad \Rightarrow \quad \chi(\mathbf{x}, \mathbf{R}) = \mathbf{R} \cdot \mathbf{f}(\mathbf{x})$$

Secondly, because translations commute, $\mathbf{f}(\mathbf{x})$ has to be a constant vector.

$$\begin{aligned} \exp(-i\frac{1}{\hbar} \mathbf{R}' \cdot \mathbf{p}) \exp(-i\mathbf{R} \cdot \mathbf{f}(\mathbf{x})) &= \exp(-i\mathbf{R} \cdot \mathbf{f}(\mathbf{x})) \exp(-i\frac{1}{\hbar} \mathbf{R}' \cdot \mathbf{p}) \\ \Rightarrow 0 &= \left[-\mathbf{f}(\mathbf{x}), -\frac{1}{\hbar} \mathbf{p} \right] \stackrel{\text{Eq. (A.93)}}{=} i\mathbf{f}'(\mathbf{x}) \quad \Leftrightarrow \quad \mathbf{f}(\mathbf{x}) = \mathbf{k} \in \mathbb{R}^N \end{aligned}$$

In summary, a crystal wavefunction which is translated by a lattice vector $\mathbf{R} \in \mathcal{R}$ alters by a phase shift of $-\mathbf{k} \cdot \mathbf{R}$, where \mathbf{k} is a constant, N -dimensional vector. This relation is called *Bloch's theorem* and the wavefunctions $|\Psi_{n,\mathbf{k}}\rangle$ are called *Bloch functions*:

$$U_{\mathbf{R}} |\Psi_{n,\mathbf{k}}\rangle = \exp(-i\mathbf{k} \cdot \mathbf{R}) |\Psi_{n,\mathbf{k}}\rangle \quad \forall \mathbf{R} \in \mathcal{R} \quad (2.23a)$$

Alternatively, in space representation:

$$\Psi_{n,\mathbf{k}}(\mathbf{x} + \mathbf{R}) = \exp(i\mathbf{k} \cdot \mathbf{R}) \Psi_{n,\mathbf{k}}(\mathbf{x}) \quad (2.23b)$$

The Bloch theorem proves that \mathbf{k} characterises the state $|\Psi_{n,\mathbf{k}}\rangle$ like a quantum number, i.e. states with different \mathbf{k} (up to a reciprocal lattice vector, vide infra) are mutually exclusive.

$$\begin{aligned}\langle \Psi_{n,\mathbf{k}} | \Psi_{n,\mathbf{k}'} \rangle &= \langle \Psi_{n,\mathbf{k}} | U_{\mathbf{R}}^{-1} U_{\mathbf{R}} | \Psi_{n,\mathbf{k}'} \rangle = \langle \Psi_{n,\mathbf{k}} | \exp(i\mathbf{k} \cdot \mathbf{R}) \exp(-i\mathbf{k}' \cdot \mathbf{R}) | \Psi_{n,\mathbf{k}'} \rangle \\ &= \langle \Psi_{n,\mathbf{k}} | \Psi_{n,\mathbf{k}'} \rangle \exp(i(\mathbf{k} - \mathbf{k}') \cdot \mathbf{R}) \quad \forall \mathbf{k}, \mathbf{k}' \in \mathbb{R}^N, \mathbf{R} \in \mathcal{R} \\ &\Rightarrow \langle \Psi_{n,\mathbf{k}} | \Psi_{n,\mathbf{k}'} \rangle = \delta_{\mathbf{k},\mathbf{k}'}\end{aligned}\tag{2.24}$$

The continuity of \mathbf{k} motivates the notation of the Bloch states as functions of \mathbf{k} :

$$|\Psi_{n,\mathbf{k}}\rangle \rightarrow |\Psi_n(\mathbf{k})\rangle$$

As the quantum-number nature of \mathbf{k} depends on the translation symmetry, it is also called *crystal momentum*, analogously to momentum conservation following from spatial homogeneity in classical mechanics.

The reciprocal lattice. The Bloch phase $\mathbf{k} \cdot \mathbf{R}$ in Eqs. (2.23) is periodic on the addition of a vector $\mathbf{G} \in \mathbb{R}^N$ to \mathbf{k} with

$$\mathbf{G} \cdot \mathbf{R} = 2\pi n, n \in \mathbb{Z}.$$

A basis for the \mathbf{G} vectors is defined by a set $\{\mathbf{G}_j\}$ with:

$$\mathbf{G}_j \cdot \mathbf{R}_i = 2\pi \delta_{i,j}, \quad \mathbf{R}_i \in \mathcal{R}, \quad i, j = 1, \dots, N$$

Or more compactly written as matrices:

$$G := (\mathbf{G}_1, \dots, \mathbf{G}_N), R := (\mathbf{R}_1, \dots, \mathbf{R}_N) \quad \Rightarrow \quad G^T \cdot R = 2\pi I \quad \Leftrightarrow \quad G^T = 2\pi R^{-1}$$

The column vectors of G are the *reciprocal basis vectors* $\{\mathbf{G}_j, j = 1, \dots, N\}$, in accordance with their calculation from the (transposed) inverse of the matrix R . The parallelepiped

$$C_G := \left\{ \sum_j s_j \mathbf{G}_j \mid s_j \in [0, 1] \right\}\tag{2.25a}$$

is the *reciprocal unit cell* and the set

$$\mathcal{G} = \left\{ \sum_j n_j \mathbf{G}_j \mid n_j \in \mathbb{Z} \right\}\tag{2.25b}$$

is the *reciprocal lattice* of the crystal. The *Brillouin zone* is the reciprocal analogon of the Wigner-Seitz cell: the set of points being closer to $\mathbf{G}_0 = 0$ than to any other $\mathbf{G} \in \mathcal{G}$.

Since the Bloch phase $\exp(-i\mathbf{k} \cdot \mathbf{R})$ is periodic on \mathcal{G} , \mathbf{k} is only well defined within the reciprocal unit cell C_G (or within the Brillouin zone).

$$|\Psi_n(\mathbf{k} + \mathbf{G})\rangle = |\Psi_n(\mathbf{k})\rangle \quad \forall \mathbf{G} \in \mathcal{G}\tag{2.26}$$

Eq. (2.26) completes the classification of the eigenspace of a crystal Hamilton operator: Every eigenstate $|\Psi_n(\mathbf{k})\rangle$ has an N -dimensional, continuous quantum number $\mathbf{k} \in C_G$ and a *band index* $n \in \mathbb{N}$. Consequently, the eigenenergies are continuous functions of $\mathbf{k} \in C_G$. The band index n is discrete for bound states, which exist in every condensed-matter system. Hence, a band with fixed n describes a hypersurface in the $N + 1$ dimensional \mathbf{k} -energy space. As paper is only capable of displaying two-dimensional plots, a section of the hypersurface can be drawn by plotting the bands along a \mathbf{k} -path in C_G . The result is the *band structure*.

2.2.1 Basis changes

The Bloch states $|\Psi_n(\mathbf{k})\rangle$ are unhandy in practical applications since they are non-periodic (Bloch theorem) and delocalized (they do not decay). These problems can be encountered by basis changes which, of course, do not affect the physics. There are different levels of transformations: those acting separately on each individual state $|\Psi_n(\mathbf{k})\rangle$, those mixing states with different \mathbf{k} -vectors at a fixed band n , and those mixing different bands n at a fixed \mathbf{k} -vector. The two important bases presented here are the Bloch factors and the Wannier functions, which solve the above-mentioned problems about periodicity and localisation, respectively.

The Bloch factors

The first basis change exploits the quantum-number nature of \mathbf{k} and the gauge transformation rules in Eqs. (A.99). The application of a \mathbf{k} -dependent phase to the Bloch functions transforms the stationary Schrödinger equation (2.21) into new eigenvalue equation for the *Bloch Hamiltonian* $h(\mathbf{p}, \mathbf{x} | \mathbf{k})$, which \mathbf{k} enters as a parameter.

$$|u_n(\mathbf{k})\rangle := \tilde{U}_{\mathbf{k}} |\Psi_n(\mathbf{k})\rangle = \exp(-i\mathbf{k} \cdot \mathbf{x}) |\Psi_n(\mathbf{k})\rangle \quad (2.27a)$$

$$h(\mathbf{p}, \mathbf{x} | \mathbf{k}) := \tilde{U}_{\mathbf{k}} H(\mathbf{p}, \mathbf{x}) \tilde{U}_{\mathbf{k}}^{-1} \stackrel{\text{Eq. (A.99b)}}{=} H(\mathbf{p} + \hbar\mathbf{k}, \mathbf{x}) \quad (2.27b)$$

$$\Rightarrow h(\mathbf{p}, \mathbf{x} | \mathbf{k}) |u_n(\mathbf{k})\rangle = E_n(\mathbf{k}) |u_n(\mathbf{k})\rangle \quad (2.27c)$$

In contrast to the original states $|\Psi_n(\mathbf{k})\rangle$, the *Bloch factors* $|u_n(\mathbf{k})\rangle$ are periodic on \mathcal{R} . This is a great simplification of the eigenvalue problem as techniques like Fourier series become applicable. On the other hand, the periodicity in \mathbf{k} on \mathcal{G} is lost and phase-shifted boundary conditions on C_G hold instead. That is $\forall \mathbf{R} \in \mathcal{R}, \mathbf{G} \in \mathcal{G}$:

$$U_{\mathbf{R}} |u_n(\mathbf{k})\rangle = U_{\mathbf{R}} \exp(-i\mathbf{k} \cdot \mathbf{x}) U_{\mathbf{R}}^{-1} U_{\mathbf{R}} |\Psi_n(\mathbf{k})\rangle \quad (2.28a)$$

$$\stackrel{\text{Eq. (2.23)}}{=} \exp(-i\mathbf{k} \cdot (\mathbf{x} - \mathbf{R})) \exp(-i\mathbf{k} \cdot \mathbf{R}) |\Psi_n(\mathbf{k})\rangle = |u_n(\mathbf{k})\rangle$$

$$|u_n(\mathbf{k} + \mathbf{G})\rangle = \exp(-i(\mathbf{k} + \mathbf{G}) \cdot \mathbf{x}) |\Psi_n(\mathbf{k} + \mathbf{G})\rangle = \exp(-i\mathbf{G} \cdot \mathbf{x}) |u_n(\mathbf{k})\rangle \quad (2.28b)$$

The Wannier functions

Since the Bloch functions are periodic in \mathbf{k} on \mathcal{G} , they have an N -dimensional Fourier series. The Fourier coefficients, which are indexed by the direct lattice vectors $\mathbf{R} \in \mathcal{R}$

(Eqs. (A.94), but with swapped spaces), are the *Wannier functions* $|a_n(\mathbf{R})\rangle$.

$$|a_n(\mathbf{R})\rangle := \frac{1}{|\mathcal{C}_G|} \int_{\mathcal{C}_G} d\mathbf{k} \exp(-i\mathbf{k} \cdot \mathbf{R}) |\Psi_n(\mathbf{k})\rangle \quad (2.29a)$$

$$|\Psi_n(\mathbf{k})\rangle = \sum_{\mathbf{R} \in \mathcal{R}} \exp(i\mathbf{k} \cdot \mathbf{R}) |a_n(\mathbf{R})\rangle. \quad (2.29b)$$

With respect to the Bloch theorem, the \mathbf{R} th Wannier function results from shifting all states of a fixed band n into the \mathbf{R} th unit cell and taking the sum over \mathbf{k} .

$$\langle \mathbf{x} | a_n(\mathbf{R}) \rangle \stackrel{\text{Eq. (2.23)}}{=} \frac{1}{|\mathcal{C}_G|} \int_{\mathcal{C}_G} d\mathbf{k} \langle \mathbf{x} - \mathbf{R} | \Psi_n(\mathbf{k}) \rangle =: a_n(\mathbf{x} - \mathbf{R}) \quad (2.30)$$

Therefore, each band n has *one* Wannier function $a_n(\mathbf{x})$ which is centred at 0 and defined on the entire space \mathbb{R}^N . This permits the definition of a *centre of charge*:

$$\langle \mathbf{x}_n \rangle = \frac{1}{|\mathcal{C}_R|} \int_{\mathbb{R}^N} d\mathbf{x} \mathbf{x} |a_n(\mathbf{x})|^2 \quad (2.31)$$

In order to show that Eq. (2.31) is well defined, the existence of the integral and the gauge-invariance have to be proven.

The space integral in Eq. (2.31) can be partitioned into a series of unit-cell integrals. The definition of the cell-periodic Bloch factors (Eq. (2.27a)) then yields:

$$\begin{aligned} \langle \mathbf{x}_n \rangle &= \sum_{\mathbf{R} \in \mathcal{R}} \frac{1}{|\mathcal{C}_R|} \int_{\mathcal{C}_R + \mathbf{R}} d\mathbf{x} \mathbf{x} |a_n(\mathbf{x})|^2 = \sum_{\mathbf{R} \in \mathcal{R}} \frac{1}{|\mathcal{C}_R|} \int_{\mathcal{C}_R} d\mathbf{x} (\mathbf{x} - \mathbf{R}) |a_n(\mathbf{x} - \mathbf{R})|^2 \\ &= \frac{1}{|\mathcal{C}_R|} \int_{\mathcal{C}_R} d\mathbf{x} \mathbf{x} \sum_{\mathbf{R} \in \mathcal{R}} |a_n(\mathbf{x} - \mathbf{R})|^2 - \frac{1}{|\mathcal{C}_R|} \int_{\mathcal{C}_R} d\mathbf{x} \sum_{\mathbf{R} \in \mathcal{R}} \mathbf{R} |a_n(\mathbf{x} - \mathbf{R})|^2 \\ &\stackrel{(*)}{=} \frac{i}{|\mathcal{C}_G|} \int_{\mathcal{C}_G} d\mathbf{k} \frac{1}{|\mathcal{C}_R|} \int_{\mathcal{C}_R} d\mathbf{x} \langle u_n(\mathbf{k}) | \mathbf{x} \rangle \nabla_{\mathbf{k}'} \langle \mathbf{x} | u_n(\mathbf{k}') \rangle \Big|_{\mathbf{k}'=\mathbf{k}} \\ &= \frac{i}{|\mathcal{C}_G|} \int_{\mathcal{C}_G} d\mathbf{k} \langle u_n(\mathbf{k}) | \nabla_{\mathbf{k}} | u_n(\mathbf{k}) \rangle \end{aligned} \quad (2.32)$$

In step (*), the Parseval identity (Eqs. (A.95) and (A.96)) was used.

$$\begin{aligned} \sum_{\mathbf{R} \in \mathcal{R}} |a_n(\mathbf{x} - \mathbf{R})|^2 &= \frac{1}{|\mathcal{C}_G|} \int_{\mathcal{C}_G} d\mathbf{k} |\langle \mathbf{x} | \Psi_n(\mathbf{k}) \rangle|^2 \stackrel{\text{Eq. (2.27a)}}{=} \frac{1}{|\mathcal{C}_G|} \int_{\mathcal{C}_G} d\mathbf{k} |\langle \mathbf{x} | u_n(\mathbf{k}) \rangle|^2 \\ \sum_{\mathbf{R} \in \mathcal{R}} \mathbf{R} |a_n(\mathbf{x} - \mathbf{R})|^2 &= \frac{-i}{|\mathcal{C}_G|} \int_{\mathcal{C}_G} d\mathbf{k} \langle \Psi_n(\mathbf{k}) | \mathbf{x} \rangle \nabla_{\mathbf{k}'} \langle \mathbf{x} | \Psi_n(\mathbf{k}') \rangle \Big|_{\mathbf{k}'=\mathbf{k}} \\ &\stackrel{\text{Eq. (2.27a)}}{=} \frac{-i}{|\mathcal{C}_G|} \int_{\mathcal{C}_G} d\mathbf{k} \langle u_n(\mathbf{k}) | \mathbf{x} \rangle \nabla_{\mathbf{k}'} \langle \mathbf{x} | u_n(\mathbf{k}') \rangle \Big|_{\mathbf{k}'=\mathbf{k}} + \frac{1}{|\mathcal{C}_G|} \int_{\mathcal{C}_G} d\mathbf{k} \mathbf{x} |\langle \mathbf{x} | u_n(\mathbf{k}) \rangle|^2 \end{aligned}$$

Eq. (2.32) is thus well defined because $\langle \mathbf{x} | u_n(\mathbf{k}) \rangle$ is differentiable with respect to \mathbf{k} .

To prove the gauge invariance, the centre of charge is calculated for Bloch factors which are shifted by a \mathbf{k} -dependent phase $\chi(\mathbf{k})$. In doing so, a variant of the Gauß identity is used telling that the volume integral of a gradient field equals the surface integral of the potential, $\chi(\mathbf{k})$ in this case. The surface integral can be evaluated with the restriction on $\chi(\mathbf{k})$ that its values on two opposite faces of C_G must differ by integer multiples of 2π so as to retain boundary conditions of the Bloch factors (Eq. (2.28b)).

$$\begin{aligned}
 |\tilde{u}_n(\mathbf{k})\rangle &= \exp(-i\chi(\mathbf{k})) |u_n(\mathbf{k})\rangle \\
 \Rightarrow \langle \tilde{\mathbf{x}}_n \rangle &= \langle \mathbf{x}_n \rangle + \frac{1}{|C_G|} \int_{C_G} d\mathbf{k} \nabla_{\mathbf{k}} \chi(\mathbf{k}) = \langle \mathbf{x}_n \rangle + \int_{[0,1]^N} d\mathbf{s} \sum_{j=1}^N \frac{\mathbf{R}_j}{2\pi} \cdot \nabla_{\mathbf{s}} \chi(\mathbf{s}) \\
 &= \langle \mathbf{x}_n \rangle + \mathbf{R}, \quad \mathbf{R} \in \mathcal{R}
 \end{aligned}$$

Thus, the centre of charge is only well defined modulo a direct lattice vector \mathbf{R} . This is expectable as translating all Wannier functions by \mathbf{R} corresponds to a reindexing.

Part I: Rare-earth silicide nanowires on silicon surfaces

Rare-earth silicide nanowires are intriguing examples of systems on the nanoscale. As the name suggests, they are derived from the rare-earth silicides, a compound of silicon and the rare-earth elements (REs), which is often addressed by the chemical formula “RESi₂”, irrespectively of the exact stoichiometry. Horizontal thin streaks of these hard, brittle metals form on several silicon surfaces by self-organised growth, i.e. after RE deposition and successive annealing without further structuring measures. As their cross sections extend to only a few nanometres, while their lengths can reach several 100 nm, these streaks are referred to as *nanowires*. As a result of the small lateral dimensions, quantum confinement effects are expected to dominate the electronic system. Hence, RESi₂ nanowires are promising candidates for metallic systems of one-dimensional electronic character.

The RESi₂ nanowires establish a special class of nanowires as they combine a bunch of unique and peculiar properties. In contrast to many other nanowire systems (e.g. the not less interesting gold nanowires on Si(*hkk*) [P13, P14]), RESi₂ nanowires can be considered a cut-out of a bulk structure, the bulk RESi₂ prototypes in this case. These cut-outs extend to heights and widths of a few unit cells and to lengths of hundreds of unit cells. Such a structure bears several advantages: Firstly, since the individual streaks are subdivided into small building blocks, structure models of arbitrary widths, heights and lengths can be set up in principle. Secondly, the streaks incorporate a silicon network, which links to the substrate via strong Si–Si bonds and guarantees stability against delamination. Thirdly, there is a vast number of nanowire@silicon configurations because RESi₂ occurs in two different phases and silicon provides surfaces of very different morphologies. For these reasons, RESi₂ nanowires provide an inexhaustible number of possibilities to synthesise and explore samples.

The research began in the 1980s when scientists experimented with metallic silicides on pristine silicon. In particular, the integrated-circuit community was interested in these systems as they establish metal-semiconductor contacts. Since epitaxy permits the production of high-quality films, those silicides which grow epitaxially on silicon attracted the most scientific attention. The REs stand out from the silicide-forming elements as they produce very low Schottky barriers of 0.3 eV to 0.4 eV on *n*-type silicon, the smallest known for this substrate in the 1980s [32]. Subsequent experiments proved that the silicides of yttrium (Y, *Z* = 39) and all REs from gadolinium (Gd, *Z* = 64) to lutetium (Lu, *Z* = 71) are suitable for epitaxy on the Si(111) surface. This is due to a match between the structure of the silicon-rich RESi₂ bulk phases and the geometry of the Si(111) surface: Both have a trigonal/hexagonal symmetry axis and

similar lattice constants, which deviate by -2.55% to $+0.83\%$ [33]. The thickness of the RESi_2 films on Si(111) can be tuned so that it spans only a few nanometres. In particular, RE coverages corresponding to one monolayer lead to the formation of a very thin and smooth silicide film with a thickness of one axial lattice constant of the respective RESi_2 bulk phase [34]. Such a film has an electronic band structure which resembles that of a two-dimensional (semi-)metal with a Schottky barrier of ~ 0.1 eV [35]. It is remarkable that the experimental outcomes for different REs are almost identical [P8, P12, 34–53].

The silicide epitaxy was also investigated on the Si(001) surface. In 1998, Kalka et al. prepared a clean silicon sample with dysprosium (Dy, $Z = 66$) at a coverage corresponding to one monolayer. Surprisingly and differently from the Dy@Si(111) system, subsequent annealing at a few 100°C lead to the formation of rectified, rectangular islands instead of a smooth film [42]. Short after, Preinesberger et al. reduced the RE coverage to sub-monolayer and observed the formation of strongly anisotropic DySi_2 structures. Because the lateral dimensions measured a few nanometres, while their lengths reached up to 200 nm, they referred to the structures as “nanowires” [54]. Not only did they report the first fabrication of RESi_2 nanowires, but they also assessed the process to be quite simple as the nanowire formation was self-organised, controlled mainly by macroscopic parameters like the RE coverage and the annealing temperature. Since their discovery, RESi_2 nanowires have been an active research field in which many groups published fabrication details, topographical data (e.g. STM), hypothetical structure models and electronic properties (e.g. ARPES or STS) [P3, P6, 54–67].

RESi_2 nanowires do not only grow on Si(001), as in the pioneering work. Also vicinal Si(111) surfaces (Si($h\bar{h}k$)) produce nanowires as the steps and terraces cause discontinuities in the monolayer film [P8, 64, 68–70]. This part of the thesis is dedicated to the theoretical exploration of RESi_2 nanowires on the Si(557) surface (nanowire-RE@Si(557)). Although structure models have been proposed based on the RESi_2 monolayer on Si(111) and experimental findings [64, 68, 70], the real structure is still unknown. Therefore, a major part of this work consists in setting up reasonable structure models, optimising them by means of DFT and evaluating their stability by means of ab initio thermodynamics. Once verified, the stable structure model is used to explain the experimental outcomes of this system, particularly the electronic properties measured by ARPES (band structure and Fermi surfaces). Trivalent terbium (Tb, $Z = 65$) is employed as a representative RE as it produces the desired nanostructures in the experiment [70]. To a certain extent, the results are transferable to other trivalent REs, in particular dysprosium (Dy, $Z = 66$) and erbium (Er, $Z = 68$), as proven by experimental evidence [64, 68], and holmium (Ho, $Z = 67$), as it lies between Dy and Er in the lanthanoid series. The purpose of all investigations is answering the following questions:

- Are the proposed structure models for the nanowire-Tb@Si(557) system stable?
- Does the electronic structure of the nanowire-Tb@Si(557) system have (quasi-) one-dimensional electronic properties?

Before the RESi_2 nanowires are addressed, some related systems are considered at first. The respective insights will be absolutely crucial for understanding the physics of the nanostructures. In the first instance, the chemical background of the constituent elements, the rare-earth elements and silicon, is collated in Chap. 3. The focus of this literature research is on the role of the 4f electrons in chemistry and the general properties of the silicide compound class. After that, the bulk phases of RESi_2 are analysed in Chap. 4 since they are the three-dimensional bulk prototypes for the nanostructures. Attention is paid to how the characteristic Si vacancies affect the structural and electronic properties of the bulk phases. Furthermore, two important approximations which are employed in the subsequent chapters are validated: the frozen-core approach for treating the f electrons of Tb and the omission of the lattice dynamics in *ab initio* thermodynamics.

Chap. 5 concerns the first nanostructure: the monolayer-Tb@Si(111) system, which is the surface prototype for the nanowire-Tb@Si(557) system. Contrarily to the nanowires, the monolayer provides detailed experimental data on the lattice parameters. Therefore, it serves as a test system for the approach. Furthermore, although the RESi_2 monolayers have already been treated in several experimental and theoretical works (*vide supra*), the peculiarities about the established structure model are not sufficiently understood. This in particular concerns the reason for the buckling direction of the covering Si honeycomb, which is inverse to that of the substrate. A detailed analysis of the structural and electronic properties illuminates the underlying physics of the monolayer and explains the peculiarities. The chapter concludes with a critical revision of the popular statement that mechanical strain is responsible for the details of the established structure model. The nanowire-Tb@Si(557) system is the matter of Chap. 6. The structure models are derived from those of the monolayer and optimised by means of DFT. The RE coverage of the surface is varied between dense and sparse so as to derive a corresponding phase diagram for the nanowire system. For the stable structure models the electronic properties are calculated. The chapter concludes with the proof of a unique dimensional crossover from 2D to 1D, which has never been observed in this system before.

3 Chemical background

3.1 The rare-earth elements

The *rare-earth elements* are a group of 17 elements: scandium (Sc, $Z = 21$), yttrium (Y, $Z = 39$) and the 15 *lanthanoids*¹. The latter are the first row of the f-block plus the first 5d element (inner transition metals), a series starting with lanthanum (La, $Z = 57$) and terminating with lutetium (Lu, $Z = 71$) [71, p. 51]. The rare-earth elements are often abbreviated to REE or, more like a chemical symbol, RE. The lanthanoids are often denoted by the chemical symbol Ln = [La–Lu]. Since the individual members of the REs are unfamiliar to most non-specialists, they are more than once addressed by their name, chemical symbol and atomic number Z in this section.

The REs are very homogeneous concerning their chemical behaviour, while their physical properties (in particular optical and magnetic properties) differ considerably. This makes the REs important technology metals in nearly every high-tech branch. “Though there are no uniform classifications for rare-earth applications, the markets are commonly divided into nine sectors: catalysts, polishing, glass, phosphors and pigments, metallurgy, batteries, magnets, ceramics, and others” [72]. A very prominent RE is neodymium (Nd, $Z = 60$) as the alloy Nd₂Fe₁₄B is the base for strong permanent magnets used for efficient electric motors and generators [73, p. 78]. The high spin multiplicity of gadolinium (Gd, $Z = 64$) is exploited in contrast agents for magnetic resonance tomography (MRT). The paramagnetic ions enhance the relaxation times of the surrounding protons (hydrogen atoms) and thereby increase the image contrast [73, p. 70]. Erbium (Er, $Z = 68$) is known from optical devices, e.g. erbium-doped fibre amplifiers: The shielded 4f levels of the Er³⁺ ions produce a near-infrared transition (from $J = \frac{15}{2}$ to $J = \frac{13}{2}$) with a long lifetime of ~10 ms. Thus, most Er³⁺ ions in the fibre can be excited (“pumped”) so that optical signals passing the fibre are amplified by stimulated emission [74, 75]. The chemical similarity between the REs is due to analogous valence electron configurations (VECs) which all yield the oxidation state III in most compounds [18, p. 2230], as well as in aqueous solutions (Tab. 3.1). While this is expectable for scandium (Sc, $Z = 21$), yttrium (Y, $Z = 39$) and lanthanum (La, $Z = 57$), which represent the third column of the periodic table, the trivalence of the other 14 lanthanoids despite their consecutive atomic numbers is an “aperiodic” behaviour. This phenomenon is unique in the periodic table and due to the special role of the 4f electrons in chemistry.

¹Most of the (older) literature refers to the elements from La to Lu as “lanthanides”. However, this term is misleading since the suffix “-ide” denotes anionic constituents (cf. oxide O²⁻, fluoride F⁻). In contrast, the suffix “-oid” indicates an instance similar to the word root. Therefore, the IUPAC recommends the term “lanthanoids” for the group La–Lu, including La and Lu [71, p. 52].

The role of f electrons in chemistry

The VEC can partially be derived from the shell model and the standard occupation rules which lead to the periodic table. These rules correctly predict a trivalent VEC of $4s^2 3d^1$ and $5s^2 4d^1$ for the non-lanthanoids scandium (Sc, $Z = 21$) and yttrium (Y, $Z = 39$), respectively. Furthermore, they predict that the first f shell, the 4f shell, is empty up to the alkaline earth metal barium (Ba, $Z = 56$, VEC = $6s^2$) and fills up from lanthanum (La, $Z = 57$) to ytterbium (Yb, $Z = 70$). Hence, the VEC of the n th lanthanoid would be $6s^2 4f^n$, $n \in [1, 14]$, according to the periodic table. The termination of the lanthanoid series lutetium (Lu, $Z = 71$) would then be the first 5d-element with a VEC of $6s^2 5d^1 4f^{14}$. Since the complete 4f shell is expected to remain inert, Lu is correctly predicted to be trivalent with two s electrons and one d electron in the outermost shells, analogously to Sc and Y. The trivalence of the other lanthanoids is not obvious, in particular because the 4f levels are incomplete, except for ytterbium (Yb, $Z = 70$), and lie in the chemically relevant energy range near the Fermi level. Though, the energy levels and occupations of a shell are not the only conditions for its ability to participate in chemical bonding. In addition, the atomic orbitals have to spatially overlap with those of another atom to form molecular orbitals. However, the spatial distribution of the atomic 4f orbitals is enclosed by the shells with higher main quantum numbers, in particular the 6s shell, the 5d shell and the 5p shell. Hence, the 4f electrons could only participate in chemical bonding, if all outer shells did also. While this is the case for the 6s and 5d electrons, the 5p electrons are part of the xenon noble gas configuration and thus inert. As a consequence, they screen the 4f electrons from the environment and render them inert as well. Applying this to the lanthanoids from lanthanum (La, $Z = 57$) to ytterbium (Yb, $Z = 70$) would imply a divalent state from the two 6s electrons, not the observed trivalent state².

Obviously, the rules of the periodic table cannot explain the trivalence of the lanthanoids. They even fail in predicting the correct atomic ground state for lanthanum (La, $Z = 57$), cerium (Ce, $Z = 58$) and gadolinium (Gd, $Z = 64$). The apparent contradictions are due to an oversimplification of the real electronic situation and can be resolved by considering the ionisation energies of different VECs. A detailed analysis of this can be found in [75]. The key is that the atomic terms belonging to the divalent VEC ($6s^2 5d^0 4f^n$) and the trivalent VEC ($6s^2 5d^1 4f^{n-1}$) are energetically very close to each other for most of the lanthanoids. Therefore, one electron leaves the 4f shell if the drop in the electronic chemical potential, e.g. caused by an electronegative reaction partner, is large enough. The ability of the Ln^{2+} ions to donate the third electron depends on the third ionisation energies of the isolated Ln atoms. These grow gradually from lanthanum (La, $Z = 57$) to europium (Eu, $Z = 63$) by +5.7 eV, show a sharp drop at gadolinium (Gd, $Z = 64$) by -4.3 eV, grow again from gadolinium (Gd, $Z = 64$) to ytterbium (Yb, $Z = 70$) by +4.4 eV, and finally drop at lutetium (Lu, $Z = 71$) by -4.1 eV [75]. The zigzag pattern is the manifestation of Hund's second rule

²The terms "divalent" and "trivalent" denote the number of electrons in the outermost 6s and 5d shells plus the charge state of the atom/ion. For example, the VEC of the neutral Gd atom ($6s^2 5d^1 4f^7$) is trivalent as well as that of the Gd^{3+} ion ($4f^7$). On the other hand, the VEC of the neutral Yb atom ($6s^2 5d^0 4f^{14}$) is divalent as well as that of the Yb^{2+} ion ($4f^{14}$). This nomenclature makes sense as the only possibility for a formal valence electron not to take part in chemistry is to be part of the 4f shell.

3 Chemical background

	La	Ce	Pr	Nd	Pm	Sm	Eu	Gd	Tb	Dy	Ho	Er	Tm	Yb	Lu
(a)	3	3 4	3	3	3	2 3	2 3	3	3	3	3	3	3	2 3	3
(b)	4f⁰	4f ¹	4f ²	4f ³	4f ⁴	4f ⁵	4f ⁶	4f⁷	4f ⁸	4f ⁹	4f ¹⁰	4f ¹¹	4f ¹²	4f ¹³	4f¹⁴

Table 3.1: (a) “Valencies of the lanthanoids occurring in aqueous solution” [76]. (b) VEC of the trivalent Ln³⁺ ion. Empty, half-filled and filled 4f shells are bold.

that the spin configuration of a specific shell tends to maximise its spin multiplicity. More precisely, parallel spins occupying orbitals with different magnetic quantum numbers reduce the total energy by their exchange energy. An overview over the behaviour of the atomic terms and the third ionisations energies of the lanthanoids can be found in the appendix (Sec. B.1).

Hund’s second rule is very helpful for predicting the valences. The trivalent state is the most frequent for all lanthanoids (Tab. 3.1). If the electronic chemical potential is not too low, e.g. if the reaction partners are not too electronegative, an additional electron will go into the 4f shell to maximise the spin multiplicity. This is particularly relevant for europium (Eu, $Z = 63$) and ytterbium (Yb, $Z = 70$) since their divalent VEC provides a (half-)full 4f shell. For the left neighbours samarium (Sm, $Z = 62$) and thulium (Tm, $Z = 69$), the trivalent state is already quite stable, so the electronic chemical potential has to be high in order to push an additional electron into the 4f shell. On the other hand, if the electronic chemical potential is very low, cerium (Ce, $Z = 58$) and (less likely) terbium (Tb, $Z = 65$) can oxidise to tetravalent Ln⁴⁺ ions [18, pp. 2300]. The valence of the REs has a large impact on the properties of their compounds wherefore it is necessary to care about it. While isovalent RE compounds may differ only slightly in most properties, different valences usually lead to very different properties. A demonstrative example for this issue are the lanthanoid monochalcogenides, whose chemical formulae Ln(S, Se, Te) suggest divalence. However, the properties of these compounds strongly depend on the atomic number of the employed lanthanoid. While the monochalcogenides of Sm, Eu and Yb are salt-like, those of the other lanthanoids are metallic. The reason for this is a deviation between the formal oxidation state II and the actual valence of the Ln ions: They are divalent in the salt-like compounds, described by the formula Ln^{II}(S, Se, Te)^{-II}. In the metallic compounds, the Ln ions lose an additional 4f electron to the conduction bands, whereupon their valence formally increments by +I and gives rise to an “electride” Ln^{III}(S, Se, Te)^{-II}e⁻ [76].

The lanthanoid contraction

Although the 4f electrons are prevented from chemical bonding, their presence has some indirect consequences on the chemistry. Most notably, despite the valences of the REs are analogue, the atomic/ionic radii differ. For the first three REs without f-electrons (Sc, Y and La), the ionic radius increases, as expected for columns in the periodic table. On the contrary, the horizontal lanthanoid series from La to Lu shows

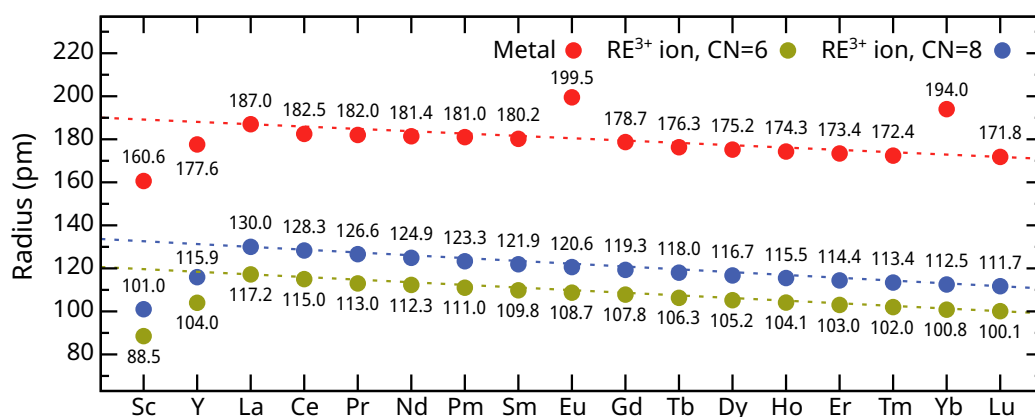


Figure 3.1: Atomic radii of the REs [17, Anhang IV]. Dashed lines between La and Lu highlight the lanthanoid contraction. CN: coordination number of RE³⁺ ions.

the aperiodic trend of decreasing ionic radii for incrementing atomic numbers. The *lanthanoid contraction* follows from two effects: the relativistic orbital contraction (Sec. 8.1) and the filling of the core-like 4f shell: Because every additional 4f electron screens the increment of the nuclear charge only partially, the fifth and sixth shells of heavier REs feel steeper potentials whereupon they contract [17, p. 374]. This affects the radii of the isolated atoms (with analogue VEC) as well as the radii of the trivalent ions and the metallic radii (Fig. 3.1 (a)). The lanthanoid contraction is strong enough to fully compensate the radius increase from the fifth to the sixth period at holmium. Therefore, the light yttrium (Y, $Z = 39$) is sometimes indexed between holmium (Ho, $Z = 67$) and erbium (Er, $Z = 68$). The discontinuities of europium (Eu, $Z = 63$) and ytterbium (Yb, $Z = 70$) in the otherwise smooth contraction trend of the metallic radii are due to their divalent VECs in the metals.

If REs compounds with analogous VECs are compared, the RE radius has the largest impact on the geometry. This can be very important in some cases, for example, if two structural phases are energetically close to each other. Small differences in the ion sizes, as caused by the lanthanoid contraction, then determine the favourability of the one or the other phase. This proves to be a critical point when investigating the RE silicides (Chap. 4). On the other hand, the smoothness of the lanthanoid contraction permits the structural tuning of some RE compounds by varying the employed RE. This is, for instance, utilised for the growth of RE-containing structures on surfaces.

The lanthanoid contraction is the f-analogue of the d-block contraction, which explains the otherwise unexpectedly small atomic radii of the post-transition metals (in particular those following the 3d-elements: Ga and Ge in group 13 and 14)³. The

³Analogously to the post-transition elements, the post-lanthanoids have unexpectedly small atomic radii. For the first post-lanthanoids, the f-block contraction is strong enough to fully compensate the incrementing main quantum number of the outer shells from the fifth to the sixth row. The group-4 elements zirconium (Zr) and hafnium (Hf) have almost identical ionic radii, as well as the group-5 elements niobium (Nb) and tantalum (Ta). As a consequence, naturally occurring minerals of these elements are often solid solutions between the respective two homologues. Niobium and Tantalum were identified as different elements in the mid of the 19th century. Hafnium was discovered even later in the 1920s, after having been predicted by the Bohr model [18, pp. 1809, 1831].

main difference between the f-block and the d-block contraction is that the lanthanoids have the same trivalent properties in most compounds and the same-period d-elements not. In principle, the lanthanoid contraction should occur also in the actinoids, whose 5f shell fills up. In fact, the radii of isovalent actinoid ions contract for incrementing atomic numbers. However, the trivalent state of the actinoids is less stable because relativistic effects makes the inner s orbitals collapse, which in turn expands the outer d and f orbitals. Consequently, the 5f orbitals can participate in the chemistry [17, 18, pp. 372ff, 2230, 2320f]. The homologues neodymium (Nd, $Z = 60$) and uranium (U, $Z = 92$) demonstrate this: While Nd is trivalent in most compounds, U tends to employ all valence electrons and assumed a main valence of VI [18, p. 2323]. Hence, the lanthanoid contraction is indeed unique in the periodic table.

3.2 Silicon and silicides

Silicon (Si, $Z = 14$) is the second most abundant element in Earth's crust (26.3 wt%), after oxygen (48.9 wt%) [17, p. 1063]. It belongs to the third row and 14th group, the carbon group. While carbon (C, $Z = 6$) is the basis of organic life on Earth, silicon is mainly known as the most important technology material as it is employed in the vast majority of integrated circuits (Sec. 1.1). However, silicon plays a role also in physiology, e.g. in the hair and nails of animals [17, p. 1062], in the cell walls of plants [77] and in the global oxygen generation (diatoms, "Kieselalgen") [78].

Silicon shares several physical and chemical properties with its lighter homologue carbon. They have analogous VECs (C: $2s^22p^2$, Si: $3s^23p^2$) with four valence electrons to be paired for chemical bonding. The s and p orbitals tend to hybridise to four equivalent sp^3 -hybrid orbitals in tetrahedral geometry, which is the origin of the alternative name of the carbon group: the *tetrels*. In the elemental phases, the sp^3 hybridisation leads to the diamond structure, a three-dimensional network in which each atom has four equivalent, σ -bound neighbours⁴. This structure is a stable phase for both elements on a certain thermodynamic domain. On the other hand, the elemental phases reveal an important difference between C and Si: C adopts the graphite structure at normal pressures, a layered structure of flat honeycombs which stick together by vdW interactions. Therein, the C atoms are sp^2 -hybridised and mutually bind via sp^2 bonds in trigonal-planar geometry. The remaining p orbitals pointing out of the plane (conventionally denoted p_z) connect with each other to a delocalised system of p_π bonds, which stabilises the individual sheets [17, pp. 997ff]. To a certain extent, these are even stable in isolated form, the *graphene* sheets [79], for which Andre Geim and Konstantin Novoselov were awarded with the Nobel Prize in Physics in 2010⁵. In contrast to C, Si avoids the graphite structure as well as p_π bonds

⁴In fact, there are two possibilities of fourfold coordinated networks. The classical diamond structure is based on the fcc lattice. Changing the layer stacking in the (111) direction from ABCABC to ABAB leads to a related structure: the hexagonal diamond or lonsdaleite, which is based on the hcp lattice. Being stable only under extreme thermodynamic conditions, lonsdaleite can be found in shockwave-treated graphite and meteorites [17, p. 1002].

⁵All Nobel Prizes in Physics, <https://www.nobelprize.org/prizes/lists/all-nobel-prizes-in-physics/> (visited on 04/03/2022).

in general. A demonstrative example of this are the properties of the oxides: While CO_2 with double bonds is a stable, gaseous molecule ($\langle \text{O}=\text{C}=\text{O} \rangle$), SiO_2 polymerises to single-bonded $[\text{SiO}_4]$ tetrahedrons which connect via the O atoms to crystals under normal conditions [17, pp. 1078ff, 1099ff]. For the same reason, the Si analogon of graphene (“silicene”) is unstable as both flat (sp^2) and buckled (sp^3) honeycomb geometries contain unpaired electrons, which render the allotrope highly reactive.

Zintl phases

A way to stabilise honeycomb-Si geometries is to charge the Si atoms and render them isoelectronic to the right neighbour phosphorus (P, $Z = 15$). The sp^2 hybridisation is then still avoided, but the five valence electrons give rise to a sp^3 configuration with three bonds and a non-binding electron pair. This allows the Si atoms to form a buckled honeycomb with closed shells. Alkali (M^{I}) and alkaline earth metals (M^{II}) can serve as electron donators since their electronegativities are smaller than that of Si by >0.7 (except Mg and Be, Allred-Rochow scale, [17, Tafel III]). This leads to a partially heterovalent compound M_nSi_m , which belongs to the class of *Zintl phases*, named after Eduard Zintl, who first investigated intermetallic compounds with high electronegativity differences. In 1963, W. Klemm and E. Busmann completed Zintl’s ideas to the extended Zintl-Klemm-Busmann concept (ZKB concept): When an alkali or alkaline earth metal (non-noble component) reacts with a metallic/semiconducting p-block element (noble component), the valence electrons of the non-noble component are formally completely transferred to the noble one. Depending on the VEC after the transfer, the noble component pairs the residual electrons by inter-se bonding and forms the anionic partial lattice, into which the cations are embedded. The formal strict charge transfer is then relaxed by introducing covalent bonds between the free electron pairs of the anionic lattice and the empty valence orbitals of the cations [80]. Since having four right neighbours, Si provides a particularly large variety of anionic partial lattices (e.g. buckled honeycombs, zigzag chains, dumb-bells and isolated atoms, [17, p. 1070]).

The ZKB concept can successfully explain some structural aspects of M_nSi_m compounds and will play an important role in explaining the inevitable vacancies of the bulk phases of the RE silicides. Though, it does not predict the exact geometry and the properties of the resulting compounds. Depending on the electronegativity difference of the reactants, the properties of Zintl phases can range from salt-like to metallic. For instance, alkali/alkaline earth metal chalcogenides (selenides and tellurides) are similar to the classical salts (oxides, halides) since the high electronegativity difference (>1.0 , except Mg and Be, Allred-Rochow scale, [17, p. 158]) implies a strong heterovalent (ionic) bonding. In particular, the reaction enthalpies are high and the compounds are brittle and isolating/semiconducting. On the contrary, if the electronegativity difference is less pronounced, the bonding has a more covalent character. Consequently, the bandgap decreases and the compound resembles more a metal than a salt concerning the electronic and optical properties [17, 80]. Moreover, covalent bonding can influence the partial anionic lattice because the empty d orbitals of the heavier alkali/alkaline earth metal cations can be activated and exert a steric effect on their binding partners [17, pp. 400ff].

4 The rare-earth silicide bulk phases

The RE silicides have been investigated since the end of the 1950s [81–108]. In 1959, Perri et al. systematically analysed the “disilicides” of several REs by means of XRD [81]. They found that the lighter REs crystallise in the tetragonal ThSi_2 structure, while the heavier REs (up to Dy) assume an orthorhombically distorted version of it. The clear trend is that the orthorhombic distortion increases with higher RE atomic numbers, corresponding to smaller ionic radii (lanthanoid contraction, Sec. 3.1). For the heaviest RE silicide investigated in that work, DySi_2 , the distortion is considerable with a b/a ratio of 97.8%. Only Eu disrupts the otherwise monotone development as it adopts the undistorted, tetragonal ThSi_2 structure. Since coinciding with the discontinuity in the lanthanoid contraction, this is a clear evidence that Eu is divalent in its silicide while all other investigated REs are trivalent [81]. Subsequent work found that the orthorhombic distortion reversibly vanishes at temperatures of several 100 °C, so all investigated RE silicides assume the tetragonal ThSi_2 structure as a high-temperature phase. On the other hand, the tetragonal silicides of Pr and Eu distort at -120 °C and -150 °C, respectively [82]. Mayer et al. [83] completed the list by the REs not investigated by Perri et al. They found that the silicides of Er and the heavier REs crystallise in the hexagonal AlB_2 structure, which is quite different from the ThSi_2 structure at first glance. Ho and all lighter REs join the findings of Perri et al. as they adopt tetragonal/orthorhombically distorted ThSi_2 structure, depending on the ionic radius. The silicide of Y was found to adopt both structures depending on the preparation temperature, in accordance with its ionic radius lying between those of Ho and Er [83]. This dimorphism motivated the same group to test whether the other RE silicides show the $\text{AlB}_2/\text{ThSi}_2$ transition as well. In fact, the silicides of Gd, Tb, Dy, Ho and Y can assume either the tetragonal/orthorhombic ThSi_2 structure or the hexagonal AlB_2 structure, the latter apparently being the low-temperature phase. The REs lighter than Eu show only the tetragonal/orthorhombic ThSi_2 structure, and the heavier REs Er, Tm and Lu show only the hexagonal AlB_2 structure [85].

The aim of this chapter is to illuminate the microscopic reasons for the peculiar behaviour of the RE silicides and to investigate their structure. At first, the prototypes (ThSi_2 and AlB_2) are systematised in a novel and unconventional manner. This helps to understand how the structures respond to specific variations, in particular concerning vacant Si sites, which are inevitably present in all RE “disilicides” and which have not been sufficiently investigated. Then, different structure models are optimised and their stability is analysed by *ab initio* thermodynamics. The following points are addressed: the stoichiometric structure models, the role of the 4f electrons, the lattice dynamics and the Si vacancies. The findings on the structures are confirmed by band structure analyses. The chapter concludes with a discussion of the mechanisms which determine the structure of the RE silicides.

4.1 Structure prototypes

The RE silicide structures can be classified into two prototypes: the ThSi_2 structure (Fig. 4.1 (a)) and the AlB_2 structure (Fig. 4.1 (b)). Both are characterised by a skeleton of mutually threefold coordinated Si atoms in trigonal-planar geometry, denoted M-stars, into which the RE atoms are embedded. The simpler realisation of this is the AlB_2 structure. It consists of parallel, congruent sheets of flat-honeycomb-Si between which hexagonal layers of RE atoms are embedded at hole position. The honeycomb sheets can also be viewed as staggered rows of M-stars, as indicated by blue shadows in (Fig. 4.1 (b)). The space group is $P6/mmm$ (No. 191) and the atoms occupy the Wyckoff positions¹ $\text{RE} \rightarrow 1a$ and $\text{Si} \rightarrow 2d$, so the conventional unit cell contains one formula unit RESi_2 . The ThSi_2 structure is the alternative realisation. It can be derived from the AlB_2 structure by rotating the M-stars of every second row by 90° and staggering the rows to form a three-dimensional network. The RE atoms occupy the interstices and are visible from both views along the basis. The space group is $I4_1/amd$ (No. 141) and the atoms occupy the Wyckoff positions $\text{RE} \rightarrow 4b$ and $\text{Si} \rightarrow 8e$, so the conventional unit cell contains four formula units RESi_2 .

In order to clarify the relationship between the two structures, consider the building blocks which both of them have in common [88]. These building blocks are cuboids of width x , depth y and height z with Si atoms at the vertices and an RE atom in the centre (orange boxes in Fig. 4.1). Their stacking in the z -direction determines the structure. If stacked in a zigzag manner, i.e. alternately translated by $\pm \frac{x}{2}$ in the x -direction, the blocks form the AlB_2 structure. x is then the lattice constant a ($[11.0]$ direction), z is $\sqrt{3}a/2$ for a perfect hexagonal symmetry ($[\bar{1}1.0]$ direction), and y is the lattice constant c ($[00.1]$ direction). Alternatively, the blocks can be stacked in a helical manner, i.e. alternately translated by $\pm \frac{x}{2}$ in the x -direction and $\pm \frac{y}{2}$ in the y -direction, which result is the ThSi_2 structure. x is then the lattice constant a ($[100]$ direction), y is b ($[010]$ direction) and z is $c/4$ ($[001]$ direction). The building blocks demonstrate a further structural aspect concerning the ways how the Si atoms at the vertices are connected. The splices between two block faces consist of parallel rows of zigzag-chain-Si (different shades of blue in Fig. 4.1) which accrete to *zigzag planes*. In the AlB_2 structure, all zigzag chains point into the same $[11.0]$ direction. In the ThSi_2 structure, the zigzag planes are alternately oriented in the $[100]$ direction (light blue) and the perpendicular $[010]$ direction (dark blue).

Silicon vacancies

The stoichiometries of real RE silicides deviate considerably from RESi_2 in that Si atoms are missing. Hence, the structures in Fig. 4.1 should be considered only as prototypes. The empty Si sites, the *vacancies*, in the real structures are unordered² and their concentration depends on the fabrication technique, the temperature and the atomic number of the RE. As the real stoichiometries range between $\text{RESi}_{1.6}$ and

¹The numbers preceding the letters denote the multiplicity of the positions.

²In thin RESi_2 films of the AlB_2 phase, which are epitaxially grown on Si(111), the vacancies are ordered in-plane and give rise to a $R30^\circ(\sqrt{3} \times \sqrt{3})$ superstructure [36, 37, 39, 46, 50–52].

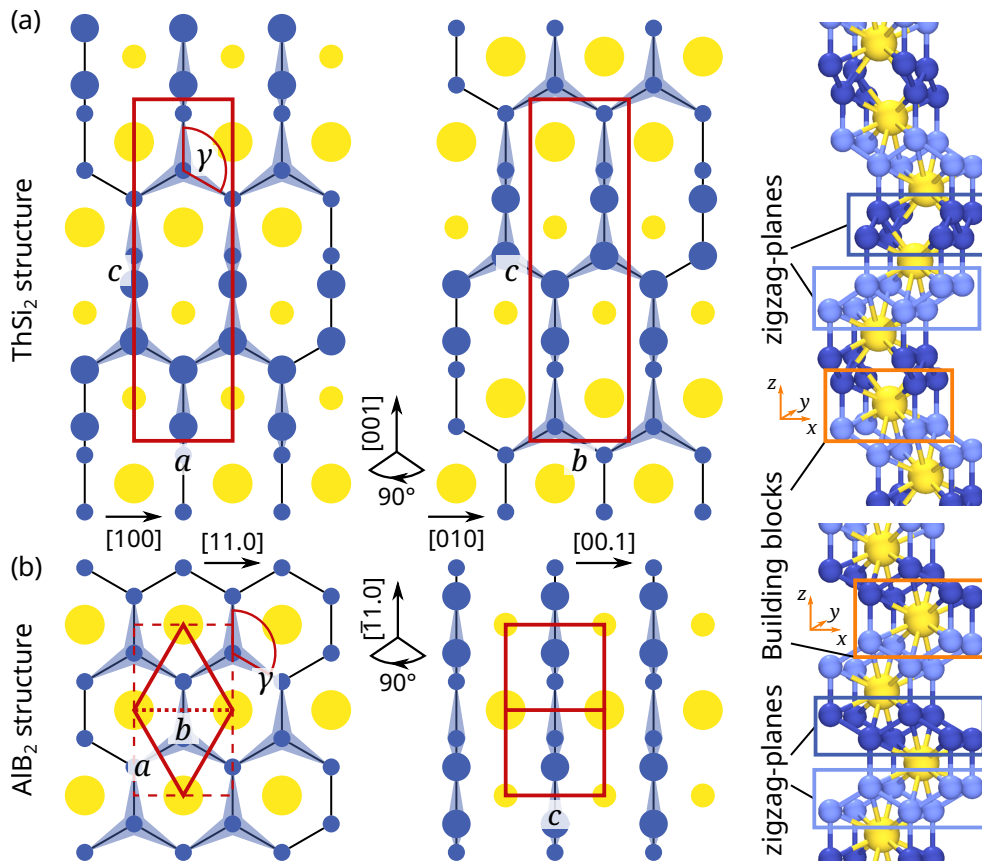


Figure 4.1: Overview over the RESi_2 structure prototypes. (a) ThSi_2 prototype; (b) AlB_2 prototype. Blue circles are Si atoms; Yellow circles are RE atoms; Circle sizes indicate the out-of-plane positions. Left and centre: Views along perpendicular crystallographic axes. Red lines mark conventional unit cells. Blue shadings mark threefold coordinated Si atoms in the Si sublattice (M-stars). Right: Stacking of the cuboid building blocks (orange lines). Light and dark blue Si atoms highlight Si zigzag planes.

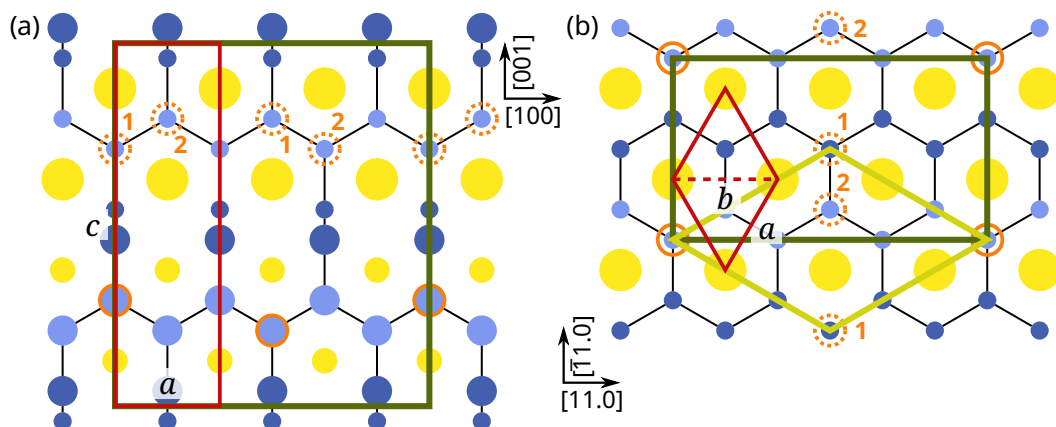


Figure 4.2: Possible configurations of ordered Si vacancies in $\text{RESi}_{1.67}$. (a) ThSi_2 ; (b) AlB_2 . Colouring: Fig. 4.1. Solid orange circles mark the first set of vacancies, labelled dashed orange circles possible second sets. Green lines mark the supercells.

RESi_{1.9} [81, 85–93], the RE “disilicides” should always be referred to as RESi_{2-x}, where x is the number of Si vacancies per RE atom. A value of $x = 0.33$, as present in many RE silicide preparations, implies that every sixth Si site is vacant. The large number of vacancies affects the Si sublattice and, thus, the entire prototype in a considerable, but predictable manner: Since experimental diffraction patterns do not indicate any long-range ordering, the vacancies have to be assumed statistically distributed. A uniform distribution retains the symmetries of the prototypes (AlB₂ → hexagonal, ThSi₂ → tetragonal), while a non-uniform distribution is likely to distort them. In detail, removing a Si atom makes the three neighbours of the respective M-star move inwards, towards the vacant site. This combined with the topography of the zigzag chains suggests how a given vacancy distribution alters the lattice constants. Fig. 4.2 shows exemplary snapshots of ordered vacancy configurations (orange circles) for the ThSi₂ and the AlB₂ structure in RESi_{1.67} stoichiometry.

The conventional unit cell of the ThSi₂ structure contains four alternately orthogonal zigzag planes, of which every second is equivalent due to the body-centred unit cell (highlighted by light and dark blue circles in Fig. 4.2 (a)). If the vacancies populate both inequivalent zigzag planes to a similar extent (i.e. every sixth Si site is vacant in both the light and dark blue zigzag chains, not shown in Fig. 4.2), the basal lattice constants a and b are expected to shrink equally. Also the axial lattice constant c will shrink as the zigzag planes move closer together. In summa, the cell volume will contract while retaining the tetragonal symmetry of the prototype. The situation changes if the vacancies concentrate in one of the two inequivalent zigzag planes (e.g. every third Si site is vacant in the light blue zigzag chains, Fig. 4.2 (a)). Then, a is expected to shrink, as well as c , while b will remain unchanged. In summa, the structure will undergo an orthorhombic distortion along with a reduction of the symmetry. Such an effect was confirmed in TbSi_{1.67} by Schobinger-Papamantellos et al., who measured a distortion of $\approx 2\%$ (neutron diffraction, [89]). If the vacancies populate the zigzag planes of the AlB₂ structure to an equal extent (configuration 1 in Fig. 4.2 (b)), the basal lattice constants a and b will equally contract while retaining the hexagonal symmetry of the prototype. As a response to the squeezing of the basis, the interstitial RE atoms will push the silicon layers apart and increase the axial lattice constant c . On the other hand, if the vacancies concentrate in one of the two inequivalent zigzag planes (e.g. configuration 2 in Fig. 4.2 (b)), an orthorhombic distortion is expected as a and b shrink differently. Such an effect was observed in hexagonal ErSi_{1.67} [91] and TbSi_{1.67} [93] by Auffret et al. (neutron diffraction). However, the distortion of the AlB₂ structure ($<0.5\%$) seems to be much weaker than that of the ThSi₂ structure. While the vacancies underlie a probability distribution in most RESi_{2-x}, Yb₃Si₅ can adopt the ordered version of configuration 1 in the bulk, as indicated by a R30°($\sqrt{3} \times \sqrt{3}$) superstructure (light green unit cell) (XRD, [87]).

As a final remark on the stoichiometry, the nomenclature of the RE silicides is quite chaotic in the literature. Some publications refer to them as RESi₂, irrespectively of the large number of vacancies. Others refer to the silicides with a ThSi₂-derived structure as RESi₂ and to those with an AlB₂-derived structure as RE₃Si₅. Although this agrees with the relative positions in the temperature-composition phase diagrams (vide infra), the stoichiometries are still incorrect. Moreover, it is rather confusing

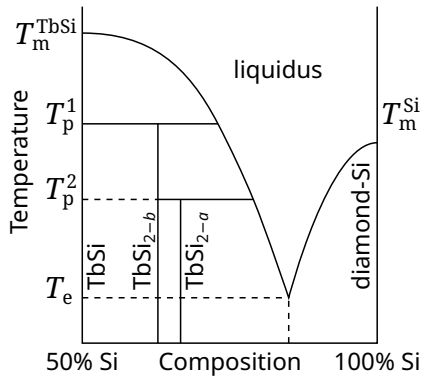
that the orthorhombically distorted ThSi_2 structure is often referred to as the GdSi_2 structure. On the one hand, the structure-determining vacancies are not ordered in GdSi_{2-x} , so it has to be related to the ThSi_2 structure anyway. On the other hand, GdSi_2 is dimorphic and can adopt the AlB_2 structure as well, depending on the preparation conditions. In order to avoid misunderstandings, the following nomenclature is used in this work. All RESi_{2-x} structures are assigned to one of the two prototypes: the AlB_2 phase or the ThSi_2 phase. If relevant, the presence or absence of orthorhombic distortion is explicitly mentioned by a symmetry tag (“hex”: hexagonal, “tet”: tetragonal, “ort”: orthorhombic). The chemical formula is RESi_{2-b} for the AlB_2 -type silicides and RESi_{2-a} for the ThSi_2 -type silicides (as introduced by [102]), where b is (slightly above) 0.33 and a between 0.33 and 0. For example, orthorhombically distorted ThSi_2 -type terbium silicide is denoted ort- ThSi_2 - TbSi_{2-a} and hexagonal AlB_2 -type erbium silicide is denoted hex- AlB_2 - ErSi_{2-b} . The structure-neutral chemical formula is RESi_{2-x} .

The phase diagrams of the RE–Si systems

The silicides of the heavy REs always contain vacant Si sites, as the temperature-composition phase diagrams of the RE–Si systems prove [102–107]. Summarising reviews on the phase diagrams can be found for Gd, Tb, Dy, Ho and Er [109–113]. This group is simply denoted by RE in the following paragraphs. Fig. 4.3 shows a sketch of the silicon-rich half of the phase diagram of the Tb–Si system, to which those of Gd, Dy, Ho and Er are similar. It furthermore contains a table with the respective peritectic and eutectic temperatures.

The solubility of RE in Si and Si in RE is negligible (<1 at%) [102–104]. Several compounds RE_xSi_y exist, whose melting points are higher than those of elemental hcp-RE and diamond-Si ($T_m^{\text{RE}} > 1300\text{ }^\circ\text{C}$ and $T_m^{\text{Si}} = 1414\text{ }^\circ\text{C}$). All RE–Si systems have a compound at a Si content of 50 at% (RE_1Si_1), which melts congruently at a high temperature ($T_m^{\text{RESi}} \approx 1850\text{ }^\circ\text{C}$). On the Si-rich side, all RE–Si systems have a compound at a Si content of ≈ 62.5 at%, which transitions by a peritectic reaction into solid RE_1Si_1 and liquidus at a peritectic temperature of $T_p^1 \approx 1650\text{ }^\circ\text{C}$. This compound is the AlB_2 phase with a stoichiometry of RESi_{2-b} ($b \approx 0.33$, $\text{RESi}_{1.67}$ or RE_3Si_5). In the Er–Si system, AlB_2 - ErSi_{2-b} forms a eutectic with diamond-Si at a Si content of 81 at% and a eutectic temperature of $T_e = 1210\text{ }^\circ\text{C}$. The Ho–Si, Dy–Si, Tb–Si and Gd–Si systems, in contrast, have an additional, peritectic compound at a Si content between 62.5 at% (RESi_{2-b}) and 66.7 at% (RESi_2). The peritectic temperature T_p^2 decreases monotonously from Gd (1601 $^\circ\text{C}$) to Ho (1290 $^\circ\text{C}$). This compound is the ThSi_2 phase with a stoichiometry of RESi_{2-a} ($a \in [0, 0.33]$, lower vacancy density than in AlB_2 - RESi_{2-b}). Similarly to AlB_2 - ErSi_{2-b} in the Er–Si system, ThSi_2 - RESi_{2-a} forms a eutectic with diamond-Si at Si contents between 82 at% and 87 at% and eutectic temperatures of $T_e \approx 1200\text{ }^\circ\text{C}$. Both the AlB_2 and the ThSi_2 phases show a reversible dimorphism (orthorhombic distortion) at lower temperatures, in accordance with [82, 89, 91]. Furthermore, the RESi_{2-x} phases have narrow homogeneity ranges of ≈ 1 at% [87, 104].

Several conclusions can be drawn from the phase diagrams. The first is that the formation of the AlB_2 and ThSi_2 phases depend rather on the initial compositions than on the temperature. In particular, the initial Si concentration of 62.5 at% is a critical value beyond which AlB_2 - ErSi_{2-b} is saturated with silicon [87], and the silicon-richer



RE	T_p^1 (°C)	T_p^2 (°C)	T_e (°C)
Gd	1664	1601	1226
Tb	1638	1517	1222
Dy	1635	1437	1224
Ho	1620	1290	1210
Er	1620	—	1210

Figure 4.3: Left: Schematic phase diagram of the Tb–Si system. Adapted from [111]. Right: Peritectic and eutectic temperatures of some RE–Si systems [109–113].

$\text{ThSi}_2\text{-RESi}_{2-a}$ forms beside $\text{ALB}_2\text{-RESi}_{2-b}$ for the REs lighter than Er [88, 89, 93]. The findings of Mayer et al. that ThSi_2 seems to be the high-temperature phase and ALB_2 the low-temperature phase [85] can be explained by the incompleteness of the reaction if the temperature during the preparation is too low [108]. The second conclusion concerns the peritectic transitions. For example, consider an initial preparation of 33 at% RE and 67 at% Si (RESi_2). If the sample heats up to a temperature between T_p^1 and T_p^2 (~ 1600 °C), $\text{ALB}_2\text{-RESi}_{2-b}$ crystals form beside a RE/Si melt on the liquidus curve. Slow annealing drives the transition across the peritectic line T_p^2 whereupon the $\text{ALB}_2\text{-RESi}_{2-b}$ crystals vanish and solid $\text{ThSi}_2\text{-RESi}_{2-a}$ forms plus solid excess Si. Such peritectic transitions require a particular care about the temperature variation during annealing in order to obtain the desired single phase silicides. If the temperature drops too fast, the product will contain considerable amounts of residual $\text{ALB}_2\text{-RESi}_{2-b}$ which is kinetically inhibited from transitioning into the equilibrium ($\text{ThSi}_2\text{-RESi}_{2-a}$ plus diamond-Si).

Moreover, the peritectic and eutectic temperatures T_p^1 , T_p^2 and T_e show an interesting dependence on the RE atomic numbers. While T_p^1 and T_e vary only slightly, T_p^2 shows a rapid drop from Gd to Ho. In detail, T_p^2 lies short below T_p^1 in Gd–Si and approaches T_e in Ho–Si. If the trend was extrapolated from Ho to Er, T_p^2 would drop below T_e , which coincides with the non-existence of $\text{ThSi}_2\text{-ErSi}_{2-a}$. The behaviour of the peritectic temperatures also confirms that the RE radius does not directly influence the stability of the ALB_2 structure, as stated in [85], but rather the stability of the ThSi_2 structure. The latter becomes unstable if the ratio between the atomic radii of RE and Si is too small [84]. If the trend was extrapolated to the REs lighter than Gd, T_p^2 would rise beyond T_p^1 , which implies that the ThSi_2 phase melts congruently. This is indeed the case for Sm–Si and Nd–Si [114, 115] (Eu left out because of its anomalous valence). Hence, Gd, Tb, Dy and Ho are a unique quadruple concerning the peritectic transition between $\text{ThSi}_2\text{-RESi}_{2-a}$ and $\text{ALB}_2\text{-RESi}_{2-b}$.

Valence considerations

In early studies, the wrong assumption of vacancy-free, stoichiometric RESi_2 led to the idea that the silicon sheets in the hex- ALB_2 structure are analogous to the

carbon sheets in graphite, including the presence of delocalised π -electron systems. For instance, Mayer et al. calculated a Si–Si bond distance of 2.16 Å from the basal lattice constants of hex- $\text{AlB}_2\text{-LuSi}_2$. That the result is shorter than the single bond length in diamond-Si (2.35 Å) indicates the presence of sesqui or double bonds. The ratio between the two values (0.919) seems to confirm this as it is similar to the bond-distance ratio of graphite-C and diamond-C (0.921) [83, 85]. However, as will be proven, the Si–Si bond distance in hex- $\text{AlB}_2\text{-RESi}_2$ is close to that in diamond-Si. Only the contraction of the basis due to the vacancies is such that a corresponding vacancy-free honeycomb-Si sheet produces the above ratio by coincidence. Magaud et al. were the first who theoretically investigated vacancy-populated YSi_2 with DFT (RE ionic radius similar to Ho and Er, no f electrons, [96]). It turned out that the stoichiometry is decisive for the agreement between theoretical and experimental lattice constants. Relatively to $\text{AlB}_2\text{-YSi}_2$, $\text{AlB}_2\text{-Y}_3\text{Si}_5$ (ordered vacancies, configuration 1 in Fig. 4.2 (b), light green unit cell) has an inverted c/a ratio as the basis of the unit cell shrinks and the axial lattice constant grows (as predicted, vide supra). The authors concluded that the vacancies allow the Si honeycomb to “release a part of the constraint imposed by the two adjacent Y planes”, i.e. the vacancies are due to mechanical strain [96]. However, as Zavala Aké et al. pointed out, both $\text{AlB}_2\text{-YSi}_2$ and $\text{AlB}_2\text{-Y}_3\text{Si}_5$ are unstrained zero-pressure structures and the Si–Si distances of respectively 2.37 Å and 2.44 Å are quite close to that in diamond-Si (2.35 Å) (DFT, [100]). This indicates that the Si atoms are singly bonded in both $\text{AlB}_2\text{-YSi}_2$ and $\text{AlB}_2\text{-Y}_3\text{Si}_5$ and that the removal of Si atoms *causes* the basal contraction, not vice versa.

The electronic density of states (DOS) gives an important hint at the true reason for the stability of the vacancy-populated phases: The DOS of $\text{AlB}_2\text{-YSi}_2$ shows a peak at the Fermi level, which is not present in $\text{AlB}_2\text{-Y}_3\text{Si}_5$ [95, 100]. Obviously, the Si vacancies partially deplete the conduction band and thereby reduce the total energy. In order to find a simple explanation for this, the system will be illuminated within the ZKB concept (p. 33). Since the anionic lattice of vacancy-free $\text{AlB}_2\text{-YSi}_2$ consists of Si honeycomb sheets, the Si atoms have a formal valence of $-I$. However, each RE^{3+} cation donates three electrons into the system, of which two are accepted by two Si atoms and one is spare. The compound formula can thus be written as an electride $\text{RE}^{\text{III}}\text{Si}_2^{-I}\text{e}^-$, indicating that one electron per RE atom occupies the conduction band. The removal of a Si atom primarily reduces the number of acceptors by one. On the other hand, having lost their bonding partner, the three Si atoms adjacent to the vacant Si site can each accept an additional electron to complete the shells. In summa, the capacity of the anionic partial lattice increases by two electrons for each vacancy. The compound formula for RE_3Si_5 is thus $\text{RE}_3^{\text{III}}\text{Si}_2^{-I}\text{Si}_3^{-\text{II}}\text{e}^-$, so the number of conduction band electrons per RE atom is reduced to $1/3$. Hence, the vacancies are expected to improve the charge balance, which will be proven later.

According to the ZKB concept, the bonding in the vacancy-populated AlB_2 structure is as follows: The two Si^{-I} atoms per unit cell bind each to the three $\text{Si}^{-\text{II}}$ atoms via in-plane sp^2 -hybrid orbitals. The free electron pair of each Si^{-I} atom thus occupies the out-of-plane p_z orbital. The three $\text{Si}^{-\text{II}}$ atoms per unit cell bind each to the two Si^{-I} atoms in an angled geometry. They are presumably sp^3 -hybridised and use the two in-plane hybrid orbitals for the Si–Si bonds. The other two hybrid orbitals, which are inclined out of the Si plane towards the vacancy, accept the two free electron pairs. Of

course, the charge transfer is formal and bonds have to be established between the free electron pairs of the Si atoms and the empty orbitals of the RE atoms. While the former have the above-mentioned geometry, the geometry of latter can be neglected in first approximation as the s and d orbitals can hybridise in a quite flexible manner [17, p. 396]. The electronegativity difference between Si and the REs from Gd to Er ($\Delta\chi = 1.74 - 1.11 = 0.63$, Allred-Rochow scale [17, Tafel III, Tafel V]) suggests a partial ionic character of ca. 10% [17, p. 158]. Thus, a covalent bonding between the RE-sd orbitals and the Si-sp/Si-p_z orbitals is expected to dominate the chemistry.

4.2 Structure optimisation

The preliminary considerations about the structure of bulk RE₂Si_{2-x} are inspected by means of DFT (Sec. 2.1). For this purpose, several structure models based on the AlB₂ and ThSi₂ prototypes are set up in suitable unit cells and optimised with respect to the cell vectors and the ionic positions (mechanical equilibrium). After that, the thermodynamic properties are calculated in order to determine the most stable phases under given conditions. The focus of the investigations is on the silicides of Tb since Tb lies in the mid of the quadruple from Gd to Ho and is employed for the nanostructures in Chap. 5 and Chap. 6. At certain points, the TbSi_{2-x} are compared to ErSi_{2-x} as it is the lightest RE not assuming the ThSi₂ phase.

4.2.1 Methodological details

Volume relaxation

All bulk phases in this work are considered to be in mechanical equilibrium with the vacuum, so the zero-pressure volumes of the structure models have to be found. The first method to conduct the *volume relaxations* employs the code-level relaxation routines which optimise the atomic positions, the volume and the shape of the unit cell simultaneously. This is a quick way, but some systematic errors limit the reliability of the results. On the one hand, Pulay stress arises, i.e. artificial stress from the link between the unit-cell volume and the Fourier sampling. This can be reduced by iterative restarts of the relaxation. On the other hand, the results depend on the way how the minimum is approached, which is due to the finite stop criterion (energy difference, forces, etc.). In particular, starting from volumes smaller and larger than the optimum can result in different unit cells. These errors are avoided if sample unit cells are optimised at fixed volumes and the Murnaghan equation of state is used [116]. In detail, the free energy $F(V, T, N_\bullet)$, depending on the volume V , the temperature T and the particle number N_\bullet of the atomic species \bullet , is minimised.

$$K(p) = -V \left(\frac{\partial p}{\partial V} \right)_T = K_0 + K' p \Rightarrow F(V) = F_0 + \frac{K_0 V}{K'} \cdot \left[\frac{1}{K'-1} \left(\frac{V_0}{V} \right)^{K'} + 1 \right] - \frac{K_0 V_0}{K'-1} \quad (4.33)$$

where $K(p)$ is the compressive modulus at p , $K_0 = K(0)$ and $K' = K'(0)$.

The function $F(V)$ is fitted to the samples $(V, F(V))$, whereupon the fit parameters finally yield the minimum (V_0, F_0) as well as the bulk mechanical properties K_0 and K' . As the prerequisite of Eq. (4.33) is the linear behaviour of $K(p)$, the Murnaghan equation of state is valid only on a small region around the minimum.

Thermodynamical framework

Since this chapter is preparatory work for the nanostructures on silicon surfaces, the investigations concern only the Si-richest bulk RESi_{2-x} phases under Si-rich conditions. In other words, the most stable structures are searched for a given amount of RE and an infinitely large reservoir of Si provided by bulk diamond-Si. This translates into the *thermodynamic boundary conditions* that the pressure p , the temperature T , the RE amount N_{RE} and the Si chemical potential μ_{Si} are constant. The situation is best described by a thermodynamical potential $G_{\text{RE}}(p, T, N_{\text{RE}}, \mu_{\text{Si}})$ derived from the internal energy $U(V, S, N_{\text{RE}}, N_{\text{Si}})$ by Legendre transformation.

$$G_{\text{RE}}(p, T, N_{\text{RE}}, \mu_{\text{Si}}) = U(V, S, N_{\text{RE}}, N_{\text{Si}}) + pV - TS - \mu_{\text{Si}}N_{\text{Si}} \quad (4.34)$$

where V is the volume, S the entropy, N_{\bullet} the particle number of the atomic species \bullet and μ_{\bullet} the respective chemical potential. Under given boundary conditions, those structures are stable which minimise G_{RE} . According to Euler's theorem, G_{RE} comprises only the term $N_{\text{RE}}\mu_{\text{RE}}$ and can easily be transformed into an intensive quantity by dividing by N_{RE} . The remainder is then identical to the RE chemical potential.

$$\frac{1}{N_{\text{RE}}} G_{\text{RE}}(p, T, N_{\text{RE}}, \mu_{\text{Si}}) = \frac{\mu_{\text{RE}}N_{\text{RE}}}{N_{\text{RE}}} = \mu_{\text{RE}}(p, T, \mu_{\text{Si}}) \quad (4.35)$$

The boundary conditions immediately replace some of the variables in Eq. (4.34) with known quantities. The structure models determine $\{N_{\bullet}\}$. μ_{Si} is fixed to $\mu_{\text{Si}}^{\text{d-Si}}$, the Si chemical potential of diamond-Si. The pV terms are zero because the structure models are relaxed into their zero-pressure volumes (vide supra). Concerning S and T , an approximation will be made, although its validity is not obvious a priori: The internal energy U is replaced by the DFT total energy $E_{\text{DFT}}^{\text{cell}}$ and the TS terms are omitted. This is based on the close relatedness between the RESi_2 prototypes, which are both characterised by cages of mutually three-fold coordinated Si atoms, into which the RE atoms are embedded. Therefore, the vibrational contributions to U and S are expected to be similar in different RESi_{2-x} structures, so the TS terms cancel out in energy differences. This is a common practice when related structures are compared at low temperatures [53]. The validity of the TS cancellation will be tested on two samples in Sec. 4.2.4. With these replacements, Eq. (4.35) reduces to:

$$\mu_{\text{RE}} \approx \frac{1}{N_{\text{RE}}} \left(E_{\text{DFT}}^{\text{cell}} - \mu_{\text{Si}}^{\text{d-Si}} N_{\text{Si}} \right) - \mu_{\text{RE}}^{\text{hcp-RE}} \quad (4.36)$$

Referring μ_{RE} to $\mu_{\text{RE}}^{\text{hcp-RE}}$, the RE chemical potential of bulk hcp-RE, is necessary because only chemical potential differences have a physical meaning. As the reference is arbitrary, $\mu_{\text{RE}}^{\text{hcp-RE}}$ could be substituted by the RE chemical potential of other phases, e.g. by that of gaseous RE atoms. In the present form, Eq. (4.36) equals the free

formation enthalpy of $\text{RE} + (2-x)\text{Si} \longrightarrow \text{RESi}_{2-x}$ under Si-rich conditions. As μ_{RE} is intensive, structure models of different sizes and, particularly, containing different numbers of RE and Si atoms can directly be compared regarding their stability. In detail, if a set of RESi_{2-x} structures is given, only those are in chemical equilibrium with diamond-Si which minimise μ_{RE} . The $\mu_{\text{RE}}^{\text{hcp-RE}}$ term cancels in μ_{RE} differences, which shows that the reference is indeed arbitrary. If, in addition, the stoichiometry of the two structures is equal, also the $\mu_{\text{Si}}^{\text{d-Si}}$ term cancels, so knowledge about any referential chemical potentials is not necessary in this case. A major part of the investigations concerns the question whether the AlB_2 phase or the ThSi_2 phase is more stable under certain conditions (e.g. the Si vacancy density or the theoretical treatment). Therefore, it is instructive to define the difference:

$$\Delta\mu_{\text{RE}}^{\text{T-A}} := \mu_{\text{RE}}^{\text{ThSi}_2} - \mu_{\text{RE}}^{\text{AlB}_2} \quad (4.37)$$

where $\mu_{\text{RE}}^{\text{ThSi}_2}$ and $\mu_{\text{RE}}^{\text{AlB}_2}$ are the RE chemical potentials of the most stable ThSi_2 - RESi_{2-x} and AlB_2 - RESi_{2-x} structure models at a certain x . Hence, $\Delta\mu_{\text{RE}}^{\text{T-A}} < 0$ implies that the ThSi_2 phase is more stable than the AlB_2 phase and vice versa.

Vibrational contributions to the free energy

The omission of the lattice dynamics in Eq. (4.36) is based on the cancellation of the *vibrational contributions* upon comparing similar structures. In order to check the validity, it has to be proven that the lattice dynamics of the structures to be compared yield similar free energies. Lattice dynamics covers a broad field of different effects and methods which would exceed the purposes of this work. A quite feasible concept for estimating lattice-dynamical effects at not too high temperatures is the *frozen-phonon method*, which is applied in this work.

In principle, the dynamics of N_{K} ions in a DFT system are described by the Hamilton operator H_{K} with the DFT total energy $E_{\text{DFT}}(\{R_k\})$ acting as an effective potential. The latter depends on the ionic positions $\{R_k\}$, $k \in [1, 3N_{\text{K}}]$ (Born-Oppenheimer approximation, Eqs. (2.2); from now on, the positions are written component-wise). For small displacements from the equilibrium, $E_{\text{DFT}}(\{R_k\})$ can be approximated by a second-order expansion, the *harmonic approximation*. The coefficient of the quadratic term, the Hessian matrix of $E_{\text{DFT}}(\{R_k\})$ or *dynamical matrix*, can be calculated by finite differences. Its eigenvalues are (the square of) frequencies ω_k and its eigenvectors are harmonic vibrations. Hence, as long as the harmonic approximation is valid, i.e. the temperature is not too high, the lattice dynamics is described by an ensemble of $3N_{\text{K}}$ independent quantum-mechanical harmonic oscillators. Since $E_{\text{DFT}}(\{R_k\})$ is periodic in crystals, an approach similar to the Bloch theorem (Sec. 2.2) can be employed to reduce the vibrating ions to the $N_{\text{K}}^{\text{cell}}$ ions of the unit cell. The band structure of the eigenfrequencies gives rise to $3N_{\text{K}}^{\text{cell}}$ discrete branches, the *phonons*, which depend on a continuous parameter \mathbf{q} confined to the Brillouin zone [6, pp. 41ff]. The “frozen-phonon” method consists in calculating the phonons at zero temperature and using them for describing the lattice dynamics at finite temperatures. The exact calculation of state variables of a phononic system involves \mathbf{q} -integrations over the Brillouin-zone and summations over discrete branches. In this work, the

VASP-built-in phonon routines are employed, which calculate only the N_K^{cell} phonons at $\mathbf{q} = 0$. The sum over them corresponds to sampling the Brillouin-zone solely by the Γ -point, which is insufficient particularly for small unit cells. To resolve this issue, the unit cells are multiplied to supercells so that the Γ -point includes also $\mathbf{q} \neq 0$ points according to band-folding. In doing so, symmetry-equivalent entries of the dynamical matrix are identified so as to reduce the computational demand.

Once the eigenfrequencies ω_k are determined, the vibrational free energy $F_{\text{vib}}(T)$ at finite temperatures T can be calculated by the quantum statistics of independent harmonic oscillators.

$$Z = \prod_{k=1}^{3N_K^{\text{cell}}} \text{tr}[\exp(-\beta\hbar\omega_k(n + \frac{1}{2}))] = \prod_{k=1}^{3N_K^{\text{cell}}} (2 \sinh(\beta\hbar\omega_k/2))^{-1}, \quad \beta = 1/k_B T$$

$$\Rightarrow F_{\text{vib}}(T) = -\frac{1}{\beta} \ln(Z) = k_B T \sum_{k=1}^{3N_K^{\text{cell}}} \ln(2 \sinh(\hbar\omega_k/2k_B T)) \stackrel{T \rightarrow 0}{\simeq} \sum_{k=1}^{3N_K^{\text{cell}}} \frac{\hbar\omega_k}{2} \quad (4.38)$$

Adding this to the electronic free energy $\approx E_{\text{DFT}}^{\text{cell}}$ yields the total free energy $F(T)$.

$$F(T) = E_{\text{DFT}}^{\text{cell}} + F_{\text{vib}}(T) \quad (4.39)$$

In the low-temperature limit, $F_{\text{vib}}(T)$ approaches the sum of the ground-state energies of the harmonic oscillators. Consequently, vibrational contributions can be relevant even at low temperatures, at which the TS terms vanish.

The theoretical treatment of the rare-earth elements

As the considerations in Sec. 3.1 point out, the lanthanoids have a strongly correlated, incomplete 4f shell. Therefore, pure DFT predicts the wrong ground state with fractionally occupied 4f levels lying at the Fermi level. The first of two possible solutions for this problem is the LDA+U method (Sec. 2.1.1), which works quite well for the 4f electrons of the lanthanoids since they obey Hund's rules. The alternative solution makes use of the inertness of the 4f electrons and "freezes" them in the core during the pseudopotential generation. The major a-priori decision to be made is then the VEC of the Ln atom, i.e. how many 4f electrons are kept frozen in the core. Of course, the second approach is only possible if the valence is known a priori.

The explicit treatment of the 4f electrons with LDA+U is a quite universal approach as the valence of the Ln atoms is not set at the beginning, but rather develops self-consistently in the respective structure model. However, this approach has important drawbacks. Firstly, the computational demand is significant, in particular for the heavy trivalent lanthanoids, as $2 + n$ electrons per Ln atom have to be considered, while only $2 + 1$ electrons determine the chemistry. Secondly, the convergence into the ground state can be rather difficult, so many test calculations may have to be done until the spin configuration is correct. The third drawback consists in the parameters U and J , which depend on the VEC and alter the total energy by a gauge. Therefore, calculations with different U and J and, hence, different VECs cannot directly be

compared. Instead, test calculations are necessary, from which the correct VEC can be determined by comparing observable quantities with the experiment (cohesive energies, bond lengths, lattice constants etc.). Since this limits the ab initio character of the explicit f-electron treatment, the frozen-core approach often gives satisfying results while saving computational demand. It will be the method employed in this work, while the explicit f-electron treatment will be tested.

Computational parameters

The DFT calculations are carried out with VASP [2, 3] using PAW potentials and the PBE xc-functional [10, 21, 22]. The 4f electrons of the REs are kept frozen in the core, while the 5p electrons are treated explicitly as semi-core electrons. As the considered REs are trivalent in their silicides [81, 83], the REs have a PAW valence of $5p^65d^16s^2$. Si has a PAW valence of $3s^23p^2$. The validity of freezing the 4f electrons in the core will be tested for TbSi₂ and ErSi₂ (Sec. 4.2.3). The kinetic energy cutoff is $E_{\text{cut}} = 400$ eV. The Brillouin zone is sampled by a Γ -centred Monkhorst-Pack mesh [117] at a density of $16 \times 16 \times 16$ k-points for the hexagonal unit cell and $16 \times 16 \times 8$ k-points for the conventional tetragonal unit cell. For the supercells, the sampling density is scaled accordingly. The Brillouin-zone integration is carried out by a Gaussian occupation with a smearing of 20 meV for the ionic relaxations and by the tetrahedron method with Blöchl corrections [118] for all static calculations. A convergence test proves that increasing the energy cutoff or the sampling density alters the total energy by ≈ 1 meV per atom. The ionic forces are calculated according to the Hellmann-Feynman theorem [119]. The ions move along them towards the equilibrium positions and stop to relax if the forces acting on each ion are smaller than 0.005 eV/Å.

4.2.2 The stoichiometric RESi₂ phases

The mechanical equilibria of the vacancy-free prototypes of TbSi₂, DySi₂, HoSi₂ and ErSi₂ are determined by Murnaghan relaxations. For this purpose, the unit cells of AlB₂-RESi₂ and ThSi₂-RESi₂ are set up according to Fig. 4.1 and their zero-pressure volumes V_0 are estimated by the code-level routines. After that, eleven samples in a $\pm 10\%$ interval around the estimated V_0 are set up and relaxed with respect to the atomic positions and the shape of the unit cell, but at constant volume V . The DFT total energies are taken as free energies F , neglecting vibrational contributions (vide supra). The samples (V, F) are fitted by the Murnaghan equation of state $F(V)$ (Eq. (4.33)), which returns the bulk mechanical parameters. For the ThSi₂ prototype, V and F are rescaled by 1/4 so that they become comparable with those of the AlB₂ prototype. Furthermore, F is reset to F_0 .

The Murnaghan fits excellently retrace the sample points for all silicides and phases (Plots: Fig. 4.4, parameters: Tab. 4.1). The equilibrium volumes per formula unit V_0 contract almost linearly towards heavier REs, in accordance with the lanthanoid contraction. Hex-AlB₂-RESi₂ is slightly denser than tet-AlB₂-RESi₂, i.e. V_0 of the former is smaller than that of the latter (-0.4% , -0.5% , -0.7% and -0.9% for TbSi₂, DySi₂,

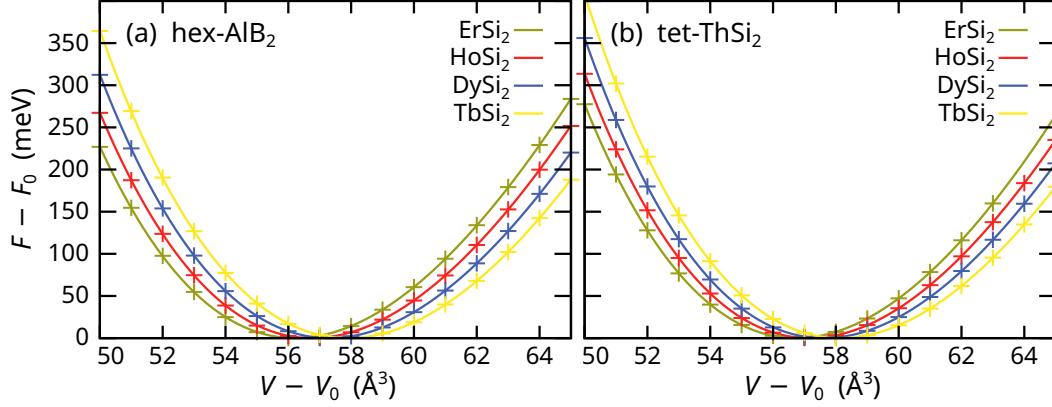


Figure 4.4: Murnaghan fits of TbSi_2 , DySi_2 , HoSi_2 and ErSi_2 in (a) the hex- AlB_2 and (b) the tet- ThSi_2 phase. Crosses: sample points, lines: Murnaghan fits. All extensive quantities are scaled by the number of RE atoms per unit cell.

	hex- AlB_2 prototype			tet- ThSi_2 prototype		
	V_0 (\AA^3)	K_0 ($\text{eV}/\text{\AA}^3$)	K' ($\text{eV}/\text{\AA}^6$)	V_0 (\AA^3)	K_0 ($\text{eV}/\text{\AA}^3$)	K' ($\text{eV}/\text{\AA}^6$)
Tb	57.901	0.524181	4.10229	58.141	0.540657	4.39081
Dy	57.308	0.527378	4.15985	57.617	0.543023	4.43436
Ho	56.756	0.530427	4.24312	57.162	0.547184	4.35291
Er	56.215	0.533331	4.38906	56.741	0.553545	4.19432

Table 4.1: Bulk mechanical properties of TbSi_2 , DySi_2 , HoSi_2 and ErSi_2 in the hex- AlB_2 and the tet- ThSi_2 phase.

	This work				Exp. reference		
	a (\AA)	c (\AA)	c/a	$\Delta\mu_{\text{RE}}^{\text{T-A}}$ (meV)	a (\AA)	c (\AA)	c/a
hex- AlB_2 prototype							
Tb	4.100	3.978	0.970		3.84	4.14	1.078
Dy	4.097	3.943	0.962		3.83	4.12	1.076
Ho	4.096	3.907	0.954		3.80	4.10	1.079
Er	4.090	3.881	0.949		3.78	4.08	1.079
tet- ThSi_2 prototype							
Tb	3.977	14.707	3.698	-49	4.05 (3.96)	13.38	3.304
Dy	3.953	14.747	3.731	-44	4.04 (3.95)	13.33	3.300
Ho	3.916	14.912	3.808	-40	4.03 (3.97)	13.31	3.303
Er	3.891	14.995	3.854	-37	—	—	—

Table 4.2: Lattice parameters and relative RE chemical potentials of TbSi_2 , DySi_2 , HoSi_2 and ErSi_2 in the hex- AlB_2 and the tet- ThSi_2 phase. Numbers in parentheses indicate orthorhombic distortion. Experimental reference: [82, 83, 85].

HoSi₂ and ErSi₂, respectively). The compressive moduli K_0 of all RESi₂ are comparable, as well as those of the AlB₂ and the ThSi₂ phase. They range from 0.52 eV/Å³ to 0.56 eV/Å³, i.e. ~80 GPa. The rigidity slightly grows from the lighter to the heavier REs and from the hex-AlB₂ to the tet-ThSi₂ phase.

The lattice parameters (Tab. 4.2) reveal that the volume contraction from TbSi₂ to ErSi₂ is anisotropic. This can be linked to how the Si anionic sublattice is expected to respond to shrinking RE cations. Concerning the hex-AlB₂ structure, the honeycomb-Si layers are quite rigid, so the shrinkage of the cations in between is mostly compensated by the interlayer distance, the axial lattice constant c . From TbSi₂ to ErSi₂, c shrinks by -2.4 %, while the basal lattice constant a is almost constant (-0.2 %). In summa, the volume contracts by -2.9 %. The situation in the tet-ThSi₂ structure is more complicated as the anionic sublattice comprises a three-dimensional network of Si atoms. From TbSi₂ to ErSi₂, the a shrinks by -2.2 %, while c grows by +2.0 %. In summa, the volume shrinks by -2.4 %, similarly to the hex-AlB₂ phase. The chemical potential differences $\Delta\mu_{\text{RE}}^{\text{T-A}}$ (Eq. (4.37)) tell that the tet-ThSi₂ phase is considerably more stable than the hex-AlB₂ phase for all stoichiometric RESi₂. Although, the ThSi₂ phase slightly destabilises from TbSi₂ to ErSi₂, the potential difference is still higher than $k_{\text{B}}T$ at low and medium temperatures ($k_{\text{B}} \cdot 100 \text{ K} = 8.6 \text{ meV}$). Therefore, the formation of hex-AlB₂-RESi₂ is not possible.

The results for stoichiometric RESi₂ conflict with several experimental observations. The first contradiction is that the AlB₂ phase is unstable, even for ErSi₂, although it is adopted by the silicides of all REs and the only prevailing phase in ErSi₂ [85]. Furthermore, the lattice constants deviate considerably from the experimental reference, not only absolutely by several percent. Also the c/a ratios strongly differ by more than 10 % and are even inverted for hex-AlB₂-RESi₂. The last major deviation from the experiment is the missing orthorhombic distortion in ThSi₂-RESi₂ as a and b remain equal during relaxation, even if the symmetry of the starting configuration is broken by hand. The origin of the discrepancies lies in the high amount of Si vacancies in the real RESi_{2-x} structures, as it will be proven in Sec. 4.2.5. Before addressing this, the validity of two technical approximations will be verified by testing them on the stoichiometric RESi₂ structures: The frozen-core approach of the 4f electrons (Sec. 4.2.3) and the omission of vibrational contributions (Sec. 4.2.4).

4.2.3 The role of the 4f electrons in RESi₂

In order to test if the 4f electrons have effects on the structures, the Murnaghan relaxations are repeated for the TbSi₂ and ErSi₂ structures with f-valent PAW potentials³. The DFT calculations employ spin polarisation and the rotationally invariant, simplified LDA+U approach, proposed by Dudarev et al. [14, 15] (Sec. 2.1.1). Since only the 4f shell of the RE atoms must be corrected, one set of U and J parameters has to be determined. U is calculated with the self-consistent linear-response approach (Eqs. (2.14) and (2.15), [13]). For this purpose, the unit cells from the previous section are

³Potentials which treat the 4f electrons explicitly as valence electrons. The corresponding calculations are referred to as f-valent, in contrast to the trivalent ones above.

multiplied to supercells ($(2 \times 2 \times 2)$ for hex- $\text{AlB}_2\text{-RESi}_2$, $(2 \times 2 \times 1)$ for tet- $\text{ThSi}_2\text{-RESi}_2$) so that the penalised RE atom is separated from its periodic replica. The k-point mesh is adapted to the supercells. The results for U are 5.0 eV and 4.9 eV for $\text{AlB}_2\text{-TbSi}_2$ and $\text{ThSi}_2\text{-TbSi}_2$, respectively. Since the values are consistent, a common $U = 5.0$ eV is used for all f-valent TbSi_2 calculations. $\text{AlB}_2\text{-ErSi}_2$ yields a self-consistent U parameter of 7.4 eV, used for all f-valent ErSi_2 calculations. According to Eq. (2.13), U and J enter the Dudarev correction only by their difference. The exact value of the effective parameter ($U - J$) is irrelevant, though, once it passes a certain threshold (idempotent occupation matrix, Hund's rules). Therefore, ($U - J$) can safely be set to U . Once the individual RE atoms adopt the correct spin configuration, the atomic magnetic moments provide different ways of ordering. Since magnetic order is not the focus of this work, only orderings which are collinear and commensurate with the conventional unit cells are considered. Containing one RE atom, the unit cell of $\text{AlB}_2\text{-RESi}_2$ is described as ferromagnetically ordered (FMO). The four atoms in $\text{ThSi}_2\text{-RESi}_2$ permit additional antiferromagnetically ordered (AMO) configurations, out of which only that with alternating FMO (001)-planes is considered. Since the symmetry group of the unit cell can prevent orbitals from splitting and artificially retain degeneracies, the symmetry reduction of the Brillouin zone is switched off and the lattice of the initial unit cell is slightly distorted before relaxation.

The results of the Murnaghan relaxations for f-valent TbSi_2 are compiled in Tab. 4.3. As expected from the inertness of the 4f shell, the f-valent $\text{ThSi}_2\text{-TbSi}_2$ unit cell is almost equal to the trivalent one (a : +0.1 %, c : -0.7 %, V : -0.6 %). In particular, it retains the tetragonal symmetry. The structural deviations due to magnetic ordering are negligible. On the contrary, the f-valent $\text{AlB}_2\text{-TbSi}_2$ unit cell incurs a considerable orthorhombic distortion with regard to trivalent hex- $\text{AlB}_2\text{-TbSi}_2$, resulting in a new ort- $\text{AlB}_2\text{-TbSi}_2$ structure. In detail, the dashed orthorhombic envelope of the primitive AlB_2 unit cell in Fig. 4.1 (b) expands in the $[\bar{1}1.0]$ -direction and contracts in the perpendicular $[11.0]$ -direction. Thereby, the formerly isotropic basal lattice constants split into a larger one in the $[10.0]$ -direction (denoted a , 4.214 Å,

	a (Å)	c (Å)	c/a	V/N_{Tb} (Å ³)	γ	$\Delta\mu_{\text{Tb}}$ (meV)
trivalent potentials						
hex- $\text{AlB}_2\text{-TbSi}_2$	4.100	3.978	0.970	57.90	120.0°	17
ort- $\text{AlB}_2\text{-TbSi}_2$	4.229 (3.878) ^a	4.002	0.946	58.34	124.7°	0
tet- $\text{ThSi}_2\text{-TbSi}_2$	3.977	14.707	3.698	58.14	122.5°	-32
f-valent potentials						
fmo-ort- $\text{AlB}_2\text{-TbSi}_2$	4.214 (3.886) ^a	3.986	0.946	57.92	124.4°	0
fmo-tet- $\text{ThSi}_2\text{-TbSi}_2$	3.979	14.606	3.671	57.82	122.3°	-31
amo-tet- $\text{ThSi}_2\text{-TbSi}_2$	3.978	14.617	3.674	57.83	122.2°	-38

Table 4.3: Lattice parameters and relative Tb chemical potentials of TbSi_2 in the AlB_2 and the ThSi_2 phase under different f-electron treatments. The unit cells were optimised by Murnaghan relaxations. ^aorthorhombic distortion.

+2.8 % compared to that of trivalent hex- $\text{AlB}_2\text{-TbSi}_2$) and a smaller one in the $[11.0]$ -direction (denoted b , 3.878 Å, -5.4%). The orthorhombic distortion also redistributes the three M-star angles of 120° to two larger ones of $\gamma = 124.4^\circ$ (cf. Fig. 4.1 (b)) and a smaller one of 111.2° . Remarkably, the axial lattice constant c , as well as the unit-cell volume V remain constant ($+0.2\%$ and $\pm 0.0\%$, respectively). In other words, the orthorhombic distortion is an area-conserving deformation of the basis. In order to clarify whether mechanisms other than the f-electron treatment are responsible for this, the $\text{ort-ALB}_2\text{-TbSi}_2$ unit cell is again subjected to a Murnaghan relaxation, this time with trivalent PAW potentials. Instead of relaxing back into hex- $\text{AlB}_2\text{-TbSi}_2$, it retains the orthorhombic distortion (Tab. 4.3). All deviations in the lattice constants of the trivalent and f-valent structures are below 0.5% and the f-valent volume is slightly smaller (-0.7%), similarly to tet- $\text{ThSi}_2\text{-TbSi}_2$. Therefore, the orthorhombic distortion of $\text{ALB}_2\text{-TbSi}_2$ is indeed physical and was merely inhibited by the fixed symmetry group in the previous trivalent calculations. It is remarkable that the volumes per TbSi_2 formula unit of $\text{ort-ALB}_2\text{-TbSi}_2$ and tet- $\text{ThSi}_2\text{-TbSi}_2$ are almost equal and that the three angles of the M-stars assume similar values.

To facilitate the comparison, the Tb chemical potentials μ_{Tb} in Tab. 4.3 are reset by that of $\text{ort-ALB}_2\text{-TbSi}_2$, respectively for the trivalent and the f-valent calculations.

$$\Delta\mu_{\text{Tb}}^\bullet = \mu_{\text{Tb}}^\bullet - \mu_{\text{Tb}}^{\text{ort-ALB}_2\text{-TbSi}_2}$$

Concerning the trivalent calculations, the orthorhombic distortion stabilises the $\text{ALB}_2\text{-TbSi}_2$ structure by -17 meV. As a consequence, the ALB_2 and the ThSi_2 phase are energetically closer together ($\Delta\mu_{\text{Tb}}^{\text{T-A}} = -32$ meV). Concerning the f-valent calculations, tet- $\text{ThSi}_2\text{-TbSi}_2$ is more stable in the AMO than in the FMO configuration by -7 meV. Comparing the two FMO structures, fmo-tet- $\text{ThSi}_2\text{-TbSi}_2$ is more stable than fmo-hex- $\text{ALB}_2\text{-TbSi}_2$ by $\Delta\mu_{\text{Tb}}^{\text{T-A}} = -31$ meV, in agreement with the trivalent calculations.

The results for f-valent ErSi_2 may be found in Tab. 4.4. The overall trends are very similar to those of TbSi_2 , including the well agreement between the trivalent and

	a (Å)	c (Å)	c/a	V/N_{Er} (Å ³)	γ	μ_{Er} (meV)
trivalent potentials						
hex- $\text{ALB}_2\text{-ErSi}_2$	4.090	3.881	0.949	56.22	120.0°	24
ort- $\text{ALB}_2\text{-ErSi}_2$	4.240 (3.840) ^a	3.914	0.923	56.82	125.4°	0
tet- $\text{ThSi}_2\text{-ErSi}_2$	3.891	14.995	3.854	56.74	124.3°	-13
f-valent potentials						
fmo-ort- $\text{ALB}_2\text{-ErSi}_2$	4.234 (3.847) ^a	3.912	0.924	56.67	125.2°	(0) ^b
fmo-tet- $\text{ThSi}_2\text{-ErSi}_2$	3.897	14.924	3.829	56.66	124.0°	(-185) ^b
amo-tet- $\text{ThSi}_2\text{-ErSi}_2$	—	—	—	—	—	(-190) ^b

Table 4.4: Lattice parameters and relative Er chemical potentials of ErSi_2 in the ALB_2 and the ThSi_2 phase under different f-electron treatments. The unit cells were optimised by Murnaghan relaxations. ^aorthorhombic distortion. ^bnot reliable due to numerical problems.

f-valent lattices (<0.5 %) and the orthorhombic distortion of $\text{AlB}_2\text{-ErSi}_2$. The stability gain from the orthorhombic distortion is higher for $\text{AlB}_2\text{-ErSi}_2$ (–24 meV) than for $\text{AlB}_2\text{-TbSi}_2$ (–17 meV). Consequently, trivalent ort- $\text{AlB}_2\text{-ErSi}_2$ is energetically close to trivalent tet- $\text{ThSi}_2\text{-ErSi}_2$ ($\Delta\mu_{\text{Er}}^{\text{T-A}} = -13$ meV). Although, the relaxation of f-valent $\text{ThSi}_2\text{-ErSi}_2$ was performed only in the FMO configuration, the dependence of $\Delta\mu_{\text{Er}}$ on the magnetic ordering can be estimated by the total energy of the FMO-relaxed cell in the AMO configuration. The latter is more stable by –5 meV, similarly to the TbSi_2 case. The potential difference $\Delta\mu_{\text{Er}}^{\text{T-A}}$ of the FMO structures (–185 meV) is much higher than that of the trivalent structures (–13 meV), which is the only incongruity. Since the deviation is not linked to any structure differences, it is likely that the ground state configurations – at least that of fmo-ort- $\text{AlB}_2\text{-ErSi}_2$ – were incorrect. In detail, although the total on-site charge and magnetisation were as expected, the spin ordering within the 4f shell could be wrong. Supporting evidence for this is that the Murnaghan relaxations produced several classes of images which had equal on-site charges, magnetisations and equilibrium volumes, but different energy offsets. The nature of such problems is clearly numerical, so the f-valent $\Delta\mu_{\text{Er}}$ in Tab. 4.4 are not reliable. That such problems were absent in f-valent TbSi_2 agrees with the this assumption as Tb has only one electron in the second half-shell, not four like Er.

In conclusion, neither the explicit treatment of the 4f electrons, nor the magnetic ordering have major effects on the RESi_2 structures, as expected. Also the relative stabilities between the phases are retained, provided that the magnetic ordering is analogue. Therefore, the frozen-core approach is safe for use and the trivalent potentials are employed for all further RESi_2 calculations (bulk, films and nanowires).

4.2.4 Vibrational contributions in RESi_2

The lattice-dynamical effects on μ_{Tb} will be quantified for $\text{AlB}_2\text{-TbSi}_2$ and $\text{ThSi}_2\text{-TbSi}_2$ by calculating the vibrational free energies within the frozen-phonon approach and the harmonic approximation (vide supra). The error due to the omitted thermal expansion can be estimated by the experimentally determined linear thermal expansion coefficients of $\approx 15 \cdot 10^{-6} \text{ K}^{-1}$ for $\text{AlB}_2\text{-RESi}_{2-x}$ [98]. Since this approaches the error bars for the lattice constants in this work ($\approx 0.5\%$, vide infra) at room temperature, the approach is considered to be safe up to 300 K. The unit cells are multiplied to supercells so as to increase the effective Brillouin-zone sampling for the phonons (vide supra). The comparability between the AlB_2 and the ThSi_2 structure at different effective samplings is ensured by embedding the AlB_2 structure into an orthorhombic unit cell (the dashed red cell in Fig. Fig. 4.1 (b) doubled in the $[\bar{1}1.0]$ -direction), which matches the tetragonal unit cell of the ThSi_2 structure by the dimensions. These Tb_4Si_8 cells, denoted ThSi_2 -type unit cells to demarcate them from the conventional ones, are optimised by Murnaghan relaxations analogous to Sec. 4.2.2. The results are compiled in Tab. 4.5. The lattice parameters of tet- $\text{ThSi}_2\text{-TbSi}_2$ are equal to those in Tab. 4.3. The AlB_2 phase splits into three slightly different structures. Two of these are hex- $\text{AlB}_2\text{-TbSi}_2$ ($\gamma = 120^\circ$) and ort- $\text{AlB}_2\text{-TbSi}_2$ ($\gamma = 124.7^\circ$), whose lattice parameters are almost equal to those in Tab. 4.3. The third structure, denoted ort2- $\text{AlB}_2\text{-TbSi}_2$ ($\gamma = 118.1^\circ$), is new and represents the other possibility of

	a (Å)	b (Å)	c (Å)	V/N_{Tb} (Å ³)	γ	$\Delta\mu_{\text{Tb}}$ (meV)
hex-AlB ₂ -TbSi ₂	4.10	3.98	14.19 (4.10) ^a	57.9	119.9°	18
ort-AlB ₂ -TbSi ₂	3.88	4.00	15.04 (4.23) ^a	58.4	124.7°	0
ort2-AlB ₂ -TbSi ₂	4.20	3.98	13.87 (4.05) ^a	58.0	118.1°	17
tet-ThSi ₂ -TbSi ₂	3.98	3.98	14.71	58.1	122.6°	-32

Table 4.5: Lattice parameters and relative Tb chemical potentials of TbSi₂ in the AlB₂ and the ThSi₂ phase in orthorhombic Tb₄Si₈ cells. The unit cells were optimised by Murnaghan relaxations. The lattice constants a , b and c refer to the ThSi₂-type unit cells⁴. ^alattice constant a in the conventional [10.0]-direction.

orthorhombic distortion, contrary to that in ort-AlB₂-TbSi₂, i.e. dilation in the [11.0]-direction and contraction in the perpendicular [$\bar{1}$ 1.0]-direction. This new structure is discarded as it is not more stable than hex-AlB₂-TbSi₂. For the other three structures, the (static) values for $\Delta\mu_{\text{Tb}}$ are equal to those in Tab. 4.3.

The Γ -point phonons are calculated in $(1 \times 1 \times 1)$, $(2 \times 2 \times 1)$ and $(3 \times 3 \times 1)$ supercells of the optimised ThSi₂-type unit cells. This corresponds to a convergence test for the effective sampling. The restriction of the multiplication to the basal plane is due to the aspect ratio of the ThSi₂-type unit cell. The $(3 \times 3 \times 1)$ supercell is almost cubic so that the effective sampling of the reciprocal space is nearly isotropic. The vibrational free energy $F_{\text{vib}}(T)$ of each supercell is calculated with Eq. (4.38), scaled by the respective number of Tb atoms N_{Tb} and plotted from $T = 0$ K to 270 K (Fig. 4.5 (a) – (c)). While the changes in $F_{\text{vib}}(T)$ from the $(1 \times 1 \times 1)$ to the $(2 \times 2 \times 1)$ supercells are visible (≈ 8 meV at $T = 0$ K), the free energies of the $(2 \times 2 \times 1)$ and the $(3 \times 3 \times 1)$ supercells are almost equal (deviation < 1 meV at $T = 0$ K). Thus, the $(3 \times 3 \times 1)$ supercells provide well converged absolute vibrational free energies. The lattice dynamical effects can be introduced into the Tb chemical potentials μ_{Tb} simply by adding the vibrational free energies per Tb atom, since the stoichiometries of all structures are equal. They are reset by $\mu_{\text{Tb}}^{\text{ort-AlB}_2\text{-TbSi}_2}(T) =: \mu_{\text{Tb}}^0(T)$.

$$\begin{aligned} \Delta\mu_{\text{Tb}}^{\bullet}(T) &\stackrel{\text{Eq. (4.35)}}{=} \frac{F^{\bullet}(T) - N_{\text{Si}}^{\bullet}\mu_{\text{Si}}}{N_{\text{Tb}}^{\bullet}} - \frac{F^0(T) - N_{\text{Si}}^0\mu_{\text{Si}}}{N_{\text{Tb}}^0} \\ &\stackrel{\text{Eq. (4.39)}}{=} \frac{1}{N_{\text{Tb}}} \left(E_{\text{DFT}}^{\bullet} - E_{\text{DFT}}^0 + F_{\text{vib}}^{\bullet}(T) - F_{\text{vib}}^0(T) \right) \end{aligned}$$

The plots of $\Delta\mu_{\text{Tb}}(T)$ for the $(1 \times 1 \times 1)$ and the $(3 \times 3 \times 1)$ supercells can be found in Fig. 4.5 (d). Those of the $(2 \times 2 \times 2)$ supercells (not shown) respectively lie in between. Comparing the $(1 \times 1 \times 1)$ and $(3 \times 3 \times 1)$ curves of the same structure, the differences in the (relative) $\Delta\mu_{\text{Tb}}(T)$ (2 meV at 0 K, 4 meV at 270 K) are smaller than the respective differences in the absolute free energies $F_{\text{vib}}/N_{\text{Tb}}$ (5 meV to 10 meV for all T). This indicates an error cancellation which makes the relative free energies converge faster than the absolute ones. In particular, the error in $\Delta\mu_{\text{Tb}}(T)$ is near the overall DFT error of this work (1 meV per atom).

⁴The mapping between the ThSi₂-type and the conventional AlB₂ unit cell holds (cf. Fig. 4.1 (b)):

$$a_{\text{ThSi}_2} = b_{\text{AlB}_2} \text{ ([11.0]-direction)}, \quad b_{\text{ThSi}_2} = c_{\text{AlB}_2}, \quad (c_{\text{ThSi}_2}/4)^2 + (a_{\text{ThSi}_2}/2)^2 = a_{\text{AlB}_2}^2 \text{ ([10.0]-direction)}$$

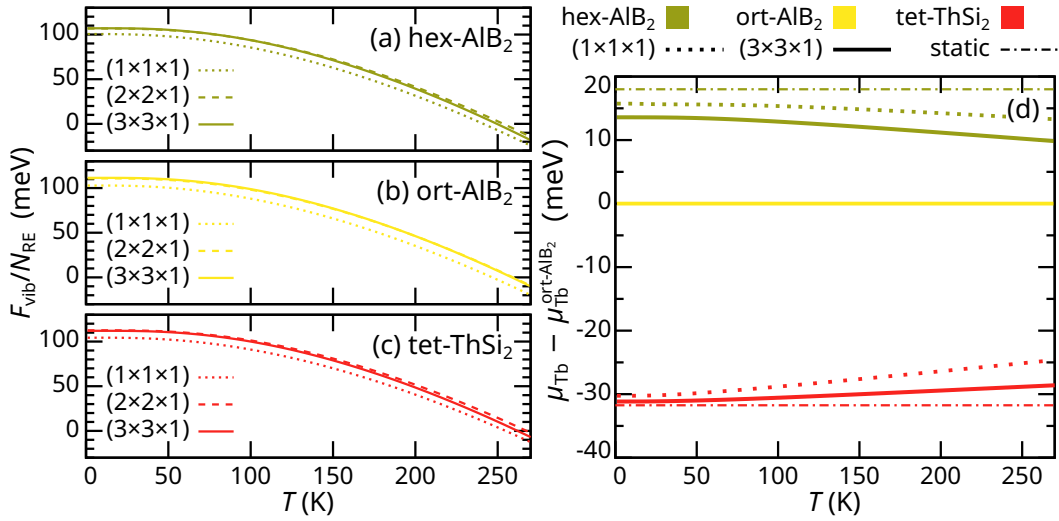


Figure 4.5: Vibrational free energies of (a) hex- $\text{AlB}_2\text{-TbSi}_2$, (b) ort- $\text{AlB}_2\text{-TbSi}_2$ and (c) tet- $\text{ThSi}_2\text{-TbSi}_2$ and (d) the corrected Tb chemical potentials $\mu_{\text{Tb}}(T)$ calculated in different supercells. The line types correspond to the supercells and the colours to the structure. Dash-dotted lines: μ_{Tb} without vibrational contributions (static).

Concentrating on the $(3 \times 3 \times 1)$ results, the two AlB_2 structures approach each other by a bit ($\Delta\mu_{\text{Tb}} = +18$ meV (static), $+14$ meV at 0 K and $+10$ meV at 270 K). Also ort- $\text{AlB}_2\text{-TbSi}_2$ and tet- $\text{ThSi}_2\text{-TbSi}_2$ approach each other, though to a lesser extent ($\Delta\mu_{\text{Tb}}^{\text{T-A}} = -32$ meV (static), -31 meV at 0 K and -29 meV at 270 K). The shifts in μ_{Tb} do not change the relative stabilities between the structures for $T < 300$ K. It is remarkable that the two AlB_2 structures differ more from each other than ort- $\text{ThSi}_2\text{-TbSi}_2$ and tet- $\text{ThSi}_2\text{-TbSi}_2$ do, with respect to the vibrational free energies. This can be explained by the Si-Si bond distances and angles within the Si sublattices: While hex- $\text{AlB}_2\text{-TbSi}_2$ provides distances of 2.37 Å, ort- $\text{AlB}_2\text{-TbSi}_2$ and tet- $\text{ThSi}_2\text{-TbSi}_2$ provide each two shorter (2.38 Å) and one longer distance (2.42 Å and 2.41 Å, respectively). Therefore, the local Si geometry seems to be more important for the lattice dynamics than the global symmetry.

In conclusion, although the two TbSi_2 prototypes look rather different, the vibrational free energies in the most stable structures (ort- $\text{AlB}_2\text{-TbSi}_2$ and tet- $\text{ThSi}_2\text{-TbSi}_2$) are almost equal. Thus, the free energies can safely be approximated by the DFT total energies up to 300 K. These results are certainly transferable to all other structurally related RESi_2 . Furthermore, they can be transferred to the nanostructures as well (films and nanowires), provided that the local Si-Si geometries are comparable.

4.2.5 The vacancy-populated RESi_{2-x} phases

Although the above theoretical results for stoichiometric RESi_2 clearly contradict the experimental observations, they reproduce the previous theoretical findings for stoichiometric hex- $\text{AlB}_2\text{-YSi}_2$ by Magaud et al. [96]. As already discussed above (pp. 39f),

that work proved that the high amount of Si vacancies, as it occurs in the real $\text{AlB}_2\text{-YSi}_{2-x}$ structures, is decisive for the agreement between the theoretical and the experimental lattice constants, in particular concerning the c/a ratios. The influence of the vacancies on the AlB_2 and the ThSi_2 prototypes will be demonstrated for TbSi_{2-b} and ErSi_{2-b} (one out of six Si sites is vacant). The vacancies are considered maximally ordered, so the conventional unit cells of the AlB_2 and the ThSi_2 phase have to be tripled to map the exact stoichiometry. Only those configurations are considered in which the vacancies are separated by at least two Si atoms from each other. Furthermore, the experimental observation is included that the orthorhombic distortion clearly affects the ThSi_2 phase, while the AlB_2 phase is at least approximately hexagonal. This confines the planar vacancy distributions to configurations 1 and 2 of $\text{ThSi}_2\text{-RESi}_{2-b}$ and configuration 1 of $\text{AlB}_2\text{-RESi}_{2-b}$ (Fig. 4.2). The vacancy ordering perpendicular to the plane of projection of Fig. 4.2 (ThSi_2 : the (010) plane, the AlB_2 : (0001) plane) is congruent, i.e. the vacancies stack onto each other in that direction. All other orderings would multiply the supercells in that direction, which would exceed the scope of this work. The energetic effects from out-of-plane ordering can be estimated at ~ 30 meV per vacancy (in hex- $\text{AlB}_2\text{-YSi}_{2-b}$ [96]), which corresponds to μ_{RE} variations of ~ 10 meV.

The three RESi_{2-b} supercells to investigate comprise two $(3 \times 1 \times 1)\text{-ThSi}_2$ supercells describing $\text{ThSi}_2\text{-RESi}_{2-b}$ (1) and $\text{ThSi}_2\text{-RESi}_{2-b}$ (2) (green cell in Fig. 4.2 (a))⁵ and a rotated $\text{R}30^\circ(\sqrt{3} \times \sqrt{3} \times 1)\text{-AlB}_2$ supercell describing $\text{AlB}_2\text{-RESi}_{2-b}$ (light green cell in Fig. 4.2 (b)). The structures of all supercells are optimised by code-level relaxations, which are not as accurate as Murnaghan relaxations, but whose uncertainty is expected to be smaller than those introduced by other approximations, e.g. the out-of-plane ordering of the vacancies. Pulay stress is reduced by iterating the relaxations until the supercells remain unchanged. In order to estimate the reliability of the relaxation method, stoichiometric $\text{ort-AlB}_2\text{-RESi}_2$ and $\text{tet-ThSi}_2\text{-RESi}_2$ are optimised at code level as well and compared to the respective Murnaghan results. The deviations are very small. Only $\text{tet-ThSi}_2\text{-TbSi}_2$ shows a slightly different axial lattice constant c ($\sim 1\%$). As the Murnaghan structure is more stable by 5 meV per Tb atom, the code-level relaxation is indeed less reliable. The confidence intervals can thus be estimated to 1% for the lattice constants and 5 meV for the RE chemical potentials μ_{RE} . The k-point meshes are adapted to the supercells. The first set of calculations is conducted with the PBE xc-functional [10], a second set with PBEsol [11]. In addition to the RESi_{2-x} structures, the bulk phases of diamond-Si and elemental hcp-RE are optimised as well so as to calculate μ_{RE} according to Eq. (4.36). The results for TbSi_{2-x} are compiled in Tab. 4.6. Those for ErSi_{2-x} are in the appendix (Tab. B.1). Fig. 4.6 shows images of the optimised TbSi_{2-x} structures.

Concentrating on TbSi_{2-b} , several predictions about the effects from the vacancies are confirmed. The removal of a Si atom drives the three atoms at the corner of the respective M-star towards its centre (light blue arrows in Fig. 4.6). As a consequence, the basal lattice constant a of the AlB_2 phase contracts by -9.7% , which, in turn, pushes

⁵Mind that for internal consistency, the vacancies populate the Si zigzag chains parallel to a , so the expected orthorhombic distortion would result in $a/b < 1$. In contrast, most of the crystallographic literature uses an interchanged notation for a and b , so $b/a < 1$.

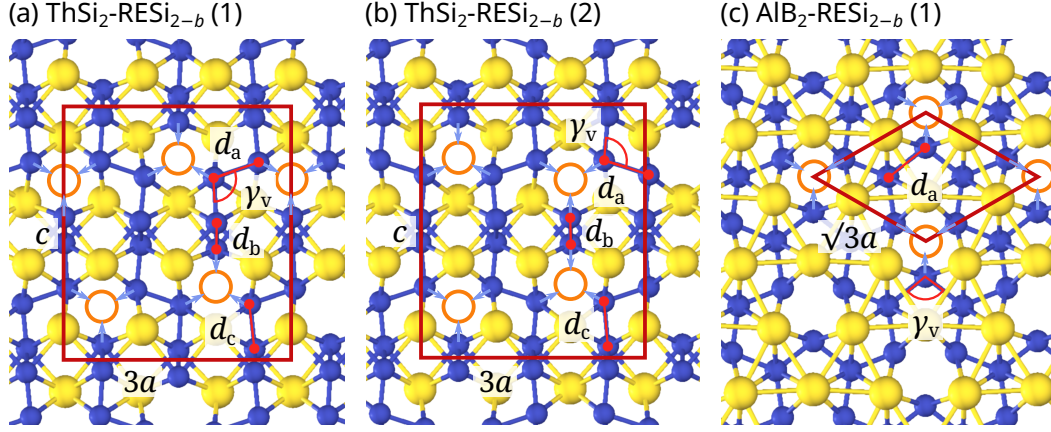


Figure 4.6: Structure models of vacancy-populated TbSi_{2-b} . Orange circles mark vacancies. Dark red lines mark the supercells. Red dumb-bells mark Si-Si bond distances; Red angles mark the bond angles γ_v near the vacancies. Light blue arrows indicate Si atoms moving towards the vacancies. All 3D images in this work are rendered with XCrySDen [120].

the (0001)-planes apart and increases the axial lattice constant c by +5.0%. The symmetry remains hexagonal, contrarily to stoichiometric $\text{AlB}_2\text{-TbSi}_2$. The impact on the ThSi_2 prototype deviates from the predictions. The basal lattice constant a does not contract, but remains almost unchanged. Instead, the perpendicular basal lattice constant b grows by +1.3% and +2.1% for $\text{ThSi}_2\text{-TbSi}_{2-b}$ (1) and $\text{ThSi}_2\text{-TbSi}_{2-b}$ (2), respectively. Consequently, the tetragonal symmetry breaks into an orthorhombic distortion of $a/b = 0.994$ and 0.979 , respectively. The axial lattice constant c strongly contracts by -9.4% and -9.0% , respectively.

The Tb chemical potentials μ_{Tb} (Eq. (4.36)) reveal that the Si vacancies clearly stabilise the RESi_2 prototypes (Tab. 4.6). In order to facilitate the stability considerations, the μ_{Tb} are reset by that of hex- $\text{AlB}_2\text{-TbSi}_{2-b}$, the most stable TbSi_{2-x} structure.

$$\Delta\mu_{\text{Tb}}^\bullet := \mu_{\text{Tb}}^\bullet - \mu_{\text{Tb}}^{\text{hex-AlB}_2\text{-TbSi}_{2-b}} \quad (4.40)$$

Two further chemical potential differences are defined:

- $\Delta\mu_{\text{Tb}}^{\text{T-A}} = \mu_{\text{Tb}}^{\text{ThSi}_2\text{-TbSi}_{2-x}} - \mu_{\text{Tb}}^{\text{AlB}_2\text{-TbSi}_{2-x}}$: the difference between the most stable ThSi_2 and AlB_2 structures with the same stoichiometry (Eq. (4.37))
- $\Delta\mu_{\text{Tb}}^{\text{vac}} := \mu_{\text{Tb}}^{\bullet\text{-TbSi}_{2-b}} - \mu_{\text{Tb}}^{\bullet\text{-TbSi}_2}$: the difference between TbSi_{2-b} and TbSi_2 in the same phase \bullet , i.e. the energy gain per Tb atom upon introducing the vacancies.

The vacancies stabilise the AlB_2 phase by $\Delta\mu_{\text{Tb}}^{\text{vac}} = -191$ meV and the ThSi_2 phase to a lesser extent (-128 meV for $\text{ThSi}_2\text{-TbSi}_{2-b}$ (1)). As a consequence, the AlB_2 phase becomes more stable than the ThSi_2 phase ($\Delta\mu_{\text{Tb}}^{\text{T-A}} = +35$ meV for TbSi_{2-b} and -28 meV for TbSi_2). However, the exact values have to be interpreted with caution because they seem to strongly depend on the vacancy ordering, as indicated by the potential difference of 42 meV between the two ort- $\text{ThSi}_2\text{-TbSi}_{2-b}$ configurations.

	a (Å)	b (Å)	c (Å)	c/a	V/N_{Tb} (Å ³)	μ_{Tb} (eV)	$\Delta\mu_{\text{Tb}}$ (meV)
PBE							
ort- $\text{AlB}_2\text{-TbSi}_2$	4.23	3.88	4.00	0.946	58.3	-1.636	191
hex- $\text{AlB}_2\text{-TbSi}_{2-b}$	3.82		4.20	1.100	53.0	-1.827	0
tet- $\text{ThSi}_2\text{-TbSi}_2$	3.97	3.97	14.82	3.734	58.3	-1.664	163
ort- $\text{ThSi}_2\text{-TbSi}_{2-b}$ (1)	4.00	4.02	13.43	3.340	54.0	-1.792	35
ort- $\text{ThSi}_2\text{-TbSi}_{2-b}$ (2)	3.96	4.05	13.48	3.328	54.1	-1.750	77
PBEsol							
ort- $\text{AlB}_2\text{-TbSi}_2$	4.17	3.88	3.92	0.940	56.2	-1.886	173
hex- $\text{AlB}_2\text{-TbSi}_{2-b}$	3.76		4.16	1.107	51.0	-2.058	0
tet- $\text{ThSi}_2\text{-TbSi}_2$	3.93	3.93	14.57	3.709	56.2	-1.918	141
ort- $\text{ThSi}_2\text{-TbSi}_{2-b}$ (1)	3.93	3.98	13.27	3.335	51.9	-2.009	49
ort- $\text{ThSi}_2\text{-TbSi}_{2-b}$ (2)	3.90	4.01	13.35	3.333	52.1	-1.964	95
Exp. reference							
hex- $\text{AlB}_2\text{-TbSi}_{2-x}$	3.84		4.14	1.078	52.9		
ort- $\text{ThSi}_2\text{-TbSi}_{2-x}$	3.96	4.05	13.38	3.304	53.6		

Table 4.6: Lattice parameters and relative Tb chemical potentials of TbSi_{2-x} in the stoichiometric and the vacancy-populated AlB_2 and ThSi_2 phases. The unit cells were optimised by code-level relaxations with different xc-functionals. Experimental reference (mind notation of a and b for ort- ThSi_2): [83, 85]. ErSi_{2-x} : Tab. B.1.

The PBEsol results are similar to the PBE results. The most important difference consist in the contraction of all lattice constants by -0.9% to -1.9% . Accordingly, the unit-cell volumes contract by -3.5% to -3.8% . The Tb chemical potentials μ_{Tb} shift relatively to each other by ~ 20 meV, which does not change the stability order, though. Notably, the stability of $\text{AlB}_2\text{-TbSi}_{2-b}$ relative to $\text{ThSi}_2\text{-TbSi}_{2-b}$ increases ($\Delta\mu_{\text{Tb}}^{\text{T-A}} = +49$ meV). The potential drop due to the vacancies is smaller ($\Delta\mu_{\text{Tb}}^{\text{vac}} = -173$ meV and -92 meV for hex- $\text{AlB}_2\text{-TbSi}_{2-b}$ and ort- $\text{ThSi}_2\text{-TbSi}_{2-b}$ (1), respectively). The absolute positions of μ_{Tb} are considerably lower by >200 meV for all structures. The smaller lattice constants and the higher reaction enthalpies (μ_{Tb} , vide supra) within PBEsol are expectable [10, 11].

The ErSi_{2-x} results (Tab. B.1) are similar to the TbSi_{2-x} results. The unit-cell volumes are smaller (RESi_{2-b} : $\approx -4\%$, RESi_2 : $\approx -2.5\%$) due to the lanthanoid contraction. The lattice distortions upon the Si removal are more pronounced, in particular concerning the axial lattice constant c of the ThSi_2 phase: While it is longer in tet- $\text{ThSi}_2\text{-ErSi}_2$ (15.0 Å) than in tet- $\text{ThSi}_2\text{-TbSi}_2$ (14.8 Å), it contracts so strongly due to the vacancies that it is shorter in ort- $\text{ThSi}_2\text{-ErSi}_{2-b}$ (13.3 Å) than in ort- $\text{ThSi}_2\text{-TbSi}_{2-b}$ (13.4 Å). In accordance with the higher structural impact, the potential drop due to the vacancies is steeper in ErSi_2 than in TbSi_2 ($\Delta\mu_{\text{RE}}^{\text{vac}} = -266$ meV and -208 meV for hex- $\text{AlB}_2\text{-ErSi}_{2-b}$ and ort- $\text{ThSi}_2\text{-ErSi}_{2-b}$ (1), respectively). As in TbSi_{2-x} , the relative stability between the AlB_2 and the ThSi_2 phase changes sign upon introducing the vacancies ($\Delta\mu_{\text{Er}}^{\text{T-A}} = +43$ meV for ErSi_{2-b} and -13 meV for ErSi_2).

The lattices of the vacancy-populated TbSi_{2-b} and ErSi_{2-b} structures compare very well with the experimental reference [83, 85], much better than the respective stoichiometric RESi_2 prototypes. In particular, the symmetry groups match the experimental observations, contrarily to the stoichiometric structures. Concerning the AlB_2 phase, the c/a -ratios correctly adopt values greater than 1. At first glance, the PBE lattice parameters are closer to the experimental reference than the those obtained with PBEsol, in particular concerning a and V/N_{RE} . On the other hand, PBEsol describes c better. It has to be kept in mind, though, that the RE silicide phases are approximated by ordered and frozen vacancies. Existing theoretical work hints that the vacancies may show considerable diffusion along the Si zigzag chains at finite temperatures [99]. Therefore, more sophisticated calculations including disorder and diffusion may affect a more than c . Concerning the ThSi_2 phase, the lattice parameters of $\text{ort-ThSi}_2\text{-TbSi}_{2-b}$ reproduce the experimental reference up to 1 % within PBE and are too small by up to -2 % within PBEsol. As in the AlB_2 phase, disorder and diffusion of the vacancies are likely to influence the lattice parameters. Furthermore, real $\text{ThSi}_2\text{-TbSi}_{2-x}$ contains more Si than TbSi_{2-b} does, so it is expectable that the lattice constants of more realistic, Si-richer structures will be larger. In summary, it is not possible to conclude on the suitability of the xc-functionals at this point. Finally, the volumes per atom of all investigated RESi_{2-x} structures are smaller than the weighted atomic volumes of the constituents in the elemental phases. The contraction ratio ranges from 13 % to 22 %, independently of the xc-functional, and hints at the partial heteropolar character of the compound [80].

Stability analysis

Both ErSi_{2-x} and TbSi_{2-x} favour the AlB_2 phase in the RESi_{2-b} stoichiometry ($x = \frac{1}{3}$) and the ThSi_2 phase in the RESi_2 stoichiometry ($x = 0$). In order to further analyse this, the relative RE chemical potentials $\Delta\mu_{\text{RE}}^\bullet$ (Eq. (4.40)) for each RE and phase \bullet are linearly interpolated with respect to x and plotted in Fig. 4.7. At the $x = \frac{1}{3}$ boundary, $\Delta\mu_{\text{RE}}^{\text{ThSi}_2}$ (dashed line) is higher than $\Delta\mu_{\text{RE}}^{\text{AlB}_2}$ (solid line). The difference ($\Delta\mu_{\text{RE}}^{\text{T-A}}$) is similar for ErSi_{2-b} (green, PBE: +43 meV, PBEsol: +56 meV) and TbSi_{2-b} (yellow, PBE: +35 meV, PBEsol: +49 meV). In other words, the relative stability of the AlB_2 phase with Si vacancies is independent of the RE radius. That RESi_{2-b} certainly adopts the AlB_2 phase agrees with the experimental observations and phase diagrams [89, 91, 93, 110, 111]. At the other boundary ($x = 0$), vacancy-free ErSi_2 and TbSi_2 both favour the (tetragonal) ThSi_2 phase over the (orthorhombic) AlB_2 phase. The potential lines intersect, as marked by black dotted lines. Because $\Delta\mu_{\text{RE}}^{\text{T-A}}$ is, according to amount, smaller in ErSi_2 (PBE: -15 meV, PBEsol: -12 meV) than in TbSi_2 (PBE: -28 meV, PBEsol: -32 meV), the intersection is closer to the Si-rich boundary for ErSi_{2-x} than for TbSi_{2-x} . This permits the conclusion that ErSi_{2-x} needs a higher Si content to form the ThSi_2 phase than TbSi_{2-x} does. Furthermore, particularly within PBEsol, the stability range of $\text{ThSi}_2\text{-ErSi}_{2-x}$ so narrow that it is possible that more sophisticated calculations shift the intersection beyond $x = 0$, which would exclude the formation of $\text{ThSi}_2\text{-ErSi}_{2-x}$ at all. Of course, the linear interpolation of $\Delta\mu_{\text{RE}}$ is a crude approximation as the real curves are convex⁶. Nevertheless, if similar shapes are assumed,

⁶It is expectable that G_{RE} , defined by Eq. (4.34), has a minimum at a certain x for a fixed phase.

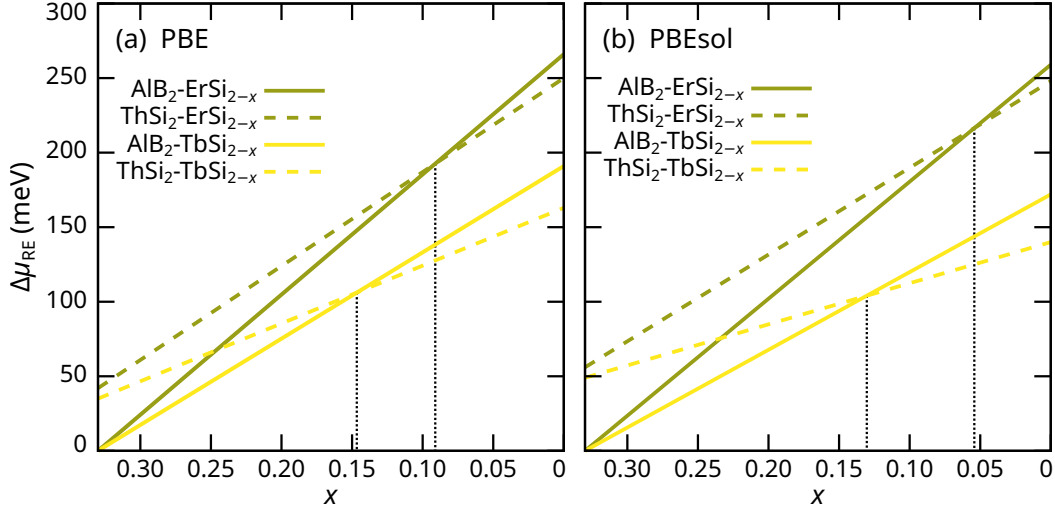


Figure 4.7: Linear interpolation of $\Delta\mu_{\text{RE}}$ for TbSi_{2-x} (yellow) and ErSi_{2-x} (green) between $x = \frac{1}{3}$ and $x = 0$. (a) PBE and (b) PBEsol. The line types correspond to the phases. Black dotted lines mark the intersections ($\mu_{\text{RE}}^{\text{T-A}} = 0$).

the real curves for the AlB_2 and the ThSi_2 phase will still be horizontally displaced from each other and this displacement will be higher for ErSi_{2-x} than for TbSi_{2-x} , reflecting the different $\mu_{\text{RE}}^{\text{T-A}}$ at the boundaries.

As a last test concerning the vacancies, a further Si atom is removed from the most stable hex- $\text{AlB}_2\text{-RESi}_{2-b}$ structure. For this purpose, the $(\sqrt{3} \times \sqrt{3} \times 1)$ supercell is doubled in both basal directions to obtain a $(2\sqrt{3} \times 2\sqrt{3} \times 1)$ supercell, in which an additional vacancy is created. The optimised $\text{RE}_{12}\text{Si}_{19}$ structures ($\text{RESi}_{1.58}$) turn out to be highly unstable against hex- $\text{AlB}_2\text{-RESi}_{2-b}$ (PBE: $\Delta\mu_{\text{Tb}} = +97$ meV, $\Delta\mu_{\text{Er}} = +98$ meV; PBEsol: $\Delta\mu_{\text{Tb}} = +135$ meV, $\Delta\mu_{\text{Er}} = +134$ meV). Consequently, the optimal composition under Si-rich conditions, at least for the AlB_2 phase, indeed seems to be near the RESi_{2-b} stoichiometry, in agreement with the phase diagrams.

Silicon bond length analysis

To complete the study of the RESi_{2-x} structures, the binding mechanisms are illuminated by analysing the geometry of the Si sublattices. Since the structures differ in the arrangement of the Si-Si nearest neighbours, it is instructive to classify the Si-Si bonds with respect to their environment by the following notation:

- Each Si atom is either twofold coordinated and adjacent to a vacancy, denoted (v)-type, or threefold coordinated, denoted (m)-type.
- The nearest-neighbours pairs of Si atoms, the *Si-Si dumb-bells*, are classified with respect to the types of the constituents, e.g. (mv)-type if the one Si atom is (m)-type and the other (v)-type.

In hex- $\text{AlB}_2\text{-RESi}_{2-b}$ (Fig. 4.6 (c)), each (v)-type Si atom is coordinated by (m)-type Si atoms and vice versa. Thus, all Si-Si dumb-bells are all equivalent and of (mv)-type

(length denoted d_a). In *ort*-ThSi₂-RESi_{2-*b*} (Fig. 4.6 (a) and (b)), the Si–Si dumb-bells point into three different directions and are unequal. Their lengths are termed after the lattice constant towards which they incline: d_a , d_b and d_c . The stoichiometric *hex*-AlB₂-TbSi₂, *ort*-AlB₂-TbSi₂ and *tet*-ThSi₂-TbSi₂ structures provide only (mm)-type Si–Si dumb-bells, which have two different lengths for the latter two. The Si–Si bond lengths of all PBE TbSi_{2-*x*} structures are compiled in Tab. 4.7. Those optimised with PBEsol and those of the ErSi_{2-*x*} structures may be found in the appendix (Tab. B.2 and Tab. B.3). The diamond-Si structure serves as reference for the length of Si–Si single bonds (PBE: 2.37 Å, PBEsol: 2.35 Å, tetrahedron angle: 109.5°).

In stoichiometric *hex*-AlB₂-TbSi₂, the Si–Si bond length amounts to $d_a = 2.37$ Å, exactly the PBE bond length in diamond-Si. This clearly indicates the presence of single bonds. The other two stoichiometric TbSi₂ structures (*ort*-AlB₂ and *tet*-ThSi₂) have (per formula unit) two Si–Si dumb-bells with lengths near the single bond (2.36 Å), while the third dumb-bell is considerably longer (2.42 Å and 2.43 Å). In terms of the zigzag planes of the Si sublattice (Fig. 4.1), the shorter bond length is that of the Si zigzag chains (in-plane), while the larger is the connection between the planes. This structural similarity underlines the above results that *ort*-AlB₂-TbSi₂ and *tet*-ThSi₂-TbSi₂ merely differ in the way how the planes stack (unidirectional vs. alternately perpendicular), but not in the local geometries. The explanation for the unequal bond lengths may lie in the charge transfer from the RE ions to the Si sublattice: When the zigzag planes move apart, the zigzag chains can accept more charge.

The bond lengths and angles in the vacancy-populated TbSi_{2-*b*} structures accord with the charge transfer model as well. In *hex*-AlB₂-TbSi_{2-*b*}, the (v)-type Si^{-II} atom formally has two binding and two free electron pairs in tetragonal coordination. However, the tetrahedron is distorted because the two free pairs are localised closer to the Si atom and push the two binding pairs away. This is reflected by the bond length of $d_a = 2.43$ Å, which is longer than a single bond, and the bond angle of $\gamma_v = 103.8^\circ$, which is smaller than the tetrahedron angle. On the other hand, the (m)-type Si^{-I} atom has three equivalent binding electron pairs in symmetric trigonal-planar geometry, while the formal free electron pair occupies the out-of-plane p_z orbital. Correspondingly, the respective M-star has inner angles of exactly 120°. The same mechanisms apply to the two *ort*-ThSi₂-TbSi_{2-*b*} structures as well. All (mm)-type Si dumb-

PBE	d_a (Å)	d_b (Å)	d_c (Å)
<i>hex</i> -AlB ₂ -TbSi ₂	2.37 (mm)		
<i>ort</i> -AlB ₂ -TbSi ₂	2.36/2.42 (mm)		
<i>hex</i> -AlB ₂ -TbSi _{2-<i>b</i>}	2.43 (mv)		
<i>tet</i> -ThSi ₂ -TbSi ₂	2.36 (mm)	2.36 (mm)	2.43 (mm)
<i>ort</i> -ThSi ₂ -TbSi _{2-<i>b</i>} (1)	2.49 (vv)	2.44 (mv)	2.36 (mm) 2.39 (mv)
<i>ort</i> -ThSi ₂ -TbSi _{2-<i>b</i>} (2)	2.50 (vv)	2.47 (vv)	2.37 (mm) 2.37 (mv)

Table 4.7: Si–Si nearest-neighbour distances in TbSi_{2-*x*} optimised with PBE. The notation accords with Fig. 4.6. Letters in parentheses indicate the types of the Si–Si dumb-bell. PBEsol: Tab. B.2; ErSi_{2-*x*}: Tab. B.3.

bells have lengths near the single bond (2.36 Å to 2.37 Å). All (mv)-type Si dumb-bells have larger bond lengths of 2.37 Å to 2.44 Å. If the Si dumb-bell connects two (v)-type Si atoms, the bond length is even larger (2.47 Å to 2.50 Å), as expected from the double repulsion from the free electron pairs at each end. The average bond angles at the (v)-type Si atoms are clearly below the tetrahedron angle ($\gamma_v = 106.6^\circ$ and 105.3° for *ort*-ThSi₂-TbSi_{2-b} (1) and *ort*-ThSi₂-TbSi_{2-b} (2), respectively).

The Si–Si bond lengths of the ErSi_{2-x} structures (Tab. B.3) are quantitatively very similar to those of TbSi_{2-x}, deviating by less than 1%. This is surprising as the lattice constants show larger differences of 1% to 2%. For instance, d_a is exactly equal in both *hex*-AlB₂-TbSi_{2-b} and *hex*-AlB₂-ErSi_{2-b} (2.43 Å). On the other hand, the basal lattice constant a of *hex*-AlB₂-ErSi_{2-b} is smaller than that of *hex*-AlB₂-TbSi_{2-b} by –1.4% (Tab. 4.6 and Tab. B.1). The lanthanoid contraction is thus not carried out by the Si–Si bond distances, but rather by the bond angles at the vacancies, which are more acute in *hex*-AlB₂-ErSi_{2-b} ($\gamma_v = 101.4^\circ$ vs. $\gamma_v = 103.8^\circ$). Similar considerations hold for the ThSi₂-ErSi_{2-b} structures. The analysis of the PBEsol structures (Tab. B.2 and Tab. B.3) yields very similar results. All bond lengths are a bit shorter, as well as the bond distance in diamond-Si (2.35 Å, experimental reference: 2.352 Å [17, p. 1065]). The bond angles at the vacancies γ_v are more acute in PBEsol than in PBE.

The effects from the vacancies can be linked to the M-stars, which both structure prototypes have in common. If vacancies are introduced into the AlB₂ structure, the remaining complete M-stars rotate and move closer together whereupon the basis contracts. As a consequence, the RE atoms are squeezed out of the Si honeycombs, which dilates the axis. Both deformations combined invert the c/a ratio. The ThSi₂ structure behaves differently as its axis locally resembles the basal $[\bar{1}1.0]$ direction of the AlB₂ structure, while its basis is a mixture between the basal $[11.0]$ and the axial $[00.1]$ direction of the AlB₂ structure. Therefore, the basis of the ThSi₂ structure responds only weakly to the vacancies, while the axis considerably contracts.

4.2.6 The CaSi₂ phases

The ZKB concept (p. 33) was introduced by means of the exemplary alkali and alkaline earth metal silicides (M_mSi_n). In the particular case of $Ca^{II}Si_2^{-I}$, the Si atoms formally accept an electron and arrange themselves in buckled honeycombs between which the Ca ions are embedded. Such a geometry reminds of the AlB₂ phase and raises the question whether the stoichiometric RE silicides might crystallise in one of the CaSi₂ phases.

As CaSi₂ is polymorphic, several structures are discussed for this compound. Three of them comprise alternating hexagonal Ca layers and buckled Si honeycombs. The first structure is the simplest way of layer stacking as the Ca atoms arrange themselves in the “holes” of the buckled Si honeycombs. Denoted h1-CaSi₂, this structure is obviously analogous to the *hex*-AlB₂-RESi₂ structure, except that the Si honeycomb is buckled in the former and flat in the latter. CaSi₂ does not occur in the h1-CaSi₂ structure, but CaGe₂ does [121]. The second structure results from the following stacking: The Ca atoms are placed above the lower Si atoms of the buckled honeycomb (T₄

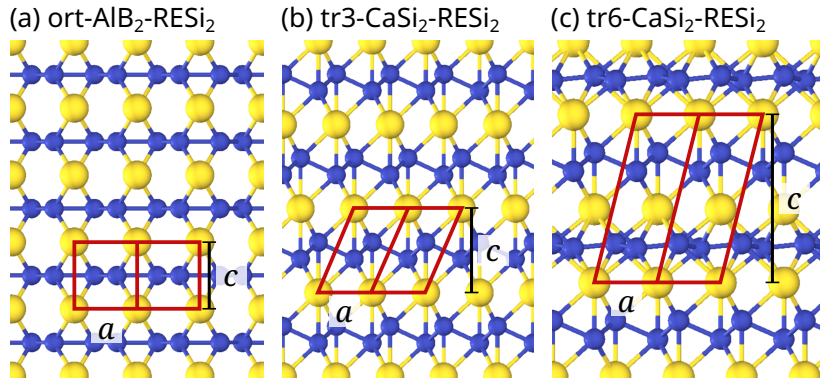


Figure 4.8: Models of TbSi_2 in the (a) $\text{ort-AlB}_2\text{-RESi}_2$, (b) $\text{tr3-CaSi}_2\text{-RESi}_2$ and (c) $\text{tr6-CaSi}_2\text{-RESi}_2$ structures. Blue circles are Si atoms; Yellow circles are RE atoms. Red lines mark the unit cells.

position), like eggs in a (hexagonal) egg box. The next Si honeycomb covers the Ca layer so that the upper Si atoms are above the Ca atoms, like a turned egg box covering a filled egg box. Denoted tr3-CaSi_2 with respect to the (ABC)-type sequence of the Ca layers, this structure is an artificial phase of CaSi_2 [122]. The third structure is a mixture between h1-CaSi_2 and tr3-CaSi_2 :

- 1) Ca atoms above the lower Si atoms of the buckled honeycomb (egg box).
- 2) Holes of the next Si honeycomb above the Ca atoms.
- 3) Ca atoms above the holes of the Si honeycomb.
- 4) Upper Si atoms of the next honeycomb above the Ca atoms (turned egg box).

Denoted tr6-CaSi_2 with respect to the (AABBCC)-type sequence of the Ca layers, this structure is one of the natural phases of CaSi_2 [121].

To answer the above question, the h1-CaSi_2 , tr3-CaSi_2 and tr6-CaSi_2 structures are set up with RE (Tb and Er) replacing Ca. The unit cells are optimised at code level with the same parameters as above (Sec. 4.2.5), for PBE and PBEsol. The h1-CaSi_2 structure proved to transition into the $\text{ort-AlB}_2\text{-RESi}_2$ structure, which is chosen as reference. Fig. 4.8 shows the optimised structure models. The PBE results for TbSi_2 (lattice parameters and relative RE chemical potentials $\Delta\mu_{\text{RE}}$) are compiled in Tab. 4.8, all other results are in the appendix (Tab. B.4). For both RESi_2 , at least one of the two CaSi_2 structures is more stable than $\text{ort-AlB}_2\text{-RESi}_2$ and even $\text{tet-ThSi}_2\text{-RESi}_2$. This is a very surprising result, particularly because the differences in the RE chemical potentials are considerable. They depend, however, strongly on the xc-functional: Switching from PBE to PBEsol affects $\Delta\mu_{\text{RE}}$ of $\text{tr3-CaSi}_2\text{-RESi}_2$ to a large extent (+60 meV and +77 meV for TbSi_2 and ErSi_2 , respectively), and $\Delta\mu_{\text{RE}}$ of $\text{ort-AlB}_2\text{-RESi}_2$ (−18 meV and −8 meV) and $\text{tr6-CaSi}_2\text{-RESi}_2$ (+15 meV and +22 meV) to an intermediate extent.

The basal lattice constants of TbSi_2 and ErSi_2 are very similar in the respective structures (deviations below 1 %). The axial lattice constant c contracts from TbSi_2 to ErSi_2 by −1.5 % to −2.3 % (lanthanoid contraction). A similar result has already been found for the hex- AlB_2 structures (Sec. 4.2.2). In accordance with the bases, the Si–Si bond lengths and angles of the respective TbSi_2 and ErSi_2 structures are very similar as

	a (Å)	c (Å)	V/N_{RE} (Å ³)	γ	d_a (Å)	$\Delta\mu_{\text{RE}}$ (meV)
TbSi ₂ , PBE						
ort-AlB ₂	4.23 (3.88) ^a	4.00	58.3	124.7° (110.6°) ^a	2.36 (2.42) ^a	0
tr3-CaSi ₂	3.78	5.56	63.4	103.6°	2.41	-30
tr6-CaSi ₂	3.94	9.34	60.9	104.9°, 118.9°	2.49, 2.29	-67

Table 4.8: Lattice parameters and relative Tb chemical potentials of stoichiometric TbSi₂ in the AlB₂ and CaSi₂ phases. The unit cells were optimised by code-level relaxations with PBE. tr6-CaSi₂-RESi₂ has two independent M-star angles γ and Si-Si bond lengths d_a . ^aorthorhombic distortion. Other results: Tab. B.4

well. Since determined by buckled Si honeycombs, the basis of tr3-CaSi₂-RESi₂ is smaller than that of ort-AlB₂-RESi₂. On the other hand, the axial lattice constant c is longer. In summa, the total volume per RE atom V/N_{RE} of tr3-CaSi₂-RESi₂ is larger than that of ort-AlB₂-RESi₂ by $\approx +9\%$. Following the ZKB concept, the Si atoms of the buckled honeycombs are sp^3 -hybridised and use three orbitals for inter-se bonding, while the fourth accepts a free electron pair. This is reflected by the bond lengths of 2.38 Å to 2.41 Å, which are longer than that of diamond-Si (within the respective xc-functional), and the bond angles, which are more acute than the tetrahedron angle. The tr6-structure shows unexpected peculiarities: On the one hand, the upper Si honeycomb of the unit cell (the tr3-like part) has very long bond lengths of 2.46 Å to 2.49 Å, which is near the length of a (vv)-type Si dumb-bell (vide supra). However, the charge accumulation in a (vv)-type dumb-bell (formal Si²⁻ ion at each end) is much larger than that in the bonds of the honeycomb (formal Si⁻ ion at each end). On the other hand, the lower Si honeycomb (the AlB₂-like part) is almost flat ($\gamma \approx 119^\circ$) and the bond lengths (2.26 Å to 2.28 Å) are considerably shorter than that in diamond-Si. Since the AlB₂-like part seems to be squeezed and the tr3-like part to be stretched, it is even more surprising that tr6-CaSi₂ is the most stable structure for TbSi₂.

In conclusion, the AlB₂ and ThSi₂ prototypes of stoichiometric RESi₂ are unstable against at least one of the CaSi₂ phases. This underlines that RESi₂ without vacancies are far away from the real structures. Furthermore, the stability of the buckled-honeycomb geometries confirms that Si tends to avoid sp^2 hybridisation, as already discussed in Sec. 3.2. Since they seem to be concurring phases for Si-rich RESi_{2-x}, the CaSi₂ structures should be taken into account when RE-Si phase diagrams are calculated by means of DFT. From the experimental phase diagrams (pp. 38ff), it is expectable that the vacancies stabilise the ThSi₂ and the AlB₂ phase more than the CaSi₂ phases, so the latter do not occur. That the relative stabilities between the four structures (tet-ThSi₂, ort-AlB₂, tr-3-CaSi₂ and tr6-CaSi₂) seem to strongly depend on the xc-functional should be verified by Murnaghan relaxations. Moreover, the CaSi₂ phases will be relevant for the monolayer-Tb@Si(111) system (Chap. 5) as they share several structural properties with the latter.

4.3 Electronic properties

The band structure $\varepsilon_n(\mathbf{k})$ and the DOS are calculated non-self-consistently, i.e. the eigenvalues are calculated for a fixed ground-state density, which was self-consistently determined on a $(16 \times 16 \times 16)$ k-point mesh. The k-paths for the band structures comprise densely sampled line segments between high-symmetry points of the Brillouin zones (according to [123, A.5. and A.10.]). The DOS is calculated on a dense, Γ -centred $(32 \times 32 \times 32)$ mesh, which produces very smooth curves while the non-self-consistency considerably saves computation time. All other parameters are analogous to those in Sec. 4.2

The band structures $\varepsilon_n(\mathbf{k})$ become rather complicated even for the smallest RESi_2 cells. Therefore, they are disentangled by projecting the wavefunctions $|\Psi_n(\mathbf{k})\rangle$ onto the spherical harmonics $|Y^{lm,I}\rangle$ centred at ion I , where l and m are the orbital and magnetic quantum numbers. The square modulus of the projection is then a measure for how strong a state is localised in the respective atomic orbitals.

$$P^{lm,I}(n, \mathbf{k}) = |\langle Y^{lm,I} | \Psi_n(\mathbf{k}) \rangle|^2 \quad (4.41)$$

The projections are very convenient in the PAW method as they equal the PAW projections. Once determined, they define the following scheme for plotting the band structures: Each band $\varepsilon_n(\mathbf{k})$ is a function of \mathbf{k} , which is plotted against the x-axis. The line width is scaled locally in \mathbf{k} by the sum of the projections $P^{lm,I}(n, \mathbf{k})$ of a certain group $\{l, m, I\}$. The portion of a subgroup in this group determines the line colour according to a colour bar. The Brillouin-zone integration for obtaining the DOS can be weighted by the projections as well. This results in the partial DOS (PDOS).

$$\text{DOS}(E) = \sum_{n=1}^{N_{\text{Band}}} \frac{1}{|C_G|} \int_{C_G} dk \delta(E - \varepsilon_n(\mathbf{k})) \quad (4.42a)$$

$$\text{PDOS}(E) = \sum_{l,m,I \in \text{group}} \sum_{n=1}^{N_{\text{Band}}} \frac{1}{|C_G|} \int_{C_G} dk \delta(E - \varepsilon_n(\mathbf{k})) P^{lm,I}(n, \mathbf{k}) \quad (4.42b)$$

where C_G is the reciprocal unit cell (Sec. 2.2). The PDOS is plotted against the energy axis (y-axis) next to the band structures.

Throughout this section, Si portions (PDOS and bands) are coloured blue, Tb portions yellow and Er portions green. As expected, the band structures of TbSi_{2-x} and ErSi_{2-x} turned out to be almost identical. Therefore, only TbSi_{2-x} band structures are analysed, while ErSi_2 band structures are compared with those of TbSi_2 when the f-valent structures are considered. Moreover, the analysis concentrates on the AlB_2 structures since their bands are clearer than those of the ThSi_2 structures.

The band structures of the RESi_2 prototypes

Fig. 4.9 shows the band structures of the stoichiometric RESi_2 prototypes (hex- AlB_2 - TbSi_2 and tet- ThSi_2 - TbSi_2), each plotted along a k-path connecting all high-symmetry

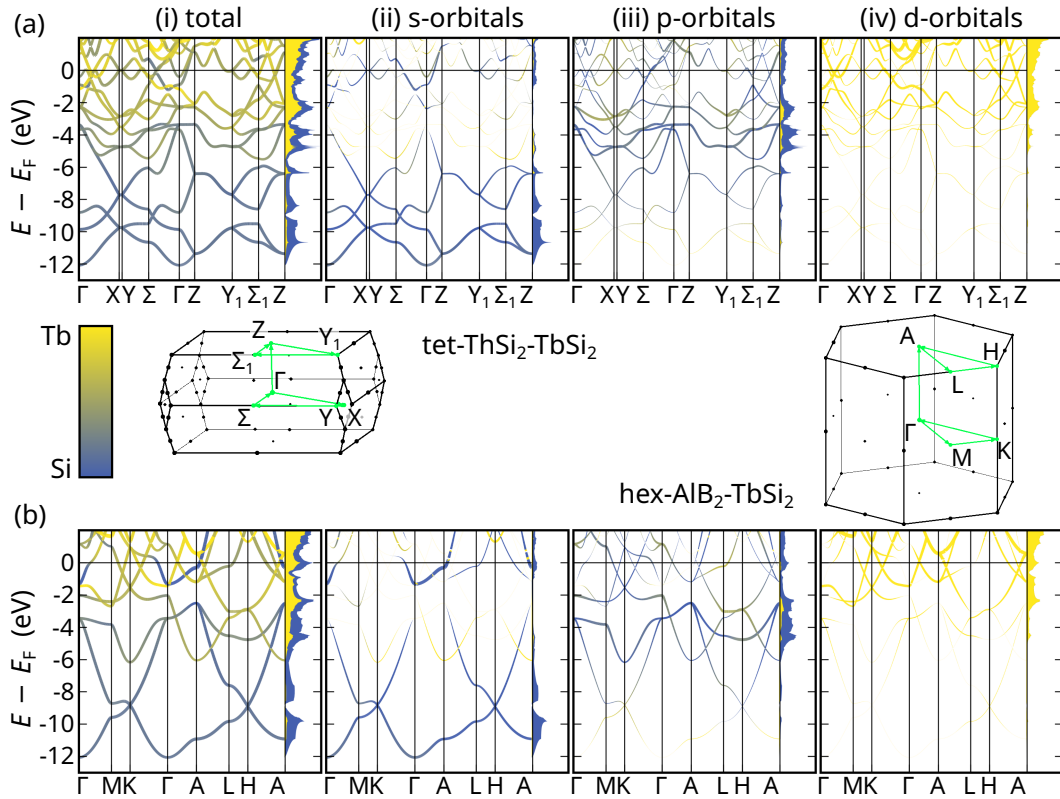


Figure 4.9: Band structures of (a) tet-ThSi₂-TbSi₂ and (b) hex-AlB₂-TbSi₂. The line width corresponds to the PAW projections of (i) all orbitals, (ii) the s orbitals, (iii) the p orbitals and (iv) the d orbitals. The line colour indicates the Tb/Si portions, according to the colour bar (yellow → Tb, blue → Si). The Brillouin zones and k-paths are shown in the middle. The respective PDOSs are plotted against the y-axis to right of the band structures in arbitrary units.

points of the primitive Brillouin zone. The DOSs and PDOSs of tet-ThSi₂-TbSi₂ are scaled by 1/2 so that they match those of hex-AlB₂-TbSi₂ by scale⁷. Panel (i) shows the summed s, p and d projections of all atoms (line width, constant). Panels (ii), (iii), and (iv) show the separate s, p and d portions in the PAW projections of all atoms. The line colour indicates Tb/Si portions. On the right hand of each band structure, the PDOS of the respective orbitals is plotted against the y-axis, where yellow and blue portions correspond to Tb and Si, respectively (stack diagram). Thus, the sum of the yellow and blue portions in panel (i) equals the total DOS.

The band structures of tet-ThSi₂-TbSi₂ and hex-AlB₂-TbSi₂ show strongly dispersing bands. They look rather different from each other at first glance, but have several common properties. The bands belonging to Si have s character at high binding energies⁸, gain p character at lower binding energies and are mostly p-like near the Fermi level. Above -5 eV, strongly dispersive d bands associated with Tb arise, which finally dominate the region between -3 eV and the Fermi level (and the empty conduction bands above). The d contributions from Si are zero (since the Si PAW potential lacks

⁷The body-centred ThSi₂ cell has two formula units RESi₂. All DOSs and PDOSs have arbitrary units.

⁸The binding energy is exactly the opposite of the energy scale in Fig. 4.9.

d projectors) and the p and s contributions from Tb are small throughout the band structure. The RESi_2 prototypes furthermore have in common that the Tb-d states mix with the Si-p states, so pure Tb states are hardly present. On the contrary, (almost) pure Si states exist in both structures.

The band structures agree with the findings of the structure analysis. The Si bands below -3 eV are sp-like, do not interfere with the Tb states and amount to $3N_{\text{Tb}}$ bands ($6N_{\text{Tb}}$ electrons, more clearly visible in hex- $\text{AlB}_2\text{-TbSi}_2$). Hence, they represent the Si-Si bonds and confirm that the bonding within the Si sublattice is single and electronically decoupled from the rest of the cell. The fourth electrons of the Si atoms and the Tb valence electrons form rather complicated Si-Tb-hybrid orbitals, which will be analysed in detail when the orthorhombic distortion is considered (vide infra). Since these bands cut the Fermi level, the RESi_2 prototypes are clearly metallic. The band structure of hex- $\text{AlB}_2\text{-TbSi}_2$ has a peculiarity which is missing in that of tet- $\text{ThSi}_2\text{-TbSi}_2$: Exactly at the Fermi level, the DOS has a rather sharp peak, which stems from Si-sp and Tb-d states, as revealed by the PDOSs. This peak has already been observed in hex- $\text{AlB}_2\text{-YSi}_2$ [95, 100]. Contrarily, the DOS of tet- $\text{ThSi}_2\text{-TbSi}_2$ is indented right beneath the Fermi level.

Orthorhombic distortion

The band structures of hex- $\text{AlB}_2\text{-TbSi}_2$ and ort- $\text{AlB}_2\text{-TbSi}_2$ can be found in Fig. 4.10. The k-path is restricted to the three spatial directions ($\overline{\Gamma\text{K}} \parallel \mathbf{e}_x$, $\overline{\Gamma\text{M}} \parallel \mathbf{e}_y$ and $\overline{\Gamma\text{A}} \parallel \mathbf{e}_z$ (inset in Fig. 4.10 (b.iv)). The changes in the bands due to orthorhombic distortion consist in a handful of features (highlighted by red markings) which agree with the results from the structure analysis.

Both structures have in common that the lowest four bands (labelled 1 to 4) majorly belong to the Si honeycomb. Band 1 is Si-s-like and decoupled from Tb. Bands 2 and 3 are each strongly dispersive in one of the basal directions and less dispersive in the perpendicular directions. They are Si-s-like at lower energies and gain Si-p character towards higher energies. Because having only weak Tb contributions, bands 1 to 3 represent exclusive Si-Si bonds (as already found above). The lm -resolved projections (Fig. B.1, labels in Fig. 4.10) reveal that the p component of bands 2 and 3 points into the direction of the more dispersive branch. In detail, the band being steep along $\overline{\Gamma\text{M}}$ (the y-direction) has only p_y projections (beside s projections at low energies). The other band being steep along $\overline{\Gamma\text{K}}$ (the x-direction) has only p_x projections. Both bands are localised along $\overline{\Gamma\text{A}}$ (the z-direction). This accords with the expectation that the electrons are mobile parallel to the bonds and less mobile perpendicular to them. Band 4 is almost flat in the basal plane (the xy-plane), but steep along the crystal axis (the z-direction). Accordingly, the Si projections are exclusively p_z . Differently from band 2 and 3, the Si-s contributions are zero and, instead, Tb-d contributions arise at the zone edges, more precisely Tb- d_{xz} and Tb- d_{yz} . As these d orbitals are crosses whose lobes point diagonally out of the basal plane, band 4 seems to represent a bond between the Si- p_z and the Tb-d orbitals.

The orthorhombic distortion affects only two of the four Si bands: band 2 and 3, whose upper parts shift into opposite directions (feature C in Fig. 4.10). This is clearly

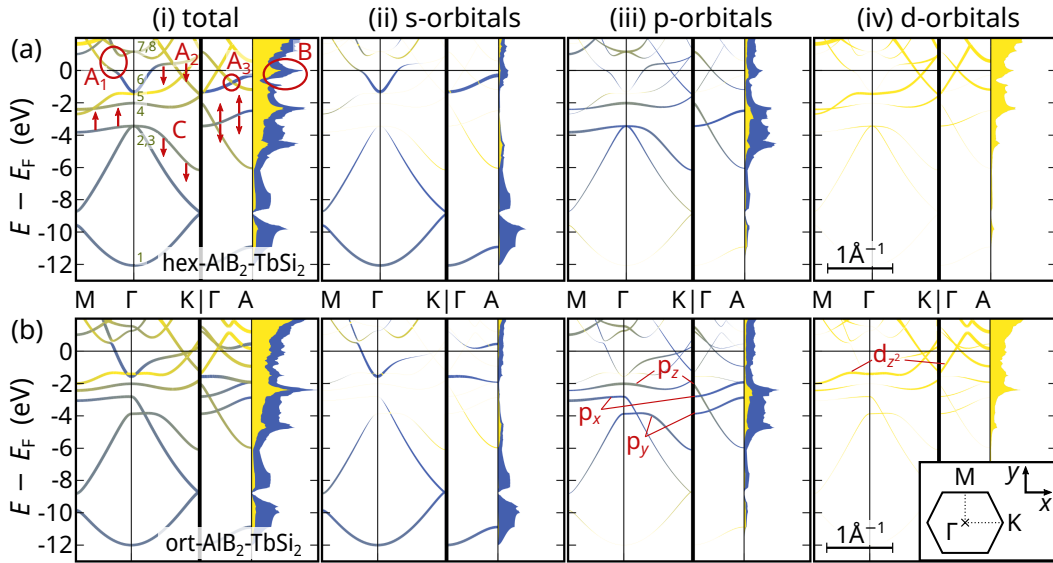


Figure 4.10: Band structures of (a) hex- $\text{AlB}_2\text{-TbSi}_2$ and (b) ort- $\text{AlB}_2\text{-TbSi}_2$. The panels and the plotting mode are analogous to Fig. 4.9. Inset in (b,iv): k -path. Red markings highlight differences between (a) and (b). Green numbers enumerate the bands at the Γ -point.

linked to the distortion of the Si honeycomb and the concomitant splitting of the Si-Si bond distances (Tab. 4.7). The dilation of the bonds in the y -direction gives rise to a gain in binding energy, which becomes manifest in the downward movement of the Si- p_y band. The other two bonds, which form the zigzag chains and have their major component in the x -direction, shorten a bit and lift the Si- p_x band to lower binding energies. The position of the Si- p_z band, on the contrary, is insensitive to the orthorhombic distortion, agreeing with the constancy of the axial lattice constant c .

Bands 5 and 6 cross the Fermi level and are, thus, partially occupied. Band 5 stems from the d_{z^2} orbitals of the Tb atom, mixed with small in-plane Si- p contributions. While it is shallow near the Γ -point on the in-plane k -paths, it is a very steep and straight line crossing the Fermi level along the out-of-plane k -path. Band 6 is Si-s-like below the Fermi level and its in-plane branch follows a quite narrow electronic parabola with an effective mass of $0.15m_e$. It abruptly bends into less steep branches beyond the Fermi level, while the character simultaneously changes into a mixture of in-plane Si- p and Tb- d . The out-of-plane branch is Si-s-like and completely below the Fermi level. It follows a wider parabola with an effective mass of $>1.5m_e$, the tenfold of the in-plane mass.

The orthorhombic distortion changes several features near the Fermi level. The Tb- d band (band 5) slightly shifts at the K -point and the M -point, which flattens the in-plane dispersion, but leaves the out-of-plane dispersion unchanged. In contrast, band 6 undergoes fundamental changes. The $\overline{\Gamma M}$ branch (y -direction) closes a gap with a conduction band above (band 7) so that the light-electron parabola continues its shape across the Fermi level. After the gap closing, it has an almost pure Si- sp character and crosses the second, Si-Tb-hybridised band without mixing (feature A_1). The $\overline{\Gamma A}$ branch (z -direction) opens a gap at the intersection with a double band (bands 7

and 8) dipping below the Fermi level halfway to the A-point. Thereby, band 6 hybridises with the band having Si- p_y -Tb- d_{yz} character and splits apart (feature A_3), while the other band having Si- p_x -Tb- d_{xz} character remains unchanged. The $\bar{\Gamma}K$ branch (x-direction) retains its shape, but is pushed below the Fermi level (feature A_2).

The band structures can be summarised as follows. The Si atoms are indeed sp^2 -hybridised and bind to each other via the trigonal-planar hybrid orbitals, forming three bands and, thus, hosting six electrons. The remaining p_z orbitals are out of plane and hybridise with out-of-plane Tb-d orbitals, forming one band (two electrons). The remaining three electrons distribute over conduction bands near the Fermi level. One of these bands stems from the inter-se hybridisation of the d_{z^2} orbitals of the Tb atoms, being rather flat in-plane, but strongly dispersive out-of-plane. A second band is the s-like conduction band of the Si honeycomb, which is strongly dispersive in-plane, and less dispersive out-of-plane. As long as the structure is hexagonal, this band transitions into Si-p-Tb-d states right at the Fermi level along with an abrupt change in curvature. This is the origin of the DOS peak. The orthorhombic distortion rehybridises this band whereupon the DOS peak flattens out (feature B). Since tet-ThSi₂-TbSi₂ is very similar to ort-ALB₂-TbSi₂ concerning the bond lengths and angles, it lacks the DOS peak as well. The orbital-resolved partial atomic charges reveal that the orthorhombic distortion transfers 0.1 electrons per unit cell from the Si- p_y orbitals to the Si- p_x orbitals, in accordance with the shifting of band 2 and 3. This confirms the assumption that the orthorhombic distortion allows more excess charge to accumulate in the zigzag chains, which stabilises the structure.

A last point to be emphasized is the incorrectness of the analogy between the Si honeycomb in ALB₂-RESi₂ and a hypothetical graphite-like (or even graphene-like) Si allotrope, sometimes stated in the literature. In order to clarify this, the band structures are calculated for the ALB₂-TbSi₂ structures (hexagonal and orthorhombic) after the removal of the Tb atoms, which results in a layered “silicene” system (Si₂, vide appendicem, Fig. B.1). The three lowest bands, representing the sp^2 single bonds, are very similar in TbSi₂ and Si₂, as well as the s-like conduction band right below the Fermi level. The major difference consists in the p_z band, whose in-plane branch is flat in TbSi₂ (bound to Tb-d \rightarrow localised in the basal plane) and dispersive in Si₂ (delocalised π -electron system). Thus, the decisive property of silicene, the delocalised π -electron system, is clearly missing in TbSi₂. Interestingly, but not unexpectedly, the effects on the Si bands from the orthorhombic distortion are similar in ALB₂-TbSi₂ and ALB₂-Si₂. Furthermore, the Si₂ structures demonstrate the better charge storage of the orthorhombically distorted structures. The total energy difference per Si atom between ort-ALB₂-Si₂ and hex-ALB₂-Si₂ is $\Delta\mu_{Si} = +65$ meV in the neutral state, so the hexagonal version is more stable. The stability relations change when excess electrons are added ($\Delta\mu_{Si} = -78$ meV for +1 electron, $\Delta\mu_{Si} = -187$ meV for +2 electrons). This underlines that the orthorhombic distortion of ALB₂-TbSi₂ is driven by charge balance issues due to the mismatch between the formal valences of Tb and Si.

Explicit f-electron treatment

Fig. 4.11 shows the band structures for f-valent fmo-ort-ALB₂-TbSi₂ and fmo-ort-ALB₂-ErSi₂, beside trivalent ort-ALB₂-TbSi₂, which serves as reference. The plotting mode

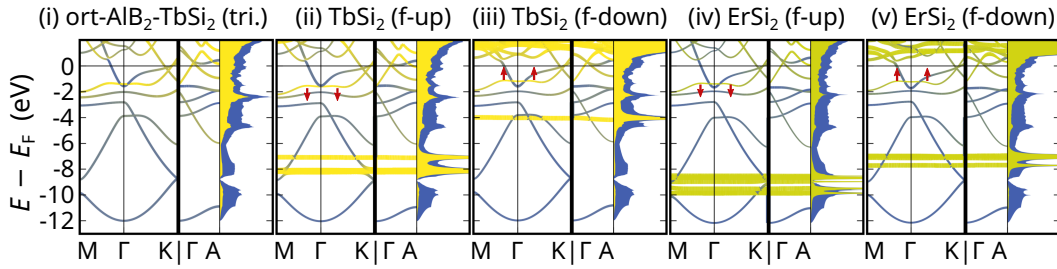


Figure 4.11: Band structures of trivalent and f-valent, FMO $\text{ort-AlB}_2\text{-RESi}_2$. (i) trivalent TbSi_2 , (ii) spin-up and (iii) spin-down of f-valent TbSi_2 , and (iv) spin-up and (v) spin-down of f-valent ErSi_2 . The plotting mode is analogous to Fig. 4.9 (b,i). Colour: yellow/green \rightarrow Tb/Er, blue \rightarrow Si. Red arrows mark band shifts between spin-up and spin-down. ThSi_2 structures: Fig. B.2.

and k-paths are analogous to Fig. 4.10 (i) (line width: sum of s, p, d and f contributions \rightarrow constant; line colour: RE/Si portions). Because of the spin polarisation, each f-valent RESi_2 structure yields two band structures, one per spin component.

The most prominent features in the f-valent band structures are bold, horizontal lines representing the 4f states. As expected, they are localised and occupy seven states in the spin-up component and one (TbSi_2) and four (ErSi_2) states in the spin-down component. Thus, the net spin polarisation is six (TbSi_2) and three (ErSi_2) electrons per RE atom. The 4f levels of ErSi_2 are deeper than those of TbSi_2 , reflecting the higher atomic number of Er. Furthermore, the distance between the topmost spin-up and spin-down levels is smaller in ErSi_2 than that in TbSi_2 as a consequence of the higher exchange energy in the 4f shell of Er. The only non-f bands indirectly affected by the 4f electrons are the Tb- d_{z^2} states (band 5 in the trivalent case), which split apart by 0.41 eV in TbSi_2 and 0.16 eV in ErSi_2 (red arrows in Fig. 4.11). Being larger in TbSi_2 than in ErSi_2 , this splitting is obviously linked to the net magnetic moment. All other bands are only slightly affected by the presence of the 4f states (<0.1 eV).

Apart from the 4f levels, the band structures of $\text{ort-AlB}_2\text{-TbSi}_2$ and $\text{ort-AlB}_2\text{-ErSi}_2$ look very similar. They merely differ by small band shifts of -80 meV to 170 meV, which concentrate more in the RE bands than in the Si bands. This suggests that the band shifts are caused by the differences between the TbSi_2 and ErSi_2 structures due to lanthanoid contraction. The band structures of $\text{tet-ThSi}_2\text{-TbSi}_2$ and $\text{tet-ThSi}_2\text{-ErSi}_2$ differ by higher band shifts of -230 meV to 230 meV, in accordance with the higher sensitivity of the ThSi_2 structure to the cation size (vide appendicem, Fig. B.2).

Vacancy-populated structures

The band structure of $\text{hex-AlB}_2\text{-TbSi}_{2-b}$ optimised with PBEsol is shown in Fig. 4.12 (a). For comparison, the band structure of $\text{ort-AlB}_2\text{-TbSi}_2$ optimised with PBEsol is added (Fig. 4.12 (b)). It shows merely tiny differences to the band structure of the PBE-optimised unit cell (Fig. 4.10 (b)). The plotting mode is the same as that in Fig. 4.10 (line width \rightarrow orbitals, colour \rightarrow Tb/Si portion). In order to make potential d contributions from the Si atoms visible, explicit projections on the spherical harmonics are employed instead of the PAW projections. As $\text{hex-AlB}_2\text{-TbSi}_{2-b}$ is embedded in a $R30^\circ(\sqrt{3}\times\sqrt{3}\times 1)$ supercell of the primitive AlB_2 cell, the k-path is chosen in such a way

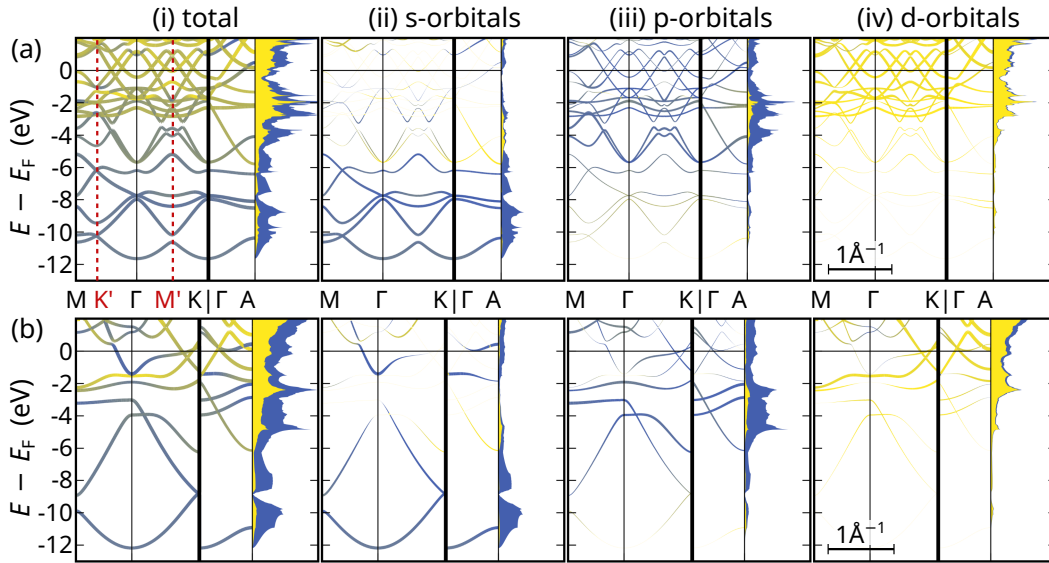


Figure 4.12: Band structures of (a) hex- $\text{AlB}_2\text{-TbSi}_{2-b}$ and (b) ort- $\text{AlB}_2\text{-TbSi}_2$. The unit cells were optimised with PBEsol. The panels and the plotting mode are analogous to Fig. 4.9. The k -path connects the high-symmetry points of the primitive Brillouin zone of the AlB_2 structure. The high-symmetry points of the supercell Brillouin zone are marked red.

that it connects the high-symmetry points of the primitive Brillouin zone identified in the reciprocal space of the supercell. The high-symmetry points of the supercell Brillouin zone M' and K' are marked red. All DOS and PDOS of the supercell are scaled by $1/3$ to reflect the different sizes of the unit cells.

Although the bands of hex- $\text{AlB}_2\text{-TbSi}_{2-b}$ are rather complicated due to band folding, some differences to ort- $\text{AlB}_2\text{-TbSi}_2$ are apparent. The bands and the PDOS reveal that the Si-s-like conduction bands disappear. The explicit projection scheme results in small Si-d contributions in ort- $\text{AlB}_2\text{-TbSi}_2$, which are zero in hex- $\text{AlB}_2\text{-TbSi}_{2-b}$. Furthermore, the Fermi energy is lowered, so the binding energies of all bands are smaller. Consequently, the Fermi level cuts the DOS in a region with a particularly low density. The last difference consists in sharper peaks in the DOS along with flat bands of Tb-Si character. All these differences accord well with the preliminary considerations that the removal of a Si atom reduces excess charge. The strong Si-p-Tb-d contributions to the DOS in the range from -1 eV to -4 eV, as well as the binding energy reduction upon lower Si content agrees with experimental photoemission data [94, 97]. Although the DOS near the Fermi level is considerably reduced, hex- $\text{AlB}_2\text{-RESi}_{2-b}$ is metallic with strongly dispersive bands cutting the Fermi level.

Charge transfer

The electronic properties are completed by a proof that RESi_2 is at least partially heteropolar. For this purpose, the superposition of atomic charge densities is subtracted from the ground state density of the unit cell, which yields the density of transferred charge. The result is plotted as isosurfaces and tomographies in Fig. 4.13 for stoichiometric ort- $\text{AlB}_2\text{-TbSi}_2$ and vacancy-populated hex- $\text{AlB}_2\text{-TbSi}_{2-b}$, both optimised

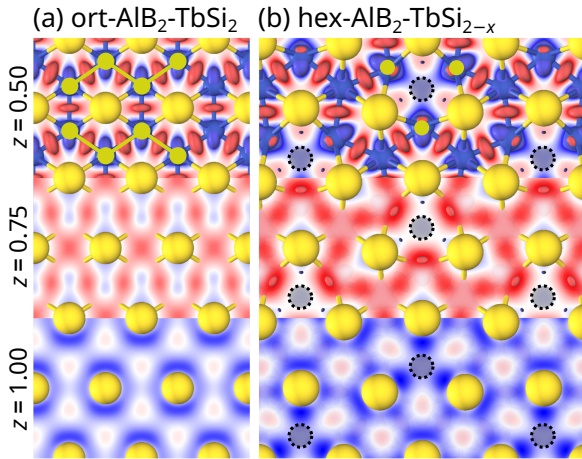


Figure 4.13: Charge transfer in (a) ort- $\text{AlB}_2\text{-TbSi}_2$ and (b) hex- $\text{AlB}_2\text{-RESi}_{2-x}$. Red \rightarrow electron gain; Blue \rightarrow electron loss. The view is along c . The bulbs are 3D isosurfaces of the electron transfer. Tomographies across (0001)-planes are inserted for three difference heights (relatively to c). Green markings highlight the zigzag chains in (a) and the (v)-type Si atoms in (b). Black dotted circles: vacancies.

with PBE. The tomographies are taken at three different heights along the axial lattice constant c : the cut through the Si atomic plane at $z = 0.5c$, the cut through the middle plane between the Si atoms and the Tb atoms at $z = 0.75c$, and the cut through the Tb atomic plane at $z = 1.0c \equiv 0.0c$.

The isosurfaces of the ort- $\text{AlB}_2\text{-TbSi}_2$ structure show that charge accumulates in the trigonal-planar bonds between the Si atoms, indicating sp^2 hybridisation. In the hex- $\text{AlB}_2\text{-TbSi}_{2-b}$ structure, the (m)-type Si atoms show three charge bulbs in trigonal-planar geometry, indicating sp^2 hybridisation. The (v)-type Si atoms show four bulbs, indicating sp^3 hybridisation. Two of them are placed on the bonds to the (m)-type Si atoms and the other two are attached to the (v)-type Si atom, pointing towards the vacancy and tilted out of the plane by a large angle. According to the tomographies, the Tb layer ($z = 1.0$) loses charge to the region between the Tb and the Si layer ($z = 0.75$). The charge transfer is as expected and confirms the partial heteropolarity of RESi_{2-x} . It is remarkable that the electrons accumulate mostly in sp^2 - or sp^3 -hybrid orbitals around the Si atoms, and not in defined bonds between the Si and Tb atoms. Integrating the plane average of the transfer reveals that the Tb layer loses 0.14 electrons per Tb atom in ort- $\text{AlB}_2\text{-TbSi}_2$ and 0.11 electron per Tb atom in hex- $\text{AlB}_2\text{-TbSi}_{2-b}$. These values have to be interpreted with caution as averaging over planes bears assignment problems, in particular because the Tb planes and the Si honeycombs are quite close together.

4.4 Discussion and summary

The treatment of TbSi_{2-x} and ErSi_{2-x} within DFT provided a detailed picture of the chemistry and the physics of the RE silicides. The novel systematisation of the RESi_2 prototypes revealed that the AlB_2 and the ThSi_2 structure are very similar to each other and merely differ in the orientations of the characteristic planes of zigzag-chain-Si (unidirectional \rightarrow AlB_2 , alternately perpendicular \rightarrow ThSi_2). The structures are determined by the Si networks, while the RE atoms are embedded in the interstices. The Si-Si bond lengths are near the single-bond length of diamond-Si, diluted

by a few percent if charge accumulates. Structure variations are thus carried out mainly by the Si–Si bond angles. That the Si sublattice behaves like a linkage of rigid rods proved to be very helpful for understanding how Si vacancies and the RE ionic radius alter the RESi_{2-x} structures.

The inspection of various RESi_{2-x} structures lead to the conclusion that both RESi_2 prototypes are stabilised by vacant Si sites. Hence, stoichiometric RESi_2 is unstable against segregation of diamond-Si from a RESi_{2-x} remainder. The stability analysis found that the AlB_2 phase is stable for Si-poorer conditions, while the ThSi_2 phase is preferred at Si-rich conditions. Furthermore, the stability of the AlB_2 phase seems to be independent of the RE atomic number. On the contrary, the ThSi_2 phase seems to destabilise when switching from Tb to Er. This agrees with expected different sensitivities of the Si sublattices towards the RE radius (layered for $\text{AlB}_2 \rightarrow$ indifferent, 3D network for $\text{ThSi}_2 \rightarrow$ anisotropic deformation). The theoretical stability analysis agrees with the experimentally determined temperature-composition phase diagrams of the RE–Si systems. Moreover, the vacancies are crucial for the agreement between the DFT-optimised lattice parameters and the experiment. They can also change the symmetry group of the structures by an orthorhombic distortion, which was traced back to an unequal vacancy concentration in the two inequivalent zig-zag planes. The lattice parameters of the herein investigated structures match the experimental reference up to 2 %, in spite of the approximated vacancy ordering.

The structural and electronic properties agree with the ZKB concept. As proven by the band structures, the Si atoms bind to each other via bonds which are rather independent of the presence of the Tb atoms. The formal free electron pairs of the Si anions occupy p_z (m-type) or sp^3 -hybrid orbitals (v-type) and bind to the d orbitals of the Tb atom in a predictable manner. All spare electrons occupy conduction bands, which dominate the DOS in the Fermi-level region and consist of Tb-d states mixed with Si-sp states. Since several bands cross the Fermi level, the RESi_{2-x} band structures are clearly metallic. The ZKB concept explains the inevitable presence of Si vacancies by an improved charge balance, as confirmed by the electronic properties. However, it fails to predict the exact stoichiometry as 1/3 electron per RE atom is still spare in the most stable RESi_{2-b} structure (the saturation of all valence electrons requires a stoichiometry of $\text{RESi}_{1.5}$, which does not exist). The partial heteropolarity of RESi_{2-x} was confirmed by the calculated charge transfer and the contraction of the volumes upon compound formation.

The findings on the bulk RE silicides have important consequences for the RESi_2 nanostructures on silicon. Firstly, the peritectic nature of the Si-rich RE silicides suggests that also the RESi_2 nanostructures might underlie a peritectic phase diagram, which would provoke kinetically inhibited structures. Secondly, the vacancy-related lattice distortions imply that one has to be very careful when employing lattice strain to explain nanostructures which lack vacancies. In particular, the inverted c/a ratio of the AlB_2 phase is an issue in the RESi_2 nanowires on Si(001) [P3, P6]. Supposed strain-induced growth is discussed for the monolayer-Tb@Si(111) system as well, which is the matter of the next chapter.

5 Monolayer films on silicon(111)

A silicon(111) substrate can be regarded as a stack of buckled Si honeycombs, sometimes referred to as *Si bilayers*, which also terminate the unreconstructed Si(111) surface. Hex-AlB₂-RESi_{2-b}, on the other hand, consists of alternating layers of hexagonally arranged RE atoms and (defective) Si honeycombs. Hence, attaching a RESi_{2-b} (0001) sheet to the Si(111) surface would be a natural continuation of the substrate. As, in addition, the lateral lattice constants match up to a few percent, the silicides of many REs are suitable for epitaxy on Si(111), among these the REs from Gd to Lu and Y (lattice mismatch between -2.55 % and 0.83 % [33, 108]). The multilayer-RESi₂ films on Si(111) are too thick for electronic quantum confinement, so their electronic properties are similar to those of bulk hex-AlB₂-RESi_{2-b}. The R30°($\sqrt{3} \times \sqrt{3}$) surface diffraction patterns indicate that the vacancies of the RESi₂ films are ordered, differently from the bulk phases [36, 37, 39, 46, 50–52]. In contrast, a RESi₂ film with a thickness of one bulk lattice constant, the monolayer-RE@Si(111) system, seems to lack Si vacancies, as indicated by (1 × 1) surface diffraction patterns. More peculiarly, the film is so thin that it confines the electronic states to a two-dimensional (semi-)metal [P8, P12, 34, 35, 38–53].

In view of the nanowire-Tb@Si(557) system, this chapter recovers the properties of the monolayer-Tb@Si(111) system. Tb can be considered a prototypical RE and the results are expected to be transferable to the other monolayer-RE@Si(111) systems, at least if the RE is trivalent. This assumption is based on the knowledge about the bulk-RESi₂ phases (Chap. 4) and on the extensive, synoptic, joint-experimental-theoretical work by Sanna et al., covering RE@Si(111) systems with thicknesses from sub-monolayer to multilayer [53]. Although the structure model of the monolayer-Tb@Si(111) system is well established, it bears peculiarities which have not been understood yet. Therefore, the chapter begins with the analysis of the structure. A systematic inspection of the configuration space of reasonable structure models proves that the established structure model is the most stable. Moreover, satisfactory microscopic explanations are found for all its peculiarities, e.g. the tendency of the covering Si honeycomb to buckle into the opposite direction of the Si honeycombs of the substrate. All findings on the structure are supported by the analysis of the electronic properties. The band structures and Fermi surfaces are compared to experimental ARPES measurements. The characteristic features are explained by relating the bands of the monolayer to those of the structurally related CaSi₂-TbSi₂ phases according to a simple particle-in-a-box model. The charge transfer is determined as well. The chapter concludes with a critical revision of the popular statement that surface-induced mechanical strain determines the morphological details of the monolayer.

5.1 Structure optimisation

The slab method

Surfaces are problematic for plane-wave codes because they break the translation symmetry. A solution for this consists in the *slab method* which employs a supercell with several atomic layers modelling the substrate and empty space representing the vacuum. The two interfaces between the vacuum layer and the substrate layer then simulate the surfaces of the substrate. It is convenient to embed the slab into a right-prismatic supercell so that the axis is parallel to the surface normal and the basis equals the surface unit cell. Both the bulk and the vacuum region have to be thick enough to prevent the states of opposite surfaces from interfering. The slab method has two flavours: The *asymmetric* approach, which models the surface of interest on the top side, while the bottom side is passivated with hydrogen; and the *symmetric* approach, which models two identical copies of the surface on the top and the bottom side of the slab. The latter is advantageous if passivation is not possible or if the computational demand can be reduced by inversion symmetry.

The monolayer structures are set up on an asymmetric Si(111) slab with a thickness of twelve atomic layers (six bilayers). The basis of the supercell represents the trigonal (1×1) unit cell of the unreconstructed Si(111) surface. A 31 Å thick vacuum layer separates the periodic replica of the slab in the axial direction (the (111)-direction or z-direction). It reduces to a still sufficient thickness of 24 Å when the slab bears the monolayer on the top side. The dangling bonds from the broken sp^3 -hybrid orbitals on the bottom side are passivated by H atoms. The clean, unreconstructed slab is sketched in Fig. 5.1 (a). The lattice parameters of the substrate were determined by a Murnaghan relaxation of the primitive unit cell of diamond-Si (PBE, $16 \times 16 \times 16$ Monkhorst-Pack mesh). The relaxation yielded a conventional lattice constant of $a_{d-Si} = 5.469$ Å, which translates into an Si(111) surface lattice constant of $a_{Si(111)} = a_{d-Si}/\sqrt{2} = 3.867$ Å and a Si-Si bond length of $d_{d-Si} = a_{d-Si} \cdot \sqrt{6}/4 = 2.368$ Å. These parameters slightly overestimate the corresponding experimental values by +0.7% ($a_{d-Si} = 5.432$ Å, $a_{Si(111)} = 3.841$ Å, $d_{d-Si} = 2.352$ Å [17, p. 1065]).

Thermodynamical framework

Following the experimental preparation, the monolayer forms in the annealing stage, i.e. during heating the sample at a constant temperature after depositing a certain amount of Tb. This translates into the thermodynamic boundary conditions of constant temperature, pressure, Si chemical potential (determined by the presence of the substrate) and amount of Tb (controlled by the Tb coverage). Similarly to the case of bulk $RESi_{2-x}$ (Sec. 4.2.1), the thermodynamic stability is determined by the Tb chemical potential, defined analogously to Eq. (4.36):

$$\mu_{Tb} \approx \frac{1}{N_{Tb}} \left(E_{DFT}^{cell} - \mu_{Si}^{d-Si} N_{Si} - \mu_H^{H-Sat} N_H \right) - \mu_{Tb}^{hcp-Tb} \quad (5.43)$$

where E_{DFT}^{cell} is the DFT total energy of the supercell and μ_{Si}^{d-Si} the Si chemical potential in diamond-Si. Structures which minimise μ_{Tb} are stable. The H chemical potential

$\mu_{\text{H}}^{\text{H-Sat}}$ refers to the H atoms, whose sole purpose is the saturation of the bottom side of the slab. It is clear that they have no physical meaning for anything happening on the top side, but their presence could have undesired effects on the thermodynamic relations if they were ignored. Therefore, the H chemical potential is calculated from a Si(111) slab which is symmetrically saturated by H atoms at both sides.

$$\mu_{\text{H}}^{\text{H-Sat}} = \frac{1}{N_{\text{H}}^{\text{H-Sat}}} \left(E_{\text{DFT}}^{\text{H-Sat}} - \mu_{\text{Si}}^{\text{d-Si}} N_{\text{Si}}^{\text{H-Sat}} \right) \quad (5.44)$$

By this means, all energetic effects from the H-saturated bottom side are stored in $\mu_{\text{H}}^{\text{H-Sat}}$ and thus removed from the thermodynamics. Of course, the H term cancels out in differences between the Tb chemical potentials of structures having the same bottom side. This is the case in all structures considered in this chapter.

Computational parameters

Many parameters are equal to those of the previous chapter (p. 45). The DFT calculations are carried out with VASP [2, 3] using PAW potentials and the PBE xc-functional [10, 21, 22]. The Tb atoms are trivalent ($5p^6 5d^1 6s^2$, 4f electrons frozen in the core). Si and H have PAW valences of $3s^2 3p^2$ and $1s^1$, respectively. The kinetic energy cutoff is increased to $E_{\text{cut}} = 450$ eV to meet the increased requirements of the H atoms. The Brillouin zone is sampled by a Γ -centred surface Monkhorst-Pack mesh [117] at a density of $15 \times 15 \times 1$ k-points. The Brillouin-zone integration is carried out by a Gaussian occupation with a smearing of 20 meV for the ionic relaxations of the metallic systems and by the tetrahedron method with Blöchl corrections [118] for all other calculations (static and relaxations of insulators). A convergence test proves that increasing the energy cutoff or the sampling density alters the total energy by ≈ 1 meV per atom. The ionic forces are calculated according to the Hellmann-Feynman theorem [119]. Differently from the relaxation of the bulk structures, the unit cell is fixed. The lowest four atomic layers of Si are held fixed at the bulk positions during all relaxations. The H atoms on the bottom side are held fixed at the equilibrium positions of the symmetrically H-saturated slab. All other ions move within the unit cell along the forces towards the equilibrium positions and stop to relax if the forces acting on each ion are smaller than 0.005 eV/Å.

The Tb@Si(111) monolayer

The structure model of the monolayer-RE@Si(111) system (Fig. 5.1) is well established by experimental analysis as well as by theoretical calculations. It is a sandwich structure of a hexagonal RE layer which is placed between the unreconstructed (1×1)-Si(111) surface and a vacancy-free, buckled Si honeycomb. The monolayers of all REs from Gd to Er and Y adopt this structure [39–41, 43, 45–48, 53]. The following nomenclature is used in this work: *terminating Si honeycomb* or *substrate termination* denotes the top Si bilayer of the substrate (Si_3 and Si_4) and *covering Si honeycomb* or *cover* denotes the Si bilayer above the RE atoms (Si_1 and Si_2). In the established structure, the three valence electrons from each RE atom complement all incomplete Si

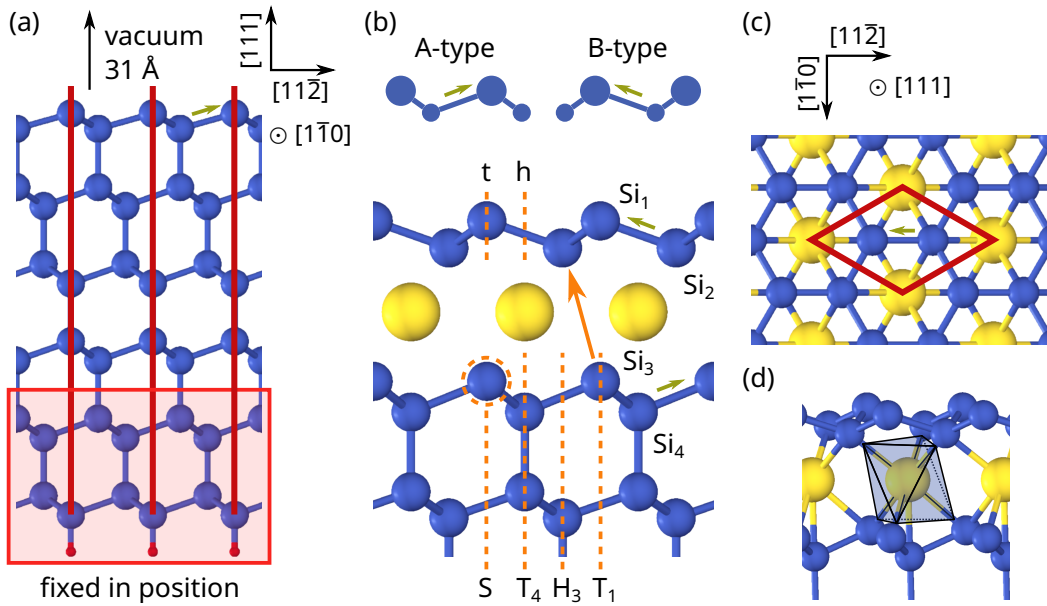


Figure 5.1: (a) Sketch of the Si(111) slab and (b) – (d) the TbSi₂ monolayer structures. Blue circles are Si atoms; Yellow circles are Tb atoms; Red circles are H atoms. The light red rectangle in (a) encircles the subset of atoms fixed in position during the relaxations. Red lines mark the unit cell. (b) shows the (1 $\bar{1}$ 0) view and (c) the (111) view of the T₄-h-B structure. Orange markings indicate the symmetry positions of the Tb atom relative to the substrate termination (T₄, H₃, T₁ and S [39]) and to the cover (t-type and h-type). Small green arrows indicate the buckling direction of the cover (A-type or B-type [39]). (d) shows the trigonal-antiprismatic/ octahedral coordination of the Tb atom by the adjacent Si₂ and Si₃ layers.

octets, i.e. they pair the dangling bonds of Si₁, Si₂ and Si₃. This closed-shell configuration is reasonable a priori and holds for all structure models which are derived from the established one by layer translation [39]. Although many publications concerning different structure models exist, a rigorous and complete evaluation of the configuration space of reasonable structures has not yet been performed. Since it helps to understand why the established structure is stable in spite of some peculiarities, the configuration space is systematically explored in the following paragraphs.

At first, the degrees of freedom to modify the established structure are identified (Fig. 5.1 (b)). The first degree of freedom has already been addressed in many works, e.g. Stauffer et al. [39]. It concerns the placement of the RE layer relative to the substrate. In reasonable structure models, the RE atom is located at one of the three symmetry points of the unreconstructed Si(111)-(1 × 1) surface [39]:

- Above the lower Si atom (egg-box position), denoted T₄
- Above the upper Si atom, denoted T₁
- Above the hole (hole position), denoted H₃

In addition, Stauffer et al. considered a structure where the RE atom substitutes the upper Si atom, denoted S. This structure does not have a closed-shell configuration, of course. The second degree of freedom consists in the placement of the covering

Si honeycomb relative to the RE layer: holes over RE atoms (h-type, hole position) or upper Si atoms over RE atoms (t-type, egg-box position). The symmetric placement analogous to T_1 , i.e. lower Si atoms over RE atoms, is discarded due to the low number of Si atoms coordinating the RE atoms¹. The cover placement has apparently not been attended to so far as the literature concerns only h-type structure models. This probably originates in the premise that the monolayer-RE@Si(111) structure is based on the AlB_2 structure. However, because the AlB_2 phase is only stable in vacancy-populated form, deriving the vacancy-free monolayer structure from the AlB_2 structure is not reasonable. Moreover, the $CaSi_2$ structures, which are the stable phases for (hypothetical) vacancy-free $RESi_2$, incorporate h-type and t-type buckled honeycomb-Si (Sec. 4.2.6). The monolayer structure will prove to be more related to the $CaSi_2$ structures than to the AlB_2 structure, which underlines the need for investigating t-type structure models. Finally, the third – and important – degree of freedom is the direction into which the cover buckles: Conform with the underlying Si substrate (A-type) or mirrored/rotated by 180° (B-type). According to this nomenclature, the established structure is denoted T_4 -h-B.

The configuration space of the monolayer-Tb@Si(111) system is sampled by each four T_4 and H_3 structure models (h-type/t-type \times A-type/B-type) and each two T_1 and S structure models (h-type \times A-type/B-type)². All structure models are optimised with respect to the atomic positions. The resulting Tb chemical potentials are plotted in Fig. 5.2 (a). The T_1 and S structures are highly unstable ($\mu_{Tb} > 0$). In the other structures, T_4 and H_3 , the covering Si honeycomb prefers the h-type to the t-type position. Interestingly, the favoured buckling direction of the cover depends on the relative positions between the substrate, the Tb layer and the cover in an unobvious manner. The most stable structure model is T_4 -h-B with $\mu_{Tb} = -806$ meV, which agrees well with the findings of Sanna et al. [53].

In order to quantify how varying the degrees of freedom affects μ_{Tb} , the respective penalties are reckoned back in the order: buckling direction, cover placement and Tb placement. The results are compiled as a decision tree in Fig. 5.2 (b), in which summing the values along a branch returns μ_{Tb} of the respective structure. Flicking the buckling direction (lowest level) puts a penalty of +135 meV to +253 meV on the T_4 and H_3 structures. The established T_4 -h-B structure lies amid the range with +189 meV, matching the findings of [53] very well. Since the flicking penalties are much higher than $k_B T$ at room temperature, the orientation of the cover is definite and experimentally observable. Concerning the position of the cover, the T_4 and H_3 structures are rather h-type than t-type ($\Delta\mu_{Tb} = +382$ meV and +274 meV, respectively). Concerning the position of the Tb layer, the T_4 position is more favourable than the H_3 position by +232 meV. The values agree very well with the difference of 225 meV in the local minima of the potential energy surface (PES) of Si(111) for the adsorption of a Dy atom [53]. The T_1 site has a penalty of +1158 meV, also in agreement with the PES in [53] and similar to the penalty of the substitutional S site (+1164 meV).

¹With respect to the findings on bulk $RESi_{2-x}$ (Chap. 4), the RE atom tends to favour Si coordination numbers of about 8 to 10. However, placing the cover in a T_1 manner would contribute only one Si atom to the coordination polyhedron, leading to a maximum Si coordination number of five. For the same reason, the T_1 placement relatively to the substrate is strongly discouraged as well.

²The t-type structure models are ignored as T_1 and S are per se strongly discouraged.

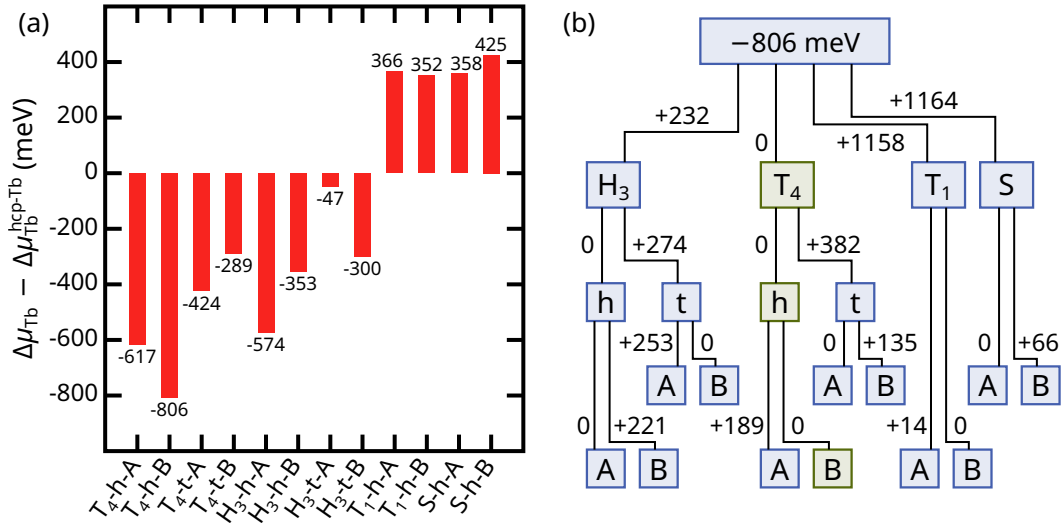


Figure 5.2: (a) Tb chemical potentials of the monolayer-Tb@Si(111) structures and (b) decision tree for the energy penalties upon structure variations. Green boxes in (b) mark the branch of the stable T_4 -h-B structure.

The tendency of the cover to buckle into a certain direction can be summarised as a simple rule: The buckling direction is favourable if the upper Si atom of the substrate termination (Si_3) is not above the lower Si atom of the cover (Si_2) (oblique, orange arrow in Fig. 5.1 (b)). This is the case in the stable T_4 -h-B structure, as well as in H_3 -h-A, T_4 -t-A and H_3 -t-B. Conversely, the structure is penalised if Si_2 is above Si_3 , as in the case in T_4 -h-A, H_3 -h-B, T_4 -t-B and H_3 -t-A. The physical reason for this will be illuminated by the band structures (Sec. 5.2). The stability relations of the other two degrees of freedom depend on how the Tb atom interacts with the Si honeycombs. In order to analyse this, the Si coordination numbers N_C of the Tb atoms are compiled for all structures in Tab. 5.1, as well as the Tb–Si bond distances and the bond distances and angles of the two Si honeycombs Si_1 – Si_2 and Si_3 – Si_4 . The vertical atomic-layer distances, which immediately follow from the bond distances, are plotted in Fig. 5.3. The energetically most stable T_4 -h-B structure is highlighted in each case. “Clean” denotes the clean, unreconstructed Si(111) surface and “H-Sat” the H-saturated Si(111) surface (the same slab used for the calculation of $\mu_{\text{H}}^{\text{H-Sat}}$, vide supra). For comparison, the respective parameters of the bulk phases of TbSi_2 are inserted as well.

Shifting the layers against each other changes the number of Si atoms coordinating the Tb atom. In the hole position (cover: h-type, substrate: H_3), the Tb atom is coordinated only by Si_2/Si_3 in a threefold manner. The egg-box position (cover: t-type, substrate: T_4) adds the Si_1/Si_4 atom to the coordination polyhedron, incrementing the coordination number by one. The coordinating Si–Tb bond distances range from 2.92 Å to 3.11 Å in the T_4 and H_3 structures. They follow the expectable trend that they dilate for higher N_C . In detail, their averages are 2.98 Å, 3.00 Å and 3.03 Å for $N_C = 6, 7$ and 8, respectively. Depending on the relative positions, the Tb atom modifies the Si honeycombs in the following manner: In the hole position, both the substrate termination and the cover (if buckled into the favourable direction) assume buckling

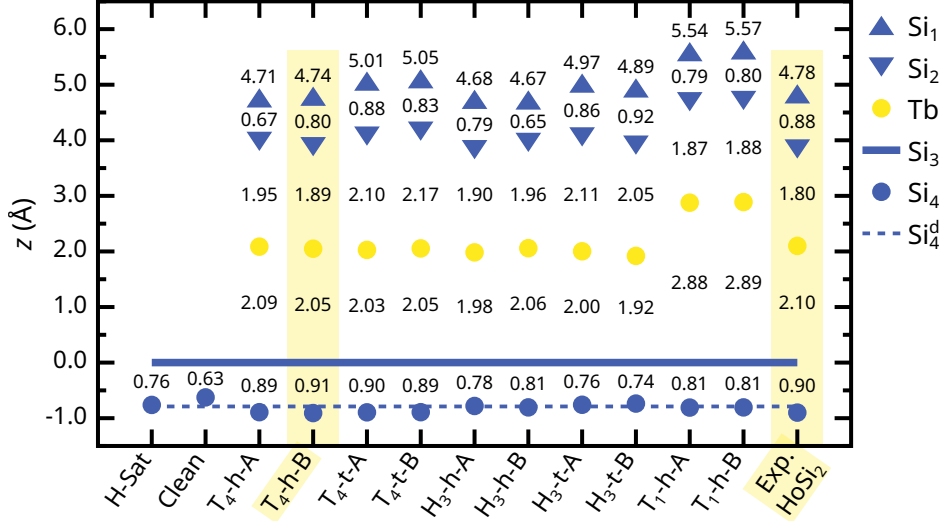


Figure 5.3: Vertical positions and distances of the atomic layers in the monolayer-Tb@Si(111) structures. All vertical positions are relative to that of Si₃. The numbers between two symbols quantify the vertical distance between the respective layers. The numbers above the up-triangles quantify the vertical distance between Si₁ and Si₃ layers and, thus, the height of the monolayer. Si₄^d marks the atomic layer distance in diamond-Si. Experimental reference for the monolayer-Ho@Si(111) system: [43].

	Si ₁ -Tb	Si ₂ -Tb	Si ₃ -Tb	Si ₄ -Tb	N_C	Si ₁ -Si ₂	Si ₃ -Si ₄
Clean							2.32 (113.0°)
H-Sat							2.36 (110.1°)
T ₄ -h-A	3.44	2.96	3.06	2.98	7	2.33 (112.1°)	2.40 (107.1°)
T ₄ -h-B	3.49	2.93	3.03	2.96	7	2.37 (109.3°)	2.41 (106.7°)
T ₄ -t-A	2.98	3.07	3.02	2.92	8	2.40 (107.4°)	2.41 (107.0°)
T ₄ -t-B	3.00	3.11	3.03	2.95	8	2.38 (108.5°)	2.40 (107.1°)
H ₃ -h-A	3.50	2.93	2.99	3.55	6	2.37 (109.4°)	2.37 (109.7°)
H ₃ -h-B	3.44	2.97	3.04	3.63	6	2.33 (112.5°)	2.37 (109.1°)
H ₃ -t-A	2.97	3.07	3.00	3.55	7	2.39 (107.9°)	2.36 (110.2°)
H ₃ -t-B	2.97	3.03	2.94	3.47	7	2.41 (106.5°)	2.35 (110.6°)
T ₁ -h-A	3.47	2.91	2.88	4.31	4	2.37 (109.5°)	2.37 (109.0°)
T ₁ -h-B	3.49	2.92	2.89	4.32	4	2.37 (109.3°)	2.37 (109.1°)
diamond-Si							2.37 (109.5°)
ort-AlB ₂ -TbSi ₂			3.04		8	2.42, 2.36 (124.7°, 110.6°)	
tr6-CaSi ₂ -TbSi ₂	2.94		3.06	3.05	7	2.29 (118.9°)	2.49 (104.9°)
tr3-CaSi ₂ -TbSi ₂			3.00	3.06	8		2.41 (103.6°)

Table 5.1: Bond distances and angles in the monolayer-Tb@Si(111) structures. The distances are given in Å; The angles are parenthesised. N_C is the number of Si atoms coordinating each Tb atom.

parameters similar to those of diamond-Si (bond length: 2.37 Å, tetrahedron angle: 109.5°). In the egg-box position, the Si–Si bond length is longer, while the bond angle is more acute. This is expectable as a higher coordination enhances the bonding between the Tb atom and the Si honeycomb at the expense of the Si–Si intra-bonds. If the buckling flicks into the unfavoured direction, the cover flattens out a bit and, thus, has more obtuse bond angles and shorter bond lengths. The H-saturated surface has a bulk-like substrate termination, while that of the clean surface is considerably flattened due to the low electron density of the dangling bond of Si₃.

The layer distances follow the bond lengths by construction. The extending effect of egg-box Tb atoms on the bonds of adjacent Si honeycombs is clearly visible. Particularly in the stable T₄-h-B structure, the cover is bulk-like, while the substrate termination is expanded. If the buckling direction is unfavourable, the cover as a whole is elevated compared to the favourable case. In the t-type structures, the height of the monolayer (Si₁–Si₃) is larger than that of the respective h-type structures by ~0.3 Å.

The calculated parameters of the most stable T₄-h-B structure equal the results of Sanna et al. [53] up to 0.1 Å, which is not surprising as the theoretical approaches are very similar. Experimental data on the vertical layer distances are not available for the monolayer-Tb@Si(111) system. Therefore, the results are compared to the homologue monolayer-Ho@Si(111) system, for which Spence et al. measured complete stratification data set by MEIS [43], plotted in the rightmost column in Fig. 5.3. The calculated expansion of the substrate termination matches the experimental results of Spence et al. very well (0.91 Å vs. 0.90 Å). The distance between the cover and the Tb layer (Si₂–Tb) is greater than that of Spence et al. (1.89 Å vs. 1.80 Å). This not a disagreement, though, if the lanthanoid contraction is taken into account: It makes the Si–RE layer distances contract by –0.2 Å to –0.3 Å per atomic-number increment [46, 53], hence adding up to –0.4 Å to –0.6 Å from Tb to Ho. The cover thickness (Si₁–Si₂) and the distance between the Tb layer and the substrate (Tb–Si₃) are smaller than those of Spence et al. (0.80 Å vs. 0.88 Å and 2.05 Å vs. 2.10 Å, respectively). However, they match the results of another study, a LEED *I-V* analysis on the same system [45] (0.82 Å and 2.03 Å, respectively). In conclusion, the T₄-h-B structure model optimised with PBE agrees with experimental evidence within the error bars.

As the comparison between the Si-Tb coordination polyhedrons in the (T₄ and H₃) monolayer structures and those in the vacancy-free bulk TbSi₂ structures reveals, that the monolayer is much more related with the CaSi₂ structures than with the AlB₂ structure. In the bulk, the coordination polyhedrons are cuboids in *ort*-AlB₂-TbSi₂, hexagonal prisms in *hex*-AlB₂-TbSi₂, trigonal antiprisms (distorted octahedra) with both bases capped in *tr3*-CaSi₂-TbSi₂ and trigonal antiprisms with one basis capped in *tr6*-CaSi₂-TbSi₂. In the monolayer, the Si₂/Si₃ coordination polyhedron is a trigonal antiprism (octahedron) if the buckling direction of the cover is favourable and a regular trigonal prism otherwise. That the Tb atom seems to prefer the trigonal-antiprismatic (octahedral) Si coordination hints at the microscopic explanation for the buckling tendency of the cover (*vide infra*). The distinction between T₄ and H₃ and, analogously, between t-type and h-type consists in the presence of a cap at the respective basis. Accordingly, the coordination polyhedron in T₄-t-A is a doubly capped trigonal antiprism, exactly like that in *tr3*-CaSi₂-TbSi₂, and that in

T_4 -h-B is a trigonal antiprism with capped bottom face (highlighted in Fig. 5.1 (d)), similar to that in $tr6$ - $CaSi_2$ - $TbSi_2$. Thus, the T_4 -h-B structure agrees with the energetic favourability of $tr6$ - $CaSi_2$ - $TbSi_2$ over $tr3$ - $CaSi_2$ - $TbSi_2$ and hex - AlB_2 - $RESi_2$ within PBE (Tab. 4.8). The analogy is underlined by an almost perfect lattice matching between the basis of $tr6$ - $CaSi_2$ - $TbSi_2$ and the Si(111) surface (3.94 Å vs. 3.867 Å, +1.9 %). As the same holds also for $tr3$ - $CaSi_2$ - $TbSi_2$ (3.78 Å, -2.2 %), it may be concluded that layered structures of Tb atoms sandwiched between buckled Si honeycombs in general are unstrained. In contrast to the $CaSi_2$ phases, the basis of hex - AlB_2 - $TbSi_2$ (4.10 Å) is too large by +6.0 %, so this structure is even farther away from the monolayer structure as already given by the geometry and the thermodynamical instability. This point will be discussed in more detail in Sec. 5.3.1.

5.2 Electronic properties

5.2.1 Band structures

The band structure calculations are carried out within the same approach as that in Sec. 4.3. The k-path in the surface Brillouin zone consists only of two line segments: $\overline{M\Gamma}$ parallel to the $[11\bar{2}]$ direction and $\overline{\Gamma K}$ parallel to the $[1\bar{1}0]$ direction. A sketch of it may be found in the inset of Fig. 5.4 (d,vi). For the calculation of accurate DOSs, the sampling density of the Brillouin zone is increased to a $(40 \times 40 \times 1)$ mesh.

The stable T_4 -h-B structure

Fig. 5.4 shows the band structures of (a) – (c) the most stable T_4 -h-B structure and (d) the clean Si(111) surface. The line width corresponds to the portion of certain groups in the PAW projections. The first row (a) shows the portions of the Tb portion, the top four Si atoms $Si_1 - Si_4$ and bulk-Si³. The second row (b) shows the orbital-resolved projections of the Tb atom, in which angular momenta with the same z-component are combined (e.g. p_x and p_y). The third row (c) shows the orbital-resolved projections of the cover (Si_1 and Si_2) and the top Si atom of the substrate Si_3 . The last row (d) concerns the clean Si(111) surface, its panels showing the total portion of Si_3 , Si_4 and bulk-Si, and the orbital-resolved projections of Si_3 . The line colour is fixed in each panel, but indicates the displayed atom group. The energies are reset by the bulk VBM E_0 and the Fermi level of the slab is inserted as a red horizontal line. By this means, the band structures of T_4 -h-B and clean Si(111) become comparable.

All Si bands in Fig. 5.4 have a characteristic set of three bands in common which stem from the three in-plane sp^3 -hybrid bonds: a U-shaped band between -12 eV and -8 eV and two bands between -8 eV and 0 eV which are shaped like a lying K and intersect at the Γ -point. The U and K bands of bulk-Si (panels (a,vi) and (d,iii)) are rather concentrated shadows resulting from the slab projection combined with

³The average of the upper two fixed Si layers in the red box in Fig. 5.1 (a).

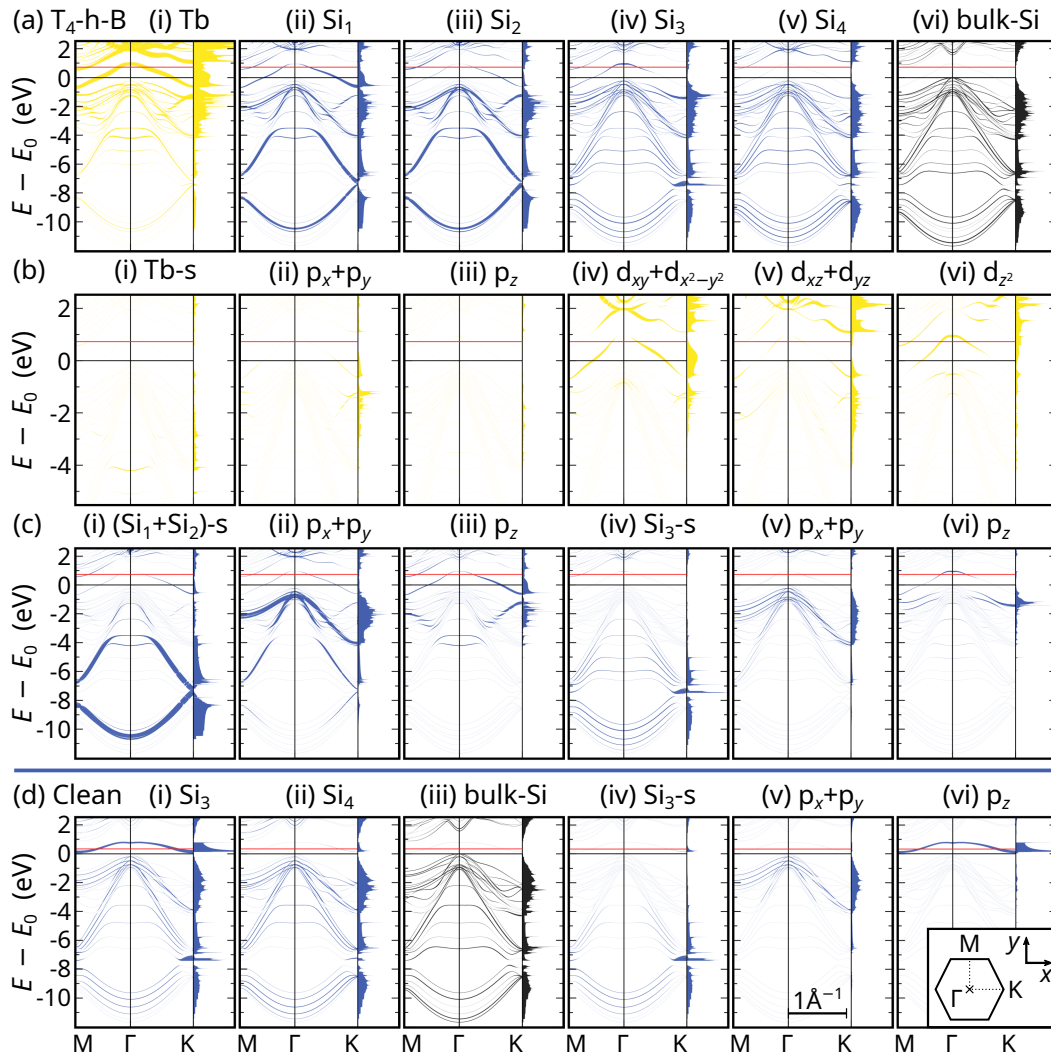


Figure 5.4: Band structures of (a) – (c) the T_4 -h-B structure and (d) the clean Si(111) surface. The line colour is fixed in each panel. The line width corresponds to: (a) the total PAW projections on (i) Tb, (ii) Si_1 , (iii) Si_2 , (iv) Si_3 , (v) Si_4 and (vi) bulk Si; (b) the (i) s, (ii) $(p_x + p_y)$, (iii) p_z , (iv) $(d_{xy} + d_{x^2-y^2})$, (v) $(d_{xz} + d_{yz})$ and (vi) d_{z^2} orbitals of the Tb atom; (c) the (i) s, (ii) $(p_x + p_y)$ and (iii) p_z orbitals of Si_1 and Si_2 , and the (iv) s, (v) $(p_x + p_y)$ and (vi) p_z orbitals of Si_3 ; (d) the total PAW projections on (i) Si_3 , (ii) Si_4 and (iii) bulk Si, and the (iv) s, (v) $(p_x + p_y)$ and (vi) p_z orbitals of Si_3 . All energies are reset by the VBM of the bulk-Si bands. The red horizontal lines indicate the Fermi levels of the slabs. The inset in the bottom right panel shows the surface Brillouin zone. Mind that the energy scale of (b) is different from that of the other rows as there are no Tb states below -4 eV.

a low dispersion in the (111) direction. In contrast, the bands from the vertical sp^3 -hybrid bonds are separated, diffuse, flat lines because they are less dispersive in-plane, but strongly dispersive out-of-plane. The similarity between the bulk-Si bands of the clean surface and T_4 -h-B proves that the slab is thick enough for the purposes of this work. The difference between the VBM and the CBM of the bulk-Si bands, the substrate band gap, amounts to 0.9 eV, which is smaller than the experimental band

gap of bulk silicon (1.1 eV), but higher than the DFT band gap of bulk silicon (0.7 eV). Thus, the DFT-related underestimation of the band gap and the gap opening due to the finiteness of the slab partially compensate each other.

Concerning the Si_3 and Si_4 bands of the clean Si(111) surface (panels (d,i) and (d,ii)), the in-plane U and K bands look similar to the bulk-Si bands, which indicates a strong coupling between the substrate termination the rest of the slab. In contrast, the diffuse out-of-plane states of Si_3 are much weaker than those of Si_4 . Instead, a surface state of exclusive p_z character appears as a single, isolated flat band just above the VBM of the slab, but completely within the substrate band gap (panel (d,vi)). As observed earlier [53], this state originates in the broken vertical sp^3 bonds of Si_3 . That the band is half-filled pins the Fermi level at +0.3 eV above the VBM. The Si_3 and Si_4 bands of the T_4 -h-B structure (panels (a,iv) and (a,v)) share several characteristics with those of the clean surface. They are almost unaffected by the presence of the TbSi_2 monolayer. The only major difference consist in a splitting of the Si_3 surface state into an occupied part at the zone edges and unoccupied part at the centre.

The bands of Si_1 and Si_2 (panels (c,i) and (c,ii)) are similar to those the substrate termination with respect to the in-plane U and K bands. However, they are sharp in the sense that the majority of their projections is concentrated in one copy. The out-of-plane bands are sharp as well and resemble an O between -4 eV and $+1$ eV (panel (c,iii)). Hence, the cover exclusively hosts surface states and is completely decoupled from the bulk. The Tb states dominate the region a few eV below the Fermi level, similarly to bulk TbSi_2 . They have strong Tb-d contributions at lower binding energies and hybridise with the dangling p_z states of Si_1 , Si_2 and Si_3 . The O-shaped double band is the most prominent band. Its lower branch is majorly of Tb- Si_2 character with smaller Si_1 portions. Its upper branch is isolated from the lower branch and lies completely within the band gap. Since the Fermi level is lifted to +0.7 eV, right below the substrate CBM, the upper O band is almost completely filled. Below the Fermi level, its character is a hybrid of Tb- d_{xy} , Tb- $d_{x^2-y^2}$ (both in-plane), Si_1 - p_z and (to a lesser extent) Si_2 - p_z . At and above the Fermi level, the character changes to out-of-plane Tb- d_{z^2} mixed with Si_3 - p_z . The upper O band is hole-like as it cuts the Fermi level with a negative curvature. Near the M-points, a second, electron-like band crosses the Fermi level. Its character is a hybrid of Tb- d_{z^2} and p_z of Si_1 and Si_2 . Since all states crossing the Fermi level are confined to the surface and completely decoupled from the rest of the substrate, the TbSi_2 film gives rise to a clearly two-dimensional, (semi-)metallic system.

Although the DFT eigenenergies are only crude approximations of real excitation energies, the theoretical band structure in Fig. 5.4 compares well with experimental ARPES images of the monolayer-Tb@Si(111) system [52] and the homologous systems monolayer-Gd@Si(111) [47] and monolayer-Dy@Si(111) [49]. In all three works, the O-shaped double band between -5 eV and 0 eV is clearly visible. Its branches are separated by a smaller gap at the K-point and by a larger gap at the M-point so that the hole-like upper branch is isolated from the substrate bands. In this work, the binding energy of the upper O band at the zone boundary is ≈ 1.4 eV, which is close to the experimental reference. Also the electron-like pockets at the M-points perfectly match the experimental observations.

Comparison between the monolayer-Tb@Si(111) structures

In order to explain why T_4 -h-B is the most stable structure model for the monolayer-Tb@Si(111) system, its band structure is compared with those of five other structure models in Fig. 5.5. The plotting mode is the same as that in Fig. 5.4 (a). Compared to T_4 -h-B (Fig. 5.5 (c)), all other structure models show characteristic changes in the upper O band, which are marked orange.

The Fermi energy depends on the relative positions between the Tb layer and the adjacent Si honeycombs in a quite predictable manner. As expected from bonding efficacy, the Fermi energy falls if the Tb atom is in the egg-box position (T_4 and t-type structures) and rises if the Tb atom is in the hole position (H_3 and h-type structures). Quantitatively, the Fermi levels relative to the bulk VBM and averaged over the two buckling directions are +0.58 eV for the T_4 -t structures, +0.76 eV for the T_4 -h and the H_3 -t structures, and +0.81 eV for the H_3 -h structures (band structures not shown). Hence, the T_4 -t structures minimise the Fermi energy.

Each variation from the stable T_4 -h-B structure gives rise to a characteristic band changes near the Fermi level. From T_4 to H_3 , the upper O band closes a gap with the CBs at the Γ -point (feature A in Fig. 5.5 (a) and (b)). Furthermore, as indicated by the sharpening, the in-plane bands of the substrate termination dehybridise from the bulk states and concentrate at the surface, along with higher binding energies. This accords with the contraction, ergo intra-bond strengthening, of the terminating Si honeycomb upon switching from T_4 to H_3 (vide supra). From h-type to t-type, the upper O band flattens and shows an electron-like furrow in the apex at the Γ -point (feature B in Fig. 5.5 (e) and (f)). Furthermore, the bands of the cover shift to lower binding energies, which accords with the expansion, ergo intra-bond weakening, of the covering Si honeycomb upon switching from h-type to t-type. Flicking the buckling direction from favoured to unfavoured entails a gap closing between the upper O band and the CBs along $\overline{\Gamma K}$ (feature C in Fig. 5.5 (a), (d) and (f)). On closer inspection, both involved bands are characterised by strong Tb-d contributions beside p_z contributions from Si_1 , Si_2 and Si_3 . After the gap closing, the steeper band of the new crossing is majorly of in-plane d_{xy} and $d_{x^2-y^2}$ character and the shallower band of out-of-plane d_{z^2} character. This confirms that the steric impact of the Tb-d states is the driving force behind the tendency of the cover to buckle into a certain direction. All band variations increase the DOS at the Fermi level for different reasons, which finally explains why T_4 -h-B is the most stable structure, despite not having the lowest Fermi energy.

Relation to the bulk $TbSi_2$ structures

That the $TbSi_2$ monolayer seems to be electronically decoupled from the Si(111) substrate suggests that the surface band structure might be derivable from the bands of bulk $TbSi_2$ by means of a simplified particle-in-box approach. For example, consider a monolayer slice of the hex- AlB_2 - $TbSi_2$ structure with a thickness of one axial lattice constant c , which would be a layer of Tb atoms sandwiched between two Si honeycombs. The lateral motion of the electrons may be undisturbed by the presence of the boundary surfaces. The vertical distribution of the wave functions then determines

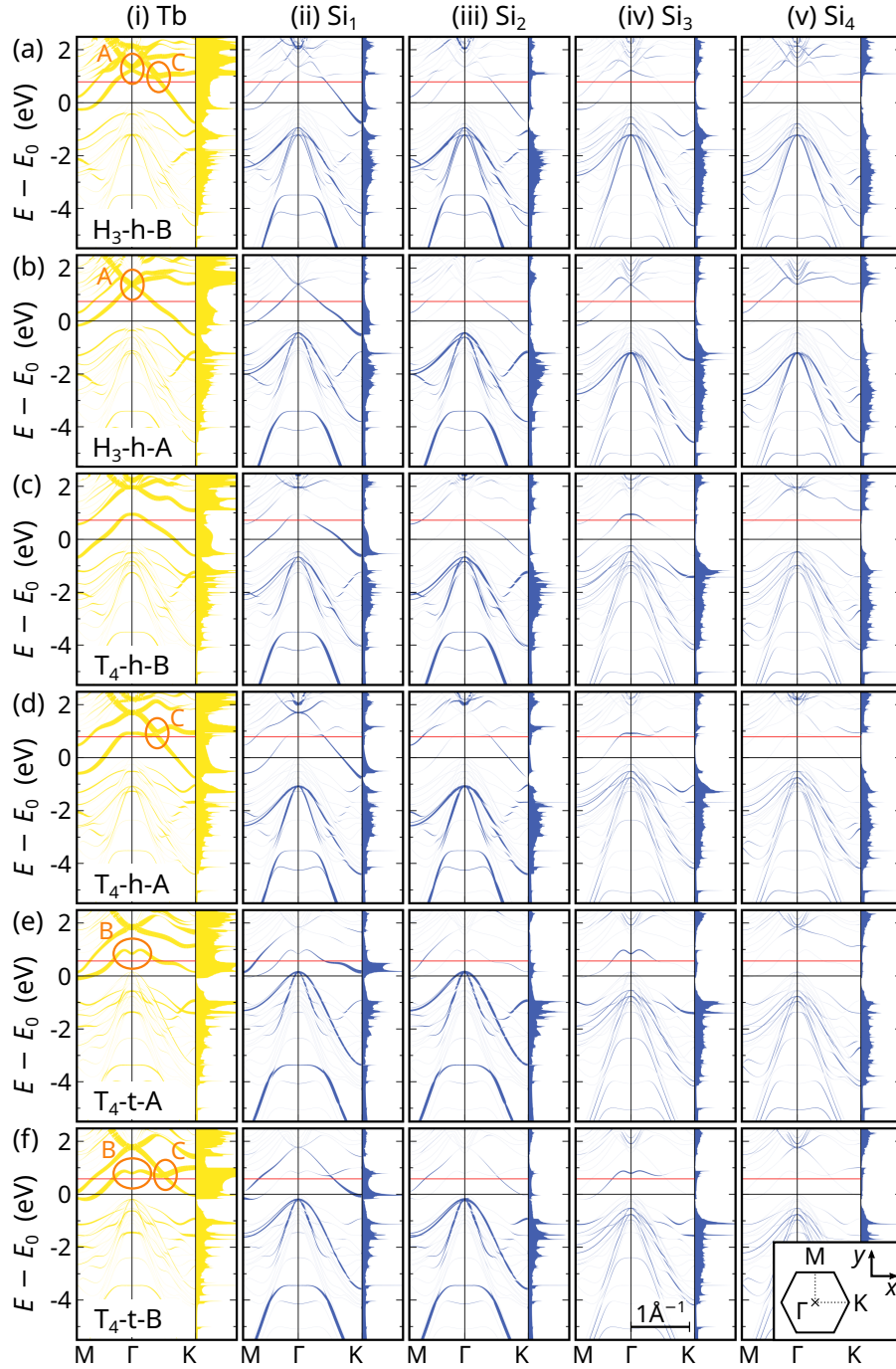


Figure 5.5: Band structures of the monolayer-Tb@Si(111) structures. (a) H₃-h-B, (b) H₃-h-A, (c) T₄-h-B, (d) T₄-h-A, (e) T₄-t-A, (f) T₄-t-B. The line width corresponds to the PAW projections of (i) Tb, (ii) Si₁, (iii) Si₂, (iv) Si₃ and (v) Si₄. All energies are reset by the VBM of the bulk-Si bands. The red horizontal lines indicate the Fermi levels. Orange markings highlight changes in the upper O band relatively to the T₄-h-B structure. The inset in the bottom right panel shows the surface Brillouin zone.

how the bulk bands have to be projected onto the surface Brillouin zone of the slice. A reasonable ansatz is a first-order, fixed-end standing wave of wavelength $2c$ and corresponding wavenumber $\frac{\pi}{c}$. Such a standing wave can be constructed from the solutions for the 3D crystal by superposing two countercurrent waves with equal lateral and opposite axial wavenumbers $\frac{\pi}{c}$ and $-\frac{\pi}{c}$. Since these lie in the opposite bases of the prismatic 3D Brillouin zone, the 2D band structure of the slice can be estimated by calculating the bands of the 3D crystal along paths in one of these (identical) bases. In the case of hexagonal unit cells, the surface k-path M– Γ –K corresponds to the k-path L–A–H in the bulk Brillouin zone.

Out of the bulk TbSi₂ structures in Sec. 4.2, three have a hexagonal basis. While the band structure of hex-AlB₂-TbSi₂, has already been analysed (Fig. 4.10), those of tr3-CaSi₂-TbSi₂ and tr6-CaSi₂-TbSi₂ are calculated from the PBE-optimised unit cells in the same manner. Fig. 5.6 shows the bands of all three structures along (a) the main path M– Γ –K| Γ –A and (b) the path for the slice projection L–A–H. In the bands of (iii) tr6-CaSi₂-TbSi₂, the blue colour refers only to the buckled Si honeycomb, while the contributions from the other, almost flat Si honeycomb are blended out. The Tb contributions are divided by two so as to retain the Tb/Si ratio. In order to facilitate the comparison, the slab band structures of (c) T₄-h-B (related with tr6-CaSi₂-TbSi₂) and (d) T₄-t-A (related with tr3-CaSi₂-TbSi₂) are shown as well.

The L–A–H bands of hex-AlB₂-TbSi₂ (Fig. 5.6 (b,i)) have some features with the surface bands of T₄-h-B in common (Fig. 5.6 (c)). The in-plane U and K bands of the Si atoms

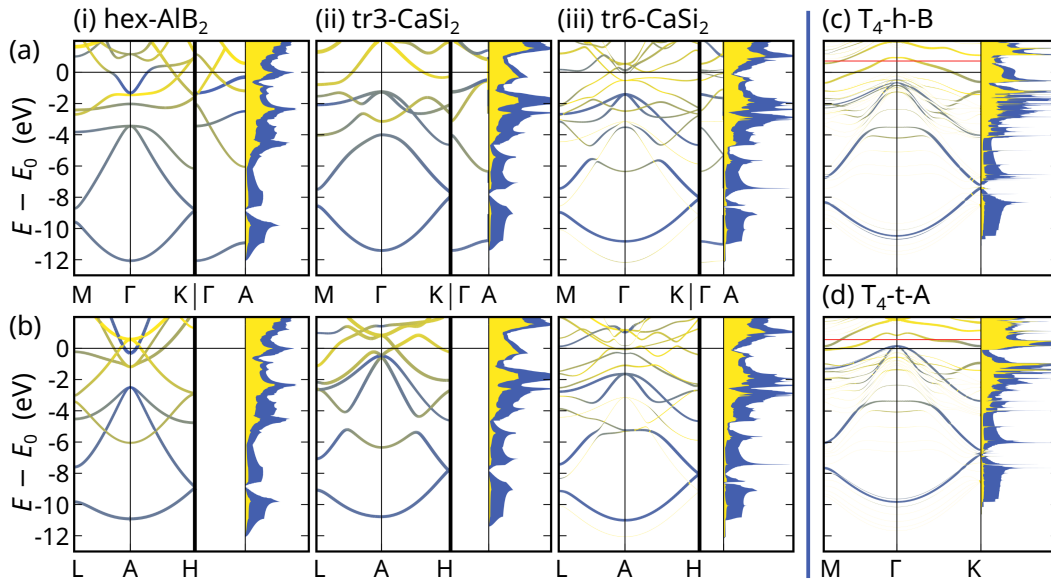


Figure 5.6: Band folding of the bulk TbSi₂ structures: (i) ort-AlB₂-TbSi₂, (ii) tr3-CaSi₂-TbSi₂, and (iii) tr6-CaSi₂-TbSi₂. The plotting mode is analogous to Fig. 4.9 (yellow → Tb, blue → Si). K-paths: (a) M– Γ –K| Γ –A; (b) L–A–H. The two Si atoms of the almost flat honeycomb in tr6-CaSi₂-TbSi₂ are suppressed. The bulk bands are reset by the Fermi level. The band structures of (c) T₄-h-B and (d) T₄-t-A are plotted in an analogous manner, considering only Tb, Si₁ and Si₂ (summed PAW projections → line width, Tb/Si portion → line colour). The slab bands are reset by the VBM of the bulk-Si bands and red horizontal lines indicate the Fermi levels.

qualitatively match. Also the O-shaped double band of Tb-d and Si- p_z character is clearly visible. However, the band widths of hex- $\text{AlB}_2\text{-TbSi}_2$ differ considerably from those of $\text{T}_4\text{-h-B}$. The Si valence bands range over ≈ 8 eV (too small by ≈ 2 eV) and the O-shaped double band ranges over ≈ 7 eV (too large by ≈ 2 eV). The L–A–H bands of $\text{tr}3\text{-CaSi}_2\text{-TbSi}_2$ (Fig. 5.6 (b,ii)) resemble the surface bands of $\text{T}_4\text{-h-B}$ much closer. Not only the band widths match, but also the shapes of the U and K bands. In particular, the latter show a gap at ≈ -5 eV due to hybridisation with the lower O band, which is missing in the bands of hex- $\text{AlB}_2\text{-TbSi}_2$. The upper O band is almost isolated, apart from gap closings at the Γ -point and along $\overline{\Gamma\text{K}}$. If these were relaxed, the upper O band would resemble that in $\text{T}_4\text{-t-A}$ quite closely, including the furrow at the Γ -point. The band structure of $\text{T}_4\text{-h-B}$ is derivable from the bulk bands without changing the band order. Interestingly, also the electron pocket at the M-point is present, an important feature missing in the bands of hex- $\text{AlB}_2\text{-TbSi}_2$.

Concerning the band structure of $\text{tr}6\text{-CaSi}_2\text{-TbSi}_2$, it has to be taken into account that the cell consists of two Tb layers, so one unit cell would be a quasi-double slice. Consequently, the surface band structure of a one-Tb-layer slice can be found in the middle of the Brillouin zone, not at the base. The focus is thus on the M– Γ –K path (Fig. 5.6 (a,iii)) instead of the L–A–H path. The bands are difficult to read because the Tb atoms hybridise with two types of Si honeycombs: a buckled one in egg-box position and a rather flat one in hole position. Although the plotting mode suppresses the contributions of the flat Si honeycomb, the respective Tb-Si hybrid states are still visible as yellow lines. If these are ignored, i.e. only blue and greenish bands are considered, several features become manifest: the U and K bands of the Si atoms having a gap and the correct shape, the O-shaped double band whose upper branch is deformed and dips into the Si valence bands, and the electron pocket at the M-point. However, the projected bands of $\text{tr}6\text{-CaSi}_2\text{-TbSi}_2$ do not agree better with the monolayers than the bands of $\text{tr}3\text{-CaSi}_2\text{-TbSi}_2$ do.

5.2.2 Charge transfer

The charge transfer in the $\text{T}_4\text{-h-B}$ structure is calculated analogously to pp. 68f and shown in Fig. 5.7. Panel (a) shows the averages over Si(111) planes, where red portions indicate electron gain and blue portions electron loss. Panel (b) shows tomographies of across three $(0\bar{1}1)$ -planes: the cuts through Si_1 , Si_2 and the Tb atom.

Fig. 5.7 (a) reveals that the plane-averaged charge transfer within the monolayer is much smaller than that within the substrate upon formation of the covalent bonds. The overall transfer into the covering Si honeycomb amounts to 0.01 electrons per surface unit cell, if the boundary is set to the middle plane between the Tb layer and the Si_2 layer. The tomographies give insight into the three-dimensional redistribution. Most of the contrast is due to the expected charge accumulation in the Si–Si intra-bonds. The Si atoms adjacent to the Tb atom (Si_2 and Si_3) show a pronounced charge bulb at their dangling p_z orbitals, whereas the charge above Si_1 is almost like that of the atomic state, as indicated by the faint colour. This leads to the conclusion that the Tb atom transfers charge only to the adjacent Si atoms, whereas all other Si

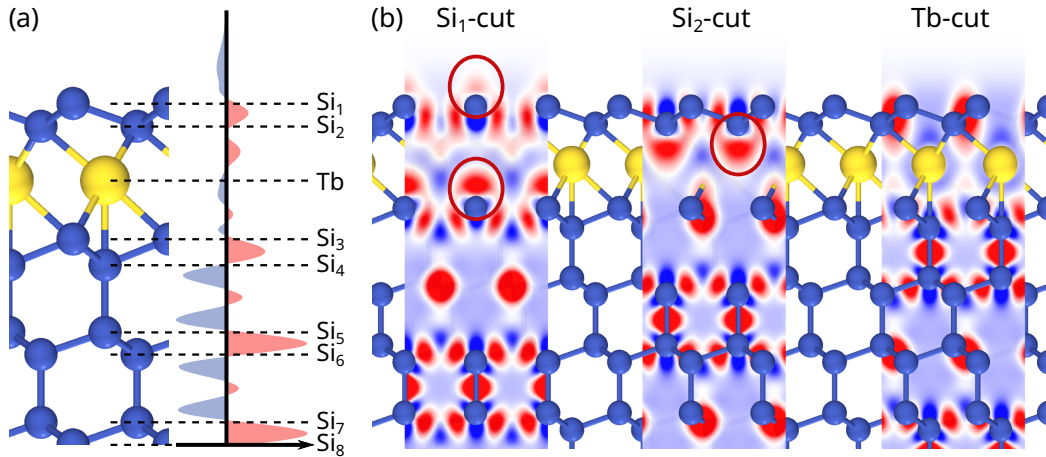


Figure 5.7: Charge transfer in T₄-h-B. Red → electron gain; Blue → electron loss. (a) average over (111)-planes; (b) tomographies across (011)-planes (parallel to a face of the surface unit cell in Fig. 5.1 (d), which is tilted away from the plane of projection by 30°). Red ellipses mark the charge bulbs of the Si atoms near the surface.

atoms do not accept additional charge. Since the charge bulbs of Si₂ and Si₃ clearly penetrate the Tb layer, the plane average suffers from false charge assignments, analogous to the problems discussed for the bulk TbSi_{2-x} structures (pp. 68f). A more sophisticated method would be worth applying on this system in order to correctly quantify the charge transfer.

5.2.3 Fermi surfaces

The analysis of the electronic properties concludes with the Fermi surfaces, which correspond to the k -resolved DOS at the Fermi energy E_F . They can thus be calculated from the DFT eigenvalues at a dense set of k -points with the following formula:

$$D_F(\mathbf{k}) = \sum_{n=1}^{N_{\text{Band}}} \delta(E_F - \varepsilon_n(\mathbf{k})) \quad (5.45)$$

The delta function is approximated as a Lorentzian with width of $\gamma = 0.1$ eV. The Fermi surfaces of different structure models may be found in Fig. 5.8. Looking very different from each other, they are a fingerprint for the respective structure. All Fermi surfaces show the hole-pocket of the upper O band at the Γ -point and the electron pockets of the conduction band at the M-points. They have different shapes and sizes, though, which is linked to the stability of the structures. The most stable T₄-h-B structure (Fig. 5.8 (a)) has the smallest pockets in accordance with the tendency to reduce the DOS at the Fermi level.

Experimentally measured Fermi surfaces exist for the monolayer-Tb@Si(111) system [52] as well as for the monolayer-Gd@Si(111) [47] and the monolayer-Dy@Si(111) [49] systems. Only the T₄-h-B structure reproduces the experimental reference almost

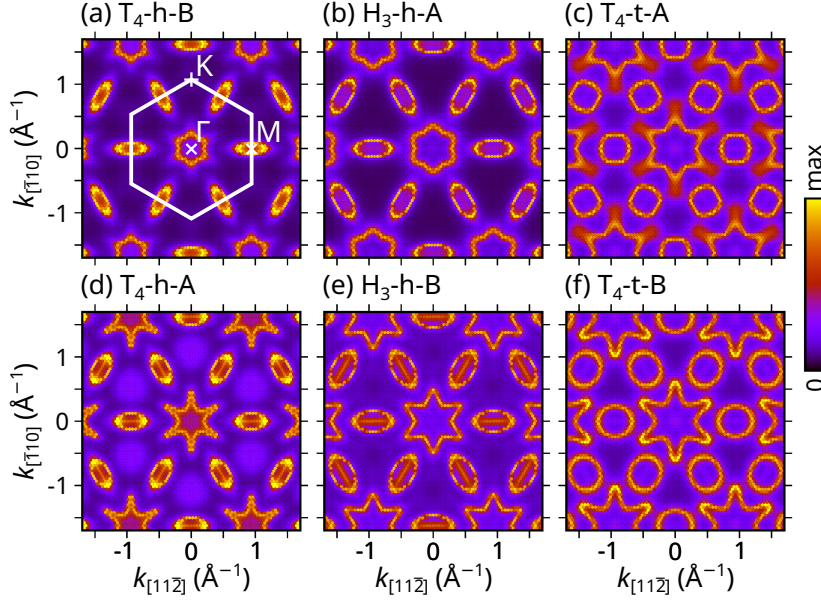


Figure 5.8: Fermi surfaces of the monolayer-Tb@Si(111) structures: (a) T_4 -h-B, (b) H_3 -h-A, (c) T_4 -t-A, (d) T_4 -h-A, (e) H_3 -h-B, (f) T_4 -t-B. The axes point into the crystallographic directions $[11\bar{2}]$ (x-axis) and $[\bar{1}10]$ (y-axis). The Brillouin zone is marked white in (a). The colouring corresponds to the colour bar on the right (a.u.).

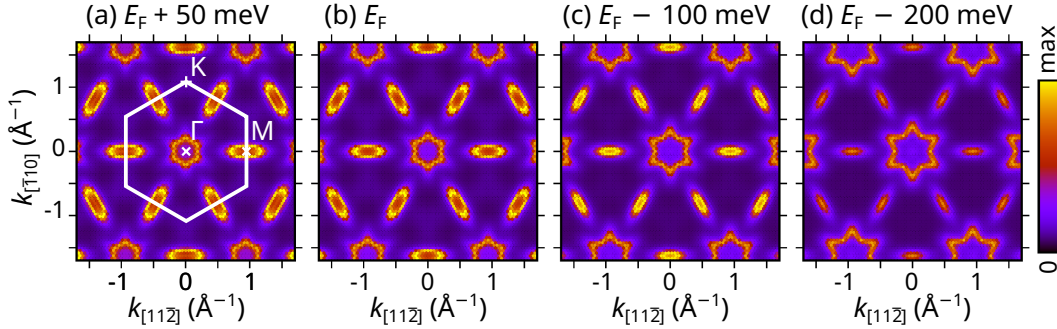


Figure 5.9: Energy surfaces of T_4 -h-B at different isoenergies: (a) $E = E_F + 50$ meV, (b) $E = E_F$, (c) $E = E_F - 100$ meV and (d) $E = E_F - 200$ meV.

perfectly. In particular the experimental Fermi surface of the monolayer-Dy@Si(111) system by Wanke et al. [49] looks like a copy of Fig. 5.8 (a), apart from the colouring. Beside the Fermi surface, Wanke et al. measured also a series of energy surfaces at different binding energies (0 meV, 100 meV and 200 meV). These measurements are simulated by inserting corresponding isoenergies in Eq. (5.45). The result (Fig. 5.9) shows that the electron pockets shrink to faint lines while the hole pocket grows and acuminates for increasing binding energies, exactly as in the respective images of Wanke et al. The theoretical energy surface at -50 meV binding energy (Fig. 5.9 (a)) worsens the agreement with the experiment. In detail, the ratio between the length of the electron pockets and the width of the hole pocket is greater than 1 in Fig. 5.9 (a), whereas it is nearly 1 in Fig. 5.9 (b) and in [49]. This leads to the conclusion that the Fermi levels of the simulated slab and the experiment are at the same position.

5.3 Discussion and summary

By means of a systematic inspection of the configuration space of reasonable structure models, the established T_4 -h-B model was found to be the most stable. Furthermore, all its peculiarities were explained. The inverse buckling direction of the covering Si honeycomb is due to a steric effect from the Tb-d orbitals, which clearly favour an octahedral Si coordination irrespectively of caps (>100 meV per surface unit cell). The preference of the Tb atoms to occupy the egg-carton positions of the substrate termination (T_4) and the hole positions of the cover (h-type) is based on two countercurrent effects. On the one hand, the egg-carton position enhances the bonding between the Tb layer and the respective Si honeycomb, which lowers the Fermi level. On the other hand, this weakens the intra-bonding of the Si honeycomb. In the case of the substrate termination, the second effect is compensated by the substrate in that the weakened in-plane states hybridise with the bulk. On the contrary, the vacuum above the cover negates such a compensation, so the t-type structures cannot profit from the Fermi level drop.

The band structures revealed that the Si atoms primarily bind to each other and the Tb atoms bind via their d-orbitals to the dangling bonds the Si honeycombs. This is remarkably analogous to the bulk $TbSi_{2-x}$ structures and accords with the ZKB concept. Moreover, the ZKB concept predicts a perfect charge balance in the monolayer structure as all valence electrons of the trivalent Tb atoms are compensated by the incomplete shells of Si_1 , Si_2 and Si_3 . The closed-shell configuration has already been noted by Stauffer et al. [39]. However, the strength of the ZKB concept in this case is that it explains in a comprehensible way why the monolayer lacks vacancies, contrarily to bulk $TbSi_2$. The Si_3 plane sharply separates the electronic states into two entities: All states below Si_3 (including the in-plane sp^3 -hybrid bonds of Si_3) are three-dimensional substrate states and all states above (including the vertical dangling bond of Si_3) are vertically confined to the thin $RESi_2$ monolayer. Therefore, the monolayer is a clearly two-dimensional (semi-)metal. The hole pocket at the Γ -point of the Fermi surface is due to hybrid states of out-of-plane Tb-d and Si_3-p_z . The electron pockets at the M-points are due to hybrid states of out-of-plane Tb-d, Si_1-p_z and Si_2-p_z . The band structures and the Fermi surfaces very well reproduce experimental ARPES images.

The structure analysis showed that the $TbSi_2$ monolayer is much more related with the $CaSi_2$ phases than with the AlB_2 phase concerning several morphological properties. Not only does the monolayer contain buckled honeycomb-Si instead of flat honeycomb-Si, but also the coordination polyhedrons are very similar to those of the $CaSi_2$ phases. The lattice matching underlines the relatedness as the bases of the $CaSi_2$ structures match the Si(111) surface very well, while that of hex- AlB_2 - $TbSi_2$ is considerably too large. In accordance with the structural relatedness, the surface band structure of T_4 -h-B can be derived surprisingly well from the bulk band structures of $CaSi_2$ - $RESi_2$ by means of a simple particle-in-a-box consideration. The respective projection of the hex- AlB_2 - $TbSi_2$ band structure disagrees with the former. The structural and electronic properties agree very well with experimental data. Therefore, the approach can be considered safe for the nanowire-Tb@Si(557) system, which is

the matter of the next chapter. Though, before treating these, the argument of strain-induced growth will be critically revised in the following section.

5.3.1 Strain induced growth?

Many previous works argued on the mechanisms which determine the structures of the monolayer- and multilayer-RE@Si(111) systems. The present findings that the monolayer-Tb@Si(111) structure resembles the CaSi₂-TbSi₂ structures much closer than the AlB₂-TbSi₂ structure is a novel point, which casts a different light on the previous, heuristic explanations. In order to appraise their validity, the main points of these explanations are summarised, in particular those stating that a strain release of the Si honeycomb leads to the morphological details.

Epitaxists often consider the lattice matching between the substrate and the layer to be grown so as to determine whether epitaxy is possible. If the lattice constants of the respective planes match, the layer can reach a high thickness without structural defects, and, otherwise, defect-free growth is limited. For the RE@Si(111) systems, the following points are taken into account:

- 1) The surface lattice constant of the unreconstructed, trigonal Si(111) surface is $a_{\text{Si(111)}}^{\text{Lit.}} = 3.841 \text{ \AA}$ [17, p. 1065].
- 2) The basis of the AlB₂ phase of RESi_{2-b} (RE ∈ [Y, Gd – Lu]) matches the Si(111) surface by the lattice constants, e.g. TbSi_{2-b}: $a_{\text{AlB}_2\text{-RESi}_{2-b}}^{\text{Lit.}} = 3.847 \text{ \AA}$ [33].
- 3) Hypothetical flat honeycomb-Si would have a lattice constant of 4.074 Å if it adopted the Si–Si bond distance of diamond-Si.

From 1) and 2), it follows that epitaxial growth of thick hex-AlB₂-RESi_{2-b} layers on Si(111) is possible.

While the growth of thick RESi_{2-b} layers can be embedded into simple geometrical considerations, major misunderstanding concerns the formation of the monolayer and thin-layer structures. Not few publications claim that the monolayer-RE@Si(111) system is a one-unit-cell slice of the bulk hex-AlB₂-RESi_{2-b} structure, which is attached to the Si(111) surface. Since the covering Si honeycomb lacks vacancies, they further argue that it buckles so as to release compressive strain exerted by the Si(111) surface, following 1) and 3). More venturesome explications concern the hex-AlB₂-RESi_{2-b} structure, which, inserted between the monolayer and the substrate, leads to multilayer-RE@Si(111) structures. Its Si layers supposedly contain vacant Si sites because they are squeezed into the surface lattice constant. Instead of buckling, they release strain by expelling every sixth Si atom so that the remaining Si atoms are allowed to increase their bond distances. These argumentations, to read e.g. in [38, 39] and from then inherited by subsequent publications, are problematic since they postulate that the AlB₂ prototype is an “ideal” structure and that buckling and vacancies are reconstructions or defects due to lattice mismatch. However, following this work so far, it is already clear that both the buckling and the vacancies are of chemical

nature and that mechanical strain is not the reason for their occurrence. The major mistake originates in the ignorance that $\text{AlB}_2\text{-RESi}_2$ incorporating flat, vacancy-free honeycomb-Si is per se highly unstable. In order to rectify the physical picture about the $\text{RE@Si}(111)$ systems, the findings on the monolayer- $\text{RE@Si}(111)$ and the bulk RESi_{2-x} structures are brought together into the following conclusive theory.

The trivalent RE atoms in the monolayer- $\text{RE@Si}(111)$ system each formally donate one electron to the dangling bonds of the substrate termination and the other two to a buckled, covering Si honeycomb. This structure is very convenient because, firstly, the Si shells are all closed and, secondly, the buckled Si honeycomb is similar to those composing the substrate. The reason for the buckling (sp^3 hybridisation) of the cover consists in the nature of Si to strongly avoid sp^2 hybridisation and in a better charge storage. This becomes manifest also in the high stability of $\text{CaSi}_2\text{-RESi}_2$ against $\text{AlB}_2\text{-RESi}_2$ (constrained RESi_2 stoichiometry). The multilayer structures can be derived from the monolayer in an inductive manner. As further investigated in [53], the (0001)-slices of bulk hex- $\text{AlB}_2\text{-RESi}_{2-b}$, comprising one RE layer and a vacancy-populated Si honeycomb, represent bulk building elements. Inserting these between the substrate and the lowermost RE layer of the precedent structure increases the thickness of the RESi_{2-x} film by one layer. The charge balance shows that the electrons donated by one RE layer are exactly compensated by the substrate and the vacancy-free, buckled covering Si honeycomb. Those of the other RE layers are compensated by the other, vacancy-populated, flat Si honeycombs to an extent of 8/9. Since the lateral lattice constants of the bulk building element and the $\text{Si}(111)$ substrate match, the stacking procedure can be repeated several times without running the risk of strain-induced stacking faults. The reason for the presence of Si vacancies is the same as that discussed for the bulk RESi_{2-x} structures, i.e. 1/6 vacancies increase the electron capacity of the Si honeycomb from 2 to 5/3 per RE atom.

In summary, the monolayer- and multiplay- $\text{RE@Si}(111)$ systems can be generalised to a stack of building elements. The top building element (RE layer + vacancy-free, buckled Si honeycomb) is always present and equals the monolayer if being the only one. The bulk building elements (RE layer + vacancy-populated, flat Si honeycomb) are facultative and increase the thickness of the RESi_{2-x} film, eventually rendering it bulk-like. The morphologies of both building elements are solely due to chemistry and independently match the $\text{Si}(111)$ surface. Consequently, the statement that surface-induced strain causes the buckling of the covering Si honeycomb or the presence of Si vacancies is incorrect.

6 Nanowires on silicon(557)

After the detailed analysis of the monolayer-Tb@Si(111) system, the next step consists in the investigation of the nanowire-Tb@Si(557) system. Derived from the Si(111) surface by inclination towards the (001) plane, Si($h\bar{h}k$) surfaces where $h < k$ provide Si(111)-like terraces which are separated by single Si(001)-like steps. The terrace width is controlled by the inclination angle in that smaller angles leads to wider terraces. If a Si($h\bar{h}k$) substrate is prepared with RE at a coverage of approximately one monolayer and successively annealed at a certain temperature, the monolayer-RESi₂ structure grows on the terraces, but is interrupted by the steps. In this manner, strips of monolayer-RESi₂ form by self-organisation and resemble nanowires from a structural point of view. Experimental investigations of the structural and electronic properties of nanowire-RE@Si($h\bar{h}k$) systems can be found for Tb [70], Dy [68, 69] and Er [68]. One of the key findings is that the electronic structure of densely covered terraces is similar to that of the monolayer-RE@Si(111) system. In particular, it is of two-dimensional character, in spite of the stripy morphology of the film.

This chapter covers the theoretical part of a joint-experimental-theoretical work on the nanowire-Tb@Si($h\bar{h}k$) system which goes a step further [P8]. It investigates how the electronic dimensionality of the system alters with the Tb coverage, subjected to the idea that lower coverages thin out the occupied terraces and separate the TbSi₂ strips by semiconducting barriers. While the above stepped film, the system of *dense nanowires*, is a two-dimensional electronic system, sparsely occupied terraces, the *sparse nanowires*, are expected to reduce the dimensionality of the individual strips so that they resemble a quasi-one-dimensional electronic system. Indeed, it turns out that separating the TbSi₂ strips by empty terraces induces anisotropy into the effective masses at the Fermi level, in accordance with the Heisenberg principle. In addition, a new state arises at the edge of TbSi₂ strips neighbouring an empty terrace. This edge state is of pure one-dimensional character and completely decoupled from the rest of the strip. The corresponding features in ARPES images are more pronounced, the narrower and thinner the nanowires are, as achieved by higher tilt angles and/or lower Tb coverages. Since the agreement between the experimental and theoretical findings is excellent, [P8] is a firm documentation of a fascinating and unique dimensional crossover.

In addition to the results already published in [P8], this chapter provides a deeper insight into the methodology and addresses the stability of the nanowire structures under certain thermodynamic conditions. Furthermore, it is proven that the band structures and Fermi surfaces of the nanowires can be derived from those of the monolayer-Tb@Si(111) system by means of a simple particle-in-a-box model. This highlights the differences between dense and sparse nanowires and illuminates the origin of the one-dimensional edge state.

6.1 Structure optimisation

Methodological details

The Si(557) substrate is modelled by tilted (5×1) (sketched in Fig. 6.1 (a)) and doubled (10×1) surface supercells of the Si(111) slab (Fig. 5.1 (a)). The slabs provide terraces having a widths of five projected surface lattice constants (“5a”), which are separated by Si(001)-like single steps. Similarly to the Si(111) slab, the Si(557) slab is twelve Si layers thick, out of which the lowest four are fixed in position to simulate the bulk of the substrate. The dangling bonds on the bottom side are saturated by H atoms, which assume their equilibrium positions for a symmetrically saturated slab (exactly that depicted in Fig. 6.1 (a)) and are then fixed in position for all further calculations. The periodic replica in the (557)-direction (the z-direction) are separated by 27 Å of vacuum, which reduces to 24 Å when the slab bears the nanowires.

Most computational parameters are equal to those of the monolayer-Tb@Si(111) calculations (p. 73). The Brillouin-zone sampling is adapted to the (5×1) supercell by a Γ -centred ($3 \times 15 \times 1$) Monkhorst-Pack mesh so that 15 k-points are placed along the wires and 3 k-points across. For the calculations of the (10×1) surfaces, the mesh is adapted to ($2 \times 20 \times 1$). A convergence test proves that increasing the sampling density alters the total energy by ≈ 1 meV per atom.

The dense nanowires

At first, the dense nanowires are analysed. For this purpose, the (5×1) slab is covered with monolayer-TbSi₂ so that each terrace bears a 5a wide strip. Since it is a priori not clear that the strips adopt the T₄-h-B structure as the monolayer does, two structure models are set up: the one derived from T₄-h-B (Fig. 6.1 (b)) and the other derived from H₃-h-A (Fig. 6.1 (c)). They are named after the corresponding monolayer structure, prefixed by the width, “5a” in this case. The H chemical potential is recalibrated with the symmetrically H-saturated slab according to Eq. (5.44).

The Tb chemical potential is calculated with Eq. (5.43) and determines the stability of the structure during the annealing stage, i.e. when the Tb coverage and the temperature are constant. The 5a-T₄-h-B structure yields $\mu_{\text{Tb}} = -327$ meV and the 5a-H₃-h-A structure $\mu_{\text{Tb}} = -53$ meV, so the former is more stable than the latter. The μ_{Tb} difference between the nanowire structure models (274 meV) is a bit higher than that between the respective monolayer structure models (232 meV). Concerning the geometric details of the optimised structure models, the mid of the TbSi₂ strip ranging from Tb₂ to Tb₄, resembles the respective monolayer structure (Tab. 5.1). In particular, the Si–Si bond lengths of the Si honeycombs adjacent to the Tb layer are similar to that of bulk Si and stretched if the Tb atom is in the egg-box position. Also the bond distances between the Tb atoms and the coordinating Si atoms accord with those of the respective monolayer structures, amounting to $\langle d_{\text{Tb}\{2,3,4\}\text{-Si}} \rangle \approx 3.0$ Å on average.

In contrast, the edges of the TbSi₂ strips near Tb₁ and Tb₅ are considerably distorted. The covering Si honeycomb at the left edge near Tb₅ is flattened and, interestingly, it adopts bond angles similar to the orthorhombically distorted Si honeycomb of the

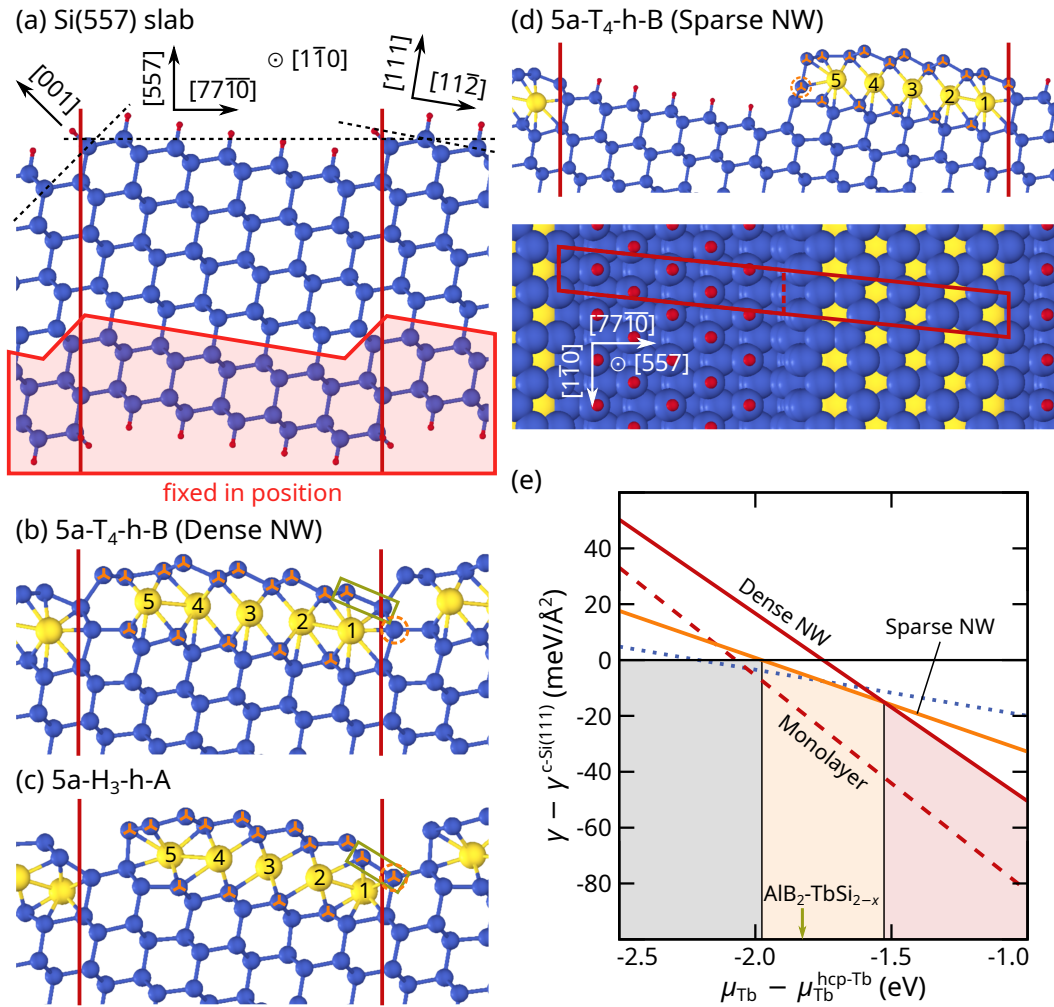


Figure 6.1: (a) Sketch of the Si(557) slab and (b) – (d) the optimised TbSi_2 nanowire structures. Blue circles are Si atoms; Yellow circles are Tb atoms; Red circles are H atoms. The light red polygon in (a) encircles the subset of atoms fixed in position during the relaxations. Red lines mark the unit cells. Orange M-stars in (b) – (d) indicate mutually threefold coordinated Si atoms near Tb. The green boxes and orange circles in (b) and (c) highlight the connection between the covering Si honeycomb and the step. The orange circle in (d) marks the stabilising Si atom. (e) shows the grand-potential-chemical-potential phase diagram of the $5a\text{-T}_4\text{-h-B}$ nanowire@Si(557) systems (solid, red \rightarrow dense, orange \rightarrow sparse). The $\text{T}_4\text{-h-B}$ monolayer@Si(111) system is inserted as well (dashed, red) as it will be used for explaining the details of the growth mechanism (vide infra). The dotted blue line sketches a hypothetical phase with lower Tb density. All $\gamma(\mu_{\text{Tb}})$ are reset to that of the clean Si(111) slab.

stoichiometric bulk $\text{ort-AlB}_2\text{-TbSi}_2$ structure, i.e. one angle is smaller and the other two are larger than 120° (Tab. 4.3). In both structure models, the Tb_5 edge is pinched in that the coordinating $\text{Tb}_5\text{-Si}$ bond distances are shorter than those in the mid of the strip ($\langle d_{\text{Tb}_5\text{-Si}} \rangle = 2.9 \text{ \AA}$). In the $5a\text{-H}_3\text{-h-A}$ structure, the other edge near Tb_1 is pinched as well ($\langle d_{\text{Tb}_1\text{-Si}} \rangle = 2.9 \text{ \AA}$), while in the $5a\text{-T}_4\text{-h-B}$ structure, it is similar to the mid of the strip ($\langle d_{\text{Tb}_1\text{-Si}} \rangle = 3.0 \text{ \AA}$). Whether the Tb_1 edge is pinched or not is clearly linked to how the covering Si honeycomb is connected to the step (green boxes in Fig. 6.1

(b) and (c)). In the 5a-T₄-h-B structure, the Tb atom lies in the same (1 $\bar{1}$ 0)-plane as the Si(001)-like Si bridge of the step. Hence, the first Si atom of the covering Si honeycomb lies in the adjacent (1 $\bar{1}$ 0)-plane and can bind to the twofold coordinated tip of the step (orange circle) in such a way that the tetrahedron of the latter completes. In particular, the beginning of the cover and the tip of the step remain distinct Si atoms. On the other hand, in the 5a-H₃-h-A structure, the Tb and Si planes of the cover are interchanged. Therefore, the tip of the step has to be the first atom of the covering Si honeycomb at the same time, so the Tb₁ edge is pinched. The different Tb₁ edges are the reason why the μ_{Tb} difference between the 5a-H₃-h-A and the 5a-T₄-h-B structure models is even larger than that between the respective monolayer structures. In other words, the geometry of the stepped Si(557) surface per se favours the T₄ position over the H₃ position.

The balance of the valence electrons is facilitated by orange M-stars marking mutually threefold coordinated Si atoms in the structure models in Fig. 6.1. In 5a-T₄-h-B, all 15 valence electrons from the 5 Tb atoms are absorbed by 15 Si acceptors, so all Si shells are closed. Although the same holds for 5a-H₃-h-A, there is an imbalance as the cover has 11 acceptors and the substrate termination 4, differently from the 2:1 ratio in the monolayer structures and the 5a-T₄-h-B nanowires.

The sparse nanowires

The next step consists in the investigation of the sparse nanowires, which are modelled on the doubled (10 × 1) slab providing two terraces per unit cell. Every second terrace is occupied by a nanowire strip, while the others are saturated by H atoms so as to remove artificial, metallic bands from the unreconstructed Si(111) planes. The following paragraphs deal only with nanowires of the 5a-T₄-h-B structure.

After emptying a terrace, a dangling bond remains at the covering Si honeycomb of the nanowire on the right. Such a structure would be unstable against hcp-Tb segregation ($\mu_{\text{Tb}} = +100$ meV) if not treated with an appropriate saturation. Therefore, a stabilising Si atom is added to the structure so that the cover can smoothly link to the Si bridge of the adjacent surface step. This lowers the Tb chemical potential to -135 meV. The relaxed structure model of the sparse nanowires is depicted in Fig. 6.1 (d), where the stabilising Si atom is marked by an orange circle. The averaged coordinating Tb–Si bond distances are equal to those in the dense nanowires for Tb₁ to Tb₄ ($\langle d_{\text{Tb}\{1,2,3,4\}\text{-Si}} \rangle \approx 3.0$ Å). The coordination polyhedron of Tb₅ has an average distance of 3.0 Å as well, so it is more voluminous than that of the dense nanowires. Hence, the Tb₅-edge pinching of the dense nanowires is absent in the sparse nanowires, which is advantageous. The balance of the valence electrons shows that the sparse nanowires have 5 Si acceptors in the substrate termination, similarly to the dense ones. However, the cover has 12 Si acceptors and thus two in excess.

The phase diagram

Obviously, given a fixed number of Tb atoms, the dense arrangement of nanowires is more advantageous than the sparse one as the Tb chemical potential of the former

is smaller than that of the latter (-327 meV vs. -135 meV). However, the thermodynamic boundary condition of a constant Tb coverage is an idealised situation in which the mobility of the Tb atoms on the substrate is infinitely high during the annealing stage. Therefore, also the converse situation is considered, in which the Tb atoms are in equilibrium with an infinite reservoir which fixes μ_{Tb} . This is described by a thermodynamical potential $\Omega(V, T, \mu_{\bullet})$ which results from the Legendre transformation of the free energy with respect to the number of atoms of all species \bullet .

$$\Omega(V, T, \mu_{\bullet}) = F(V, T, N_{\bullet}) - \sum_{\bullet} \mu_{\bullet} N_{\bullet} \quad (6.46)$$

$\Omega(V, T, \mu_{\bullet})$ is also referred to as the grand potential. Dividing by V makes this quantity intensive and returns the mechanical tension p according to Euler's theorem.

$$p(T, \mu_{\bullet}) = \frac{1}{V} \Omega(V, T, \mu_{\bullet}) \quad (6.47)$$

The potential has to be adapted to the reduced dimensionality of surfaces by replacing the volume V with the surface area A and changing the symbol p to γ . Inserting the bulk Si chemical potential and neglecting the lattice dynamics returns the following ready-to-use form:

$$\gamma(T, \mu_{\bullet}) \approx \frac{1}{A} \left(E_{\text{DFT}}^{\text{cell}} - \mu_{\text{Si}}^{\text{d-Si}} N_{\text{Si}} - \mu_{\text{H}}^{\text{bot}} N_{\text{H}}^{\text{bot}} - \mu_{\text{H}}^{\text{top}} N_{\text{H}}^{\text{top}} - \mu_{\text{Tb}} N_{\text{Tb}} \right) - \gamma^{\text{c-Si(111)}} \quad (6.48)$$

The discrimination between the H atoms of the bottom and the top side of the slab is necessary because they play a different role. Setting $\mu_{\text{H}}^{\text{bot}}$ to $\mu_{\text{H}}^{\text{H-sat}}$ (vide supra) guarantees the cancellation of any effects from the bottom side. The H atoms of the top side, only present in the sparse nanowires, have a more physical meaning as they interact with the TbSi_2 strips. If their chemical potential was set to $\mu_{\text{H}}^{\text{H-sat}}$, i.e. if the H availability was so high that the empty Si terraces completely saturate, the slab carrying the sparse nanowires would be highly preferable due to the H-saturated terraces, irrespectively of the (in-)stability of the TbSi_2 strips. Though, this situation contradicts the experiment because much effort is made to remove as much H from the vacuum chamber as possible. Thus, the H atoms of the top side deserve a separate H chemical potential $\mu_{\text{H}}^{\text{top}}$. As they sit solely on the vertical dangling bonds of the Si(111)-like terraces, $\mu_{\text{H}}^{\text{top}}$ is gauged in such a way that the top side of the H-saturated Si(557) slab is in chemical equilibrium with the clean Si(111) surface. This approximates that the availability of H is so small that the empty terraces remain clean.

Of course, the grand potential γ has to be referred to a reference system, which is chosen to be the clean Si(111) surface ($\gamma^{\text{c-Si(111)}}$) or, equivalently, the unsaturated Si(557) surface, ascertained by the gauge of $\mu_{\text{H}}^{\text{top}}$. Since the Tb chemical potential μ_{Tb} is unknown, it has to be treated as a variable. $\gamma(\mu_{\text{Tb}})$ then becomes a linear function, which can be plotted into phase diagrams. In doing so, the abscissa μ_{Tb} tunes the experimental situation: higher and lower values for μ_{Tb} correspond to Tb-rich and Tb-poor conditions, respectively. The slope of $\gamma(\mu_{\text{Tb}})$ equals the areal Tb density N_{Tb}/A . Consequently, phases with high Tb densities have steeper lines and are principally favoured for Tb-rich conditions, and vice versa. By means of the phase

diagrams, structure models with different Tb densities become comparable. The stability at a certain μ_{Tb} given by those which minimise $\gamma(\mu_{\text{Tb}})$ ¹.

Fig. 6.1 (e) shows the phase diagram of the sparse nanowires and the dense nanowires on Si(557) and the T_4 -h-B monolayer on Si(111), denoted simply *monolayer* in the following paragraphs. The domain of $\gamma(\mu_{\text{Tb}})$ is confined to Tb chemical potentials smaller than that of hcp-Tb since higher values would precipitate elemental Tb. The abscissa is reset by $\mu_{\text{Tb}}^{\text{hcp-Tb}}$ so that the domain is $\mu_{\text{Tb}} < 0$. Concentrating on the solid lines (red \rightarrow dense NW, orange \rightarrow sparse NW and black \rightarrow clean Si(111) / clean Si(557)), there are stability regions for each phase, which are shaded in the respective colour. Very small values for μ_{Tb} make the Si substrate remain clean in the sense that neither the sparse nor the dense nanowires form. Above ≈ -2.0 eV, the sparse nanowires are stable, superseded by the dense nanowires at ≈ -1.5 eV. Of course, the phase diagram is incomplete. There are probably other phases which are more stable on certain regions, e.g. sparse nanowires in which the TbSi_2 strips are separated by more than one empty terrace. An exemplary pathway of such a phase is sketched in the phase diagram as a dotted blue line. Although not checked by calculation, these phases would match the expectable trend that lower μ_{Tb} results in sparser nanowires. In the other limit, there are nanowires of heights corresponding to more than one monolayer which become stable at high μ_{Tb} . For very high μ_{Tb} , a thick film assuming the $\text{hex-AlB}_2\text{-TbSi}_{2-b}$ structure would cover the substrate (vide supra, Sec. 5.3.1), which manifests itself as a vertical line at $\mu_{\text{Tb}} = \mu_{\text{Tb}}^{\text{hex-AlB}_2\text{-TbSi}_{2-b}}$ in the phase diagram. A green arrow marks the position in Fig. 6.1 (e), employing the value of the approximated bulk structure (-1.827 eV, Tab. 4.6). At first glance, this would imply that dense nanowires would not occur at all. However, the thick film is kinetically hindered as the Tb deposition is limited by experimental controlling and because the Tb atoms are not infinitely mobile. That the silicide aggregation is locally and temporally limited effectively constrains the height of the structures, one layer in this case.

The phase diagram moreover reveals that the monolayer on Si(111) is considerably more stable than the dense nanowires on Si(557). In terms of a constant Tb amount, the difference between the Tb chemical potentials of the monolayer and the dense nanowires amounts to: $-806 \text{ meV} + 327 \text{ meV} = -479 \text{ meV}$. The nanowire formation is thus solely due to presence of the steps of the Si(*hkh*) surface, which hinder the formation of a smooth monolayer. A second consequence of the high stability of the monolayer with respect to the dense nanowires is that surfaces with wider terraces and hence wider nanowires should be more stable than those with narrow terraces. For a fixed tilt angle, a substrate can widen its terraces by step bunching, i.e. the

¹The main difference between the grand potential in Eq. (6.48) and the Tb chemical potential in Eq. (5.43) consists in the change of the thermodynamic boundary conditions from the constancy of the Tb amount N_{Tb} and the surface tension γ to the constancy of the Tb chemical potential μ_{Tb} and the surface area A . In experimental terms, this corresponds to switching from the annealing stage, where an infinite substrate with a fixed Tb coverage is held at constant temperature, to the deposition stage, where a substrate of fixed area is exposed to vaporised Tb, the chemical potential of which is controlled by the pressure of the Tb vapour. According to the Gibbs-Duhem relation, increasing the pressure at constant temperature generally increases the chemical potential of a single-species thermodynamic subsystem.

formation of double or triple steps to the benefit of the terrace widths. The formation of nanowires which are wider than the terraces of the single-stepped surface ($>18 \text{ \AA}$ for Si(557)) is indeed observed in the experiment, in particular, if nanowire samples are “cleaned” and reused [P8, 70].

6.2 Electronic properties

6.2.1 Band structures

The band structures are calculated analogously to Sec. 5.2. Since the nanowires are embedded in tilted supercells of the hexagonal (1×1) -Si(111) surface unit cell, the supercell Brillouin zones (sBZs) of the nanowires are folded versions of the primitive Brillouin zone (pBZ) of the monolayer. In order to make the band structures comparable, the Γ -point, K-points and M-points of the pBZ are identified in the sBZs. However, it is impossible to find an exact mapping because the Si(557) and Si(111) surfaces are tilted against each other by 9.4° and the steps misalign the (557)-projected (1×1) building elements of the terraces. Therefore, the M- and K-points of the pBZ are approximately addressed by their Cartesian coordinates in the sBZs, although they are not high-symmetry points in the latter. The band structures are calculated along two k-paths: $\overline{\Gamma K}$ parallel to the nanowires (x-direction) and $\overline{\Gamma M}$ perpendicular to the nanowires (y-direction). The points where the paths cross the boundaries of the sBZs are labelled X and Y, respectively. Approximate sketches of the sBZs may be found in Fig. 6.2 (c,iv). Accurate DOS calculations are carried out on dense Γ -centred $(40 \times 8 \times 1)$ and $(40 \times 4 \times 1)$ meshes for the dense and sparse nanowires, respectively. Fig. 6.2 shows the band structures of (a) the dense nanowires, (b) the sparse nanowires and (c) the monolayer. The line width corresponds to the portions of (i) all Tb atoms, (ii) all Si atoms of the cover (Si₁ and Si₂ in the monolayer), (iii) all top Si atoms of the substrate termination (Si₃ in the monolayer) and (iv) bulk-Si in the PAW projections. The line colour is fixed in panels (ii) – (iv). In panel (i), it indicates the Tb₅ portion in the PAW projections of all Tb atoms according to the colour bar. The energies are reset by the respective bulk VBMs E_0 . The Fermi level of the slab is inserted as a red horizontal line.

Before the analysis can start, the band folding between Si(111) and Si(557) has to be elaborated in more detail since the Si(557) supercells and the (1×1) -Si(111) unit cell are incommensurable. It proves to be helpful to consider the unit cell of the dense/sparse nanowires a $(6 \times 1)/(12 \times 1)$ supercell of the (1×1) unit cell of the terraces. The increment of the symbolic notations $(5 \times 1)/(10 \times 1)$ stems from the steps, which approximately add a $1a$ advance to the $5a$ wide terraces. The new reconstruction symbols suggest that the $\overline{\Gamma M}$ path contains the $\overline{\Gamma Y}$ path six and twelve times, respectively. The band structures in Fig. 6.2 (a) and (b) confirm this by the periodic features along $\overline{\Gamma M}$ having period lengths of $1/3$ and $1/6$, respectively. Conversely, the substrate bands along the Si(557)- $\overline{\Gamma Y}$ path are a superposition of respectively six and twelve differently shifted images of the bands along the Si(111)- $\overline{\Gamma M}$ path. As a consequence, the substrate bands along $\overline{\Gamma M}$ in Fig. 6.2 (a) and (b) are horizontally

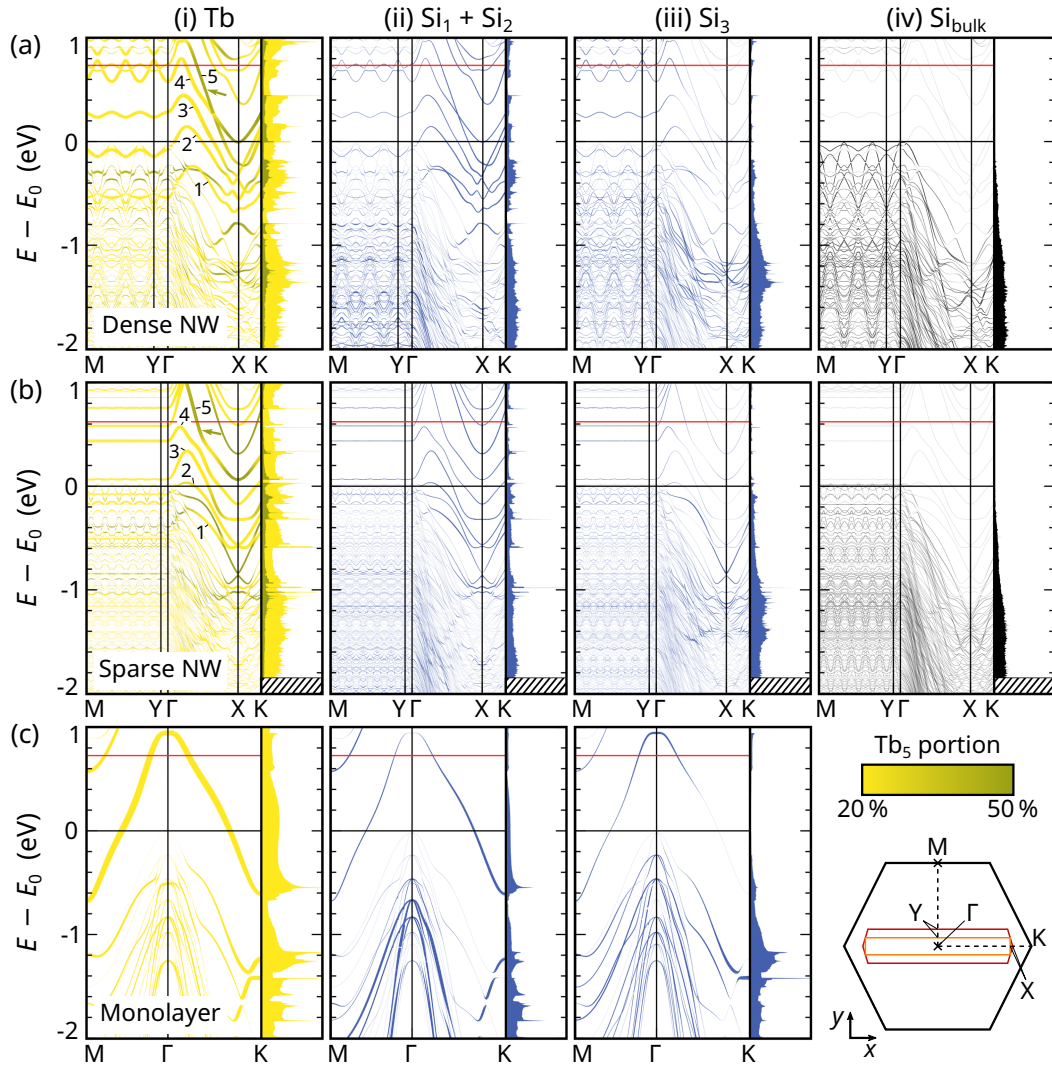


Figure 6.2: Band structures of (a) dense and (b) sparse nanowires on Si(557) and (c) the monolayer on Si(111) (all based on the T_4 -h-B structure). The line width corresponds to the PAW projections of (i) the Tb atoms, (ii) the Si atoms of the cover, (iii) the top Si atoms of the substrate termination, and (iv) bulk-Si. All projections are normalised by the number of atoms of the respective group. The line colour in (i) indicates the portion of Tb_5 in all Tb projections according to the colour bar: yellow \rightarrow 20%, green \rightarrow 50%. All energies are reset by the VBM of the bulk-Si bands. The red horizontal lines indicate the Fermi levels of the slabs. (c,iv) Brillouin zones: black \rightarrow ML on (1×1) -Si(111), red \rightarrow dense NW on (5×1) -Si(557), orange \rightarrow sparse NW on (10×1) -Si(557).

blurred, particularly in the case of the dense nanowires. On the contrary, the perpendicular Si(557)- $\bar{\Gamma}\bar{K}$ direction shows projections of bands along different, equidistant lines parallel to Si(111)- $\bar{\Gamma}\bar{K}$. After reduction by time-reversal symmetry, the multiplicity is $6/2 + 1 = 4$ for the dense and $12/2 + 1 = 7$ for the sparse nanowires. As a result, the substrate bands along $\bar{\Gamma}\bar{K}$ in Fig. 6.2 (a) and (b) are vertically diffuse and, thus, still distinguishable, in contrast to those along $\bar{\Gamma}\bar{M}$.

The bands related to the nanowires, of which the Tb bands are the most important, look different from the substrate bands. For both the dense and the sparse nanowires, they include five prominent, thick Tb bands, enumerated in Fig. 6.2 (a,i) and (b,i). Along $\overline{\Gamma K}$ (parallel to the nanowires) they point downwards with a steepness similar to that of the upper O band of the monolayer. Near the Γ -point and the K-point, they bend oppositely, so they resemble each an inverted S. Along $\overline{\Gamma M}$ (perpendicular to the nanowires) each Tb band is confined into a narrow energy range. Therein, the dense and the sparse nanowires show an important difference: While the Tb bands of the former are still wavy with strong dispersion, those of the latter are strictly flat and, hence, completely localised in that direction. All thick Tb bands are hybridised with the covering Si honeycomb on the entire Brillouin zone and with the substrate termination near the Γ -point, which is remarkably similar to the upper O band of the monolayer. While the projections of the four lowest thick Tb bands are distributed over all Tb atoms, the topmost band 5 majorly belongs to Tb_5 at the open edge of the $TbSi_2$ strips. Beside this band, there are further Tb_5 -associated bands at higher binding energies. They are thinner than band 5 and complemented by PAW projections of the adjacent Si atoms, thus indicating strong Tb–Si hybridisation.

Relation to the monolayer Tb@Si(111) system

The analogy between the Tb bands of the nanowires and the upper O band of the monolayer suggests that the former may possibly be related to the latter by projection. However, ordinary folding considerations like those above hold only for delocalised states, e.g. the substrate bands. For the bands related to the nanowires, it has to be taken into account that the $TbSi_2$ strips extend to five projected (1×1) surface lattice constants per terrace, while the sixth is the step. Therefore, it is likely that the nanowire states originate in the monolayer states by (partial) localisation perpendicular to the growth direction, i.e. by mixing countercurrent monolayer states with wave vectors \mathbf{k} and $-\mathbf{k}$ to form standing waves. In order to test this, the hexagonal Brillouin zone of the monolayer is segmented by equidistant parallel translations of the $\overline{\Gamma K}$ path. Beginning at the x-axis, the path is shifted in the y-direction until it reaches the edge of the Brillouin zone defined by \overline{KMK} . As the path crosses the zone

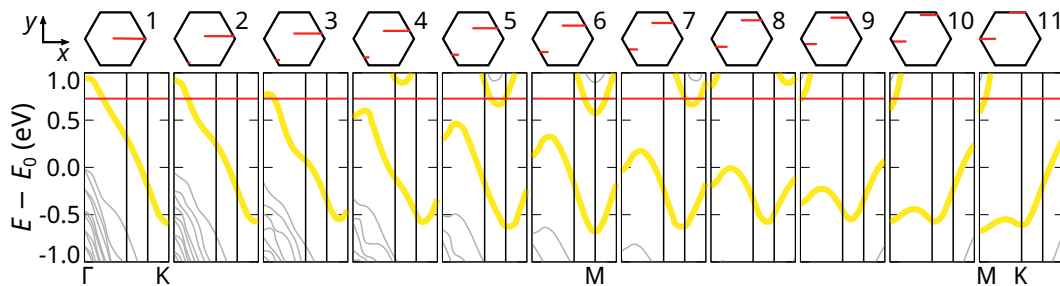


Figure 6.3: Segmentation of the Brillouin zone of the monolayer. The band structure is plotted along eleven equidistant paths parallel to $\overline{\Gamma K}$, the sketches of which are shown above the plots (red lines). The upper O band and the electron pocket, both associated with Tb, are highlighted thick and yellow. All energies are reset to the VBM of bulk-Si. The red horizontal lines indicate the Fermi level.

boundary, it reappears in the lower half of the Brillouin zone after zone reduction. The bands along 11 segments are plotted in Fig. 6.3 and the Brillouin zones with the k-paths may be found above the respective panels. The upper O band and the conduction band forming the M-point electron pocket are highlighted thick and yellow. From $\bar{\Gamma}\bar{K}$ to $\bar{M}\bar{K}^+$, the upper O band turns into an S shape similar to the Tb bands of the nanowires. The band width decreases. If the path approaches an M-point, the electron pocket appears (segments 6 and 11 in Fig. 6.3).

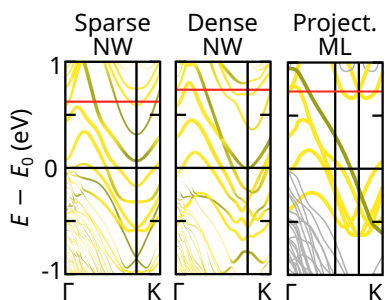


Figure 6.4: Band structures of the nanowires and projected bands of the monolayer.

Fig. 6.4 shows an overlay of the equidistant segments 1, 3, 5, 7 and 9 (right panel) and compares it with the $\bar{\Gamma}\bar{K}$ part of the band structures of the dense nanowires (middle panel) and the sparse nanowires (left panel), taken from Fig. 6.2 (a,i) and (b,i). The right and middle panels look very similar to each other. The lowest four Tb bands of the dense nanowires follow the segments 3, 5, 7 and 9 of the upper O band almost congruently, merely differing by smaller shifts. Segment 1, the topmost band (coloured green in Fig. 6.4), undergoes more shifting and rehybridisation to become the Tb₅ band of the dense

nanowires. Hence, the band structure of the dense nanowires is related to that of the monolayer by a simple zone projection in large part. It is astonishing that the discontinuities from the steps only slightly affect the intercoupling between adjacent Tb strains, even at the edges of the TbSi₂ strips. The close electronic relatedness between the dense nanowires and the monolayer proves that the former are a two-dimensional electronic system, in spite of the stripy structure.

The situation is different for the sparse nanowires (left panel). The bands related to the inner Tb atoms are shifted to higher binding energies compared to the dense nanowires and the monolayer projection, but they retain their morphology. Thus, they are still subjected to the physics of the monolayer, concerning the intercoupling of the Tb strains. However, the total localisation perpendicular to the nanowires (vide supra) shows that these states are genuine standing waves in that direction. Consequently, the TbSi₂ strip can be considered a quantum well derived from the TbSi₂ monolayer. In contrast to the inner states, the green Tb₅ band rehybridises so strongly that it completely loses the comparability with segment 1 of the monolayer. In other words, it represents a new state which cannot be derived from the monolayer any more. Because of its localisation at Tb₅, it can be considered an edge state and, thus, resembles a one-dimensional system within the sparse nanowires.

6.2.2 Fermi surfaces

The hypotheses on the dimensionality of the sparse and the dense nanowires are tested by means of the Fermi surfaces, which are calculated analogously to Sec. 5.2.3. Fig. 6.5 shows the Fermi surfaces of the monolayer and the nanowires. The Fermi level of the sparse nanowires is aligned to that of the dense nanowires (+0.1 eV).

The Fermi surface of the dense nanowires has stripy features, which are clearly linked to a folding procedure from the hexagonal pBZ into the smaller sBZ, marked white in Fig. 6.5 (a) and (b). Following the light blue dashed lines, the electron pockets at the M-points generate the thin, bright stripe at the Γ -point as well as the broad, weak stripes at the X-point. The thin, weak lines accompanying the middle bright stripe (indicated by a light green arrow) stem from the points of the star-shaped hole pocket, as clarified by the light green dashed line. These lines are the Fermi breakthroughs of band 5 (green arrow in Fig. 6.2 (a,i)). The relationship between them and the hole pocket agrees with the above observation that band 5 originates from the upper O band of the monolayer. Since all features are wavy or corrugated in the (vicinal) $[11\bar{2}]$ direction (perpendicular to the nanowires), the Fermi surface of the dense nanowires has a two-dimensional character. At first glance, the Fermi surface of the sparse nanowires looks similar to that of the dense nanowires. The major difference consists in a lack of corrugation, so all stripes are straight. Also the lines related to band 5 straighten (green arrow), so they are completely separated from the other stripes. Hence, these states gain a purely one-dimensional character, confirming the results from the band structure analysis.

In Fermi surface measurements, the electrons expelled from the sample carry a parallel momentum equal to the crystal momentum of the initial state. However, the latter does not accord with the multiply reduced zone scheme of the supercells, but with the Brillouin zone of the local periodicity of the primitive building elements, the (1×1) -Si(111) terraces in the case. The Fermi surface in the reduced zone scheme of any supercell can be *unfolded* into the extended zone scheme by weighting the k -resolved DOS (Eq. (5.45)) with the Fourier components of the wave functions and integrating it over the sBZ. In a second step, the unfolded Fermi surface can be folded back into the pBZ [124]. In detail, the unfolded Fermi surface in terms of the primitive Brillouin zone $D_F^{\text{pBZ}}(\mathbf{k})$ holds:

$$D_F^{\text{pBZ}}(\mathbf{k}) = \sum_{n=1}^{N_{\text{Band}}} \int_{\text{sBZ}} d\mathbf{K} W_{n\mathbf{k}\mathbf{K}} \delta(E_F - \varepsilon_n(\mathbf{K})) \quad (6.49)$$

$$\mathbf{K} \in \text{sBZ}, \mathbf{k} \in \text{pBZ}, \quad W_{n\mathbf{k}\mathbf{K}} = \sum_{\mathbf{g}} \sum_{\mathbf{G}} \delta(\mathbf{K} + \mathbf{G} - (\mathbf{k} + \mathbf{g})) |u_{n\mathbf{G}}(\mathbf{K})|^2$$

where \mathbf{K} and \mathbf{k} are the k -vectors of the sBZ and pBZ, respectively, \mathbf{G} and \mathbf{g} are the direct lattice vectors of the supercell and the primitive unit cell, respectively, and $u_{n\mathbf{G}}(\mathbf{K})$ are the Bloch factors of the supercell (Eq. (2.27)). In practice, this procedure works only if the super lattice vectors are linear combinations of the primitive ones with integral coefficients. Therefore, the above Fermi surface of the dense nanowires cannot be unfolded into the (1×1) Brillouin zone since the terraces advance by half a period in the parallel direction when passing a step. This issue could be resolved by calculating the dense nanowires in a doubled (10×1) supercell, which is not done in this work, though.

The sparse nanowires, on the other hand, are already modelled in a (10×1) supercell. Their unfolded Fermi surface is plotted in Fig. 6.5 (c). The unfolding procedure recovers the M-point electron pockets from the thin stripe though the Γ -point and the

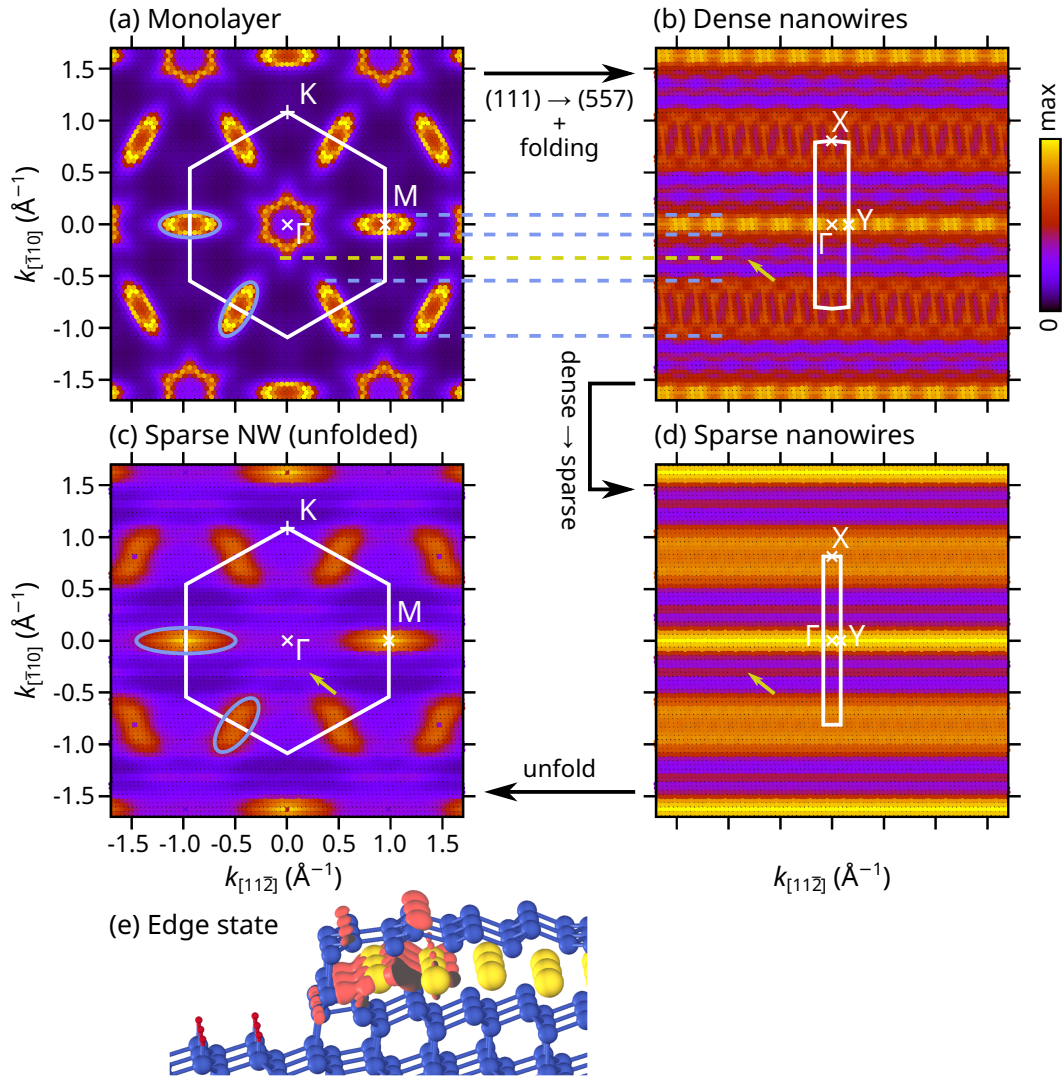


Figure 6.5: Fermi surfaces of the Tb@Si(hkh) systems: (a) monolayer, (b) dense nanowires, (c) and (d) sparse nanowires (all based on T_4 -h-B). The axes point into the directions $[11\bar{2}]$ (parallel to the NW, vicinal for NW) and $[\bar{1}10]$ (perpendicular to the NW). (c) is derived from (d) by unfolding the sBZ to the local hexagonal pBZ of the Si(111) terraces. The Brillouin zones are marked white. The colouring corresponds to the colour bar (arbitrary units, the ranges are comparable for (b), (c) and (d), but not linked to that of (a)). Ellipses highlight the electron pockets at the M-point. Green arrows indicate the new edge state. Dashed lines are guides for the eyes. (e) Real-space distribution of the edge state. Reproduced from [P8].

broad stripes through the X-points. However, the pocket shapes differ from those of the monolayer: The two horizontal pockets have a considerably stretched aspect ratio, which indicates higher effective masses perpendicular to the nanowires. Also the electron pockets at the other four M-points are stretched and effectively rotate away from the growth direction of the nanowires. Both effects indicate that the electronic mobility perpendicular to the nanowires decreases. In contrast to the electron pockets, the hole pocket is not recovered. Instead, the state linked to band 5 embraces the

region around Γ as two straight lines (green arrow). This confirms the above findings that the band-5 state has undergone so many changes that the relationship with the Tb states of the monolayer is lost. In order to clarify that this state is indeed an edge state, as inferred from the PAW projections, the corresponding real-space partial charge at the Fermi level is plotted as isosurfaces in Fig. 6.5 (e). Confirming all expectations, this state is strongly confined to a narrow channel near Tb₅.

6.3 Discussion and summary

The nanowire-Tb@Si(557) surface provided the opportunity to explore a fascinating lower-dimensional quantum system. The terraces of the substrate are indeed a template for a stripped TbSi₂ film which resembles nanowires from a structural point of view. The strips follow the stability relations of the monolayer-Tb@Si(111) film in that they locally adopt the T₄-h-B structure. Only the edges of the strips are subjected to distortions. The geometric relations between the Si(001)-like steps and the Si(111)-like terraces was shown to be very convenient for the T₄-h-B structure since the TbSi₂ strip can connect with the broken sp³ bonds of the step. This may be the reason why these types of TbSi₂ nanowires grow only on Si(*h**h**k*) surfaces where $h < k$ [70]. The phase diagram simulating the deposition stage proved that the density of terraces bearing a TbSi₂ strip is smaller/higher for Tb-poor/Tb-rich conditions. It furthermore hints that step-bunching leading to wider TbSi₂ strips is favourable. As far as visible from experimental STM images [P8], the narrow $5a$ wide TbSi₂ strips do occur in Tb@Si(557), but the surface is dominated by wider strips. TbSi₂ nanowires on step-bunched surfaces are certainly worth investigating in future work.

The dense nanowires are a two-dimensional electronic system, irrespectively of the discontinuities from the steps. Their band structures and Fermi surfaces can be derived from the monolayer by a simple zone projection. The electronic relatedness between the dense nanowires and the monolayer agrees with experimental ARPES and Fermi surface measurements [P8]. The sparse nanowires differ very much from the dense nanowires regarding the electronic properties. The states associated with the inner Tb atoms become genuine standing waves according to a simple particle-in-a-box model. In other words, the isolated TbSi₂ strips act as a quantum wells which laterally trap the electrons. In doing so, the coupling within the strips remains unaffected. The effective masses of the electron pockets agree with the Heisenberg principle: The lateral confinement of the positions broadens the lateral crystal momenta in the Fermi surface. Very similar effects were also observed in the experiment [P8]. In contrast, the edge of each isolated strip gives rise to an edge state which cannot be derived from the monolayer states. This state is laterally confined to a narrow region around the outermost Tb atom and has a clear one-dimensional character, as proven by the unfolded Fermi surface. The edge state was also observed in the measurements on the nanowire-Tb@Si(335) system [P8], whose terrace widths correspond to the Si(557) substrate of this work (step bunching). In conclusion, the Tb@Si(557) surface permits the observation of a fascinating dimensional crossover from a two-dimensional film to a system of quasi-one-dimensional nanowires.

Part II: Thin antimony layers on bismuth selenide

The discovery of topological order in solid-state physics was the door opener for a new class of materials whose state underlies the mathematical concept of topology. Topologically non-trivial materials are band insulators with intrinsic properties which are linked to the topological nature of the electronic wavefunctions. These special properties show an exceptionally high stability against many perturbations since topological non-triviality is much stronger than a plain symmetry protection.

The research of topology in materials science began in the 1980s when von Klitzing et al. discovered the integer Hall effect (IHE) in the two-dimensional electron gas of MOSFETs [125]. Their work was the first documentation of topological order in a solid-state system. Because of the topological non-triviality, the IHE is insensitive to deviations from the idealised assumption of a homogeneous, two-dimensional electron gas. Hence, it even works in the presence of impurities, the finiteness of the sample and electron-electron interaction [126]. Topologically ordered solids soon attracted the attention of the condensed-matter community, who had a great deal of work published on different systems. In doing so, several types of topological order were discovered, which are based on different topological invariants. The research was so groundbreaking that it was awarded with three Nobel Prizes [W4]:

- Klaus von Klitzing “for the discovery of the quantized Hall effect” (1985)
- Robert B. Laughlin, Horst L. Störmer and Daniel C. Tsui “for their discovery of a new form of quantum fluid with fractionally charged excitations” (1998)
- David J. Thouless, F. Duncan M. Haldane and J. Michael Kosterlitz “for theoretical discoveries of topological phase transitions and topological phases of matter” (2016)

As von Klitzing pointed out in his Nobel Prize Lecture, nobody expected at that time that semiconductor physics could produce any fundamental discoveries:

Semiconductor research and the Nobel Prize in physics seem to be contradictory, since one may come to the conclusion that a complicated system like a semiconductor is not useful for very fundamental discoveries. Indeed, most of the experimental data in solid-state physics are analyzed on the basis of simplified theories, and very often the properties of a semiconductor device are described by empirical formulas since the microscopic details are too complicated. Up to 1980 nobody expected that there exists an effect like the quantized Hall effect, which depends exclusively on

fundamental constants and is not affected by irregularities in the semiconductor like impurities. [126]

The topological class of materials is linked to certain quantities, the *topological invariants*. These quantities are fundamental properties of topological spaces and indicate whether they can be transformed into each other or not. In detail, if two topological spaces have different topological invariants, they are not homeomorphic to each other, i.e. they cannot be mapped onto each other in a continuous and bijective manner. The reverse statement does not necessarily hold.

The simple example of Euler's theorem of polyhedrons provides an easy approach towards the matter of topology. As taught in many geometry lessons, it is well known that all convex polyhedrons obey the rule that the number of vertices minus the number of edges plus the number of faces equals 2. This holds, e.g., for the cube ($8 - 12 + 6 = 2$), the tetrahedron ($4 - 6 + 4 = 2$) and the octahedron ($6 - 12 + 8 = 2$). The theorem can even be generalised to closed surfaces which are not necessarily convex or polyhedral, e.g. the smooth S^2 sphere. In this case, a triangulation produces countable vertices, edges and faces. The alternating sum of these is the Euler characteristic, which defines a topological invariant of the surface. It is thus independent of the details of the triangulation because different triangulations are homeomorphic to each other. Since Euler's theorem for polyhedrons is a special case of the Euler characteristic, it is obvious that also the sphere has an Euler characteristic of 2 as it can be mapped onto a cube, a tetrahedron or an octahedron.

The ring-shaped T^2 torus is another example for a closed surface which clarifies the usefulness of the Euler characteristic. A possible triangulation for this surface consists in a right-angled, closed arc, similar to the shape of l'Arche de la Défense, Paris, France². Comprising 16 vertices, 32 edges and 16 faces, it yields an Euler characteristic of 0, differently from the sphere. Thus, the torus and the sphere are so fundamentally different from each other that a homeomorphism between them does not exist. In this case, the hole of the torus is the central property which discriminates the topological classes. A consequence of the different topological classes which is indeed relevant for materials scientists is the existence of a global map for the torus, while a global map for the sphere does not exist³. This is the topological reason for why a 2D crystal can be mapped onto a square (more generally a parallelogram), despite being a closed torus due to the periodicity in two directions. The same holds for the Brillouin zone, whose toroidal nature will be relevant at several points in Chap. 7.

In the case of solids, topological invariants can be calculated from the electronic wavefunctions, provided that they can be separated into well-defined occupied and unoccupied manifolds, i.e. the material of interest is a band insulator. Those insulators whose topological invariants are non-trivial are called *topologically non-trivial insulators* or simply *topological insulators* (TIs). In terms of solid-state physics, the

²*La Grande Arche de La Défense*, https://fr.wikipedia.org/wiki/Arche_de_la_D%C3%A9fense#/media/Fichier:Grande_Arche_F%C3%A9vrier_2020.jpeg (visited on 24/03/2022).

³For instance, the Earth has no single, global map. Instead, it has to be described by a set of local maps which partially overlap: an atlas. More precisely, at least two local maps are necessary in order to find any geographic point on at least one of the two maps. For example, the UNO logo lacks Antarctica for this reason.

above theorem of conserved topological invariants tells that the special properties of TIs are retained as long as the band gap does not close. For this reason, the topological order of a TI is insensitive to imperfections like disorder or defects.

The practical usefulness of TIs does not necessarily consist in the intrinsic properties. If insulators of different topological classes border each other, in particular if a TI is connected to a topologically trivial insulator (*conventional insulator*, CI), the band gap closes so as to allow the bands to reorder. In other words, there are metallic edge states somewhere at the interface. Since the vacuum is also a CI, the surface of every TI bears *topologically protected surface states* (TSSs), which are indestructible by any perturbation, provided that the topological classes of the involved bulk materials are conserved. Of course, metallic surface states which exists regardless of the morphological details are very attractive for surface scientists.

This part of the thesis is dedicated to the Sb@Bi₂Se₃ system, a van der Waals (vdW) heterostructure consisting of thin layers of antimony (β -Sb) which are adsorbed on bismuth selenide substrates (Bi₂Se₃). This heterostructure is a particularly interesting system because, firstly, the β -Sb adlayer adsorbs to the Bi₂Se₃ substrate by means of vdW interactions and, secondly, the β -Sb adlayer is a CI, while bulk Bi₂Se₃ is a TI, more precisely a \mathbb{Z}_2 topological insulator. Of course, TSSs emerge as the non-trivial class of the substrate has to transition into the trivial class somewhere. However, topology does not specify any details about the transition, e.g. the location of the TSSs. A priori, the TSSs can be located anywhere, from being buried in the substrate to rising up to the surface of the Sb film. That Bi₂Se₃ and β -Sb are vdW materials does not simplify this issue as it is unclear how the adlayer and the substrate mutually affect their electronic properties.

The aim of this part is to analyse the nature of the TSSs of the Sb@Bi₂Se₃ heterostructure. Since the interplay between the topological classes of the Bi₂Se₃ substrate, the β -Sb adlayer and the vacuum is complex, elaborating the topological invariants is inevitable for analysing the formation of the TSSs and for understanding topological phase transitions. Therefore, Chap. 7 introduces the matter of geometric phases, which finally leads to the definition of the \mathbb{Z}_2 invariant for time-reversal-symmetric solids. Chap. 8 follows as a preparatory chapter which treats the constituents of the heterostructure Bi₂Se₃ and β -Sb separately. The investigations serve two purposes: testing the approach, which employs methods beyond DFT, in particular vdW and SOC, and calculating the band structures and the \mathbb{Z}_2 invariants. The actual heterostructure is the matter of Chap. 9. At first, a stable structure model is derived, where the focus is on the inversions of the Sb adlayer. After that the electronic properties are calculated for the most stable structure models. The chapter concludes with the analysis of the complex series of topological phase transitions, which occurs upon a simulated adsorption process of the Sb adlayer.

7 Geometric phases

The concept of geometric phases is unfamiliar to many scientists, but fundamentally important for understanding modern methods in condensed-matter theory. It is the mathematical basis of the topological invariants in solid-state systems. The aim of this chapter is thus to introduce the concept of geometric phases and then to derive the \mathbb{Z}_2 invariant step by step. The Aharonov-Bohm effect marks the beginning as it is a manifestation of geometric phases, granting a more or less easy access to the matter. After that, the geometric phases along with the respective geometric connections and geometric potentials are formally defined, according to the approach of Berry [127]. The modern theory of polarisation according to the review of Resta [128] follows as it is the basis of topological transport. This defines the IHE, which is introduced in a generalised manner. Based on the IHE, the chapter concludes with the related \mathbb{Z}_2 topological invariant in two and three dimensions, the objective of this chapter.

7.1 The Aharonov-Bohm effect

According to the principle of minimal coupling (Sec. A.2), a gauge transformation of the electromagnetic fields introduces a phase in the wavefunctions $|\Psi\rangle$ of charged particles. Consequently, the absolute phase of a quantum state is not a measurable quantity since gauge transformations must not change the physical observations. On the other hand, phase *differences* can be measured, e.g. in interference experiments. This raises the question how the observability of phase differences accords with the non-observability of gauge transformations. A phenomenon which is taught in every quantum-mechanics class, but whose interpretation is still the matter of vivid discussions, is the Aharonov-Bohm effect (ABE) [129–134]. After first hints by Franz [135] in 1939 and a more complete description by Ehrenberg and Siday [136] in 1949, Aharonov and Bohm [129] developed a general gedankenexperiment in 1959 which clarifies the geometrical nature of gauge potentials.

The space-dependent, magnetic ABE is based on the magnetic vector potential and can conceptually be realised by the model of an infinitely long solenoid with finite radius R . The magnetic field may be constant inside the solenoid and point into the z -direction. Outside, the magnetic field may vanish. In polar coordinates and in the Coulomb gauge, the vector potential \mathbf{A} holds:

$$\mathbf{A}(\mathbf{x}) = \begin{cases} \frac{B\rho}{2} \mathbf{e}_\varphi & , \rho < R \\ \frac{BR^2}{2\rho} \mathbf{e}_\varphi & , \rho > R \end{cases} \Rightarrow \nabla \times \mathbf{A} = \mathbf{B} = \begin{cases} B\mathbf{e}_z & , \rho < R \\ 0 & , \rho > R \end{cases} \wedge \nabla \cdot \mathbf{A} = 0 \quad (7.50)$$

Consider a particle with charge q in the hollow-cylindrical field-free region $\Omega = \{\mathbf{x} \mid \rho > R\}$. It may be in the quantum state $|\Psi\rangle$ when the solenoid is switched off. Switching the solenoid on transforms $|\Psi\rangle$ by a phase shift according to the principle of minimal coupling in combination with $\nabla \times \mathbf{A} = 0$. This phase is proportional to the line integral of \mathbf{A} along a C^1 curve $\gamma \subset \Omega_s := \Omega \setminus \{\mathbf{x} \mid \varphi = \varphi_s \in [0, 2\pi)\}$.

$$H(\mathbf{p}, \mathbf{x})|\Psi\rangle = E|\Psi\rangle \rightarrow H(\mathbf{p} - q\mathbf{A}, \mathbf{x})|\tilde{\Psi}\rangle = E|\tilde{\Psi}\rangle \Rightarrow |\tilde{\Psi}\rangle = \exp(i\frac{q}{\hbar}\chi(\mathbf{x}))|\Psi\rangle \quad (7.51a)$$

with

$$\gamma : [0, 1] \rightarrow \Omega_s, \quad \gamma(0) = \mathbf{x}_0, \quad \gamma(1) = \mathbf{x}$$

$$\chi(\mathbf{x}) = \int_{\gamma} \mathbf{A} \cdot d\mathbf{y} = \frac{1}{2}BR^2(\varphi - \varphi_0) \Leftrightarrow \mathbf{A}(\mathbf{x}) = \nabla_{\mathbf{x}}\chi(\mathbf{x}) \quad (7.51b)$$

where φ and φ_0 denote the polar angles of \mathbf{x} and \mathbf{x}_0 , respectively. The constraint on Ω for integrating \mathbf{A} is necessary for the validity of Eq. (7.51b), as will be explained below. In other words, γ must stay in a sector around the solenoid.

The phases in Eq. (7.51a) can be observed as an interference between two particle beams running clockwise and anticlockwise around the solenoid. Both beams originate in $\mathbf{x}_0 \in \Omega$, the source, and meet again in $\mathbf{x}_1 \in \Omega$, where the interference measurement is performed. The points divide Ω into two parts Ω^+ and Ω^- in which the paths of the beams are denoted $\gamma^+ \subset \Omega^+$ and $\gamma^- \subset \Omega^-$ (Fig. 7.1). The superposed probability amplitude holds:

$$\begin{aligned} |\tilde{\Psi}\rangle &= |\tilde{\Psi}^+\rangle + |\tilde{\Psi}^-\rangle = \exp(i\frac{q}{\hbar}\chi^+)|\Psi^+\rangle + \exp(i\frac{q}{\hbar}\chi^-)|\Psi^-\rangle \\ &= \exp(i\frac{q}{\hbar}\chi^-) [\exp(i\frac{q}{\hbar}(\chi^+ - \chi^-))|\Psi^+\rangle + |\Psi^-\rangle] \\ &= \exp(i\frac{q}{\hbar}\chi^-) [\exp(i\frac{q}{\hbar}\chi_{\gamma})|\Psi^+\rangle + |\Psi^-\rangle] \end{aligned} \quad (7.52)$$

with

$$\chi_{\gamma} = \int_{\gamma^+ - \gamma^-} \mathbf{A} \cdot d\mathbf{y} = \oint_{\gamma} \mathbf{A} \cdot d\mathbf{y} \stackrel{\text{Stokes}}{=} \iint_S (\nabla \times \mathbf{A}) \cdot d\mathbf{S} = \iint_S \mathbf{B} \cdot d\mathbf{S} = B\pi R^2 = \Phi_0$$

where Φ_0 is the total magnetic flux through the area S encircled by γ^+ and γ^- .

Eq. (7.52) leads to an astonishing conclusion: A magnetic field can influence the phases of particles which are strictly prevented from crossing it. The phase difference $\frac{q}{\hbar}\chi_{\gamma}$ depends neither on the point \mathbf{x}_1 where the measurement is performed, nor on the details of the paths, but it is proportional to the total magnetic flux through the solenoid. The indirect effect of a magnetic field on charged particles via its vector potential is the central result of Aharonov and Bohm [129]. As the field-free interaction sounds spooky at first glance, the ABE causes arguments about its interpretation until today [131–133]. The probably most important source of misunderstanding is the seeming observability of the gauge transformation in Eq. (7.51b).

The misunderstandings arise if one infers the integrability of \mathbf{A} from its vanishing curl $\nabla \times \mathbf{A} = 0$. Since it would then have a scalar potential, all loop integrals of \mathbf{A} would be zero. Moreover, \mathbf{A} could be “gauged away” to $\mathbf{A} \equiv 0$, which would negate any

action. However, curl-freeness is not sufficient for the integrability of a vector field, but the domain has to be simply connected in addition [137, p. 264]. As long as simply connected sectors of Ω , e.g. Ω^+ or Ω^- , are considered, \mathbf{A} is integrable and has a scalar potential χ , as explicitly shown in Eq. (7.51b). As a consequence, particles moving in the same simply connected region do not show the ABE and the phase in Eq. (7.51a) is indeed an unobservable gauge. This changes if the line integral runs around the solenoid, as effectively realised by the two countercurrent beams. Since the solenoid pierces a cylindrical hole into the field-free region, Ω is multiply connected and a scalar potential for \mathbf{A} does not exist, despite $\nabla \times \mathbf{A} = 0$ ¹. Consequently, line integrals in general depend on the integration curve and loop integrals can yield non-zero values. Moreover, \mathbf{A} cannot be gauged away any more, but it encodes the magnetic field inside the solenoid in any gauge. In mathematical terms: the equivalence class $[\mathbf{A}]$ defined by $\mathbf{A} \sim \mathbf{A} + \nabla\chi$ is non-zero. While the phases in (7.51a) depend on the gauge, the ABE phase in (7.52) is gauge invariant since additional gradient fields $\nabla\chi$ vanish in loop integrals. Therefore, it is a physical observable and can be measured in principle.

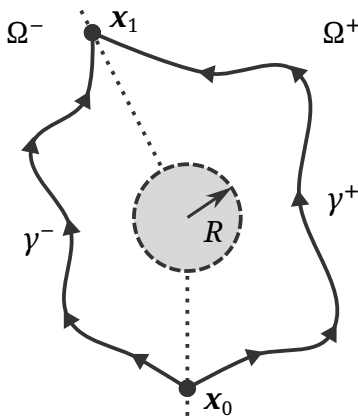


Figure 7.1: Sketch of the ABE setting. γ^+ and γ^- connect x_0 with x_1 anti-clockwise and clockwise around the solenoid (grey).

The ABE is a fascinating illustration of the role of fields and potentials in physics. Although it is not obvious in this case, the ABE phase shift can be explained solely by the magnetic field \mathbf{B} , as well as solely by its vector potential \mathbf{A} , whose equivalence class is bijectively connected to \mathbf{B} . Thus, the popular statement that \mathbf{A} contains “more information” than \mathbf{B} is not meaningful, as well as the question whether the one or the other is more important in physics. The ABE is a pure quantum effect, for which a classical analogon does not exist. For this reason, imagining a quantum particle moving in a force field leads to confusions about the ABE. Aharonov and Bohm pointed out that the idea of local force fields like \mathbf{B} determining the physics of a quantum system applies nowhere in quantum physics. Instead, the quantum state is

determined by a Hamilton operator which is constructed by locally acting potentials (local in position and momentum operators) [130]. Non-local effects naturally arise since the differential equations are solved for the entire domain of the operator. An example for the absurdity of force fields acting locally on quantum particles is the simple double-slit experiment: It is very confusing to imagine that a particle “going” through the one slit “feels” whether the other slit is covered. Hence, the non-locality of wavefunctions and the importance of path possibilities, as emerging in the ABE, are not really exotic phenomena in quantum mechanics.

¹One could have the idea to consider $\chi(\mathbf{r}) = \varphi BR^2/2$ a scalar potential. Its gradient χ indeed yields the correct vector field $\mathbf{A}(\mathbf{r})$ of Eq. (7.50). However, the domain of χ is a simply connected sector of Ω , e.g. the area $\{\mathbf{r} \mid \rho > R, \varphi \in [0, 2\pi)\}$. It is impossible to define χ continuously on Ω . More precisely, at least two local definitions of χ are necessary in order to globally calculate \mathbf{A} . One example for these definitions are χ^+ and χ^- on the sectors Ω^+ and Ω^- above (with an appropriate overlap).

Since the ABE phase depends only on the enclosed magnetic flux Φ_0 , and neither on the point of measurement, nor on the details of the paths of the particle beams, the ABE has already been observed in 1962: By means of the ABE, Möllenstedt and Bayh determined the ratio h/e with a precision of 14 % [138]. Many years followed, in which experimental evidence for the ABE was still argued to be due to leaking magnetic fields, until Tonomura et al. brought a convincing experimental proof in 1986 [139]. Obviously, the ABE phase is a fundamental property of the setup and the wavefunction domains in that it is insensitive to continuous deformations of the solenoid and of the beams. This phenomenon can be generalised by the concept of geometrical phases, which is the matter of the next section.

7.2 The Berry phase

Geometric phases are also called *Berry phases*, as Berry introduced them in 1984 by the following procedure [127].

Let H be the Hamilton operator for a quantum system which depends parametrically on a multidimensional parameter $\xi = (\xi_1, \xi_2, \dots, \xi_n) \in \mathbb{R}^N$. The corresponding stationary Schrödinger equation is then

$$H(\xi)|n(\xi)\rangle = E_n(\xi)|n(\xi)\rangle. \quad (7.53)$$

Furthermore, let $\gamma : [0, 1] \rightarrow \xi(t) \subset \mathbb{R}^N$ be a C^1 curve which describes a continuous parametric variation. It may be slow enough that the system stays in the eigenstate $|n(\xi)\rangle$ on the entire curve γ , i.e. for every parameter $\xi(t)$, the state $|n(\xi(t))\rangle$ satisfies Eq. (7.53) and the eigenvalue $E_n(\xi)$ has the same index n . In other words, level crossing during the parametric variation is explicitly forbidden.

The phase factor for $|n(\xi(t))\rangle$ at a given parameter $\xi(t) \neq \xi(0)$ is not arbitrary like in single-shot calculations, but it depends on the initial state $|n(\xi(0))\rangle$. The connection between the phases follows from considering t as time and solving the Schrödinger equation with the initial condition $|\Psi(0)\rangle := |n(\xi(0))\rangle$ and the following ansatz:

$$|\Psi(t)\rangle = \underbrace{1}_{\text{arb. phase}} \underbrace{\exp(-i\frac{1}{\hbar} \int_0^t E_n(\xi(t')) dt')}_{\text{dynamical phase}} \underbrace{\exp(i\chi_n(t))}_{\text{geometric phase}} |n(\xi(t))\rangle \quad (7.54)$$

The ansatz wavefunction $|\Psi(t)\rangle$ has three phase factors: the arbitrary phase ($\equiv 1$), the general dynamical phase from the temporal evolution, and a third term $\chi_n(t)$ which bears all other phase shifts due to the parametric variation.

$$\begin{aligned} i\hbar \frac{\partial}{\partial t} |\Psi(t)\rangle = H(\xi) |\Psi(t)\rangle &\Rightarrow \hbar \frac{\partial \chi_n(t)}{\partial t} |n(\xi(t))\rangle = i\hbar \frac{\partial \xi(t)}{\partial t} \cdot \nabla_\xi |n(\xi(t))\rangle \\ \Leftrightarrow \chi_n &= i \int_\gamma \langle n(\xi) | \nabla_\xi |n(\xi)\rangle \cdot d\xi =: \int_\gamma \mathcal{A}_n(\xi) \cdot d\xi \end{aligned}$$

with

$$\mathcal{A}_n(\boldsymbol{\xi}) = i \langle n(\boldsymbol{\xi}) | \nabla_{\boldsymbol{\xi}} | n(\boldsymbol{\xi}) \rangle \quad (7.55)$$

As it is evident, the parametric variation does not only produce the normal dynamical phase shift. There is an additional phase shift χ_n which originates in the parametric variation itself: the *geometric phase* or *Berry phase* [127]. The integrand $\mathcal{A}_n(\boldsymbol{\xi})$ is the *Berry connection*, which describes how the phase of the eigenfunction $|n(\boldsymbol{\xi})\rangle$ responds to infinitesimal variations of the parameter $\boldsymbol{\xi}$.

If γ is a closed loop, the Berry phase assumes a certain value, which can be zero or finite.

$$\boldsymbol{\xi}(1) = \boldsymbol{\xi}(0) \quad \Rightarrow \quad \chi_n(1) = \chi_n^B = \oint_{\gamma} \mathcal{A}_n(\boldsymbol{\xi}) \cdot d\boldsymbol{\xi} \quad (7.56)$$

Hence, a cyclic parametric variation of the Hamilton operator can shift the phases of the eigenstates beside the usual dynamical phase shift. Since not depending on the time lapse, the Berry phase arises even if the variation is instantaneous ($\Delta t = 0$).

$$|n_{\text{final}}\rangle = \exp(i\chi_n^B) |n_{\text{initial}}\rangle$$

If the parameter space is three-dimensional, it is instructive to apply Stokes theorem so as to obtain a surface integral:

$$\chi_n^B = \iint_S \mathcal{B}_n(\boldsymbol{\xi}) \cdot d\mathbf{S} \quad (7.57)$$

where S is the area encircled by γ and

$$\begin{aligned} \mathcal{B}_n(\boldsymbol{\xi}) &= \nabla_{\boldsymbol{\xi}} \times \mathcal{A}(\boldsymbol{\xi}) = i \langle \nabla_{\boldsymbol{\xi}} n(\boldsymbol{\xi}) | \times | \nabla_{\boldsymbol{\xi}} n(\boldsymbol{\xi}) \rangle \\ &= -\text{Im} \sum_{m \neq n} \frac{\langle n(\boldsymbol{\xi}) | \nabla_{\boldsymbol{\xi}} H(\boldsymbol{\xi}) | m(\boldsymbol{\xi}) \rangle \times \langle m(\boldsymbol{\xi}) | \nabla_{\boldsymbol{\xi}} H(\boldsymbol{\xi}) | n(\boldsymbol{\xi}) \rangle}{(E_m(\boldsymbol{\xi}) - E_n(\boldsymbol{\xi}))^2} \quad [127] \end{aligned} \quad (7.58)$$

The way how the *Berry connection* (Eq. (7.55)) and the *Berry potential* (Eq. (7.57)) influence the phase of the parametrised system are remarkably analogue to the action of a magnetic field and its vector potential on the phases of a charged quantum particle in the ABE (Eq. (7.52)). Therefore, analogously to the ABE phase, the Berry phase $\chi_n(\boldsymbol{\xi})$ is not observable for open curves as the absolute phase information is gauge-dependent. Only if the system is compared with a reference system at the same set of parameters, which effectively corresponds to a closed loop, or if the system is directly subjected to a circular parametric variation, the Berry phase is, in principle, observable. This holds because χ_n^B is gauge invariant.

$$|n(\boldsymbol{\xi})\rangle \rightarrow \exp(i\tilde{\chi}(\boldsymbol{\xi})) |n(\boldsymbol{\xi})\rangle \Rightarrow \mathcal{A}_n(\boldsymbol{\xi}) \rightarrow \mathcal{A}_n(\boldsymbol{\xi}) - \nabla_{\boldsymbol{\xi}} \tilde{\chi}(\boldsymbol{\xi}) \Rightarrow \chi_n^B \rightarrow \chi_n^B + 0 \quad (7.59)$$

In particular, the above choice of $\equiv 1$ for the arbitrary phase has not affected the physical results. The proof that the ABE can indeed be formulated in terms of Berry phases can be found in the appendix (Sec. C.1).

The line integral of the Berry connection $\mathcal{A}_n(\boldsymbol{\xi})$ is more handy for proving the connection between physical quantities and for analytical problems. For the numeric treatment, however, $\mathcal{A}_n(\boldsymbol{\xi})$ is not easy to calculate because the derivatives in Eq. (7.55) have to be replaced by finite differences with connected phase relations. In order to avoid this problem, the surface integral of the Berry potential $\mathcal{B}_n(\boldsymbol{\xi})$ can be used as it depends on well-defined derivatives of $H(\boldsymbol{\xi})$ [127].

7.3 The electric polarisation in a crystal

Geometric phases are applicable whenever the response of a quantum system to a parametric variation is the quantity of interest. An example which actually necessitates them for the correct description are null-field polarisation effects in a crystal, e.g. ferroelectricity or piezoelectricity. A naive, but wrong formula for the macroscopic polarisation \mathbf{P} of a crystal would be the summation of all electrostatic dipole moments created by the charge density $\rho(\mathbf{x})$ in the direct unit cell C_R .

$$\mathbf{P} = \mathbf{P}_{\text{ion}} + \frac{1}{|C_R|} \int_{C_R} d\mathbf{x} \mathbf{x} \rho(\mathbf{x}) \quad (7.60)$$

where \mathbf{P}_{ion} is the polarisation from the ions, $|C_R|$ the direct unit cell volume and $\rho(\mathbf{x})$ the electronic charge density given by the modulus of the Bloch functions:

$$\rho(\mathbf{x}) = \frac{-e}{|C_R|} \sum_n \frac{1}{|C_G|} \int_{C_G} d\mathbf{k} \langle \Psi_n(\mathbf{k}) | \mathbf{x} \rangle \langle \mathbf{x} | \Psi_n(\mathbf{k}) \rangle$$

where $|C_G|$ is the reciprocal unit cell volume. This definition works fine if all electrons are localised within C_R , e.g. in molecular crystals or ionic systems. In covalent systems like semiconductors, however, the electrons are not confined to a specific cell, so Eq. (7.60) fails to correctly describe the macroscopic polarisation [140]. King-Smith and Vanderbilt (1993) and Resta (1994) wrote reviews on this, analysing the quantum effects of electric polarisation and linking it to geometric phases of the electronic wavefunctions [128, 141]. The key points of these reviews are retraced in the following paragraphs as they are the basis of topological transport. From now on, electrons in a crystal are considered. They are described by the Bloch Hamiltonian (vide supra, Eqs. (2.27)) and carry the negative elementary charge $q = -e$. Being fermions, they occupy the states from the lowest band $n = 1$ to the highest band $n = \bar{n}$ at zero temperature, making \bar{n} electrons per unit cell. In the spin-degenerate case, the bands are counted with respect to their algebraic duplicity. As will be proven later, it is crucial that the system is insulating, i.e. the occupied and the unoccupied bands are well separated by a band gap $\forall \mathbf{k} \in C_G$.

Eq. (7.60) fails because the phase information of the wavefunctions is omitted by the modulus, so current terms between adjacent unit cells are missing. Beside the mathematical reason, there is another, general point, why Eq. (7.60) cannot be well defined: In real experiments, the bulk polarisation cannot be determined in a single measurement. Instead, a series of measurements has to be conducted whereupon

the polarisation changes can be deduced from the transported charge (current). The same holds in solid-state theory since Berry phases are observable only as phase *differences*. Resta begins his considerations with defining a charge redistribution between two states ($\lambda = 0$) and ($\lambda = 1$) of a crystal, where λ represents the reaction coordinate of the polarisation process. In the exemplary case of a ferroelectric, λ describes the transition from the unpolarised into the polarised state. In order to resolve the delocalisation problem of the Bloch functions, he changes the basis to the Wannier functions (vide supra, Eq. (2.29)). Since localised, the Wannier density can safely be inserted into Eq. (7.60). As a result, the change in polarisation equals a change in the centres of charge of the Wannier functions $a_n^{(\lambda)}(\mathbf{x}) = \langle \mathbf{x} | a_n^{(\lambda)}(0) \rangle$, which depend on the reaction coordinate λ via the Bloch functions $|u_n^{(\lambda)}(\mathbf{k})\rangle$.

$$\begin{aligned} \Delta \mathbf{P} &:= \frac{-e}{|\mathbf{C}_R|} \sum_{n=1}^{\bar{n}} \left(\langle \mathbf{x}_n^{(1)} \rangle - \langle \mathbf{x}_n^{(0)} \rangle \right) \stackrel{\text{Eq. (2.31)}}{=} \frac{-e}{|\mathbf{C}_R|^2} \sum_{n=1}^{\bar{n}} \int d\mathbf{x} \, \mathbf{x} \left[|a_n^{(1)}(\mathbf{x})|^2 - |a_n^{(0)}(\mathbf{x})|^2 \right] \\ &\stackrel{\text{Eq. (2.32)}}{=} \frac{-e}{(2\pi)^3} \sum_{n=1}^{\bar{n}} \int_{\mathcal{C}_G} d\mathbf{k} \left[\langle u_n^{(1)}(\mathbf{k}) | i\nabla_{\mathbf{k}} | u_n^{(1)}(\mathbf{k}) \rangle - \langle u_n^{(0)}(\mathbf{k}) | i\nabla_{\mathbf{k}} | u_n^{(0)}(\mathbf{k}) \rangle \right] \end{aligned}$$

In order to extract the geometric phases, the expression for $\Delta \mathbf{P}$ is evaluated by the components with respect to the reciprocal basis $\{\mathbf{G}_j\}$. For this purpose, let $i \in [1, N]$ be a fixed index. The polarisation component ΔP_i along \mathbf{G}_i then holds:

$$\begin{aligned} \Delta P_i &:= \mathbf{G}_i \cdot \Delta \mathbf{P} \\ &= \frac{-e}{|\mathbf{C}_R|} \sum_{n=1}^{\bar{n}} \int_{[0,1]^N} ds \left[\langle u_n^{(1)}(\mathbf{s}) | i \frac{\partial}{\partial s_i} | u_n^{(1)}(\mathbf{s}) \rangle - \langle u_n^{(0)}(\mathbf{s}) | i \frac{\partial}{\partial s_i} | u_n^{(0)}(\mathbf{s}) \rangle \right] \quad (7.61) \end{aligned}$$

where \mathbf{s} is the relative coordinate vector of the \mathbf{k} -vector in the reciprocal unit cell².

The integrand in Eq. (7.61) reminds of the Berry connection \mathcal{A} (Eq. (7.55)). In order to clarify the analogy, a two-dimensional parameter $\boldsymbol{\xi} \in [0, 1]^2$ is introduced whose first component is the reaction coordinate $\lambda =: \xi_0$. The second component is the relative coordinate $s_i =: \xi_1$ of \mathbf{k} along \mathbf{G}_i . The corresponding two-dimensional Berry connection \mathcal{A}_i then holds³:

$$\mathcal{A}_i(\boldsymbol{\xi}) = \sum_{n=1}^{\bar{n}} \prod_{j \neq i} \left[\int_0^1 ds_j \right] \left[\langle u_n^{(\lambda)}(\mathbf{s}) | i \nabla_{\boldsymbol{\xi}} | u_n^{(\lambda)}(\mathbf{s}) \rangle \right] \quad \text{with } \boldsymbol{\xi} = (\lambda, s_i) \quad (7.62)$$

²The reciprocal vector \mathbf{k} and its differential operator $\nabla_{\mathbf{k}}$ can be expressed in terms of $\mathbf{s} \in [0, 1]^N$, the relative coordinates of \mathbf{k} in the reciprocal basis $\{\mathbf{G}_j\}$.

$$\mathbf{k} = \sum_{j=1}^N \mathbf{G}_j s_j = \frac{1}{2\pi} \sum_{j=1}^N \mathbf{G}_j (\mathbf{R}_j \cdot \mathbf{k}) \quad \Rightarrow \quad \nabla_{\mathbf{k}} = \frac{1}{2\pi} \sum_{j=1}^N \mathbf{R}_j \frac{\partial}{\partial s_j}$$

³The $(N-1)$ -dimensional integral in Eq. (7.62) traces all dimensions except i , so it is an ordinary state summation like the n -sum over the bands. The i -th component of \mathbf{s} is excluded from the integration and composes the variation parameter $\boldsymbol{\xi}$ together with the reaction coordinate λ .

The line integral of $\mathcal{A}(\boldsymbol{\xi})$ along the edge of its quadratic domain $\gamma := \partial[0, 1]^2$ yields the Berry phase:

$$\begin{aligned} \chi_i^{\text{B}} &= \oint_{\gamma} \mathcal{A}_i(\boldsymbol{\xi}) \cdot d\boldsymbol{\xi} \\ &= \underbrace{\int_0^1 d\lambda \mathcal{A}_i^0(\lambda, 0)}_{\text{I}} + \underbrace{\int_0^1 ds_i \mathcal{A}_i^1(1, s_i)}_{\text{II}} + \underbrace{\int_1^0 d\lambda \mathcal{A}_i^0(\lambda, 1)}_{\text{III}} + \underbrace{\int_1^0 ds_i \mathcal{A}_i^1(0, s_i)}_{\text{IV}} \end{aligned} \quad (7.63)$$

where $\mathcal{A}_i^j(\boldsymbol{\xi})$ denotes the j -th component of \mathcal{A}_i . The terms I and III of Eq. (7.63) cancel each other because $\mathcal{A}_i(\lambda, 0) = \mathcal{A}_i(\lambda, 1) \forall \lambda$, reflecting the boundary conditions of the Bloch factors (Eq. (2.28b)). The remaining terms II and IV reproduce the electric polarisation in Eq. (7.61) up to a prefactor.

$$\Delta P_i = \frac{-e}{|C_{\text{R}}|} \chi_i^{\text{B}} = \frac{-e}{|C_{\text{R}}|} \oint_{\gamma} \mathcal{A}_i(\boldsymbol{\xi}) \cdot d\boldsymbol{\xi} \quad (7.64)$$

Eq. (7.64) is the central result of [128]. It proves that the projection of the static electric polarisation on a G-vector can indeed be considered a geometric phase of the parameter space spanned by the reaction coordinate and the \mathbf{k} -path along that G-vector. From Eq. (7.59), it is directly clear that ΔP_i is gauge-invariant under \mathcal{G} -periodic $U(1)$ transformations, which preserve the band order. However, this restriction is a problem in solid-state crystals since the bands of the occupied subspace in general swap indices when traversing the Brillouin zone or when progressing on the λ -path. For this reason, Resta generalised the proof for gauge invariance to more general $U(\bar{n})$ transformations, which mix states of the occupied subspace with different band indices [128]. The proof can be found in the appendix (Sec. C.2).

As a consequence of the boundary conditions of the Bloch factors, the parameter space is special in that its $(\lambda, s_i = 0)$ and $(\lambda, s_i = 1)$ edges are identical. In other words, the domain of the Berry connection $\mathcal{A}(\boldsymbol{\xi})$ is a cylinder without bases, like that sketched in Fig. 7.2. Its length corresponds to the progressive nature of λ and its circumference reflects the periodicity \mathcal{A} on the reciprocal lattice. One could have the idea that calculating only one part of Eq. (7.61), e.g. the $\lambda = 1$ part, might yield a physical quantity like an “absolute” polarisation. It corresponds to integrating the geometric phase solely along one of the two circles in Fig. 7.2. However, the single terms of Eq. (7.61) are ill-defined because they are gauge-dependent. More precisely, according to Eq. (C.108) and the boundary conditions of the Bloch factors (Eq. (2.28b)), the loop integrals along the individual circles are only defined up to integer multiples of 2π . Consequently, the single summands of ΔP_i are defined only modulo $2\pi \frac{-e}{|C_{\text{R}}|}$, which corresponds to an advance of the extensive polarisation $|C_{\text{R}}|\mathbf{P}$ by $-e \cdot \mathbf{R}_i$. This reflects that the Wannier centres are defined only modulo a direct lattice vector [128].

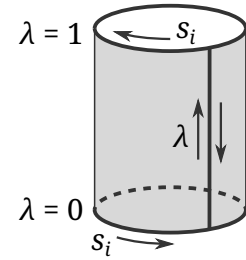


Figure 7.2: Path for calculating the electric polarisation as a geometric phase.

From a topological point of view, the subtraction of the two circles together with the cancelling λ -edges establishes a loop integral over the edge of a simply connected rectangle which is wound up to a cylinder. In other words, the loop has an inner area, so the integral assumes a distinct value according to Stokes. This is analogous to the ABE, where only the complete knowledge about the gauge fields on a simply connected region guarantees a well-defined ABE phase. Calculating only one of the circles of the cylinder in Fig. 7.2 is ill-defined because this circle has no inner region and is thus not simply connected. Although clear from the mathematics, it is quite astonishing that the existence of the λ -paths is crucial for the definition of the polarisation, despite their effective cancelling.

7.4 Topological transport

7.4.1 The integer Hall effect

The integer Hall effect (IHE) is based on topological transport, which is a straightforward application of the modern theory of polarisation. Only the points related to topology are addressed in the following paragraphs, while the details about the IHE as well as explicit calculations on the two-dimensional electron gas are passed.

Let $\{|u_n(\mathbf{k})\rangle\}$ be the occupied set of Bloch factors of an insulating, two-dimensional Bloch system with direct basis vectors \mathbf{R}_1 and \mathbf{R}_2 and reciprocal basis vectors \mathbf{G}_1 and \mathbf{G}_2 . In order to calculate the response of the Bloch factors to an in-plane, constant, homogeneous electric field \mathbf{E} , consider Faraday's law:

$$\mathbf{E} = -\frac{\partial \mathbf{A}(t)}{\partial t} \quad \Rightarrow \quad \mathbf{A}(t) = -t \mathbf{E}$$

Without loss of generality, \mathbf{E} may be antiparallel to \mathbf{G}_1 (Sketch in Fig. 7.3 (a)). According to the principle of minimal coupling⁴, the vector potential $\mathbf{A}(t)$ couples into \mathbf{k} of the Bloch Hamiltonian (Eq. 2.27):

$$h(\mathbf{p}, \mathbf{x} | \mathbf{k}) \rightarrow h(\mathbf{p} + e\mathbf{A}(t), \mathbf{x} | \mathbf{k}) = h(\mathbf{p}, \mathbf{x} | \mathbf{k} + \frac{e}{\hbar}\mathbf{A}(t)) \quad (7.65)$$

Obviously, \mathbf{E} shifts the \mathbf{k} -vector by a time-dependent term $\frac{e}{\hbar}\mathbf{A}(t) = -\frac{e}{\hbar}t\mathbf{E}$. Because of the parametric nature of \mathbf{k} in the Bloch formalism, this equals a time-dependent parametric variation of the Bloch manifold. In particular, the \mathbf{k} -vector advances once across the Brillouin zone when the elapsed time is such that $\frac{e}{\hbar}\mathbf{A}(t) = \mathbf{G}_1$:

$$\Delta t = \frac{\hbar|\mathbf{G}_1|}{e|\mathbf{E}|} = \frac{\hbar|\mathbf{R}_2|}{e|\mathbf{E}||C_R|}$$

The field-related parametric variation permits the calculation of the concomitant electric polarisation according to Sec. 7.3. For this purpose, a two-dimensional para-

⁴Mind that the charge q is replaced by $-e$

meter $\boldsymbol{\xi} \in [0, 1]^2$ is introduced. The first component ξ_1 represents the advance of the \mathbf{k} -vector due to the electric field. It equals s_1 , the coordinate of \mathbf{k} with respect to the reciprocal basis vector \mathbf{G}_1 , and corresponds to the reaction coordinate λ in Sec. 7.3. The second component ξ_2 arises from the Bloch-phase integration for obtaining the Wannier centres. It equals the relative coordinate s_i if the polarisation component along \mathbf{G}_i is considered, the same s_i as that in Sec. 7.3.

Integrating the Berry connection $\mathcal{A}_i(\boldsymbol{\xi})$ along the edge of its domain $\gamma = \partial[0, 1]^2$ yields the Berry phase χ_i^{B} , which is proportional to the polarisation $\mathbf{G}_i \cdot \Delta\mathbf{P}$.

$$\mathcal{A}_i(\boldsymbol{\xi}) = \sum_{n=1}^{\bar{n}} \langle u_n(\boldsymbol{\xi}) | i\nabla_{\boldsymbol{\xi}} | u_n(\boldsymbol{\xi}) \rangle \quad (7.66)$$

$$\mathbf{G}_i \cdot \Delta\mathbf{P} = \frac{-e}{|C_{\text{R}}|} \chi_i^{\text{B}} = \frac{-e}{|C_{\text{R}}|} \oint_{\gamma} \mathcal{A}_i(\boldsymbol{\xi}) \cdot d\boldsymbol{\xi} \quad (7.67)$$

For the same reasons as those discussed in Sec. 7.3, Eq. (7.67) is invariant under $U(\bar{n})$ transformations and, thus, the polarisation is observable in principle. The polarisation component along \mathbf{G}_1 , parallel to the electric field, vanishes since the parameter $\boldsymbol{\xi}$ has identical components (s_1, s_1) , so the line integral in Eq. (7.67) does not enclose any finite area. Therefore, $\Delta\mathbf{P}$ can be written in terms of the component perpendicular to the electric field:

$$\mathbf{G}_1 \cdot \Delta\mathbf{P} = 0 \quad \Leftrightarrow \quad \Delta\mathbf{P} = P \frac{\mathbf{R}_2}{|\mathbf{R}_2|}$$

Along the other reciprocal basis vector \mathbf{G}_2 , the polarisation is proportional to the Berry phase $\chi_2^{\text{B}} =: \chi^{\text{B}}$:

$$\mathbf{G}_2 \cdot \Delta\mathbf{P} = \frac{2\pi}{|\mathbf{R}_2|} P = \frac{-e}{|C_{\text{R}}|} \chi^{\text{B}}$$

In summary, each passage of Δt pumps a certain amount of charge along \mathbf{R}_2 , which leads to a current on average. The corresponding current density \mathbf{j} is exactly the quotient between the polarisation and the elapsed time:

$$\mathbf{j} = \frac{\Delta\mathbf{P}}{\Delta t} = \frac{-e|\mathbf{R}_2|}{|C_{\text{R}}|} \frac{1}{2\pi} \chi^{\text{B}} \frac{e|\mathbf{E}||C_{\text{R}}|}{h|\mathbf{R}_2|} \frac{\mathbf{R}_2}{|\mathbf{R}_2|} = \frac{-e^2}{h} |\mathbf{E}| \frac{1}{2\pi} \chi^{\text{B}} \frac{\mathbf{R}_2}{|\mathbf{R}_2|} \quad (7.68)$$

If χ^{B} is positive, \mathbf{j} is turned by $+90^\circ$ relatively to \mathbf{E} , as clarified by the sketch in Fig. 7.3 (a). Since the considered lattice is arbitrary, the right-angled relation between \mathbf{j} and \mathbf{E} can be summarised as Ohm's law:

$$\mathbf{j} = \boldsymbol{\sigma} \mathbf{E} = \begin{pmatrix} \sigma_{xx} & \sigma_{xy} \\ \sigma_{yx} & \sigma_{yy} \end{pmatrix} \mathbf{E} \quad \text{with} \quad \sigma_{xx} = \sigma_{yy} = 0, \quad \sigma_{xy} = -\sigma_{yx} = -\frac{e^2}{h} \frac{1}{2\pi} \chi^{\text{B}} \quad (7.69)$$

The astonishing detail about the above considerations becomes manifest if the loop integral of the Berry connection $\mathcal{A}(\boldsymbol{\xi})$ in Eq. (7.67) is written as a surface integral of

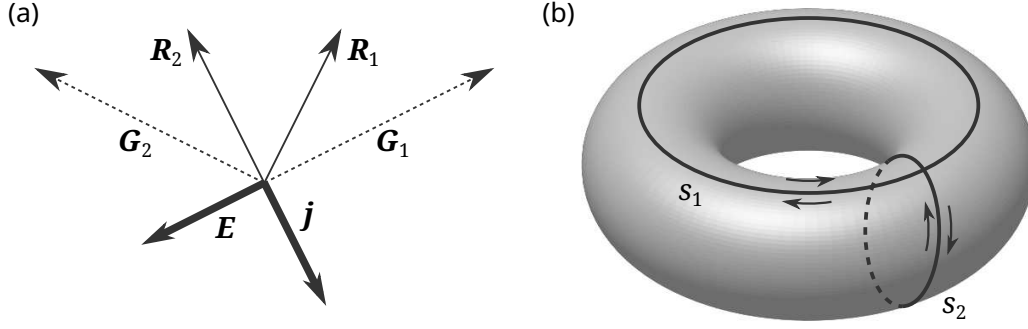


Figure 7.3: (a) Sketch of the directions of the integer Hall effect and (b) path of ξ on the Brillouin torus for calculating the topological transport.

the Berry potential $\mathcal{B}(\xi)$ according to Stokes:

$$\frac{1}{2\pi}\chi^B = \sum_{n=1}^{\bar{n}} \frac{1}{2\pi} \iint_S d\mathbf{S} \cdot \mathcal{B}(\xi) \stackrel{[127]}{=} \sum_{n=1}^{\bar{n}} \frac{i}{2\pi} \iint_S d\mathbf{S} \cdot \langle \nabla_{\xi} u_n(\xi) | \times | \nabla_{\xi} u_n(\xi) \rangle \quad (7.70)$$

where S denotes the surface enclosed by γ .

As Berry noted, the integrand in Eq. (7.70) resembles a curvature whose surface integral yields the first Chern class of the Hermitian line bundle represented by the eigenstates [127]. Moreover, and this is special about the Berry phase considered here, the surface is a closed manifold since the reciprocal unit cell is homeomorphic to the torus \mathbb{T}^2 (Fig. 7.3 (b)). As a consequence, the integral in Eq. (7.70) inclusive the prefactor assumes integral values, leading to a quantisation of the conductivity in Eq. (7.69):

$$\sigma_{xy} = -\frac{e^2}{h}i = i\sigma_{xy}^0 \quad \text{with } i \in \mathbb{Z} \quad \text{and} \quad \sigma_{xy}^0 = -\frac{e^2}{h} \quad (7.71)$$

The above considerations show that the appliance of a lateral electric field E on a two-dimensional, insulating Bloch system raises a current density j which is strictly perpendicular to E . The corresponding off-diagonal conductivity σ_{xy} is quantised by the quantum conductivity σ_{xy}^0 which depends only on natural constants, but not on any details of the system. The quantum number i depends on the system and characterises it in the manner of a topological invariant. In other words, i , or equivalently σ_{xy} , is a fundamental property of Bloch systems and categorises them into topological classes. The topological classification holds in general for *all* Bloch systems which fulfil the prerequisites of being two-dimensional and insulating. On the contrary, topological classes are ill-defined for metallic systems. The Hall conductivity of a system is protected as long as the topological class does not change, which means under all transformations which retain insulating state. This type of protection is much stronger than protection by mere symmetry since the latter permits a continuous, gap-conserving destruction of the concomitant properties. An important consequence of non-trivial Berry phases is that the Bloch functions cannot be defined within a global gauge. Instead, there are overlapping patches on the torus in Fig. 7.3

(b) where the phase factors are continuously defined. A transition function permits the change from one patch to the next by adding the necessary gauge. The integer in Eq. 7.71 “is then related to the winding number of the phase of the transition function around a non-contractable path” [142].

So far, the topologically invariant nature of σ_{xy} is proven in a general manner. One way to actually realise topologically non-trivial Bloch systems is the integer Hall effect (IHE), which occurs in a two-dimensional homogeneous electron gas subjected to a strong, vertical magnetic field at a low temperature [125, 126]. In the model picture, the magnetic field introduces Landau levels, which, when integrally occupied, render the electronic system insulating. In such a state, the Hall conductivity σ_{xy} assumes integer multiples of σ_{xy}^0 , hence the name integer Hall effect. The topological state of this system can transition from σ_{xy} to $\sigma_{xy} \pm \sigma_{xy}^0$ if the magnetic field varies. However, this entails a gap closing. Such effects from topological phase transitions are clearly visible in the IHE experiments as the parallel conductivity σ_{xx} is zero if the system is in an IHE state (\rightarrow insulating), and finite if the system changes the IHE state (\rightarrow metallic) [125, 126].

The IHE can be modelled by Laughlin’s gedankenexperiment, which will be discussed when considering the \mathbb{Z}_2 insulators (vide infra). Therein, the topological transport is explicitly derived from the wave functions of the Landau levels and Faraday’s law of induction combined with an ABE phase shift (“flux threading”) [126]. However, Laughlin’s gedankenexperiment bears problems if a periodic system is considered. Thouless, Kohmoto, Nightingale and Nijs resolved them by theoretically investigating an explicit Bloch system involving a sinusoidal potential and a vertical magnetic field. They calculated the Hall conductivity with the Kubo formula and obtained an expression equivalent to Eq. (7.67). Although they did not extract the topological nature, they argued that the emerging loop integral has to assume integer multiples of 2π , which leads to a quantised conductivity [143]. As they were the first who established a way of calculating the topological invariant for a quantum Hall state, the integer i in Eq. (7.71) is also called TKNN integer.

7.4.2 The two-dimensional \mathbb{Z}_2 insulator

The \mathbb{Z}_2 insulators are closely related to the IHE insulators. They are classified by a \mathbb{Z}_2 topological invariant, which, like the TKNN integer, describes topological transport, not of charge, but of spin or, more precisely, of time-reversal polarisation (defined later). Kane and Mele [144] were the first who demonstrated the existence of a \mathbb{Z}_2 invariant in the quantum spin Hall phase constructed from two copies of the Haldane model [145]. In the simplest case, the z-component of the spin s_z is conserved, so the copies represent each an independent IHE system with a TKNN integer classifying the topological transport of charge. Since time-reversal symmetry (T-symmetry) is presupposed, the TKNN integers of the two subsystems have equal magnitudes and opposite signs, so the total TKNN integer of the system is trivial⁵. However, “the difference [between the two integers may be] non-zero and defines a quantized spin Hall conductivity” [144]. The key point of [144] consists in the demonstration that the non-trivial property of the system is retained if the s_z -conservation is explicitly broken. The former topological transport of spin quanta s_z then degrades to a shift in the expectation value of the spin operator $\langle S_z \rangle$, which was later denoted *time-reversal polarisation* [142]. If the perturbation is strong enough, the system trivialises by a change of its \mathbb{Z}_2 invariant to zero. However, the transition involves a closing of the band gap at some point, as expected from the discontinuous nature of the change between topological classes [144]. There are many different ways to derive the topological \mathbb{Z}_2 invariant for two and three dimensions, which employ more or less abstract topological field theories, summarised in [146]. The method presented here is based on the IHE and demonstrates an alternative reason for the \mathbb{Z}_2 nature of the invariant without going too deeply into the matter of topology.

Two-dimensional T-symmetric Bloch systems

In view of the three-dimensional \mathbb{Z}_2 topological insulators relevant for this work, it is instructive to demonstrate the definition of the \mathbb{Z}_2 topological invariant for a two-dimensional T-symmetric Bloch system at first and then to generalise the findings to a three-dimensional crystal. This exactly follows the spirit of [142, 144, 147]. Hence, let $\{|u_n(\mathbf{k})\rangle\}$ be the occupied set of Bloch factors of an insulating, T-symmetric 2D Bloch system. It may host $2\bar{n}$ electrons per unit cell. The real-space domain is spanned by the direct basis vectors \mathbf{R}_1 and \mathbf{R}_2 and the reciprocal unit cell by the reciprocal basis vectors \mathbf{G}_1 and \mathbf{G}_2 . Because what follows is slightly complicated, the lattice geometry is simplified by the constraint that both R-vectors \mathbf{R}_1 and \mathbf{R}_2 have a length of 1 and are orthogonal to each other so that they equal the euclidean coordinate system. Consequently, the G-vectors \mathbf{G}_1 and \mathbf{G}_2 are also orthogonal to each other and have a length of 2π . The Brillouin zone is thus a square defined by the points $(\pm\pi, \pm\pi)$. The analysis of the IHE (Sec. Sec. 7.4.1) shows that this simplification does not alter the general findings.

⁵From an interpretational point of view, all Bloch states of a T-symmetric system occur in Kramer’s pairs (defined later), so the Wannier centres of each pair move into opposite directions under any T-symmetry-conserving variation. As a consequence, the transport of net charge is inhibited.

Time reversal is described by an antiunitary operator Θ [148], which for fermions and in the representation of [142] holds:

$$\Theta = \exp(i\frac{\pi}{2}\sigma_y)K = i\sigma_y K = \begin{pmatrix} 0 & 1 \\ -1 & 0 \end{pmatrix} K \quad (7.72)$$

where σ_y is the second Pauli matrix and K is the complex-conjugation operator.

A T-symmetric Hamilton operator implies that each eigenstate $|n\rangle$ has the same eigenenergy E_n as its time-reversed counterpart $\Theta|n\rangle$. Hence, the eigenstates occur in degenerate pairs, which are called *Kramers pairs*. The Kramers pairs of a Bloch system comprise each two states with opposite k-vectors:

$$\Theta h(\mathbf{p}, \mathbf{x} | \mathbf{k}) \Theta^{-1} = \Theta \tilde{U}_{\mathbf{k}} H(\mathbf{p}, \mathbf{x}) \tilde{U}_{\mathbf{k}}^{-1} \Theta^{-1} = \tilde{U}_{-\mathbf{k}} H(\mathbf{p}, \mathbf{x}) \tilde{U}_{-\mathbf{k}}^{-1} = h(\mathbf{p}, \mathbf{x} | -\mathbf{k}) \quad (7.73)$$

where $H(\mathbf{p}, \mathbf{x})$ is the T-symmetric Hamilton operator and $h(\mathbf{p}, \mathbf{x} | \mathbf{k})$ the corresponding Bloch Hamiltonian.

Since electronic Bloch systems host independent spin- $\frac{1}{2}$ fermions, the rotating action of $i\sigma_y$ in Θ specifies the Kramers pairs to be linked components of the same spinor. In detail, the occupied Bloch manifold of $2\bar{n}$ fermionic eigenstates groups into \bar{n} spinors, which permits identifying \bar{n} states of each component I and II, spin-up and spin-down in the s_z -conserving case. The action of Θ then holds [142]:

$$\begin{aligned} |u_{\alpha}^{\text{I}}(-\mathbf{k})\rangle &= -\exp(i\chi_{\alpha}(\mathbf{k})) \Theta |u_{\alpha}^{\text{II}}(\mathbf{k})\rangle \\ |u_{\alpha}^{\text{II}}(-\mathbf{k})\rangle &= \exp(i\chi_{\alpha}(-\mathbf{k})) \Theta |u_{\alpha}^{\text{I}}(\mathbf{k})\rangle \end{aligned} \quad (7.74)$$

The minus signs ensure that $\Theta^2 = -1$. The gauge functions $\exp(i\chi_{\alpha}(\mathbf{k}))$ seem to be arbitrary and are often replaced by 1 if topologically trivial systems are considered. Though, they turn out to be essential for \mathbb{Z}_2 -insulating systems since the non-triviality negates the existence of a global gauge for both components [142].

In the electronic band structure, two Kramers-paired bands obviously meet at the Γ -point ($\mathbf{k} = 0$) and form a twofold, same-k-vector degeneracy, i.e. the eigenspace at $\mathbf{k} = 0$ is mapped onto itself under Θ . For this reason, the Γ -point is called a *time-reversal-invariant momentum* (TRIM), denoted Γ_0 . In addition to Γ_0 , the periodicity of the Bloch functions $|\Psi_n(\mathbf{k})\rangle$ on \mathcal{G} produces three other TRIMs in C_G where the Kramers pairs meet again to form a same-k degeneracy. This makes a total of four irreducible TRIMs:

$$\{\Gamma_i\} = \{0, \frac{1}{2}\mathbf{G}_1, \frac{1}{2}\mathbf{G}_2, (\frac{1}{2}\mathbf{G}_1 + \frac{1}{2}\mathbf{G}_2)\} \quad (7.75)$$

Partial, sum and difference polarisations

While T-symmetry expectedly inhibits the transport of net charge, the individual components might still show a shifting of a non-zero quantity. This leads to the definition of *partial polarisations* \mathbf{P}^{I} and \mathbf{P}^{II} which arise in the components I and II, respectively, and which are determined by a procedure analogous to the IHE case. Since all types of polarisations \mathbf{P}^{\bullet} emerge perpendicular to the applied vector potential shift, they have only one non-vanishing component in the appropriate basis. The bold face

of \mathbf{P}^\bullet is retained so as to indicate its vectorial dimension. Whenever scalars are added, it means that they are added to the non-vanishing component.

At first, the partial Berry connections $\mathcal{A}^\sigma(\mathbf{k})$ are calculated from the Bloch factors of the respective component.

$$\mathcal{A}^\sigma(\mathbf{k}) = \sum_{\alpha=1}^{\bar{n}} \langle u_\alpha^\sigma(\mathbf{k}) | i\nabla_{\mathbf{k}} | u_\alpha^\sigma(\mathbf{k}) \rangle \quad (7.76)$$

where σ denotes the component and α enumerates the Kramers pairs. Then, the partial Berry phases $\chi^{\text{B},\sigma}$ are calculated by integrating $\mathcal{A}^\sigma(\mathbf{k})$ along the edge of the reciprocal unit cell. In order to exploit symmetries from the TRIM-nature of the Γ -point, the integration loop is shifted to the edge of the quadratic Brillouin zone (blue square in Fig. 7.4 (a)).

$$\chi^{\text{B},\sigma} = \oint_{\partial\text{BZ}} \mathcal{A}^\sigma(\mathbf{k}) \cdot d\mathbf{k} \quad (7.77)$$

Finally, each traverse of the \mathbf{k} -vector produces a partial polarisation \mathbf{P}^σ proportional to $\chi^{\text{B},\sigma}$ ⁶:

$$\frac{1}{-e} \mathbf{P}^\sigma = \frac{1}{2\pi} \chi^{\text{B},\sigma} = \frac{1}{2\pi} \oint_{\partial\text{BZ}} \mathcal{A}^\sigma(\mathbf{k}) \cdot d\mathbf{k} \quad (7.78)$$

The Kramers symmetry establishes the following link between $\mathcal{A}^{\text{I}}(\mathbf{k})$ and $\mathcal{A}^{\text{II}}(\mathbf{k})$.

$$\mathcal{A}^{\text{I}}(-\mathbf{k}) = \mathcal{A}^{\text{II}}(\mathbf{k}) + \sum_{\alpha=1}^{\bar{n}} (\nabla_{\mathbf{k}} \chi_\alpha)(\mathbf{k}) \quad (7.79a)$$

$$\mathcal{A}^{\text{II}}(-\mathbf{k}) = \mathcal{A}^{\text{I}}(\mathbf{k}) - \sum_{\alpha=1}^{\bar{n}} (\nabla_{\mathbf{k}} \chi_\alpha)(-\mathbf{k}) \quad (7.79b)$$

The proof for these equations can be found in the appendix (Sec. C.2).

The *sum* of $\mathcal{A}^{\text{I}}(\mathbf{k})$ and $\mathcal{A}^{\text{II}}(\mathbf{k})$ results in the total Berry connection of the system, denoted $\mathcal{A}^+(\mathbf{k})$. It describes the *total charge polarisation* \mathbf{P}^+ and is the same Berry connection as that constructed for the IHE system (Eq. (7.56)). Inserting the Kramers transformation (Eqs. (7.79)) and calculating the curl of $\mathcal{A}^+(\mathbf{k})$ shows that the total Berry potential $\mathcal{B}^+(\mathbf{k})$ is antisymmetric with respect to the Γ -point:

$$\mathcal{A}^+(\mathbf{k}) := \mathcal{A}^{\text{I}}(\mathbf{k}) + \mathcal{A}^{\text{II}}(\mathbf{k}) = \mathcal{A}^{\text{I}}(\mathbf{k}) + \mathcal{A}^{\text{I}}(-\mathbf{k}) - \sum_{\alpha=1}^{\bar{n}} (\nabla_{\mathbf{k}} \chi_\alpha)(\mathbf{k}) \quad (7.80a)$$

$$\mathcal{B}^+(\mathbf{k}) = \nabla_{\mathbf{k}} \times \mathcal{A}^+(\mathbf{k}) = \mathcal{B}^{\text{I}}(\mathbf{k}) - \mathcal{B}^{\text{I}}(-\mathbf{k}) \quad \Rightarrow \quad \mathcal{B}^+(-\mathbf{k}) = -\mathcal{B}^+(\mathbf{k}) \quad (7.80b)$$

For this reason, the surface integral of $\mathcal{B}^+(\mathbf{k})$ over the entire Brillouin zone vanishes, as do the total Berry phase $\chi^{\text{B},+}$ and the total charge polarisation \mathbf{P}^+ .

$$\frac{1}{-e} \mathbf{P}^+ = \frac{1}{2\pi} \chi^{\text{B},+} = \iint_{\text{BZ}} \mathcal{B}^+ \cdot d\mathbf{S} = 0 \quad (7.80c)$$

Eqs. (7.80) permits the following interpretation: The partial polarisations \mathbf{P}^{I} and \mathbf{P}^{II}

⁶Cf. Eq. (7.67) inserting the unit cell volume $|C_{\text{R}}| = 1$ and the reciprocal basis vector $|\mathbf{G}| = 2\pi$.

exactly cancel each other, implying that the Wannier centres of the Kramers pairs move equally into opposite directions. This accords with the expectations from T-symmetry and explains why the topological transport of net charge is inhibited. Of course, the vanishing total polarisation is gauge-invariant, for the same reasons as those discussed in Sec. 7.4.1.

Taking the *difference* between $\mathcal{A}^I(\mathbf{k})$ and $\mathcal{A}^{II}(\mathbf{k})$ results in the time-reversal Berry connection $\mathcal{A}^-(\mathbf{k})$. It describes the *time-reversal polarisation* \mathbf{P}^- . Inserting the Kramers transformation (Eqs. (7.79)) and calculating the curl of $\mathcal{A}^-(\mathbf{k})$ shows that the time-reversal Berry potential $\mathcal{B}^-(\mathbf{k})$ is symmetric with respect to the Γ -point:

$$\mathcal{A}^-(\mathbf{k}) := \mathcal{A}^I(\mathbf{k}) - \mathcal{A}^{II}(\mathbf{k}) = \mathcal{A}^I(\mathbf{k}) - \mathcal{A}^I(-\mathbf{k}) + \sum_{\alpha=1}^{\bar{n}} (\nabla_{\mathbf{k}} \chi_{\alpha})(\mathbf{k}) \quad (7.81a)$$

$$\mathcal{B}^-(\mathbf{k}) = \nabla_{\mathbf{k}} \times \mathcal{A}^-(\mathbf{k}) = \mathcal{B}^I(\mathbf{k}) + \mathcal{B}^I(-\mathbf{k}) \quad \Rightarrow \quad \mathcal{B}^-(\mathbf{k}) = \mathcal{B}^-(\mathbf{k}) \quad (7.81b)$$

Because of the centro-symmetry, the surface integral of $\mathcal{B}^-(\mathbf{k})$ over the entire Brillouin zone equals twice that over the positive half plane (shaded area in Fig. 7.4 (a)). Therefore, the time-reversal Berry phase $\chi^{B,-}$ and, thus, the time-reversal polarisation \mathbf{P}^- are not necessarily zero.

$$\chi^{B,-} = \iint_{\text{BZ}} \mathcal{B}^- \cdot d\mathbf{S} = 2 \iint_{\text{BZ}^+} \mathcal{B}^- \cdot d\mathbf{S} \quad (7.81c)$$

Another representation for $\chi^{B,-}$ follows from the equality of the integrals of $\mathcal{B}^I(-\mathbf{k})$ and $\mathcal{B}^I(+\mathbf{k})$ due to the centro-symmetry of the Brillouin zone:

$$\chi^{B,-} = 2 \iint_{\text{BZ}} \mathcal{B}^I \cdot d\mathbf{S} = 2\chi^{B,I} = -2\chi^{B,II} \quad (7.81d)$$

Eq. (7.81d) immediately implies that the time-reversal Berry phase $\chi^{B,-}$ is quantised: Since each component σ represents a Bloch manifold, the respective partial Berry phase $\chi^{B,\sigma}$ assumes integer multiples of 2π , for the same reasons as those discussed in Sec. 7.4.1. Consequently, the time-reversal Berry phase $\chi^{B,-}$ assumes integer multiples of 4π . In terms of polarisations, the partial polarisations \mathbf{P}^{σ} are up to the sign equal integer multiples of the unit polarisation, $-e$ in this case. The time-reversal polarisation \mathbf{P}^- thus assumes *even* multiples of $-e$.

$$\mathbf{P}^I = -\mathbf{P}^{II} = -i e, \quad i \in \mathbb{Z} \quad \Rightarrow \quad \mathbf{P}^- = -2i e \quad (7.82)$$

The link between these quantities is summarised in the upper part of Fig. 7.4 (b).

Although the time-reversal polarisation \mathbf{P}^- is quantised by a curvature integral, it is not yet an observable as the gauge invariance remains to be proven. From Eq. (C.108), it is clear that the individual partial Berry phases are invariant under $U(\bar{n})$ transformations which mix the states within a fixed component. If the components are well-defined by good quantum numbers, \mathbf{P}^- is gauge invariant in the form of Eq. (7.82) without further restrictions. However, if the components are not conserved, i.e. unitary transformations are considered which mix them, \mathbf{P}^- obviously depends

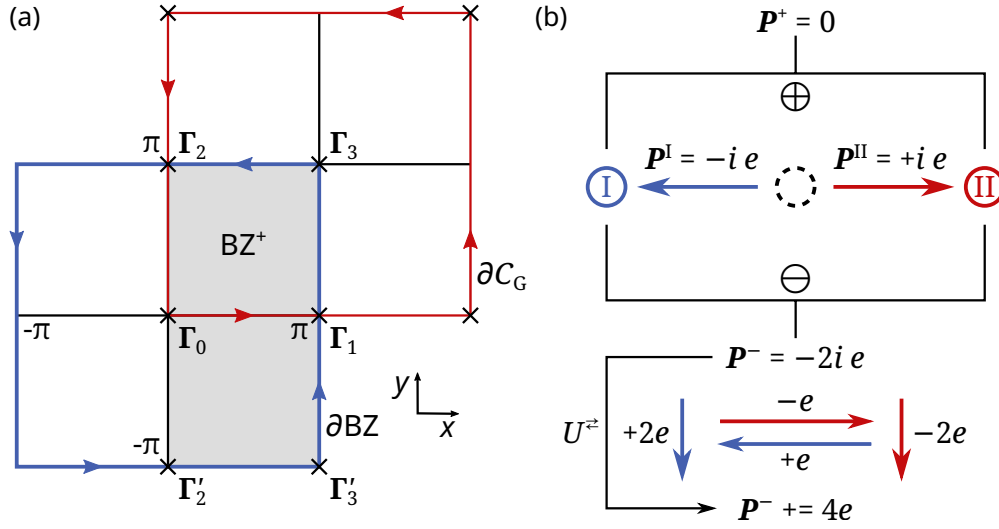


Figure 7.4: (a) Sketch of the reciprocal space of the T-symmetric Bloch system. The red lines indicate the primitive reciprocal unit cell and the blue lines the Brillouin zone. The edges of both can be chosen as the integration path for obtaining the Berry phases. Γ_i are the TRIMs. The positive half plane of the Brillouin zone is shaded grey. (b) Flow chart of the connection between the partial polarisations \mathbf{P}^I and \mathbf{P}^{II} , the total polarisation \mathbf{P}^+ and the time-reversal polarisation \mathbf{P}^- . The lower part shows how a unitary transformation U^z flipping a Kramers pair transfers one unit polarisation $-e$ between \mathbf{P}^I and \mathbf{P}^{II} , which changes them by 2 unit polarisations and increases \mathbf{P}^- by 4 unit polarisations.

on the division of the Kramers pairs into the two components and, thus, on the gauge. The question is then which part of \mathbf{P}^- remains observable. For the answer, consider the action of a unitary transformation U^z which simply swaps the components of a certain Kramers pair. According to Eq. (7.82), the transformation can transfer only even multiples of the unit polarisation from \mathbf{P}^I to \mathbf{P}^{II} . At the same time, the oppositely equal polarisation shifts from \mathbf{P}^{II} to \mathbf{P}^I , so the time-reversal polarisation \mathbf{P}^- changes by multiples of 4 unit polarisations. The effect of U^z is sketched in Fig. 7.4 (b).

The \mathbb{Z}_2 topological invariant

In summary, the time-reversal polarisation \mathbf{P}^- has two properties:

- 1) It is quantised into even multiples of the unit polarisation.
- 2) It is defined only modulo 4 unit polarisations for non-conserved components.

Analogously to the IHE, \mathbf{P}^- produces a current on average, provided that the components are characterised by good quantum numbers, e.g. in spin-conserving Bloch systems. This is exactly the quantum spin Hall effect, where an electric field gives rise to a spin current at a spin Hall conductivity σ_{xy}^- . Property 1) implies that σ_{xy}^- is quantised into even multiples of the quantum conductivity.

$$\sigma_{xy}^- = 2i \sigma_{xy}^0 = -2i e^2/h, \quad i \in \mathbb{Z} \quad (7.83)$$

The integer $2i$ is analogous to the TKNN integer and defines a topological invariant for the same reason.

For non-conserved components, the 4 modulus from property 2) restricts σ_{xy}^- to two values: zero or twice the quantum conductivity.

$$\sigma_{xy}^- = 2i \sigma_{xy}^0 = -2i e^2/h, \quad i \in \mathbb{Z}_2 \quad (7.84)$$

The cyclic structure renders σ_{xy}^- a \mathbb{Z}_2 invariant. All insulating T-symmetric 2D Bloch systems belong either to the trivial class ($i = 0$) or to the non-trivial class ($i = 1$). The latter is referred to as the class of \mathbb{Z}_2 topological insulators or simply \mathbb{Z}_2 insulators. The arbitrariness of the sign of σ_{xy}^- negates the quantum spin Hall effect and questions if there is anything observable at all. The key point is that there *exists* a topologically non-trivial shifting in topologically non-trivial phases and that these phases are distinct from the trivial systems in that they cannot be transformed into each other without closing the band gap.

The analysis presented in this work shows in a systematic and comprehensible way how the \mathbb{Z}_2 topological invariant emerges from the Kramers symmetry by applying methods which are familiar from the IHE. Furthermore, it gives concise reasons for why integrating the Berry connection over the edge of half the Brillouin zone is sufficient for calculating the \mathbb{Z}_2 invariant. The original literature concerning this issue [142, 144, 147] calculates the response of the edges by threading a half quantum flux through a Laughlin cylinder. It employs multiply valued functions and branches of logarithms and square roots in order to extract the \mathbb{Z}_2 invariant. The following equations prove that the \mathbb{Z}_2 formulation presented here is equivalent to that of Fu and Kane [142]. If dropping the factor 2, the remainder of Eq. (7.81c) is the time-reversal polarisation due to the advance of the k-vector across *half* the Brillouin zone. This can then be reformulated in terms of an edge integral of $\mathcal{A}^-(\mathbf{k})$.

$$\begin{aligned} \frac{1}{2} \frac{2\pi}{-e} \mathbf{P}^- &= \iint_{\text{BZ}^+} \mathcal{B}^- \cdot d\mathbf{S} \stackrel{\text{Stokes}}{=} \oint_{\partial\text{BZ}^+} \mathcal{A}^-(\mathbf{k}) \cdot d\mathbf{k} = \oint_{\Gamma_2' \Gamma_3' \Gamma_1 \Gamma_0} \mathcal{A}^-(\mathbf{k}) \cdot d\mathbf{k} + \oint_{\Gamma_0 \Gamma_1 \Gamma_3 \Gamma_2} \mathcal{A}^-(\mathbf{k}) \cdot d\mathbf{k} \\ &\stackrel{(*)}{=} - \int_{\Gamma_0}^{\Gamma_2} [\mathcal{A}^-(\mathbf{k}) + \mathcal{A}^-(-\mathbf{k})] \cdot d\mathbf{k} + \int_{\Gamma_1}^{\Gamma_3} [\mathcal{A}^-(\mathbf{k}) + \mathcal{A}^-(-\mathbf{k})] \cdot d\mathbf{k} \\ &\stackrel{\text{Eq. (C.110)}}{=} - \left(\int_{\Gamma_0}^{\Gamma_2} [\mathcal{A}^+(\mathbf{k}) - \mathcal{A}^+(-\mathbf{k})] \cdot d\mathbf{k} + 2 \sum_{\alpha} [\chi_{\alpha}(\Gamma_2) - \chi_{\alpha}(\Gamma_0)] \right) \\ &\quad + \int_{\Gamma_1}^{\Gamma_3} [\mathcal{A}^+(\mathbf{k}) - \mathcal{A}^+(-\mathbf{k})] \cdot d\mathbf{k} + 2 \sum_{\alpha} [\chi_{\alpha}(\Gamma_3) - \chi_{\alpha}(\Gamma_1)] \quad (7.85) \end{aligned}$$

Step (*) uses that the horizontal paths of ∂BZ^+ in Fig. 7.4 (a) cancel each other because of the boundary conditions of the Bloch factors. For the same reasons, the vertical paths can be mapped onto the upper half plane where $-\overline{\Gamma_2' \Gamma_0}$ equals $\overline{\Gamma_2 \Gamma_0}$ and $-\overline{\Gamma_3' \Gamma_1}$ equals $\overline{\Gamma_3 \Gamma_1}$. The individual terms of Eq. (7.85) equal Eq. (3.21) in [142], from which Fu and Kane derive the \mathbb{Z}_2 invariant as the product of the phases of the Pfaffians of the time-reversal matrix.

Edge states

As noted in the course of defining the \mathbb{Z}_2 invariant, a non-zero time-reversal conductivity (Eq. (7.84)) raises the question whether there is an observable current at all if the components are not conserved. Part of this question is answered in [144]: A weak perturbation which breaks spin conservation alters the former current of quantised spin to a reduced current of magnetisation density along the quantisation axis. However, although the spin quantisation is lifted, the \mathbb{Z}_2 invariant remains the same as long as the perturbation does not close the gap.

Another manifestation of the \mathbb{Z}_2 invariant is the behaviour of the edge states, as illustrated by the Laughlin gedankenexperiment in [142, 147]: Consider a sample of finite width and length which is wound up to a cylinder and has two edges at the top and the bottom. The x-coordinate of the Brillouin zone k_1 parallel to the circumference may be the direction of the applied vector-potential shift. The y-coordinate k_2 parallel to the axis is then the direction of the time-reversal polarisation. The vector potential shift is equivalent to threading a magnetic flux Φ through the cylinder. If the flux (divided by the circumference) equals the quantum flux h/e , the advance in k_1 equals \mathbf{G}_1 , the distance between the TRIM Γ_0 and its copy Γ'_0 . A half quantum flux $h/2e$ thus corresponds to an advance of $\mathbf{G}_1/2$, the distance between the TRIMs Γ_0 and Γ_1 . The setting is sketched in Fig. 7.5 (a).

Once the setting is clear, the gedankenexperiment is as follows. At zero flux ($\mathbf{k} = \Gamma_0$), all Kramers pairs are same-k degeneracies and either doubly occupied or empty. This holds also for any states arising at the edges of the cylinder. If \mathbf{k} now advances by \mathbf{G}_1 towards Γ'_0 , one of two possibilities occurs:

- 1) The band structure is trivial and the Kramers pairs associated with the edges end up in the same configuration as the initial one, i.e. states which are Kramers partners at Γ_0 are also partners at Γ'_0 , as sketched in Fig. 7.5 (b). For example, the Kramers pair denoted 1 splits up at Γ_0 , but finds together again at Γ'_0 . In particular, if this Kramers pair is doubly occupied in the beginning, it will be doubly occupied in the end. This accords with the prerequisite that the time-reversal polarisation due to the traverse of the k-vector has to be zero.
- 2) The band structure is non-trivial and the Kramers pairs associated with the edges end up in a configuration different from the initial one, i.e. the states change partners, as sketched in Fig. 7.5 (c). For example, Kramers pair 1 splits up at Γ_0 and its upper branch (red) goes to Kramers pair 2 at Γ'_0 where it finds a new partner from the bulk conduction bands. The lower branch (blue) vanishes in the bulk valence bands. In turn, the Kramers pair 1 at Γ'_0 is restored by a blue branch from Kramers pair 2 and a red branch from the bulk valence bands. As a consequence of the partner change, if Kramers pair 1 is doubly occupied and Kramers pair 2 is empty in the beginning, they both will be singly occupied in the end, which corresponds to the transport of one electron. Since the opposite happens at the other edge, the net charge transport is zero. However, the time-reversal polarisation amounts to 2 unit polarisations, which reflects the non-trivial \mathbb{Z}_2 invariant.

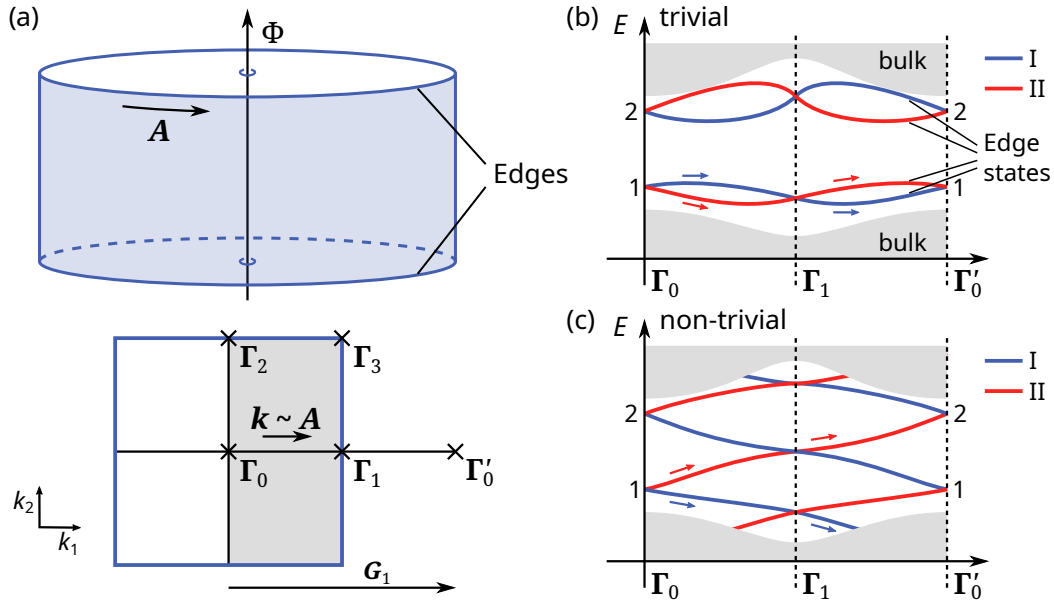


Figure 7.5: (a) Sketch of the Laughlin-type gedankenexperiment. The sample is wound up to a finite cylinder and provides two edges. A magnetic flux Φ threading the cylinder corresponds to a shifting of the vector potential A , which in turn makes the k -vector \mathbf{k} advance in that direction. (b) and (c): Sketches of possible topologies of T -symmetric edge band structures. Only the bands of one edge are shown, where red and blue lines indicate the two components. The bulk bands are shaded grey. At the TRIMs, red and blue bands have to form a same- k Kramers degeneracies. In (b), the Kramers pairs at different TRIMs are trivially connected ($\sigma_{xy}^- = 0$), which allows the edge states to form a band gap. In (c), they are non-trivially connected ($\sigma_{xy}^- = 2\sigma_{xy}^0$), which strictly prohibits the formation of band gaps. Adapted from [147].

As it is evident, the non-trivial band structure in Fig. 7.5 (c) guarantees that the Fermi level cuts at least one band associated with the edges of the cylinder. Furthermore, a Laughlin gedankenexperiment with swapped roles for k_1 and k_2 obviously yields the same results. This leads to the conclusion that the edges of a non-trivial \mathbb{Z}_2 insulator in general host metallic edge states which are topologically protected, i.e. *there is no way to introduce a band gap within an adiabatic, T -symmetric transformation*. On the contrary, the trivial band structure in Fig. 7.5 (b) either provides a gap in the edge states or the bands can be adiabatically shifted so that a gap opens.

The schematic band structures in Fig. 7.5 (b) and (c) moreover show that the topological character of the edge states does not only emerge if the Laughlin-type gedankenexperiment is performed for a full Brillouin-zone traverse of \mathbf{k} from Γ_0 to Γ'_0 . Since the T -symmetry strictly produces TRIMs halfway along the reciprocal basis vectors, also the half traverse from Γ_0 to Γ_1 causes topologically distinctive partner changes. In the trivial case, the states of each Kramers pair at Γ_0 find together again at Γ_1 . In the non-trivial case, the states of each Kramers pair at Γ_0 find new partners at Γ_1 . The Laughlin-type gedankenexperiment works also for a half quantum flux because the time-reversal Berry potential is symmetric, so integrals over the half of the Brillouin zone are sufficient for the calculation of the \mathbb{Z}_2 invariant.

7.4.3 The three-dimensional \mathbb{Z}_2 insulator

The \mathbb{Z}_2 classification of a T-symmetric 3D Bloch system is based on the behaviour of its surface states in the presence of a perturbing vector-potential shift. Analogously to the edge band structure in the 2D case, a surface band structure is topologically non-trivial if the surface states change partners when going from one TRIM to another. However, differently from the 2D case, there are more than one possibilities to make such considerations in three dimensions:

Firstly, instead of two edges in the 2D case, a 3D crystal has three main surfaces which are defined by the reciprocal basis vectors \mathbf{G}_j acting as surface normals. Secondly, instead of four TRIMs in the 2D case, the 3D Brillouin zone provides eight TRIMs $\{\Gamma_i\}$, which are determined analogously to Eq. (7.75) by taking also the third reciprocal basis vector \mathbf{G}_3 into account. For the sake of simplicity, the direct and reciprocal unit cells of the T-symmetric 3D crystal to be characterised are supposed to be both cubic. Then, the TRIMs define the vertices of a cube which is exactly an eighth of the cubic Brillouin zone (Fig. 7.6).

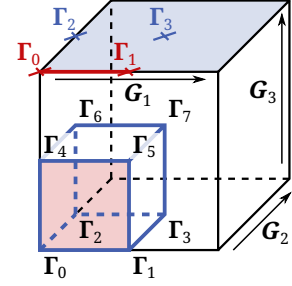


Figure 7.6: TRIMs Γ_i in a cubic Brillouin zone.

Instead of one TRIM pair per edge in the 2D case, each surface of a T-symmetric 3D crystal provides six different TRIM pairs between which the surface band structure can be topologically trivial or non-trivial. The topological character is determined by quantifying the topological transport on a square which is defined by the respective TRIM pair and the two opposite TRIMs of the TRIM cube. In detail, the identification of non-trivial phases is analogous to the following example:

- Consider the surface defined by the surface normal \mathbf{G}_3 (shaded blue in Fig. 7.6).
- Consider the first surface k-path defined by $\overline{\Gamma_0\Gamma_1}$, which is parallel to \mathbf{G}_1 (red labels in Fig. 7.6).
- Calculate the time-reversal polarisation along \mathbf{G}_3 due to a vector-potential shift along \mathbf{G}_1 by integrating $\mathcal{B}^-(\mathbf{k})$ in the square spanned by \mathbf{G}_1 and \mathbf{G}_3 . According to Eq. (7.85), this corresponds to an integration within the TRIM square $(\Gamma_0, \Gamma_1, \Gamma_5, \Gamma_4)$ (red face in Fig. 7.6).

If the time-reversal polarisation in that square is zero, the surface band structure along $\overline{\Gamma_0\Gamma_1}$ is trivial and looks like that Fig. 7.5 (b). Otherwise, it is non-trivial and characterised by partner changes (Fig. 7.5 (c)). The above procedure can be repeated for all surface paths defined by pairs out of $\{\Gamma_0, \Gamma_1, \Gamma_2, \Gamma_3\}$. If the \mathbf{G}_3 -surface is completely characterised, the above procedure can be performed also for the two other surfaces defined by \mathbf{G}_1 and \mathbf{G}_2 .

It is obvious that the above procedure has many redundancies. For example, if the \mathbf{G}_3 -surface paths $\overline{\Gamma_0\Gamma_1}$ and $\overline{\Gamma_0\Gamma_2}$ are both non-trivial, the \mathbf{G}_3 -path $\overline{\Gamma_1\Gamma_2}$ must be trivial because the \mathbb{Z}_2 invariant is only defined modulo 2. Moreover, the \mathbf{G}_3 -surface path $\overline{\Gamma_0\Gamma_1}$ and the \mathbf{G}_1 -surface path $\overline{\Gamma_0\Gamma_4}$ share the topological character because the TRIM

square for calculating the \mathbb{Z}_2 invariant is the same⁷. In order to remove those redundancies, Fu and Kane simplified the characterisation by transforming Eq. (7.85) into a form which relates the topological transport to a product of units $\delta_i(\mathbf{k})$ which are evaluated at each TRIM of the respective TRIM square. These units are the ratio between the square root of the determinant of the time-reversal matrix $w(\mathbf{k})$ and the Pfaffian of $w(\mathbf{k})$. In doing so, the branch of the square root has to be continuous between TRIM pairs. For a T-symmetric 2D Bloch system, the \mathbb{Z}_2 invariant is non-trivial if the product of the four δ_i is -1 . If the product is $+1$, the system is trivial [142].

$$(-1)^v = \prod_{i=0}^3 \delta_i, \quad \delta_i = \frac{\sqrt{\det(w(\Gamma_i))}}{\text{Pf}(w(\Gamma_i))} \in \{-1, +1\} \Rightarrow v \in \mathbb{Z}_2 \quad (7.86)$$

A T-symmetric 3D Bloch system has eight TRIMs and thus eight δ_i . Consequently, there are still many possibilities of how the signs can be distributed over the cube. However, five important cases can be distinguished:

- 1) All eight δ_i are positive.
- 2) Two δ_i on an edge of the cube are negative, while the others are positive.
- 3) Two δ_i on a face diagonal are negative, while the others are positive.
- 4) Two δ_i on a space diagonal are negative, while the others are positive.
- 5) One δ_i is negative, while the others are positive.

All other configurations can be transformed into one of the above cases by gauge transformations, i.e. by changing the signs of four δ_i lying in the same plane. In particular, case 5) is equivalent to all cases where an odd number of δ_i is negative.

Case 1) is the trivial case as each TRIM square yields a δ_i product of $+1$. Consequently, each surface path supports a topologically trivial surface band structure. Cases 2), 3) and 4) produce topologically non-trivial surface band structures for a differing number of surfaces and paths. These systems can be imagined as a stack of independent 2D \mathbb{Z}_2 insulators whose one-dimensional edges host topologically protected metallic states. However, because the non-triviality is unstable against redefining the Brillouin zone, as it may occur in the presence of disorder, the edge states are not protected against all adiabatic, T-symmetric transformations. For this reason, these systems are referred to as *weak topological insulators* [147].

The last case 5) is relevant for this work. Since only one δ_i is negative, any surface contains one TRIM from which all surface paths produce non-trivial band structures. Since case 5) is equivalent to all cases with an odd number of negative δ_i , a 3D \mathbb{Z}_2 invariant ν_0 can be defined via the sign of the product of all eight δ_i .

$$(-1)^{\nu_0} = \prod_{i=0}^7 \delta_i, \quad \delta_i = \frac{\sqrt{\det(w(\Gamma_i))}}{\text{Pf}(w(\Gamma_i))} \in \{-1, +1\} \Rightarrow \nu_0 \in \mathbb{Z}_2 \quad (7.87)$$

⁷This is the reason why the T-symmetric 2D Bloch system with two edges and four TRIMs is characterised by only one \mathbb{Z}_2 invariant.

As the non-triviality is stable against redefining the Brillouin zone, the metallic surface states enjoy a topological protection which is similar to that of the metallic edge states of the 2D \mathbb{Z}_2 insulator. For this reason, systems with non-trivial ν_0 are referred to as *strong topological insulators* [147] and the subsequent surface states as *topologically protected surface states* (TSSs). As strong \mathbb{Z}_2 TIs are the only TIs considered in this work, the term topological insulator is used for them in an equalising manner.

Topological insulators with inversion symmetry

Although the definition and general properties of \mathbb{Z}_2 insulators are clear, the calculation of the \mathbb{Z}_2 topological invariant for a concrete system remains complicated. The definition via the time-reversal Berry potential (Eq. (7.81c)) in principle resolves the continuous-gauge problem since the Berry potential can be calculated locally by the matrix elements of well-defined derivatives of the Hamilton operator (Eq. (7.58)). On the other hand, the evaluation will be tedious in the 3D case because of the above-mentioned combinatorial inflation due to the different surfaces and paths. The approach of [147] provides a simplification of the combinatorics by defining a single 3D \mathbb{Z}_2 invariant via the product of the δ_i of all TRIMs (Eq. (7.87)). Though, concrete calculations still involve some exertion since the branches of the numerator and the denominator of Eq. (7.87) have to be continuous over the entire TRIM cube.

Fortunately, there is one case in which the evaluation of Eq. (7.87) becomes particularly simple: If inversion symmetry (P-symmetry) is present, then the δ_i equal the product of the parity eigenvalues of the respective Kramers pairs. Thus, if the solving Bloch eigenspace is given, the δ_i can directly be determined from the Bloch factors without need for caring about the continuity of the branches of Eq. (7.87).

$$\delta_i = \prod_{\alpha=1}^{\bar{n}} p_{\alpha}(\Gamma_i) \quad (7.88)$$

where $p_{\alpha}(\Gamma_i)$ denotes the parity eigenvalue of the Kramers pair with index α at the TRIM $\mathbf{k} = \Gamma_i$ [147]. Of course, Eq. (7.88) works both in the 2D and the 3D case.

As a last remark, the parity method does not only simplify the topological classification of insulators with P-symmetry. Also systems without P-symmetry are suitable for it if they are proven to be adiabatically connected to a TI with P-symmetry. This holds because any adiabatic transformation which retains the band gap conserves the topological invariants. This considerably broadens the applicability of the parity method and makes it the method of choice for identifying \mathbb{Z}_2 insulators [147].

8 The bulk phases of bismuth selenide and antimony

Bismuth selenide and antimony, the materials composing the $\text{Sb@Bi}_2\text{Se}_3$ heterostructures, have two properties in common:

- 1) They involve heavy p-block elements: the medium-heavy fourth-row element selenium (Se, $Z = 34$), the heavier fifth-row element antimony (Sb, $Z = 51$), and the sixth-row element bismuth (Bi, $Z = 83$), the heaviest stable element of the periodic table¹. As a consequence of the high atomic numbers, strong relativistic effects are expected to determine the physical properties of both the Bi_2Se_3 substrate and the β -Sb adsorbate.
- 2) They are van der Waals materials, i.e. they comprise chemically saturated layers whose mutual bonding underlies vdW interactions.

These peculiarities make approaches beyond standard DFT necessary in order to correctly describe the $\text{Sb@Bi}_2\text{Se}_3$ heterostructures. Spin-orbit coupling (SOC) allows for the most important relativistic effects in the valence shells (Sec. 2.1.2). The vdW interactions are introduced by adding the London dispersion to the total energy (Sec. 2.1.3).

The first purpose of this chapter is to test the SOC and vdW approaches on the bulk phases of Bi_2Se_3 and β -Sb, for which experimental lattice parameters exist, contrarily to the heterostructures. Particularly the vdW corrections have to be tested because there are several implementations with different degrees of empiricism. The interlayer distances are the central quantities to check since it is expectable that the vdW corrections mostly influence those. Furthermore, the structural effects from SOC are paid a special attention. In many previous investigations, SOC is only included for calculating the final band structures, while it is omitted during the structure optimisations. It will turn out that SOC alters the interlayer distances in a non-negligible manner.

The second purpose of this chapter concerns the electronic and topological properties of Bi_2Se_3 and β -Sb, which are absolutely crucial for understanding the topological phase transitions in the heterostructures. In detail, the band structures of bulk Bi_2Se_3 and β -Sb and, in addition, the two-dimensional band structures of free-standing thin β -Sb sheets are calculated and analysed. The \mathbb{Z}_2 invariant is explicitly calculated for these systems with the parity method (Sec. 7.4.3).

¹In fact, bismuth is radioactive. However, the decay is extremely slow with an half-life of $1.9 \cdot 10^{19}$ yr. It was not before 2003 until the instability of the most abundant isotope was proven [149].

8.1 Bismuth selenide

Bismuth selenide is a compound of the pnictogen² bismuth (Bi) and the chalcogen³ selenium (Se). Its structure belongs to the trigonal, P-symmetric $R\bar{3}m$ space group (No. 166), in which the atoms occupy the Wyckoff positions $\text{Se} \rightarrow 1a$, $\text{Se} \rightarrow 2c$ and $\text{Bi} \rightarrow 2c$. Bi_2Se_3 belongs to the class of *van der Waals materials* or *sparse matter*. It is clearly layered, consisting of covalently bound sheets which in turn stick together by vdW interactions. In detail, each Bi_2Se_3 unit forms a *quintuple layer* (QL) of five atoms, which arrange themselves as hexagonal atomic layers according to an (ABCAB) sequence. The QLs in turn stack in such a way that the layer sequence continues, implying an axial periodicity length of 15 atomic layers or 3 QL: (ABCAB)(CABCA)(BCABC). The structure is sketched in Fig. 8.1 (a) and (b).

The microscopic reason for the layered structure is a closed-shell configuration of the individual QLs [150]. However, the octet rule is obviously not fulfilled as the Bi and Se atoms coordinate each other in (half-complete) octahedral geometry. Since Se is more electronegative than Bi by $\Delta\chi = 2.48 - 1.67 = 0.81$ according to the Allred-Rochow scale [17, Tafel III], the bonding is expected to be covalent with a partial ionic character of ca. 10% [17, p. 158]. The Se atoms are in a negative oxidation state of $-II$, which completes the octets. The Bi atoms, on the other hand, are in a positive oxidation state of III , two less than the maximum of V for members of group 15.

The reasons for the stability of the III -valent state of Bi are numerous, but all based on the low ability of the 6s electrons to participate in chemical bonding. A comparison between the pnictogens (Pn) shows that P assumes the oxidation state V in many compounds, while all other Pn prefer the oxidation state III . This manifests itself, for instance, in the redox potentials of the $\text{Pn}(V)/\text{Pn}(III)$ acidic systems: they are negative for P, positive for N, As and Sb, and by far the highest for Bi [17, p. 962]. Four different, countercurrent effects are responsible for this:

- 1) The higher main quantum number of heavier homologues loosens the valence electrons. Therefore, P is more willing to donate its s electrons than N.
- 2) The d-block contraction binds the valence electrons closer the nucleus. Therefore, As and Sb are less willing to donate their s electrons than P.
- 3) The f-block contraction or lanthanoid contraction binds the valence electrons closer the nucleus. Therefore, Bi is even less willing to donate its s electrons than As and Sb.
- 4) The relativistic effects contract mainly the s orbitals and bind them closer to the nucleus. They are considerable for the heaviest elements, to which Bi belongs.

As a consequence of 2), 3) and 4), the 6s electrons of Bi are so tightly bound that they behave almost like core states and become chemically inert. Hence, this effect is called the *inert-pair effect* (or lone-pair effect) [17, pp. 335ff, 373ff, 961ff]. As only the 6p orbitals of the Bi atoms are left for binding, the bonds arrange themselves in

²Also denoted pentels, group 15, the nitrogen group: N, P, As, Sb and Bi.

³Group 16, the oxygen group: O, S, Se, Te and Po.

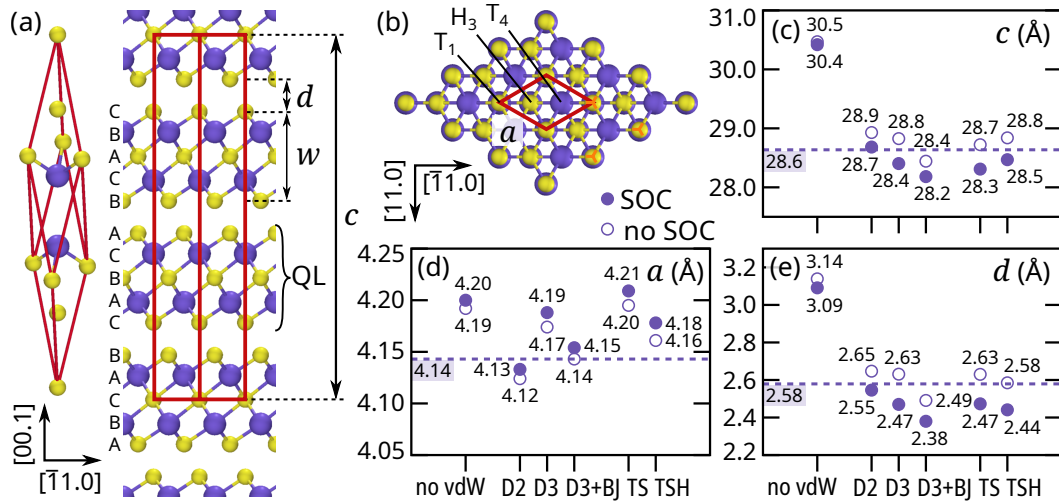


Figure 8.1: Bulk structure of Bi_2Se_3 . Purple circles are Bi atoms; Light green circles are Se atoms. (a) Side view; (b) Top view. The conventional unit cell is marked red. (a) shows the rhombohedrally centred primitive unit cell as well. Orange stars in (b) mark some T_1 positions of the (0001) surface. (c) – (e) Lattice parameters a , c and d of the structures optimised by code-level relaxations within different approaches for the vdW corrections (x-axis, see text) and SOC (empty and filled circles). The experimental reference [153] is inserted as dashed lines.

an octahedral geometry with angles close to 90° . This obviously holds in Bi_2Se_3 quite strictly as Bi and Se coordinate each other in (half-)complete octahedral geometries. That also the Se atoms obviously underlie p bonding without hybridising with the 4s electron is presumably due to a steric effect from the p orbitals of the Bi atom. In the lighter homologous compounds Sb_2Se_3 and As_2Se_3 , the pnictogens coordinate the Se atoms in a twofold and threefold manner [151, 152], not in a sixfold manner as in the case of the Se atom in the middle of the QLs.

8.1.1 Structure optimisation

Computational parameters

The DFT calculations are carried out with VASP [2, 3] using PAW potentials and the PBE xc-functional [10, 21, 22]. The Bi and Se atoms have PAW valences of $5d^{10}6s^26p^3$ and $4s^24p^4$, respectively. The kinetic energy cutoff is $E_{\text{cut}} = 400$ eV. The Brillouin zone is sampled by a Γ -centred Monkhorst-Pack mesh [117] at a density of $12 \times 12 \times 3$ k-points for the hexagonal unit cell. The Brillouin-zone integration is carried out by the tetrahedron method with Blöchl corrections [118] for all calculations as the compound is a semiconductor. A convergence test proves that increasing the energy cutoff or the sampling density alters the total energy by ≈ 1 meV per atom. The ionic forces are calculated according to the Hellmann-Feynman theorem [119]. The ions move along them towards the equilibrium positions and stop to relax if the forces acting on each ion are smaller than 0.005 eV/Å.

For different combinations of vdW approaches and SOC/no SOC, the volume of the hexagonal unit cell is optimised by the code-level routines. For the combination reproducing the experimental reference best, the volume optimisation is repeated by the more exact Murnaghan equation of state (vide supra, p. 41). The six vdW approaches tested are: no vdW correction, DFT-D2 [26], DFT-D3 + zero-damping [27], DFT-D3 + Becke-Johnson damping [28], the Tkatchenko-Scheffler method [29], and the Tkatchenko-Scheffler method with iterative Hirshfeld partitioning [30, 31].

Volume optimisation

The relevant lattice parameters of the hexagonal unit cell of Bi_2Se_3 are: the basal lattice constant a , the axial lattice constant c , the interlayer distance d , defined as the difference between the z -coordinates of the outer Se atoms of adjacent QLs, the QL width $w = c/3 - d$, and the Wyckoff parameters of the rhombohedral centring u (Bi atoms) and v (outer Se atoms). The results for a , c and d may be found in Fig. 8.1 (c), (d) and (e), respectively. The experimental lattice parameters (XRD, [153]) are inserted as dashed lines.

The vdW correction strongly affects the interlayer distance d , which is expectable for a vdW material. Compared to the calculations without dispersion correction (no vdW), the QLs move closer together by more than 0.5 \AA when any vdW implementation is enabled. This corresponds to a shrinkage of d by more than -15% . Once vdW is enabled, the different implementations alter d to a lesser extent. All vdW-corrected values vary by ca. 0.15 \AA and approach the experimental reference up to a few percent. The QL width w and the basal lattice constant a are almost indifferent to the vdW implementation. Their values range around the experimental reference by ca. 1% , even if vdW is disabled. As w is rigid, the axial lattice constant c congruently follows the interlayer distances d . Concerning the effects from SOC, the geometry of the individual QLs is almost indifferent. Both a and w slightly increase by ca. $+0.3 \%$ upon enabling SOC, which is far less than the already small variations due to the vdW implementation. In contrast, d is surprisingly quite sensitive to whether SOC is enabled or not. It contracts by -1.5% when vdW is disabled, and even stronger by ca. -5% when any vdW correction is enabled. The axial lattice constant c inherits the behaviour of d .

As the combination of DFT-D2 and SOC yields lattice parameters which are very close to the experimental reference, the volume for this set is redetermined with a Murnaghan relaxation. The resulting lattice parameters are compiled and compared with the experimental reference [153] in Tab. 8.1. The Murnaghan-relaxed DFT-D2+SOC structure is very close to the experimental one. The lattice constants deviate by less than 0.5% . The unit-cell volumes are even closer together, deviating by only -0.1% . The distribution of c into d and w shows a bit more deviation (-0.9% and $+0.8 \%$, respectively). The experimental and theoretical Wyckoff parameters u and v agree. The bond distances in the DFT-D2+SOC structure are 2.87 \AA for the outer Bi-Se bond and 3.06 \AA for the inner Bi-Se bond. This accords with the coordination polyhedrons: Because the inner Se atom is higher coordinated (six Bi atoms), the individual Bi-Se bonds are expected to be weaker and thus to be longer than those of the lower coordinated outer Se atom (three Bi atoms). Another point of view on this

	a (Å)	c (Å)	c/a	d (Å)	w (Å)	u	v
Exp. [153]	4.143	28.636	6.91	2.579	6.966	0.4008	0.2117
DFT-D2 + SOC	4.134	28.732	6.95	2.556	7.021	0.4000	0.2111
Deviation	-0.2 %	+0.3 %		-0.9 %	+0.8 %		

Table 8.1: Lattice parameters of bulk Bi_2Se_3 . The unit cell was optimised by Murnaghan relaxations, including DFT-D2 and SOC. Experimental reference: [153].

is based on the ionic character of the Se–Bi bonds: The inner one is expected to be more ionic wherefore it is closer to the sum of the respective ionic radii. On the contrary, the outer one is expected to be closer to the sum of the respective covalent radii [153]. The bond angles are all close to 90° : 92.1° , 91.3° , 84.9° , 84.9° and 95.1° from the outer to the inner angles. Hence, the Bi–Se octahedrons are almost regular, which indicates a bonding majorly based on the p orbitals.

8.1.2 Electronic properties

The band structure of the bulk phase of Bi_2Se_3 is calculated in a manner which is analogous to Sec. 4.3. All system-specific parameters are the same as those of the relaxations above. In particular, the bands are calculated with SOC. The trigonal unit cell of the DFT-D2+SOC structure is used. As the (0001) surface of the hexagonal unit cell is of special interest later in this work, the corresponding symmetry points K, M and Z are identified in the trigonal unit cell and chosen as vertices for the k-path⁴. Fig. 8.2 shows the bands. The line colour corresponds to the colour bars above the panels: (a) Bi/Se portions in all PAW projections, (b) s-orbital/p-orbital portions in all PAW projections, (c) $(p_x + p_y)$ -orbital/ p_z -orbital portions in all p-orbital projections. The line widths in (a) and (b) are constant and that in (c) corresponds to the sum of the p-orbital projections of all atoms.

The first conspicuous feature of the band structures consists in a strict separation of the p bands lying near the Fermi level from the s bands lying at higher binding energies. The three lower, electron-like s bands accept the six Se-4s electrons. The two higher, hole-like s bands accept the four Bi-6s electrons. The two sets of s bands are separated by a gap of ≈ 1.5 eV. The s bands in total are separated from the p bands by a gap of ≈ 2.5 eV. That the deep and almost localised s electrons do not contribute much to the bonding between the Bi and Se atoms perfectly agrees with the expectations from the inert-pair effect. The nine p bands below the Fermi level host the 18 p electrons from the constituents and are separated from the conduction bands by a global band gap of ≈ 0.3 eV. The mixed Se-Bi character indicates a nearly covalent binding between the p orbitals, which agrees well with the intermediate electronegativity difference and the regular coordination octahedrons in the Bi_2Se_3 structure.

⁴The $\overline{\text{M}\Gamma}$ path and the $\overline{\Gamma\text{K}\text{M}}$ path in Fig. 8.2 are straight, perpendicular line segments. Since the two M-points are not the same in the rhombohedral centring, they provide different eigenvalues. They become identical in the hexagonal unit cell up to C_3 and PT symmetry operations.

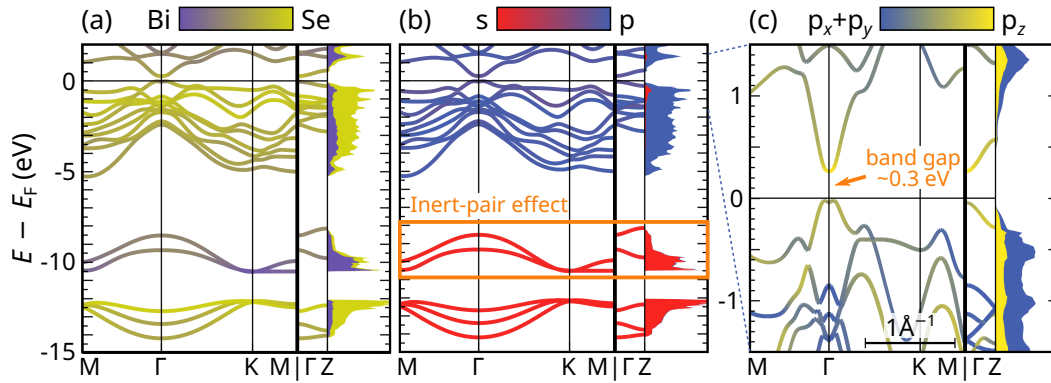


Figure 8.2: Band structure of Bi_2Se_3 for the rhombohedrally centred DFT-D2+SOC structure. The symmetry points correspond to the hexagonal unit cell. The line colour corresponds to the colour bars above the panels. (a) Bi portion (purple) vs. Se portion (light green) in all PAW projections; (b) s-orbital portion (red) vs. p-orbital portion (blue) in all PAW projections; (c) $(p_x + p_y)$ -orbital portion (blue) vs. p_z -orbital portion (yellow) in the p-orbital projections of all atoms (line width) round the Fermi level. The respective PDOSs are plotted against the y-axis to right of the band structures in arbitrary units.

The \mathbb{Z}_2 invariant

The relativistic effects are so strong in Bi_2Se_3 that its bands distort into a \mathbb{Z}_2 insulating system. From an interpretational point of view, SOC gives rise to a repulsion between states having the same parity and total angular momentum, e.g. $|p_z^+, \uparrow\rangle$ and $|p_{x+iy}^+, \downarrow\rangle$. In Bi_2Se_3 , the repulsion inverts the band order at the Γ -point in that a P-symmetric p_z band and a P-antisymmetric p_z band swap occupations. At the other TRIMs, the band order remains the same [154]. The remainder of the band inversion is visible in Fig. 8.2 (c). Near the Γ -point, the CBM and the VBM are of p_z character. The valence band shows a clear furrow and the conduction band is apparently flatter than a parabola. This is the result of overlaying two parabolae and introducing gaps at the intersections. A comparison between the Bi_2Se_3 band structures with and without SOC which clarifies this issue can be found in [154]. The new point about the band structures presented here consists in the colouring which proves that the band inversion at the Γ -point indeed happens in the p_z states, as schematised in [154].

In order to verify that Bi_2Se_3 is indeed a TI, the \mathbb{Z}_2 topological invariant is explicitly calculated by means of the parity method. For this purpose, the Quantum Espresso (QE) package [4, 5] is employed because the parities are difficult to extract from the VASP output. The pseudopotentials are taken from the pslibrary (straightforward valency + d electrons, PAW, PBE, full-relativistic). The ground-state density of the above rhombohedrally centred DFT-D2+SOC structure is obtained at a cutoff energy of 60 Ry and a k-point mesh of $12 \times 12 \times 12$. For this ground-state density, the eigenvalues and eigenfunctions are calculated at the eight TRIMs $\{\Gamma_i\}$. Then δ_i is calculated for each TRIM by extracting the parities of the Kramers pairs and inserting them into Eq. (7.88). The product of all eight δ_i returns the \mathbb{Z}_2 invariant by Eq. (7.87). The rhombohedral unit cell of Bi_2Se_3 has 78 valence electrons (30 Se-3d + 20 Bi-5d + 6 Se-4s + 4 Bi-6s + 12 Se-4p + 6 Bi-6p). Including all the bands returns $\delta_0 = -1$ for Γ_0 ,

the Γ -point, and $\delta_i = +1$ for all other TRIMs. Thus, Bi_2Se_3 is a topologically non-trivial \mathbb{Z}_2 insulator. According to the classification by Fu and Kane [147], the topological class is $1;(000)$, where the first integer indicates the 3D \mathbb{Z}_2 invariant. Repeating the procedure for the s and p electrons only, leaving the d electrons out, yields the same result, as expected from the non-binding nature of the complete d shells. A more interesting case consists in calculating the \mathbb{Z}_2 invariant for the p electrons only and leaving the s electrons out. This is rectified as the two submanifolds are separated by a finite band gap. The s bands yield a trivial \mathbb{Z}_2 invariant, while the p bands yield a non-trivial \mathbb{Z}_2 invariant. This underlines the inert-pair effect and that the topological non-triviality is solely due to the ordering of the p bands. Repeating the procedure for the hexagonal unit cell yields the same results, as expected from the stability of the 3D \mathbb{Z}_2 invariant against band folding.

8.2 Antimony

Antimony denotes the elemental phase of the pnictogen Sb^5 , the lighter, fifth-row homologue of Bi. Before analysing its structure, also in view of the heterostructures, it is instructive to compare the different bulk phases of the pentels: In order to complete the octets, the pentels tend to cross-link in mutual trigonal-pyramidal coordination. There are several possibilities for saturating all bonds, the *allotropes*, whose stability depends on the thermodynamic boundary conditions. Phosphorus, for instance, adopts two metastable phases: white phosphorus (P_4 tetrahedrons) and violet phosphorus (cross-linked tubes). Mediated by pressure, they transition into the orthorhombic black phase, which is stable under normal conditions. Under high pressure ($>80\,000$ bar), the black phase reversibly transitions into a further, rhombohedral modification [17, pp. 849ff]. Both the orthorhombic, low-pressure phase (the α -phase⁶) and the rhombohedral, high-pressure phase (the β -phase) are vdW materials consisting of few-atoms layers wherefore they are of special interest in this work. Bulk As adopts both the α -phase and the β -phase under normal conditions, with the difference to P that the α -phase (semiconducting, black) is only metastable and the β -phase (semimetallic, grey-lustrous) is stable. For Sb and Bi, the α -phase becomes

⁵There are two Latin words for the mineral stibnite Sb_2S_3 : the medieval word *antimonium* and the ancient word *stibium*. While the origin of the former is unclear, the latter stems from an ancient cosmetic product. Today, antimony refers only to the elemental metal, while for derivatives, the root *stib-* should be used. Of course, the latter name is the origin of the chemical symbol Sb.

Heilen mit Antimon: Von der Chiematrie zur Chemotherapie, <https://www.pharmazeutische-zeitung.de/inhalt-10-2000/titel-10-2000/> (visited on 21/05/2022).

The ancient Romans used “stimii” or “stibi” for pharmaceutical and cosmetic purposes. Plinius Maior wrote in his famous encyclopedia “Naturalis Historia” that the drying and tightening properties of stibium were used by women, who covered the area round their eyes with stibnite additives so as to widen them. The literal translation of “platyophthalmion” exactly means that.

Gaius Plinius Secundus (Plinius Maior), *Naturalis Historia*, Liber XXXIII.101f

⁶The terminology is not unique as, in fact, α -P and β -P denote modifications of white phosphorus P_4 [17, p. 850]. The nomenclature used in this work concentrates on the distinction between the isolated layers from the two layered phases (black phosphorus and high-pressure phosphorus). It is common in most works dealing with thin Pn sheets [P5, P10, 155–157].

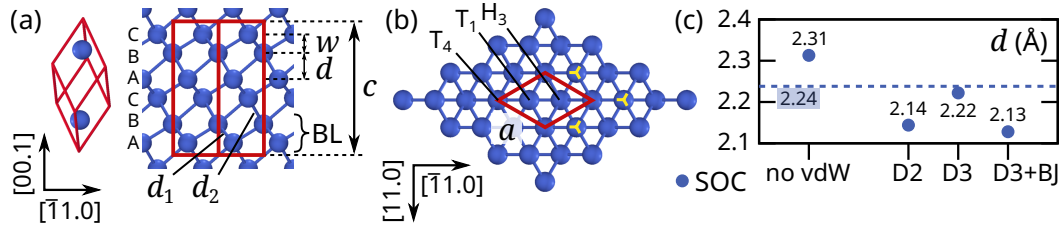


Figure 8.3: Bulk structure of β -Sb. Blue circles are Sb atoms. (a) Side view; (b) Top view. The conventional unit cell is marked red. (a) shows the rhombohedrally centred primitive unit cell as well. Yellow stars in (b) mark some T_1 positions of the (0001) surface. (c) Interlayer distance d of the structures optimised by Murnaghan relaxations with SOC and different vdW schemes (see text). The experimental reference [158] is inserted as a dashed line.

entirely unstable and only the β -phase remains stable under normal conditions. β -Sb is a semimetal like β -As, while β -Bi is a metal [17, pp. 943ff].

Like Bi_2Se_3 , β -Sb belongs to the trigonal, P-symmetric $R\bar{3}m$ space group (No. 166). The Sb atoms occupy the Wyckoff position $2c$. β -Sb consists of covalently bound sheets of buckled-honeycomb-Sb which stack in a manner that the lower Sb atom of the next sheet is over the H_3 position of the previous one. The individual sheets are considered as *bilayers* (BLs), which stack according to a layer sequence with an axial periodicity of 6 atomic layers or 3 BL: (AB)(CA)(BC). The structure of β -Sb is sketched in Fig. 8.3 (a) and (b). Obviously, the BLs come so close together that the distance between them is not much larger than their width. In terms of bond distances, d_1 , the Sb–Sb distance within the BLs, is not much larger than d_2 , the distance across. This is a trend in the pnictogens as the d_2/d_1 ratio decreases from P to Bi so that the β -phase approaches the cubic primitive structure [17, p. 943].

8.2.1 Structure optimisation

Computational parameters

The DFT calculations are carried out with VASP [2, 3] using PAW potentials and the PBE xc-functional [10, 21, 22]. The Sb atoms have a PAW valence of $5s^25p^3$. The kinetic energy cutoff is $E_{\text{cut}} = 300$ eV. The Brillouin zone is sampled by a Γ -centred Monkhorst-Pack mesh [117] at a density of $16 \times 16 \times 16$ k-points for the rhombohedrally centred unit cell. The Brillouin-zone integration is carried out by a Gaussian occupation with a smearing of 5 meV for the ionic relaxations and by the tetrahedron method with Blöchl corrections [118] for all static calculations. A convergence test proves that increasing the energy cutoff or the sampling density alters the total energy by ≈ 1 meV per atom. The ionic forces are calculated according to the Hellmann-Feynman theorem [119]. The ions move along them towards the equilibrium positions and stop to relax if the forces acting on each ion are smaller than 0.005 eV/Å. SOC is enabled in all calculations. For different vdW approaches, the volume of the rhombohedrally centred unit cell is optimised by the Murnaghan equation of state. The four approaches tested are: no vdW correction, DFT-D2 [26], DFT-D3 + zero-damping [27], and DFT-D3 + Becke-Johnson damping [28]

Volume optimisation

The relevant lattice parameters of the hexagonal unit cell are: the basal lattice constant a , the axial lattice constant c , the interlayer distance d , the BL width w , and the Wyckoff parameter of the rhombohedral centring z . The results for d may be found in Fig. 8.3 (c). The experimental reference (XRD, [158]) is inserted as a dashed line.

As in the case of Bi_2Se_3 , the vdW correction makes the BLs come closer together. Though, d does not shrink as strongly as in Bi_2Se_3 , only by -0.1 \AA to -0.2 \AA (-4% to -8%) upon activating any vdW implementation. In fact, disabling the vdW corrections already produces an interlayer distance which lies only $+3\%$ above the experimental reference. DFT-D2 and DFT-D3+BJ even underestimate d by -4% , while DFT-D3 yields a good value for d lying only -0.7% below the reference. However, d is not the only vdW-sensitive lattice parameter. Also a varies up to 2% , where DFT-D2 and DFT-D3+BJ yield good values and DFT-D3 a value which is too large by $+1.4\%$. Interestingly, all vdW approaches as well as disabling vdW overestimate w by ca. $+2\%$. The unit-cell volumes V agree with the experiment in the order: DFT-D3+BJ (-0.6%), DFT-D2 (-1.2%), DFT-D3 ($+3.1\%$) and no vdW ($+6.5\%$). The different qualities of the approaches can be summarised by the Sb–Sb bond distances d_1 and d_2 (Tab. 8.2 (a)): DFT-D2 describes d_1 better, DFT-D3 describes d_2 better and omitting the vdW correction overestimates both distances. Since DFT-D2+SOC yielded good results for Bi_2Se_3 and will be chosen as the central approach for the heterostructures, the complete set of lattice parameters of the respective β -Sb unit cell are compiled in Tab. 8.2 (b).

(a)	Exp. [158]	no vdW	DFT-D2	DFT-D3	DFT-D3+BJ
d_1 (Å)	2.90	2.95 (+1.8 %)	2.92 (+0.7 %)	2.95 (+1.5 %)	2.94 (+1.2 %)
d_2 (Å)	3.34	3.43 (+2.5 %)	3.29 (-1.7%)	3.36 (+0.5 %)	3.28 (-1.8%)

(b)	a (Å)	c (Å)	V (Å ³)	d (Å)	w (Å)	z
Exp. [158]	4.301	11.222	179.75	2.238	1.503	0.2336
DFT-D2 + SOC	4.311	11.033	177.59	2.144	1.534	0.2362
Deviation	+0.2 %	-1.7%	-1.2%	-4.2%	+2.1 %	

Table 8.2: Lattice parameters of bulk β -Sb. (a) Bond distances d_1 and d_2 under different vdW treatments. (b) Lattice parameters optimised with DFT-D2 and SOC. The unit cell was optimised by Murnaghan relaxations. Experimental reference: [158].

8.2.2 Electronic properties

The band structure of the DFT-D2+SOC structure of β -Sb is plotted in Fig. 8.4 (a) and (b), where the plotting procedure is analogous to that in Fig. 8.2 (b) and (c). In addition, the bands of the isolated Sb sheets are inserted in (c) \rightarrow 1 BL and (d) \rightarrow 2 BL. Their structures are the peeled-off structures from the respective heterostructures in Sec. 9.1, i.e. the heterostructure optimised with DFT-D2+SOC after removal of the substrate. In this manner, the bands of the isolated sheets can directly be compared

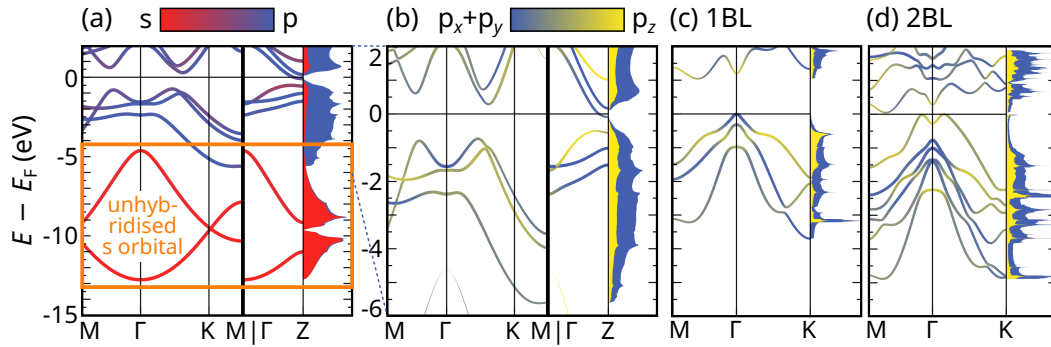


Figure 8.4: Band structure of (a) and (b) bulk β -Sb and (c) and (d) isolated β -Sb sheets. For bulk β -Sb, the rhombohedrally centred DFT-D2+SOC structure was used. The β -Sb sheets are the peeled-off structures of the respective Sb@Bi₂Se₃ heterostructures. The symmetry points correspond to the hexagonal unit cell. The line colour corresponds to the colour bars above the panels. (a) s-orbital portion (red) vs. p-orbital portion (blue) in all PAW projections for bulk β -Sb; (b) – (d) ($p_x + p_y$)-orbital portion (blue) vs. p_z -orbital portion (yellow) in the p-orbital projections of all atoms (line width) for (b) bulk β -Sb, (c) an isolated 1 BL sheet and (d) an isolated 2 BL sheet of β -Sb. The respective PDOSs are plotted against the y-axis to right of the band structures in arbitrary units.

with the Sb bands in the layer-desorption-and-readsorption procedure for tracking the topological phase transitions in Sec. 9.3. Since the bands of the isolated sheets thematically fit better to this chapter, they are presented here.

β -Sb is a semimetal in which the valence bands and the conduction bands are separated locally in \mathbf{k} , but not by a global band gap. In other words, the band gap is negative, which will be important for the \mathbb{Z}_2 classification. There are two s bands, which host the four 5s electrons from the two Sb atoms. The other three valence bands are of p character and host the six 5p electrons. The s bands and the p bands are clearly separated from each other at every k-point, which reminds of the Bi₂Se₃ case. Though, the band width of the s bands is larger than that of Bi₂Se₃. That the s orbitals do not hybridise with the p orbitals indicates a certain unwillingness of the s electrons to take part in chemistry and agrees with the nearly right-angled geometry of the BLs (95.0° bond angle within the BLs).

While the local band gap is large in-plane, the valence bands and the conduction bands approach each other near the out-of-plane Z-point. The p_z -resolved bands show a peculiarity there: The uppermost valence band is of p_z character and has a positive slope on most of the $\bar{\Gamma}\bar{Z}$ path. Near the Z-point, however, it bends down and changes to a hybrid between p_z and ($p_x + p_y$). That the opposite happens in the lowermost conduction band hints at a band inversion at that point. This might produce a topologically non-trivial state if the negativeness of band gap is ignored.

The \mathbb{Z}_2 invariant

The supposed topologically non-trivial state due to the apparent band inversion can easily be checked by calculating the \mathbb{Z}_2 invariant. In doing so, the negative band gap is ignored, i.e. the bands are assumed to be separated into a well-defined set of

valence and conduction bands by making the local band gaps global. The procedure is completely analogous to the calculation of the \mathbb{Z}_2 invariant of Bi_2Se_3 . Again the QE package [4, 5] is employed with a $5s^25p^4$ -valent, full-relativistic PAW-PBE potential for Sb. The rhombohedrally centred DFT-D2+SOC structure used as input. All other parameters are the same as those in the Bi_2Se_3 case (vide supra).

Applying the parity method on all ten bands returns a set of five positive and three negative δ_i . Their negative product proves that the valence manifold is topologically non-trivial wherefore β -Sb can be considered a 3D topologically non-trivial \mathbb{Z}_2 semimetal. A series of gauge transformations on the TRIM cube reduces the number of negative δ_i to one, which then sits at the vertex Γ_7 , the space-diagonally opposite of Γ_0 . According to the classification of Fu and Kane [147], the full topological class is $1;(111)$, in agreement with earlier results [159]. Repeating the \mathbb{Z}_2 classification for the s bands only yields a trivial character, while the p-band subspace produces the same results as those above. In particular, the position of the non-trivial δ_i at Γ_7 implies that the band inversion happens the Z-point of the hexagonal unit cell, which confirms the presumed band inversion in Fig. 8.4.

The classification of bulk β -Sb as a topologically non-trivial semimetal is per se not very useful due to the fractional occupation. The practical consequences emerge in thin films: Since the band widths of a bulk material decrease for thin slices, the band gaps increase and, in particular, semimetals (negative band gap) can adiabatically turn into semiconductors/insulators (positive band gap). For (0001)-slices of β -Sb, this happens at a thickness of ~ 20 BL [160]. In doing so, the valence manifold of the β -Sb slice inherits the topological character from the bulk semimetal as the bands do not reorder. Therefore, such films of β -Sb are 3D \mathbb{Z}_2 TIs with two surfaces bearing the corresponding TSSs. A further reduction of the slice thickness below 8 BL opens a small band gap in the TSSs as the bulk character vanishes. However, being a 2D insulator, the thin slice permits the calculation of the 2D \mathbb{Z}_2 invariant, with the result that it is a 2D \mathbb{Z}_2 TI. Finally, at a thickness of 3 BL, the gap closes and reopens at a thickness of 2 BL. This is a topological phase transition which renders β -Sb sheets with thicknesses of 2 BL and 1 BL topologically trivial 2D insulators [160]. This is confirmed in this work, as the δ_i are negative for all four (2D) TRIMs. As a last remark, the band structures of the isolated sheets in Fig. 8.4 (c) and (d) already hint at the band inversion in bulk β -Sb. In the 1 BL structure, the VBM is at the Γ -point and the three p bands resemble a rehybridised superposition of a blue, hole-like parabola, a yellow p_z band shaped like a lying B and a deeper, greyish, W-shaped band. When a second BL is added to the structure, one of the B bands is shifted to the Fermi level and approaches the conduction bands. Adding further BLs is likely to invert the band order at the Γ -point. If the band gap reopens after such a reordering, the system will be in a topologically non-trivial state. This exactly agrees with the observations in [160] and furthermore confirms the band inversion of the bulk band structure at the Z-point, which coincides with the Γ -point of the (0001) surface.

8.3 Discussion and summary

The investigations of the bulk phases proved that it is absolutely crucial to take vdW corrections into account when treating a vdW material like Bi_2Se_3 within DFT. Omitting them results in too large interlayer distances. The DFT-D2 approach in combination with SOC produced lattice parameters for Bi_2Se_3 which agree with the experimental reference [153] up to 1 %. The unit cell volumes deviate by only 0.1 %. While the strong attractive effect between the QLs from the vdW corrections is expectable, the intermediate, also attractive effect from SOC is uncommon. There are not many detailed works on the first-principles structure of Bi_2Se_3 , probably because not giving attention to all peculiarities of the material results in lattice constants which considerably deviate from the experiment. An extensive DFT work testing more vdW approaches than this work was published by Luo et al. [161]. Their DFT-D2+SOC lattice constants (QE) are very close to those obtained in this work (VASP). Luo et al. investigated the SOC-related effects on the structure as well. Although they found that SOC reduces the interlayer distances, in agreement with this work, they doubt the physical relevance (“it is still unclear if SOC is truly important for structural optimization” [161]). There is, however, a good reason why SOC is likely to exert physical effects on the structure: Since Bi_2Se_3 is a TI, the orbital occupation changes at the Γ -point when SOC is enabled. This point is certainly worth investigating in more detail, e.g. by analysing partial charges with and without SOC.

While the results for Bi_2Se_3 agree with the experiment very well, those obtained for β -Sb show slightly larger deviations. Although DFT-D3 produces better interlayer distances, DFT-D2 is considered more suitable for describing β -Sb for two reasons. Firstly, the bond distance within the BLs is better predicted by DFT-D2. Secondly, the unit-cell volume within DFT-D2 is close to the experimental one, contrarily to that of the DFT-D3 structure. This will be important for the heterostructures since the Bi_2Se_3 substrate strains the thin Sb adlayer, so part of the substrate-adlayer distance is due to anisotropic deformation. In this case, a correct description of the volumes is obligatory. Aktürk et al. had a work published which investigates the structure of β -Sb with VASP [155]. Although, they used a parameter set very similar to that of this work (PBE, cutoff energy, k-mesh), they obtained DFT-D2+SOC lattice constants which are closer to the experiment [153] than those of this work. Thus, it is not excluded that the approach of this work was not free of errors. It is certainly worth testing further vdW functionals on β -Sb in order to explain the deviances.

β -Sb and Bi_2Se_3 have in common that the bond angles are close to the right angle (regular coordination octahedrons in the QLs and right-angled trigonal-pyramidal coordination in the BLs). This accords very well with the electronic properties as the major part of the bonding is due to the p orbitals, while the s orbitals are proven not to hybridise with them. This is much pronounced in Bi_2Se_3 , where the inert-pair effect prevents the s electrons from chemical bonding. The topological classes were calculated and agree with previous knowledge. The band inversion in the bulk phases is clearly visible from the p_z -resolved bands. In the topologically trivial, isolated 1 BL and 2 BL sheets of β -Sb, the beginning band inversion at the surface Γ -point was demonstrated.

9 The antimony on bismuth selenide heterostructure

The (0001) surface of Bi_2Se_3 , denoted BS(0001), results from cleaving the material exactly between two QLs, in accordance with the layered structure of the vdW material [157, 162]. Since the atomic shells of the QLs are closed, the surface morphology is determined by a unreconstructed buckled honeycomb. The upper atoms are the outer Se atoms of the terminating QL and the lower atoms are Bi atoms (vide supra, Fig. 8.1 (b)). The metallic TSSs of BS(0001) give rise to a single Dirac cone at the Γ -point, as confirmed by DFT calculations and ARPES measurements [P7, P9, 154, 163–166].

The adsorption of Sb on BS(0001) produces the Sb@BS system, a class of vdW heterostructures consisting of a Sb adlayer which binds to the Bi_2Se_3 substrate by vdW interactions. The thinnest films occur in two different phases depending on the thermodynamic boundary conditions: the α -phase and the β -phase, named after the two layered bulk phases of the pnictogens (vide supra, Sec. 8.2). The films can indeed be considered as single sheets from the respective bulk phases, which are attached to the substrate. The α -Sb adlayers are incommensurate with BS(0001) due to different 2D symmetry groups (orthorhombic vs. trigonal). In contrast, the β -Sb adlayers have the same symmetry as BS(0001) and, in addition, similar basal lattice constants ($a_{\beta\text{-Sb}} = 4.30 \text{ \AA}$ and $a_{\text{Bi}_2\text{Se}_3} = 4.14 \text{ \AA}$, vide supra). Therefore, they are commensurate with the substrate and can reach heights of several BLs by vdW epitaxy [157, 166, 167]. The α -phase can be transformed into the β -phase by a temperature-induced phase transition [P5, P10].

Beside the structural peculiarities of the system, the electronic properties attract scientific attention as well. The interplay between the TSSs of the substrate and the 2D states of the β -Sb adlayer (CIs for thicknesses of 1 BL and 2 BL, vide supra) is complex. Although the adsorption is based on vdW interactions, the electronic band structure of the heterostructure looks rather different from that of the constituents. Theoretical work on the heterostructures has been published [166, 168], though the origin of the features has not yet been satisfyingly understood. Furthermore, high-quality band structures and ARPES images are missing and the connection between the band structures and the structural details has not been investigated yet.

The aim of this chapter is thus to understand the electronic properties of commensurate β -Sb films with thicknesses of 1 BL and 2 BL by means of DFT. For this purpose, structure models are set up and subjected to ionic relaxations. The focus of the structure analysis is on the way how the Sb BLs stack on the substrate, which has not yet been paid sufficient attention, but proves to be thermodynamically relevant. Also the effects from vdW corrections and SOC are illuminated. In particu-

lar, the effects from SOC are paid a special attention since one tends to deactivate SOC during the relaxations to save computation time. For the thermodynamically stable structure models, the electronic band structures are calculated and compared with experimental ARPES measurements. Furthermore, *ab initio* STM simulations are performed and the results are compared with experimental STM measurements. The last section contains a simulated desorption-and-readsorption process for the β -Sb adlayer which permits tracking the evolution of the TSSs upon Sb layer adsorption. By this means, a complex series of topological phase transitions is illuminated. The deep analysis finally explains all details of the electronic band structures of the heterostructures. The results have already been published [P5, P7, P9].

9.1 Structure optimisation

The Bi_2Se_3 slab

The topological non-triviality of Bi_2Se_3 discourages the asymmetric-slab approach since the passivation of the metallic surface states is impossible. Therefore, the Bi_2Se_3 substrate is modelled by a symmetric, right-prismatic slab, which provides identical, hexagonal surfaces on the top and the bottom side. The lattice parameters of the slab are taken from the Bi_2Se_3 unit cell optimised with DFT-D2 and SOC (vide supra, Tab. 8.1). The thickness of the slab amounts to 6 QL, which is thick enough so that the TSSs of the two surfaces do not interfere¹. The periodic replica in the z-direction are separated from each other by 60 Å of vacuum, which reduces to 40 Å when the slab bears the Sb adlayers. The slab is sketched in Fig. 9.1 (a) and (b).

Computational details

The computational parameters for the heterostructure are similar to those used for the constituents (Chap. 8). The DFT calculations are carried out with VASP [2, 3] using PAW potentials and the PBE xc-functional [10, 21, 22]. The Bi, Se and Sb atoms have PAW valences of $5d^{10}6s^26p^3$, $4s^24p^4$ and $5s^25p^3$, respectively. The kinetic energy cutoff is $E_{\text{cut}} = 400$ eV. The Brillouin zone is sampled by a Γ -centred surface Monkhorst-Pack mesh [117] at a density of $12 \times 12 \times 1$ k-points. The Brillouin-zone integration is carried out by a Gaussian occupation with a smearing of 5 meV for the ionic relaxations and by the tetrahedron method with Blöchl corrections [118] for all static calculations. The ionic forces are calculated according to the Hellmann-Feynman theorem [119]. The unit cell is fixed. The atoms of the inner four QLs are held fixed at the bulk positions during all relaxations. All other ions, the top QL right below the surface and the Sb adlayer, move within the unit cell along the forces towards the equilibrium positions and stop to relax if the forces acting on each ion are smaller than 0.005 eV/Å. Unless otherwise noted, SOC is explicitly included also in the relaxations and the DFT-D2 method [26] is employed for the vdW contributions.

¹Test calculations show that the real-space distributions of the wavefunctions near the Dirac points of the two surfaces overlap up to 5 QL, although the band gap already closes at a thicknesses of 3 QL.

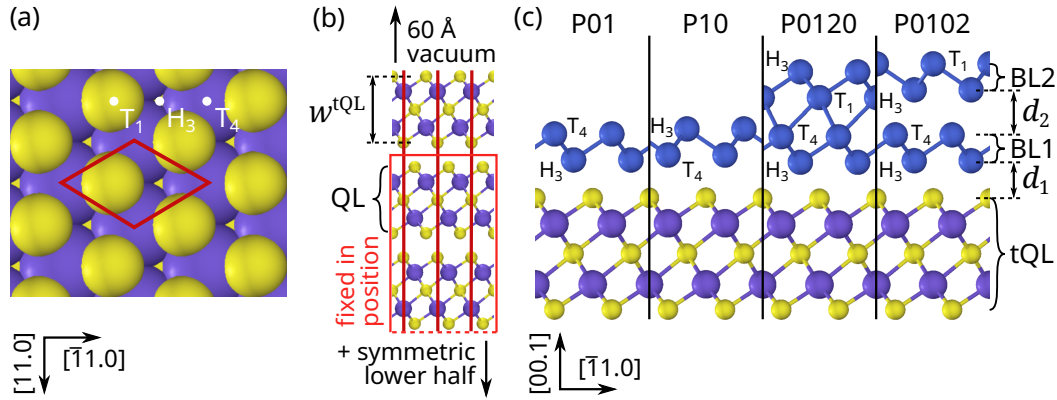


Figure 9.1: Sketch of the BS(0001) slab. Purple circles are Bi atoms; Light green circles are Se atoms; Blue circles are Sb atoms. (a) Top view of the slab. (b) Upper half slab in side view. The lower half results from inversion symmetry. Dark red lines mark the unit cells. The light red rectangle in (b) encircles the subset of atoms fixed in position during the relaxations. (c) Examples for Sb adlayers with heights of 1 BL and 2 BL. The symmetry positions of the substrate T_1 , T_4 and H_3 are indicated in (a) and (c). Reproduced from [P9].

9.1.1 The stacking sequence of the adlayer

The structure models for a vdW heterostructure in general have many degrees of freedom, in particular if the adlayer is not commensurate with the substrate. In the case of Sb@BS, the experimentally confirmed commensurateness [P5, 157] constrains the configuration space to those structures where the Sb atoms of the first BL sit at the symmetry positions of the terminating buckled honeycomb of the BS(0001) surface: T_1 , T_4 and H_3 (Fig. 9.1 (a)). The adsorption of multiple BLs can be understood in a successive manner as the BLs themselves are buckled honeycombs, which provide each a new triple of symmetry positions for the next BL.

The bulk phases of both Bi_2Se_3 and $\beta\text{-Sb}$ underlie a stacking which consists in the strict repetition of the atomic-layer sequence ABC with differing vdW-layer interruptions (Chap. 8). In order to transfer this to the Sb@BS heterostructure, let tQL, BL1 and BL2 be the top QL of the substrate, the first BL of $\beta\text{-Sb}$ and the second BL of $\beta\text{-Sb}$, respectively. If BL1 continues the sequence of tQL (ABCAB) by (CA), the lower Sb atom is above H_3 and the upper Sb atom above T_4 . BL2 can proceed with the indices (BC). Though, this is not the only possibility to stack the Sb adlayer in a reasonable manner: An *inverted* BL1 having the atomic-layer indices (AC), i.e. lower Sb atom above T_4 and upper Sb atom above H_3 , would fit into the same two surface symmetry positions as the non-inverted (*natural*) BL1. Of course, the combinatorics inflate the configuration space with growing thicknesses of the Sb adlayer. Therefore, the configurations are systematised by the following nomenclature: The three original symmetry positions of the BS(0001) surface are mapped onto integers: $H_3 \rightarrow 0$, $T_4 \rightarrow 1$ and $T_1 \rightarrow 2$. A Sb@BS structure model is denoted “P” plus the sequence of integers which the adsorbed Sb atoms occupy. Thus, the single, natural BL is called “P01”, the single, inverted BL is called “P10” and two natural BLs are called “P0120”. The nomenclature simplifies the identification of inverted structures as it reduces to permutations between integers.

Fig. 9.1 (c) shows examples for the nomenclature. Furthermore it defines the interlayer distance between tQL and BL1 d_1 and that between BL1 and BL2 d_2 , which will be used for the analysis of the structures.

In order to compare the different structure models regarding their thermodynamical stability, consider the following boundary conditions: The Sb adlayer forms in the annealing stage, which translates into a constant temperature T , a constant pressure ($p = 0$, UHV) and a constant amount of Sb N_{Sb} . If Sb diffusion into the Bi_2Se_3 substrate is negligible, the amounts of Bi and Se can be considered constant, as well as their chemical potentials. Consequently, the substrate contributes a constant term to the DFT total energy of the Sb@SB slabs $E_{\text{DFT}}^{\text{Sb@BS}}$. If this term is set to the DFT total energy of the “clean” slab without adsorbates $E_{\text{DFT}}^{\text{Clean}}$ and subtracted from $E_{\text{DFT}}^{\text{Sb@BS}}$, the remainder approximately equals the internal energy of the Sb adsorbate only. Transforming it into the Gibbs free energy and dividing it by N_{Sb} results in the Sb chemical potential μ_{Sb} . This is the quantity to minimise and permits the direct comparison between structure models with different amounts of Sb [P5, P9, P10, 157]. The Sb chemical potential of (natural) bulk β -Sb $\mu_{\text{Sb}}^{\text{b-nat}}$ is chosen as the reference point.

$$\mu_{\text{Sb}} = \frac{G^{\text{adlayer}}}{N_{\text{Sb}}} - \mu_{\text{Sb}}^{\text{b-nat}} \approx \frac{1}{N_{\text{Sb}}} \left(E_{\text{DFT}}^{\text{Sb@BS}} - E_{\text{DFT}}^{\text{Clean}} \right) - \mu_{\text{Sb}}^{\text{b-nat}} \quad (9.89)$$

Analogously to the RESi_2 case, the phononic contributions to the free energy are neglected (vide supra, Sec. 4.2.1). This approximation is based on the similar, layered structures, suggesting that each Sb BL has similar lattice-dynamical contributions.

Since the following analysis concentrates on the adsorption of different β -Sb adlayers, it is instructive to consider hypothetical phases of elemental β -Sb:

- An alternative bulk phase in which every second BL is inverted (b-inv). The stacking sequence is thus (AB)(CB). Its structure is optimised at code level.
- Free-standing β -Sb sheets, whose structures are optimised by the 2D-version of the Murnaghan equation of state: the 1 BL sheet (f1BL) and the 2 BL sheet with natural (f2BL-nat) and inverted stacking (f2BL-inv).

Tab. 9.1 shows the Sb chemical potentials μ_{Sb} , the basal lattice constants a and the interlayer distances d for these structures and for the stable bulk phase (b-nat).

System	Abbr.	μ_{Sb} (meV)	a (Å)	d (Å)
Bulk (natural stacking)	b-nat	0	4.31	2.14
Bulk (inverted stacking)	b-inv	40	4.12	2.84
Free-standing 1BL sheet	f1BL	276	4.05	—
Free-standing 2BL sheet (nat. stacking)	f2BL-nat	178	4.16	2.43
Free-standing 2BL sheet (inv. stacking)	f2BL-inv	173	4.08	2.97

Table 9.1: Sb chemical potentials μ_{Sb} , basal lattice constants a and interlayer distances d of 2D and 3D β -Sb systems. Reproduced from [P9].

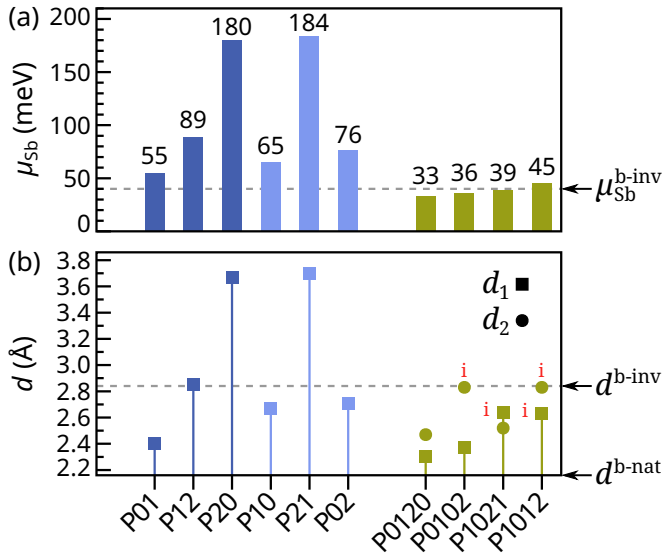


Figure 9.2: (a) Sb chemical potentials μ_{Sb} and (b) interlayer distances d_1 (squares) and d_2 (circles) of the structure models for the Sb@BS system optimised with DFT-D2+SOC. The two bulk phases of β -Sb b-nat (stable) and b-inv (hypothetical) are inserted as dashed lines. Red “i” symbols mark inverted Sb BLs. Reproduced from [P9].

At first, 1 BL thick β -Sb adlayers (1BL-Sb) are investigated by optimising the structure of all six adsorption possibilities. The results for μ_{Sb} and d_1 are plotted in Fig. 9.2 (blue). P01 is the most stable structure with $\mu_{\text{Sb}} = 55$ meV. Hence, it is indeed favourable if BL1 continues the stacking sequence of the Bi_2Se_3 substrate. Surprisingly, P10, the inverted BL, is only slightly less stable by $\Delta\mu_{\text{Sb}} = +10$ meV. Since the difference is below $k_{\text{B}}T$ at room temperature, the two structures are energetically so close to each other that a conclusion about their relative stability is not possible. The next stable pair of structures are P02 and P12, where the upper Sb atom is above T_1 . Their μ_{Sb} are higher than that of P01 by +21 meV and +34 meV, also in the order of $k_{\text{B}}T$ at room temperature. Only P20 and P21, where the lower Sb atom is above T_1 , are clearly unstable against P01 by $\Delta\mu_{\text{Sb}} > +100$ meV.

The interlayer distances d_1 congruently follow μ_{Sb} . This permits the conclusion that the binding energy between the substrate and BL1 depends on how close the former lets the latter approach. Continuing the stacking sequence of the substrate, P01 has the smallest interlayer distance of all 1BL-Sb structures ($d_1 = 2.40$ Å, +0.25 Å compared to $d^{\text{b-nat}}$), which minimises μ_{Sb} . In contrast, in P20 and P21, the top Se atom of the substrate pushes the BL quite far away ($d_1 > 3.5$ Å). This reduces the binding energy to such an extent that the BL is energetically closer to the free-standing 1 BL sheet (f1BL) than to P01. In all other structures, d_1 is close to $d^{\text{b-inv}}$.

The results for 2 BL thick β -Sb adlayers (2BL-Sb) are plotted in Fig. 9.2 (green). Using the 1BL-Sb results, only those 2BL-Sb structures are considered where both BLs successively occupy the convenient H_3 and T_4 positions. These are P0120 (BL1 nat, BL2 nat), P0102 (BL1 nat, BL2 inv), P1021 (BL1 inv, BL2 nat) and P1012 (BL1 inv, BL2 inv). Similarly to the 1BL-Sb case, it is favourable if the BLs continue the stacking sequence of the substrate (P0120). However, the μ_{Sb} of the other three structures are surprisingly close to that of P0120 ($\Delta\mu_{\text{Sb}} \leq 12$ meV $\sim k_{\text{B}}T$). Hence, it remains unclear which structure model represents the real 2BL-Sb structure. The interlayer distances clearly conform with the layer inversions: If the BL is natural/inverted, the corresponding d_i is closer to $d^{\text{b-nat}}/d^{\text{b-inv}}$ (red “i” symbols in Fig. 9.2).

Tab. 9.1 shows that in both cases of natural and inverted stacking, the basis of bulk β -Sb is larger than that of a free-standing 2 BL sheet, which in turn is larger than that of a free-standing 1 BL sheet. This suggests that a free-standing β -Sb sheet laterally expands with growing thickness. In the bulk limit, the basal lattice constant of b-inv is smaller than that of b-nat (-4.4%). The behaviour of the sheets has important consequences for the lattice matching between the Sb adlayer and the Bi_2Se_3 substrate (surface lattice constant $a_{\text{BS}} = 4.13 \text{ \AA}$): Considerations based on natural bulk β -Sb would lead to the wrong conclusion that the Sb adsorbate underlies compressive strain (-4.0%). On the contrary, the strain is even tensile in the 1BL-Sb heterostructure ($+2.1\%$ w.r.t. f1BL), while in 2BL-Sb, the lattice matching is almost perfect (f2BL-nat: -0.7% , f2BL-inv: $+1.2\%$). For thick, bulk-like Sb adlayers, the inverted stacking (b-inv) produces an almost perfect lattice matching ($+0.2\%$), while a naturally stacked layer (b-nat) has to be compressed by -4.0% (vide supra). Since adapting the bases to BS(0001) makes $\mu_{\text{Sb}}^{\text{b-nat}}$ approach $\mu_{\text{Sb}}^{\text{b-inv}}$, it is not clear which of the two stackings occurs even for thick Sb adlayers [P9].

The free-standing 2 BL sheets demonstrate why the inversion of BL1 and BL2 in the 2BL-Sb heterostructure has such a low impact on the stability. Firstly, μ_{Sb} is almost equal in both free-standing 2 BL sheets, differing only by 5 meV. Secondly, both sheets match the substrate equally well, so the adsorption energy per atom depends only on the relation between BL1 and the substrate. Thirdly, BL1 is indifferent to inversions in the 1BL-Sb case. These three points combined explain why all four investigated 2BL-Sb structures are energetically so close together that a conclusion about the real structure is not possible. In spite of this, the subsequent work concentrates on the heterostructures with natural stacking: P01 and P0120.

9.1.2 The effects from SOC and vdW on the heterostructure

Although DFT-D2+SOC is the approach of choice in this chapter, it is interesting to investigate how SOC and the vdW corrections affect the heterostructures. For this purpose, the structure models for 1BL-Sb and 2BL-Sb are optimised with disabled corrections: pure PBE, DFT-D2 only, SOC only. All other parameters remain unchanged. The results for the interlayer distances d_1 and d_2 are plotted in Fig. 9.3. Similarly to bulk Bi_2Se_3 , both vdW and SOC make the adlayer move closer to the substrate. In 1BL-Sb, d_1 (blue squares) shrinks by a similar percentage if either vdW or SOC is enabled (-15% and -10% , respectively). If both are enabled, the shrinkage amounts to -20% . The overall contractive effect and the importance of SOC are more pronounced in the heterostructure than in bulk Bi_2Se_3 . In 2BL-Sb, d_1 (green squares) is generally smaller, but the relative shrinkage is similar (-17% if enabling vdW and SOC). d_2 (green circles) behaves differently from d_1 as it contracts upon enabling vdW (-5% to -6%), but varies much less due to SOC ($+1\%$ to $+2\%$).

Back to DFT-D2+SOC, while d_1 and d_2 vary considerably, the other lattice parameters are close to the respective bulk values. The thickness of tQL and the interlayer distance beneath tQL are very close to w and d in bulk Bi_2Se_3 , deviating by $<0.5\%$ and $<1\%$, respectively. The Sb-Sb bond distances in the adsorbed BLs (2.88 \AA to 2.89 \AA) are close to the respective bond distance in bulk β -Sb (2.92 \AA , -1.4% to -1.0%).

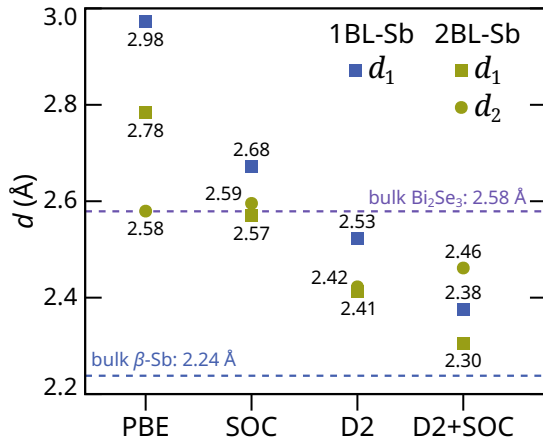


Figure 9.3: Interlayer distances d_1 (squares) and d_2 (circles) of 1BL-Sb (blue) and 2BL-Sb (green) optimised with different corrections. Treatments: 1) pure PBE, 2) SOC only, 3) DFT-D2 only, 4) DFT-D2 and SOC. The experimental interlayer distance of the bulk phases are inserted as horizontal dashes lines: purple \rightarrow Bi_2Se_3 [153]; blue \rightarrow β -Sb [158].

9.2 Electronic properties

The band structures of the three slabs (clean Bi_2Se_3 , 1BL-Sb and 2BL-Sb, all optimised with DFT-D2+SOC) are calculated analogously to Sec. 4.3 and may be found in Fig. 9.4. All system-specific parameters are the same as those of the relaxations above. The surface k-path comprises two line segments: $\overline{K}\overline{\Gamma} \parallel (11\overline{2}0)$ in the x-direction and $\overline{\Gamma}\overline{M} \parallel (\overline{1}100)$ in the y-direction (sketch in Fig. 9.4 (b)). The bands associated with the surface are separated from the bands of the simulated bulk by means of the PAW projections. In detail, the summed PAW projections of the atoms of the upper half slab divided by the sum over all PAW projections of the slab minus 0.5 defines the line width. Thus, a band which is totally localised in the upper half slab is displayed at the maximum line width, while bands localised to less than 50% in the upper half are displayed as hair lines. The colour corresponds to whether the bands are associated with the substrate (Bi and Se atoms, blue) or with the adlayer (Sb atoms, red). The projected bands of bulk Bi_2Se_3 are shaded grey.

9.2.1 Band structures

The bands of the clean substrate (Fig. 9.4 (a)) show that the topologically protected surface states arising from the bulk (TSS_{BS}) manifest themselves as a single Dirac cone at the Γ -point. The Dirac point D is right above the VBM and defines the Fermi energy of the slab. The presence of an odd number of Dirac cones located at the surface Γ -point confirms the expectations from the parities of bulk Bi_2Se_3 , according to the extended topological classification of TIs with inversion symmetry [159]. The theoretical band structure compares qualitatively well with ARPES measurements [P7, 165, 166, 169]. However, there are two minor, quantitative discrepancies: Firstly, the experimental binding energy of D is positive in ARPES, e.g. 0.2 eV in [166], while the theoretical one is zero. The reason for this deviation is that Bi_2Se_3 samples are often *n*-type due to Se vacancies [166, 169]. Furthermore, ARPES measurements on TIs suffer from the problem that the inherent UV illumination varies the binding energy of D by 0.2 eV over the time of measurement [165]. The second quantitative

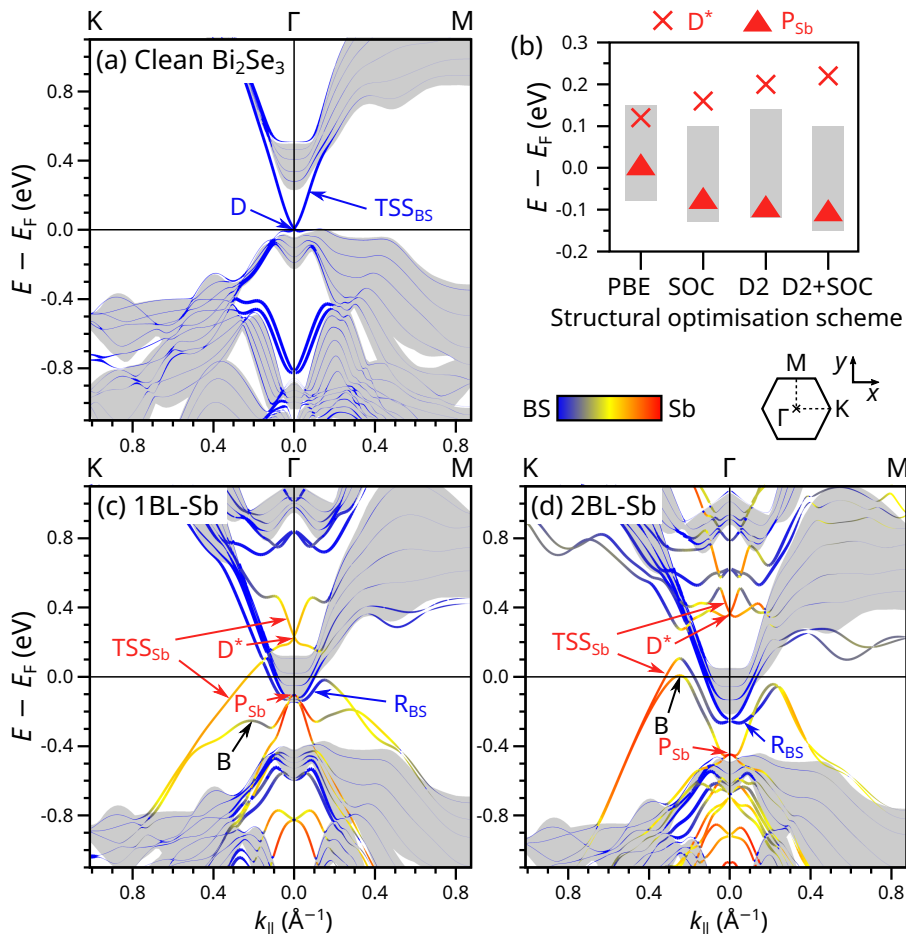


Figure 9.4: Band structures of (a) the clean Bi_2Se_3 surface and the heterostructures (b) 1BL-Sb and (d) 2BL-Sb optimised with DFT-D2+SOC. All energies are reset by the Fermi levels of the respective slabs. The line colour corresponds to the colour bar: blue \rightarrow substrate; red \rightarrow Sb adlayer. The line width corresponds to the localisation in the upper half slab (see text). The projected bands of bulk Bi_2Se_3 are shaded grey. Arrows highlight special features. (b) Positions of the Γ -point features (red uptriangles \rightarrow P_{Sb} ; red crosses \rightarrow D^* ; grey boxes \rightarrow bulk conduction bands) of the 1BL-Sb structure optimised with different schemes (pure PBE, PBE+SOC, PBE+D2, PBE+D2+SOC). Reproduced from [P7].

discrepancy consists in differing shapes of the Dirac cone. The lower part is rather flat in the theoretical band structure, while it is more X-like in ARPES [P7, 169]. The origin of this lies in the many-body effects which are insufficiently accounted for by DFT. The correction of the self-energy of the quasiparticles within GW partially reverts the band inversion so that the furrow at the Γ -point bulges out [170]. As a further consequence, the band gap *decreases*, which is exactly the opposite of what is expectable from GW corrections in other, topologically trivial semiconductors [170]. Concerning the surface, GW renders the shape of the Dirac cone more X-like, which then compares very well to the ARPES bands [163, 164].

When the first Sb BL adsorbs to the substrate, the band structure undergoes fundamental changes (Fig. 9.4 (c)). The Fermi level rises into the CBs of bulk Bi_2Se_3 . The

original Dirac cone is not recognisable any more and new surface features emerge instead. Above the first set of bulk CBs, two X-shaped bands form a Dirac point D^* at -0.2 eV binding energy. They are interrupted by the bulk CBs and have a visible gap in the $\overline{\Gamma M}$ direction, while the gap along $\overline{\Gamma K}$ vanishes. If they are nevertheless continued across the bulk CBs, they represent a set of surface bands which are more associated with the Sb adlayer than with the substrate. Since it seems that they preserve the topological non-triviality of the surface band structure, they are denoted TSS_{Sb} . A detailed analysis of the topological properties can be found below (Sec. 9.3). Beside TSS_{Sb} , there are three further important surface features: A band resembling a lying B, a hole-like double parabola P_{Sb} with apex at 0.1 eV binding energy and Rashba-like bands R_{BS} at the bulk CBs. The B band is more associated with the substrate than with the adlayer. P_{Sb} is completely localised in the adlayer and represents the Sb–Sb bonds as indicated by the strong $(p_x + p_y)$ character (not shown). The R_{BS} states are completely localised in the surface region of the substrate, more precisely mostly in tQL. Since they are right and left shifted versions of the bulk CBs, they seem indeed to represent a Rashba splitting at tQL.

The addition of a second BL alters the band structure further (Fig. 9.4 (d)), though, the qualitative features of the 1BL-Sb band structure are all still present. Compared to 1BL-Sb, the Fermi level rises by 0.1 eV. TSS_{Sb} becomes completely localised in the adlayer and overall steeper. It has a clear gap where the bulk CBs pass, in both along $\overline{\Gamma M}$ and $\overline{\Gamma K}$. The lower part of the former X-shaped band around D^* bends upwards. The B band is steeper and its apices are near the Fermi level. In contrast, P_{Sb} shifts to higher binding energies so that it is right above the bulk VBM. The Rashba splitting R_{BS} is much stronger. An additional feature, which is less pronounced in 1BL-Sb, consists in the wavy bands in the $\overline{\Gamma M}$ direction at -0.2 eV binding energy.

The interlayer distance d_1 of 1BL-Sb influences the alignment of the bands, which becomes visible in the bands of the structure models which were optimised with different corrections disabled (Sec. 9.1.2). Fig. 9.4 (b) shows the schematic alignment between the bulk CBs, P_{Sb} and D^* for these structures. The more the adlayer moves away from the surface (from right to left in the diagram), the closer P_{Sb} and D^* are together, until D^* finally dips into the CBs. It confirms the importance of accounting for both vdW corrections and SOC during the relaxations. A detailed explanation for the dependence between D^* , P_{Sb} and d_1 can be found below (Sec. 9.3).

Comparison with ARPES

The theoretical band structures are in well agreement with ARPES measurements, which were performed by the experimental collaborators of the joint-experimental-theoretical work [P7] (Fig. 9.5). The surface states TSS_{Sb} and B are clearly visible in ARPES and conform with the theory regarding the relative binding energies, slopes and curvatures. Also the quantitative differences between 1BL-Sb and 2BL-Sb and between the directions of the k-path are well reproduced. The ARPES image of 2BL-Sb clearly confirms the Rashba splitting R_{BS} . In the ARPES image of 1BL-Sb, R_{BS} is difficult to recognise as the splitting is weaker and superposed by blurry bulk CBs. The peak P_{Sb} is missing because in-plane p_x and p_y bands are generally suppressed by matrix-element effects [P7].

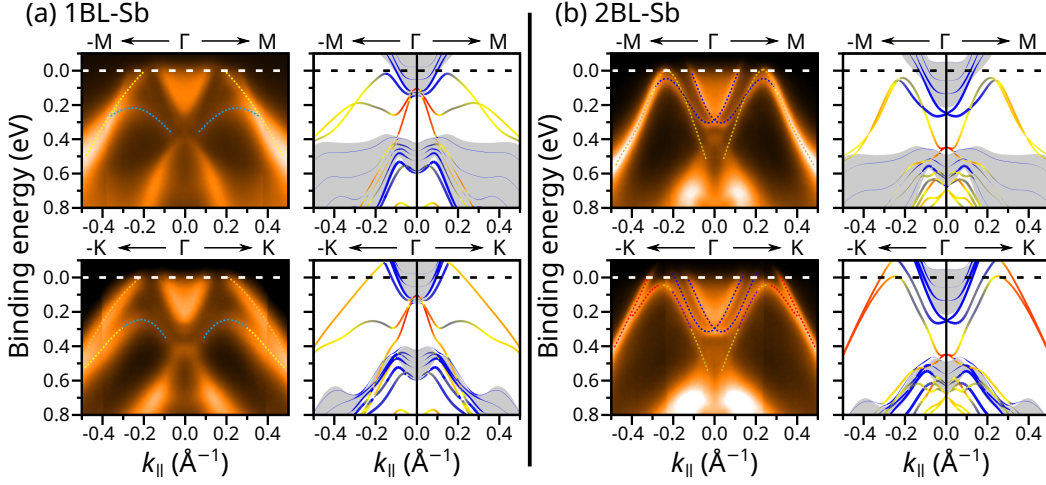


Figure 9.5: Comparison between the theoretical band structures (right, cut out from Fig. 9.4) and ARPES images (left, features highlighted) of the heterostructures (a) 1B-Sb and (b) 2BL-Sb. Top row: mid part of $\overline{-M\Gamma M}$; Bottom row: mid part of $\overline{-K\Gamma K}$. Reproduced from [P7].

The good agreement between the ARPES image of the 2BL-Sb system and the respective theoretical band structure supports the P0120 structure model. The energetically competitive, inverted structure models P0102, P1012 and P1021 yield band structures which look similar at first glance, but differ in the details. The band structures can be found in the appendix (Fig. C.1). Along $\overline{\Gamma M}$, the inwards bending of TSS_{Sb} towards the Γ -point and the crossing between the B band and R_{Bs} are unique for P0120. Along $\overline{\Gamma K}$, P0120 produces a slope for TSS_{Sb} which agrees with the ARPES image, while the slopes of all other structure models are too steep. The two BL-Sb band structures are too similar to each other to evaluate them by the ARPES image. The main distinctive feature is the distance between P_{Sb} and D^* , which is 0.3 eV for P01 and 0.2 eV for P10. However, both points are not visible in ARPES. The changes in the band structures upon layer inversion can partially be attributed to the larger interlayer distances, as further elaborated in Sec. 9.3.

The spin texture

The magnetic projections $m_i^{lm,I}(n, \mathbf{k})$ are analogous to the band projections $P^{lm,I}(n, \mathbf{k})$ in Eq. (4.41):

$$m_i^{lm,I}(n, \mathbf{k}) = \frac{1}{2} \langle \Psi_n(\mathbf{k}) | Y_{lm}^I \rangle \cdot \sigma_i \cdot \langle Y_{lm}^I | \Psi_n(\mathbf{k}) \rangle \quad (9.90)$$

where σ_i are the Pauli matrices, i is the spatial direction, $|\Psi_n(\mathbf{k})\rangle$ is the spinor at band index n and \mathbf{k} -point \mathbf{k} , and $|Y_{lm}^I\rangle$ are the spherical harmonics centred at atom I . The sum over lm of the magnetic projections of a specific atom I for a specific \mathbf{k} and n is simply denoted atomic magnetisation $m_i^I(n, \mathbf{k})$. The atomic magnetisations permit a band colouring which is completely analogous to that based on the PAW projections. In order to obtain the local spin texture, the upper half slab is divided into two groups: the substrate and the adsorbate. For each group, the magnetisation $m_i(n, \mathbf{k})$ is obtained by summing the $m_i^I(n, \mathbf{k})$ of the respective atoms. The line colour corresponds to a colour bar: blue \rightarrow negative magnetisations and red \rightarrow positive

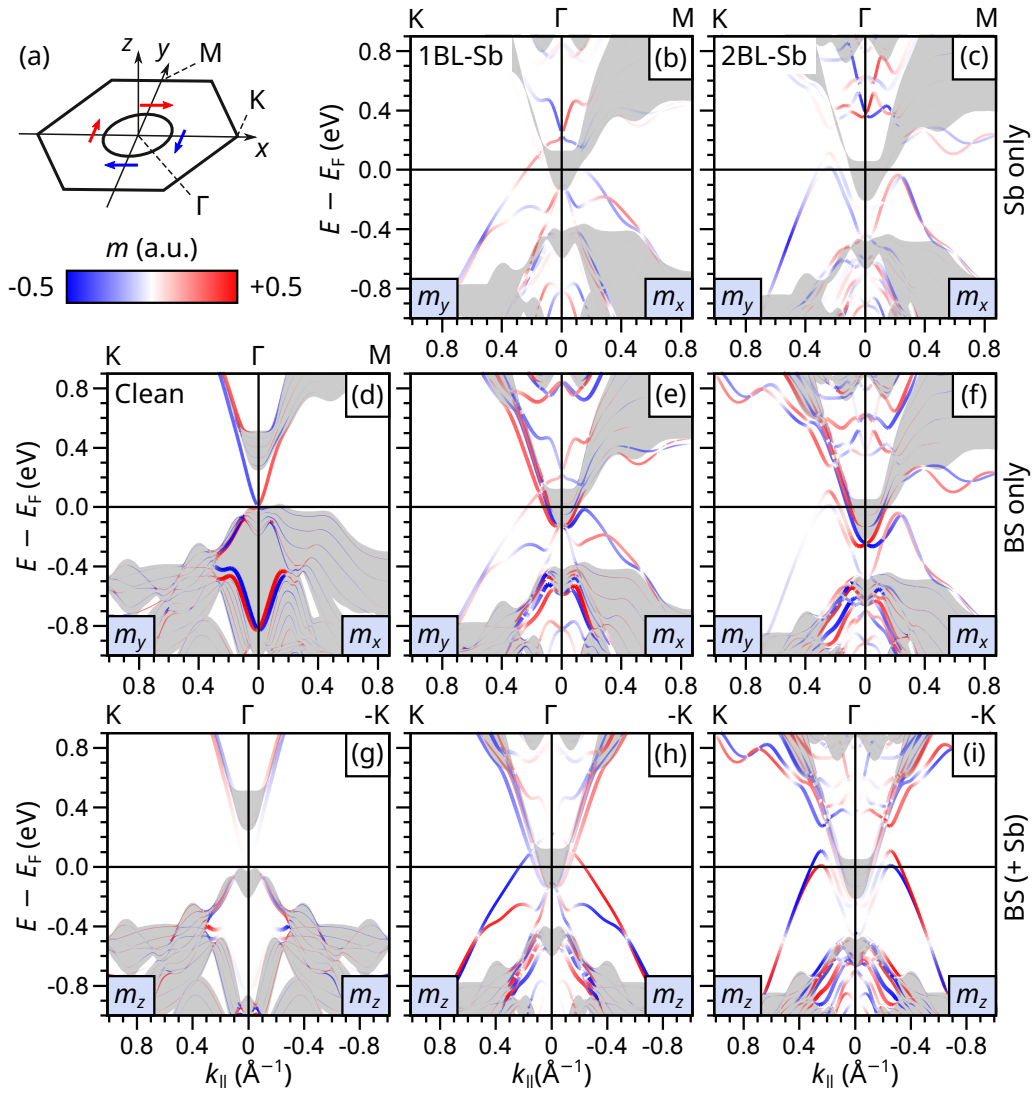


Figure 9.6: Spin texture of (d), (g) the clean Bi_2Se_3 surface and the heterostructures (b), (e), (h) 1BL-Sb and (c), (f), (i) 2BL-Sb. The line width and Fermi levels are analogous to Fig. 9.4. The line colour corresponds to the colour bar in (a): blue \rightarrow negative magnetisations; red \rightarrow positive magnetisations. (b), (c): m_y along $\overline{\Gamma\text{K}}$ and m_x along $\overline{\Gamma\text{M}}$ of the Sb adlayer; (d) – (f): the same for the Bi_2Se_3 substrate only; (g) – (h): m_z along $\overline{\Gamma\text{K}}$ and $\overline{\Gamma\text{K}}$. (a) Brillouin zone with a schematic helical spin texture. Reproduced from [P7].

magnetisations. The line width corresponds to the localisation in the upper half slab (as in Fig. 9.4) and suppresses bands of the simulated bulk and the other surface. The results are shown in Fig. 9.6. The three columns represent the clean substrate, 1BL-Sb and 2BL-Sb. The first row shows $m_y(n, \mathbf{k})$ along $\overline{\Gamma\text{K}}$ (the x-direction) and $m_x(n, \mathbf{k})$ along $\overline{\Gamma\text{M}}$ (the y-direction) for the Sb adlayer only. The second row shows the same for BS only. The third row shows the z-component $m_z(n, \mathbf{k})$ along $\overline{\text{K}\Gamma\text{K}}$ (the x-direction) for the entire half slab. The Kramers degeneracy (Eq. (7.74)) tells that the magnetisations along $\overline{\Gamma\text{X}}$ and $\overline{\Gamma\text{X}}$, $X \in [\text{K}, \text{M}]$, are equal up to the sign, which was explicitly confirmed (not shown). All other components, e.g. $m_x(n, \mathbf{k})$ along $\overline{\Gamma\text{K}}$, vanish.

The Dirac cone of the clean substrate (panel (d)) is characterised by a magnetisation which is strictly perpendicular to the \mathbf{k} -vector. The in-plane magnetisations rotate clockwise in the upper cone (sketched in (a)) and anticlockwise in the lower cone. The perpendicular relation between the magnetisation (“spin”) and the \mathbf{k} -vector (“momentum”) is called *spin-momentum locking*: In the model of nearly free electrons, the spins of surface states underlying strong SOC are perpendicular to the momenta, as the CPD Hamiltonian shows (Eq. (2.17), $\nabla V \parallel \mathbf{e}_z \Rightarrow \boldsymbol{\sigma} \perp \mathbf{p} \sim \mathbf{k}$, [171]). The spin-momentum locking is confirmed by the band structures of this work as all magnetisations parallel to \mathbf{k} and associated with the surface remain white (not shown). The T-symmetry causes the rotation (Kramers degeneracy). Panel (g) shows that the magnetisation is in-plane near the Γ -point, but gains a finite out-of-plane component m_z along $\overline{\Gamma\text{K}}$. This component positive for three C_3 -related K-points, negative for the other three K-points and zero along $\overline{\Gamma\text{M}}$. The wave-like out-of-plane tilting of the spin when circling D is due to the hexagonal warping effect, as arising from higher-order $\mathbf{k} \cdot \mathbf{p}$ theory combined with the spatial symmetries of the surface [172].

In 1BL-Sb, the Dirac cone around D^* (b) has the same spin texture as the original Dirac cone of the clean substrate (d). However, progressing on the $\overline{\Gamma\text{K}}$ path, the spin of TSS_{Sb} rotates from $(m_y > 0, m_z = 0)$ via $(m_y = 0, m_z < 0)$ to $(m_y < 0, m_z < 0)$ ((b) and (h)). The B band behaves similarly, but with opposite signs and an additional sign change when it connects to double peak P_{Sb} . The latter has thus a coloured upper branch, while the lower branch shows only weak magnetisations. The overall m_z contributions are considerably stronger than those of the clean substrate, indicating a stronger hexagonal warping effect. Along $\overline{\Gamma\text{M}}$, the magnetisations of TSS_{Sb} , B and P_{Sb} remain strictly in plane and are rather constant due to hexagonal warping. The magnetisations furthermore show that the substrate (e) the adlayer (b) equally contribute to TSS_{Sb} and the B band, while P_{Sb} is only barely visible in the substrate bands. The magnetisations of R_{BS} are completely in-plane and localised in the substrate (e). They resemble a double parabola, whose branches are shifted leftwards (red) and rightwards (blue). This agrees with the expectations from the Rashba effect. The spin texture of 2BL-Sb looks very similar to that of 1BL-Sb. The states around D^* have the same spin texture as the original Dirac cone and are mainly localised in the adlayer (c). The in-plane magnetisation of TSS_{Sb} is weaker and the out-of-plane component very strong (i). Also the Rashba splitting is stronger than in 1BL-Sb (f).

9.2.2 Simulated STM images

Scanning tunnelling microscopy STM sheds light on the morphology of surfaces. For the above systems, theoretical STM images are simulated according to the theorem of Tersoff and Hamann [173]. For this purpose, the local density of states (LDOS) is integrated over an energy frame from the Fermi level to the STM bias voltage V_{bias} . The experimental STM images of 1BL-Sb and 2BL-Sb were taken by the collaborators of [P7] at $V_{\text{bias}} = +0.2$ V in constant-current mode, where the positive sign indicates the probing of empty states (for details, see [P7]). Therefore, the STM simulation consists in summing the partial charges of all states between E_{F} and $E_{\text{F}} + 0.2$ eV. The resulting isosurfaces are shown in Fig. 9.7.

The experimental STM image of 1BL-Sb (panel (a)) is characterised by a hexagonal pattern of bright spots. The theoretical image (b) reproduces this very well and the underlying structure (c) shows that these spots indeed stem from charge bulbs above the upper Sb atoms. Since the lower Sb atoms are invisible due to the strong signal from the upper Sb atoms, the symmetry of the STM image is hexagonal, despite the trigonal symmetry of the atomic arrangement. The STM image of 2BL-Sb (d) looks different from 1BL-Sb, despite the same isocurrents and same geometry of the uppermost atomic layer. The bright spots are triangular and connected by bridges. Consequently the symmetry of the image is clearly trigonal. The theoretical image (e) reproduces this very well. An astonishing detail is that the triangular spots point upwards, not downwards as the geometry of the top BL (f) suggests. In other words, the apparent buckled-honeycomb pattern is exactly inverted with respect to the real buckled Sb honeycombs: The bright spots are above the upper Sb atoms of the top BL, the bridges above the holes and the apparent holes above the lower Sb atoms. The reason for this is that the charge bulbs of the upper Sb atoms of BL1 penetrate the holes of BL2 and are thus probed beside the bright charge bulbs of the upper Sb atom of BL2. This demonstrates that STM only measures charge densities, which can deviate from real atomic arrangements.

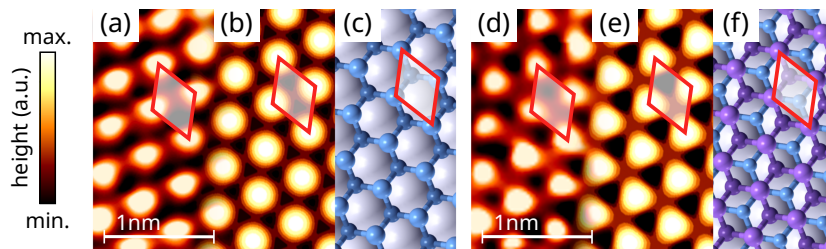
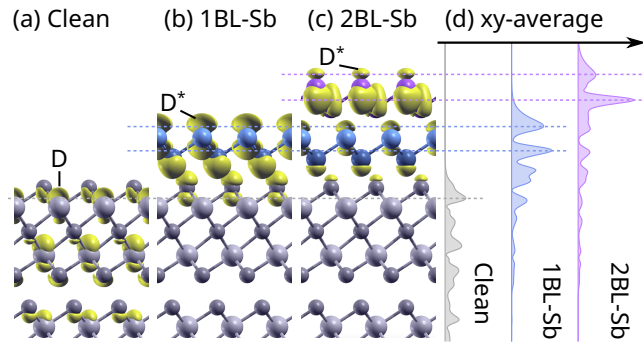


Figure 9.7: STM images of (a) – (c) 1BL-Sb and (d) – (f) 2BL-Sb. (a) and (d) are experimental images taken at $V_{\text{bias}} = +0.2$ V and $I = 20$ nA (empty states). (b) and (e) are theoretical images simulated at the same voltage. (c) and (f) show the underlying structure of the simulated images. Grey circle are Se atoms; Blue/purple circles are the Sb atoms of BL1/BL2. Red rhombi indicate the surface unit cell. Reproduced from [P7].

The last point of this section concerns the real-space distribution of the Dirac points D and D^* . As these points are fourfold degenerated due to T-symmetry and the P-symmetry of the entire slab, the DFT code produces states which are artificially localised at both surfaces, although the partial charges still show a thick region with vanishing density in the simulated bulk. Averaging all four states of the Dirac points solves this symmetrisation problem. Fig. 9.8 shows the isosurfaces of the partial charges of the Dirac points in real space. For the clean substrate, the isosurface (panel (a)) as well as the plane average (d) show that the partial charge of D extends deeply into the substrate, far beyond tQL . This explains why the slab has to be so thick in order to entirely disentangle the simulated surfaces. The highest peak in the plane average coincides with the bond between the top Se atom and the Bi atom below (grey dashed line). The partial charge of D^* in 1BL-Sb (b) is more localised in the surface region as it already decays to near zero in tQL . The two largest peaks in (d) stem from charge bulbs at the top Sb atom (blue dashed lines), which look like p_z orbitals. The PAW projections indeed confirm that TSS_{Sb} has strong Sb- p_z contributions (not

Figure 9.8: Real-space isosurfaces of the wavefunctions at the Dirac points D and D^* of (a) the clean substrate, (b) 1BL-Sb and (c) 2BL-Sb. Grey circles are Bi and Se atoms; Blue/purple circles are the Sb atoms of BL1/BL2. (d) Corresponding plane averages. Reproduced from [P7].



shown). In 2BL-Sb (c) the partial charge even more concentrates in the top Sb layer. As in 1BL-Sb, the p_z orbitals of the top Sb atom contribute most to the plane average (purple dashed lines). The comparison between the three systems shows that the TSSs are transported to the surface upon Sb layer adsorption and that the vertical confinement of the states strengthens from the clean substrate to the 2BL-Sb heterostructure. This clearly hints that the transition between different topological classes of the bulk and the vacuum occurs in the topmost vdW layer. For this reason, the Sb adlayer can be considered *topologised* in that it quasi belongs to the non-trivial substrate and produces TSSs at its interface with the trivial vacuum [P7].

9.3 The topological phase transition

The chapter concludes with a deeper analysis of the electronic interplay between the Bi_2Se_3 substrate and the Sb adlayer and confirms that latter indeed topologises. For this purpose, the distances between the Sb BLs and the substrate are varied between long (free-standing sheets plus clean substrate) and short (heterostructure). By calculating the bands for each configuration, the electronic properties can be tracked along a simulated desorption-and-readsorption process.

According to pp. 126ff, the fundamental behaviour of surface states follows from the topological class of the underlying bulk. The combined band structure of the clean substrate and a free-standing, thin Sb sheet is expected to be a superposition of two uncoupled entities: the non-trivial surface bands of the former (analogous to Fig. 7.5 (c)) and the trivial 2D bands of the latter (analogous to Fig. 7.5 (b)). In the adsorption process, which finally results in the bands of the heterostructure (Fig. 9.4), the non-trivial Dirac cone of BS(0001) and the trivial 2D bands of the Sb sheet obviously vanish and, instead, a joint, non-trivial band structure appears. Thus, at a certain point, the Kramers pairs of the Sb sheet have to change partners so that they integrate themselves into the non-trivial surface states of the substrate. Such a partner change is a *topological phase transition*. The topological class of surface states can be checked by means of the connections between the surface Kramers pairs (SKPs) at the four surface TRIMs. Fig. 9.9 shows the hexagonal surface Brillouin zone and the TRIM rhombus (bold). One TRIM is Γ^0 , the Γ -point of the zeroth Brillouin zone (black). Two further TRIMs are the M-points M_{10}^0 and M_{01}^0 . The last TRIM is M_{11}^0 , which equals

M_{11}^1 of the next Brillouin zone (grey) and is thus identical to M_{11}^0 . The original k-path of Fig. 9.4 connects the non-TRIM K_{11}^0 and the TRIMs Γ^0 and M_{11}^0 . It is prolonged in the x-direction so that it comprises the line segments $\overline{\Gamma^0 M_{11}^0}$ and $\overline{\Gamma^0 M_{11}^0}$ (dashed lines in Fig. 9.9). The symmetries of BS(0001) imply that all M-points yield the same δ_i product². Thus, the SKP connections between Γ^0 and any of the M-points characterises the entire surface band structure. Nevertheless, the complete k-path in Fig. 9.9 is employed for the band structure calculations as it permits tracking the spin texture at the same time.

The details of the desorption-and-readsorption procedure are as follows: Starting from the stable 2BL-Sb heterostructure ($d_1 = 2.3 \text{ \AA}$ and $d_2 = 2.5 \text{ \AA}$), BL2 is rigidly lifted by 6.0 \AA in the first stage so that $d_2 = 8.5 \text{ \AA}$. This represents the 1BL-Sb heterostructure plus an isolated 1 BL sheet. In the second stage, BL1 is lifted by 6.0 \AA as well so that $d_1 = 8.3 \text{ \AA}$ and $d_2 = 2.5 \text{ \AA}$. This represents the clean substrate plus an isolated 2 BL sheet. In the third and last stage, the 2 BL sheet is lowered by -6.0 \AA so that the original 2BL-Sb heterostructure is restored. Each stage is linearly sampled by 20 structures, the *images*, so that the BLs move vertically by 0.3 \AA from image to image. For each image, the band structure is calculated and plotted according to four different modes:

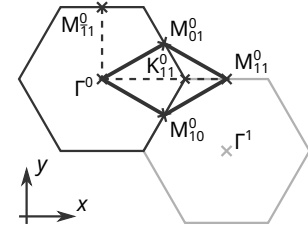


Figure 9.9: Hexagonal Brillouin zone with TRIMs.

- 1) Line width \rightarrow localisation in the upper half slab; RGB colour \rightarrow localisation in BL2, BL1 and tQL, respectively. This extracts the surface bands and indicates whether they belong to BL2 (red), BL1 (green) and/or tQL (blue).
- 2) Line width \rightarrow tQL; blue/red colour \rightarrow magnetisation of tQL. This extracts the bands of tQL and shows their spin texture. The direction of the plotted magnetisation is perpendicular to the k-path (spin-momentum locking, vide supra).
- 3) Same as 2) for BL1.
- 4) Same as 2) for BL2.

Fig. 9.10 shows the band structures of 16 out of the total 56 images.

The energies are reset to the VBM of bulk Bi_2Se_3 . The Fermi energy of the slab is inserted as a black horizontal line. Four special cases provide important subsystems (yellow background, blue labels): (a) the 2BL-Sb heterostructure, (e) the 1BL-Sb heterostructure plus an isolated 1 BL sheet, (i) the quasi clean substrate plus two quasi isolated 1 BL sheets, (m) the clean substrate plus an isolated 2 BL sheet. For these images, all four plotting modes are shown. For all other images, only mode 1) is shown. The respective structure model with the interlayer distances is displayed next to the band structures. Red arrows indicate the order of the images. The full set of images is available as an mp4 file in the supplementary material of [P9].

²This restriction of the combinatorics is the central reason why it is easier to realise TIs in trigonal systems, than in any other symmetry class.

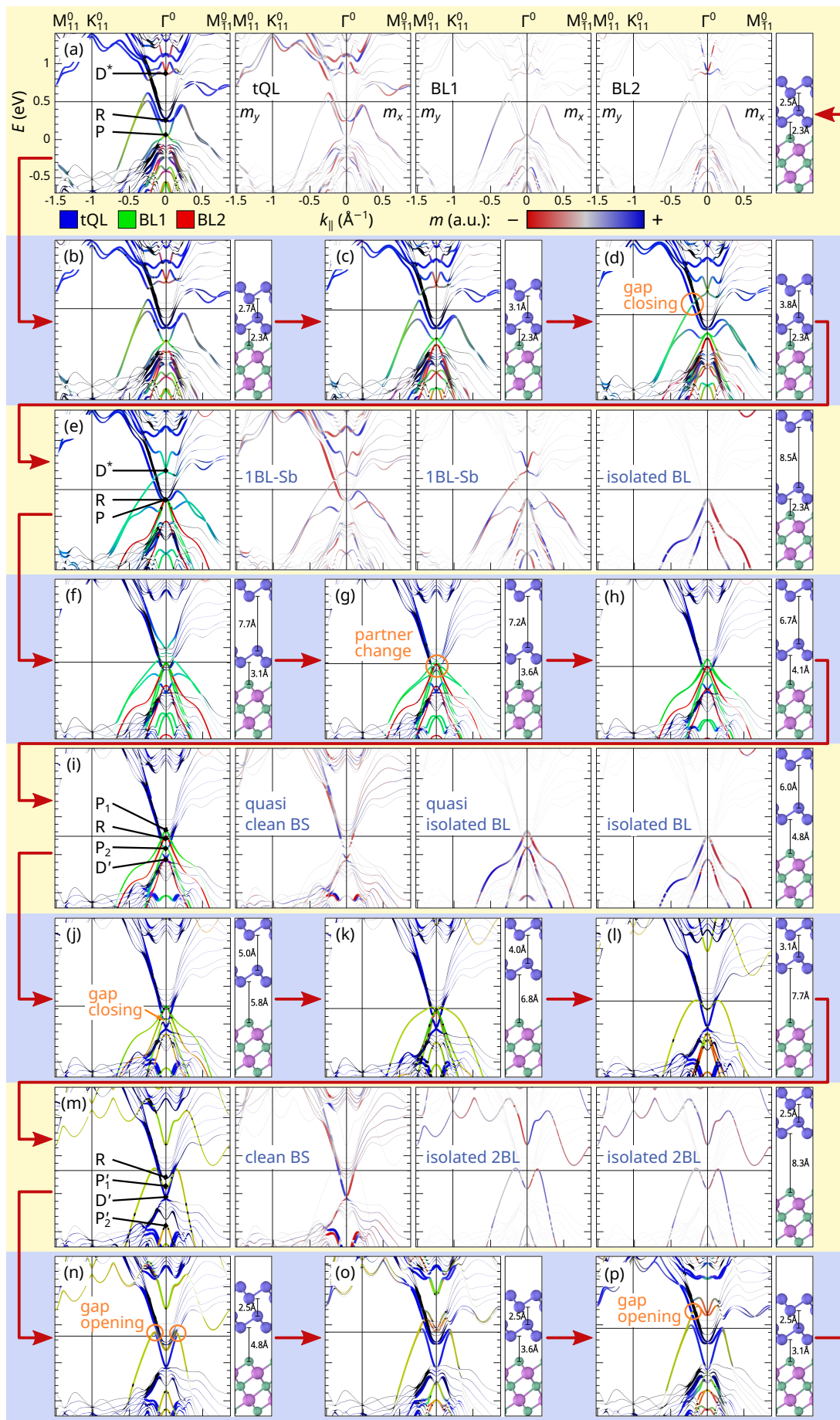


Figure 9.10: Topological phase transitions in the Sb@BS heterostructure (details in text). Reproduced from [P9].

In the first image (a), the surface band structure of 2BL-Sb is recognisable as well as the SKPs D^* , R_{BS} (abbreviated to R) and P_{Sb} (abbreviated to P). The SKP connections are as follows: Both branches of P are connected to the VBs (denoted *v-trivial*) and both branches of D^* are connected to the CBs (denoted *c-trivial*). Only the branches of R are connected to the VBs and CBs (denoted *non-trivial*) wherefore this SKP reflects the topological non-triviality of the substrate. That the lower branch going from R into the VBs changes its character from tQL to Sb indicates a strong mixing between the substrate and the adlayer.

Lifting BL2 deforms the bands. The lower branch of D^* bends down from (a) to (d) and closes a gap along $\Gamma^0M_{11}^0$, while the character changes from BL2 (red) to BL1 (green). The gap closing does not entail any partner changes, though, as R is still non-trivially connected along $\Gamma^0M_{11}^0$. At the same time, P rises towards R and two further *v-trivial* peaks belonging to BL2 (red) emerge from the bulk VBs. From (d) to (e), the band structure changes only slightly when it transforms into a superposition of the surface band structure of 1BL-Sb and the (red) 2D band structure of an isolated 1 BL sheet (Fig. 8.4 (c)). The Kramers pairs of the latter are *v-trivial*. The SKPs of 1BL-Sb show the same connections as those of 2BL-Sb, even though P and R are very close together. The PAW projections shift so that TSS_{Sb} has a mixed BL1+tQL character (cyan). Since no partner change occurs from (a) to (e), the desorption of BL2 does not involve topological phase transitions. In the reverse direction of adsorbing a second BL to 1BL-Sb, the transport of the TSSs across BL2 towards the surface of the 2BL-Sb heterostructure consists in a continuous shifting of the PAW projections, while the valence bands of BL2 disappear in the bulk VBs.

Lifting BL1 drops D^* into the bulk CBs (f). At $d_1 = 3.6 \text{ \AA}$ (g), D^* touches P and R whereupon a partner changing occurs: The upper branch of D^* connects with the upper branch of R, which produces a *c-trivial* SKP, again denoted R. The lower branch of R connects with the upper branch of P, which produces a *v-trivial* SKP, denoted P_1 . The lower branch of P connects with the lower branch of D^* , which produces a non-trivial SKP, denoted P_2 . The partner change is a topological phase transition which detaches the topological non-triviality from R and stores it into a new point P_2 . It furthermore unravels the zigzag manner in which P_{Sb} is connected in the 1BL-Sb bands (the B band is connected to the same TRIM as TSS_{Sb} , while the lower branch goes elsewhere). As a consequence, the upper Sb peak it is allowed to form the twofold degenerated peak of the isolated 1 BL sheet. In the course of the topological phase transition, the projections of TSS_{Sb} shift from tQL+BL1 (cyan) to BL1 (green). In addition to the three new SKPs from mixing the old ones, an additional, *v-trivial* SKP denoted D' emerges from the bulk VBs. The middle image of the second stage (i) represents a system of two quasi isolated 1 BL sheets and the quasi clean substrate. The SKPs are clearly visible, as well as the almost complete formation of the valence band peaks of the isolated BL1.

Lifting BL1 further towards BL2 closes a gap (j) which restores the Dirac cone of the substrate. By this means P_2 swaps SKP connections with D' whereupon P_2 is *v-trivial* and D' is non-trivial. This proves that D' is indeed the original D . From (i) to (m), the bands of the two isolated 1 BL sheets transform into the bands of an isolated 2 BL sheet (Fig. 8.4 (d)). At $d_2 = 4.0 \text{ \AA}$ (k), the upper peak of BL2 and the two peaks of BL1

(P_1 and P_2) merge whereupon the topmost band with its characteristic furrow comes off. After the merging, the two topmost 2D Kramers pairs are denoted P'_1 and P'_2 . As no gap closing occurs in the bands of the Sb BLs, the topological class of the 2 BL sheet is trivial, as already confirmed in Sec. 8.2.2.

In the last stage, the 2 BL sheet is lowered towards the substrate. At $d_1 = 4.8 \text{ \AA}$ (n), the topmost (twofold degenerate) band of the sheet (the 2 BL band) arranges with the bulk CBs so that P'_1 touches R. At the same time, a gap opens between the 2 BL band, the Dirac cone of the substrate and the lowermost bulk CB. As a result, D' , P'_1 and R change the SKP connections: The inner upper branch of D' connects to the outer lower branch of the 2 BL band, which produces the B band and renders D' v -trivial. The inner upper branch of P'_1 connects to the outer upper branch of the Dirac cone and the inner lower branch of P'_1 connects to the bulk CBs, so P'_1 c -trivial. The inner lower branch of R connects to the outer upper branch of the 2 BL band, which produces $\overline{\text{TSS}}_{\text{Sb}}$ and renders R non-trivial. The new connections are better visible along $\overline{\Gamma^0 M_{11}^0}$, while along $\overline{\Gamma^0 M_{11}^0}$, R is *apparently* c -trivial and P'_1 non-trivial due to the vanishing gap. This gap opens at $d_1 = 3.1 \text{ \AA}$ (p) as well and, after a reordering between D' and the lower Sb peak, the final band structure of 2BL-Sb is restored (a).

The magnetisations show that the twofold degenerate bands of the Sb sheets polarise when they approach the substrate. The spin texture of the Dirac cone picks the band with the same magnetisation and hybridises with it, while the other band remains unaffected. This explains why D^* inherits the spin texture of D. If a Sb sheet approaches the substrate, the first topological phase transition happens in the topmost VB, if the sheet is 2 BL thick, and in the second top VB (lower Sb peak) if the sheet is 1 BL thick. The latter is quite surprising at first glance, but can be explained: The bands of the isolated sheets in Fig. 8.4 (c) and (d) show that the topological phase transition happens in those VBs which provide p_z contributions. On the contrary, the topmost VB of a 1 BL thick sheet provides only $(p_x + p_y)$ contributions. This leads to the conclusion that the p_z orbitals play the decisive role in the surface topological phase transitions, similarly to the band inversion in the bulk TIs.

9.4 Discussion and summary

The analysis of the 1BL-Sb@BS and 2BL-Sb@BS heterostructures showed that the structure models in which the BLs continue the natural stacking sequence of the substrate are indeed favourable. However, structure models with inverted BLs are less stable by only $\sim 10 \text{ meV}$ per Sb atom, less than $k_B T$ at room temperature. Hence, it is likely that inverted structures are thermodynamically relevant. Similarly to the case of bulk Bi_2Se_3 , vdW corrections and SOC reduce the interlayer distance between the substrate and the Sb adlayer. SOC is even more important in the heterostructures than in bulk Bi_2Se_3 . The favourable natural stacking minimises the interlayer distances for geometrical reasons and thus the Sb chemical potential.

The band structures were calculated for the naturally stacked heterostructures as well as for the inverted ones. The bands of the latter have never been published be-

fore, while the bands of the former are unprecedented in detail and clarity. The theoretical band structures of the natural structure models compare very well with ARPES measurements. Unfortunately, the band features which distinguish the natural structure models from those with inverted BLs, D^* and P_{Sb} , are invisible in ARPES due to negative binding energies and matrix-element effects. Thus, ARPES is limited in identifying BL inversions. The STM simulation of the natural structure models agrees very well with experimental STM images. In particular, the differences in the symmetries of the image and the atomic geometry, hexagonal vs. trigonal for 1BL-Sb and inversion for 2BL-Sb, were proven to be due to deviations between the charge densities at the Fermi surface and the atomic geometries.

The topological phase transitions during a simulated desorption-and-readsorption process illuminated how the Dirac cone of the clean BS(0001) surface merges with the bands of a thin Sb sheet to produce the joint bands of the heterostructure. When a 1 BL or a 2 BL thick Sb sheet approaches the substrate, a complicated series of topological phase transitions occurs. It begins in the p_z bands of the Sb sheet and trivialises the Dirac cone, whose Dirac point D is buried in the bulk valence bands. The Dirac point D^* is shown to be a remainder of the Sb peaks and topologically trivially connected to the conduction bands. The only non-trivial surface Kramers pair is R_{BS} , the crossing of the Rashba split conduction bands. Its lower branch follows an electron-like parabola near the Γ -point and bends down away from the Γ -point to form TSS_{Sb} , which is visible in ARPES. The topological phase transitions occur only when the first (set of) BLs approach the BS surface. The addition of a second BL to 1BL-Sb is continuous in that there are no partner changes.

The literature on DFT band structures of the Sb@BS system is sparse. Two works with intersecting author lists exist, containing band structures for 1BL-Sb (Jin et al. [168]) and 2BL-Sb (Kim et al. [166]). The band structures look rather different from those presented here. The 1BL-Sb band structure of Jin et al. shows a strong misalignment of D^* and P_{Sb} , the former being in the bulk CBs and the latter being 0.2 eV below D^* , not 0.3 eV. The desorption-and-readsorption process shows that the misalignment is due to a too large interlayer distance d_1 (Jin et al.: 2.71 Å vs. this work: 2.38 Å). Jin et al. obtained the structure by DFT relaxations, but they do not mention whether they employed vdW corrections and/or SOC. The large d_1 suggests that they omitted at least one of the two. The 2BL-Sb band structure of Kim et al. shows the major qualitative difference that there is no gap in the $\bar{\Gamma}K$ direction, contrarily to the bands presented here. Unfortunately, Kim et al. give neither details on whether they employed vdW corrections or SOC during the DFT relaxations, nor structure parameters like the interlayer distances. In both [168] and [166], the band structures of the $\bar{\Gamma}M$ path are missing, despite the pronounced gaps in TSS_{Sb} which show that D^* does not reflect the topological non-triviality of the substrate. Jin et al. calculated also the band structures under variation of the interlayer distance between a 1 BL sheet and a Bi_2Te_2Se substrate. Although this reminds of the desorption-and-readsorption process of this work, they did not analyse the details and did not extract the topological phase transitions. In particular, they did not notice that R_{BS} is non-trivially connected while D^* is trivially connected to the CBs. Consequently, the SKP method developed in this thesis is indeed a novel tool for extracting surface topological phase transitions in a systematic manner.

10 Conclusions

In this PhD thesis, two classes of nano-scaled systems were successfully investigated by means of DFT: rare-earth silicide nanowires on silicon surfaces and thin antimony layers on bismuth selenide. A close inspection of the configuration spaces of the nanostructures resulted in different structure models, which were optimised with respect to the atomic positions and whose stability was evaluated by means of ab initio thermodynamics. The detailed analysis of the structural and electronic properties lead to several conclusions about the underlying chemistry and provided a deep insight into the physics of the nanostructures. All results agree well with experimental reference on lattice parameters as well as ARPES measurements, Fermi surfaces and STM images. Finally, the systematic approach of this work and the detailed cross-linking between the structural and electronic properties permitted the identification of fascinating novel phenomena: the dimensional crossover in the nanowire-Tb@Si(557) system and the complex series of multiple topological phase transitions in the Sb@Bi₂Se₃ heterostructure.

The heavy sixth-row elements which occur in both systems were shown to have properties which are unique in the periodic table. The lanthanoids Tb and Er have a stable trivalent state in the bulk RESi_{2-x} phases, despite the incompleteness of the 4f shell. Also the lanthanoid contraction was demonstrated for the silicides from TbSi₂ to ErSi₂. The element Bi is even more peculiar as the relativistic effects give rise to the inert-pair effect of the 6s electron, as explicitly demonstrated in bulk Bi₂Se₃. Furthermore, the relativistic effects are so strong that Bi₂Se₃ transitions into a topological insulator. Similarly, bulk β -Sb turned out to be a topological semimetal. The heavy elements necessitated methods beyond DFT: the LDA+U method, vdW corrections and spin-orbit coupling, which all proved to be crucial for obtaining correct results for the respective systems. The Z_2 invariant was elaborated in order to explicitly calculate the topological classes of Bi₂Se₃ and β -Sb. Furthermore, it is the basis of the novel SKP method, which was developed in this thesis in order to track and understand the topological phase transitions in the Sb@Bi₂Se₃ heterostructure. This method can be applied to all surfaces which establish a connection between a substrate and an adsorbate of different topological classes.

It proved to be indispensable to analyse the related higher-dimensional systems before treating the actual nanostructures. These were the bulk RESi_{2-x} phases and the monolayer-Tb@Si(111) system in the case of the TbSi₂ nanowires, and bulk Bi₂Se₃ and β -Sb in the case of the Sb@Bi₂Se₃ heterostructures. Though, the connection between the bulk and the respective nanostructure is not as obvious as one may assume. For example, the popular argument of surface-induced strain, which can describe the epitaxy of bulk-like layers on substrates, was proven to be inapplicable

for the herein investigated nanostructures. On the contrary, surface strain is negligible in both the monolayer-Tb@Si(111) and the Sb@Bi₂Se₃ systems, while a large strain would follow from the lattice constants of the respective bulk phases. Hence, the strain in nanostructures has to be evaluated with special caution in order to avoid wrong conclusions. The bulk structures are useful because they permit to understand fundamental structural mechanisms, which apply to the nanostructures as well, e.g. the silicon cages in RESi_{2-x} or the layer-layer interaction in Bi₂Se₃ and β -Sb. Furthermore, the electronic properties of the higher-dimensional systems can help to identify the origins of the band structures of the nano-scaled systems. In this work, the bands of the nanowire-Tb@Si(557) system were shown to be derivable from the bands of the monolayer-Tb@Si(111) system, which in turn can be derived from the bands of (hypothetical) CaSi₂-TbSi₂ by zone projection. In the case of the Sb@Bi₂Se₃ system, the topological classes of Bi₂Se₃ and β -Sb were absolutely crucial for understanding the topological phase transitions in the heterostructure.

Outlook: Rare-earth silicide nanowires on silicon surfaces

The investigations of the RESi₂ nanowires give rise to at least two further scientific questions. Firstly, the bulk phases of RESi_{2-x} were shown to be a complex system, despite the small unit cells of the structure prototypes. The results for the supercells with ordered Si vacancies give only an idea about the underlying physics. In order to fully understand the RESi_{2-x} phases, it is necessary to introduce probability into the distribution of the Si vacancies and to calculate the temperature-concentration phase diagrams. This may finally explain why the stoichiometry of AlB₂-RESi_{2-b} is equal for all REs ($b \approx \frac{1}{3}$), while the stoichiometry of ThSi₂-RESi_{2-a} depends on the atomic number of the employed RE ($a < \frac{1}{3}$).

The second scientific question concerns the RESi₂ nanowires on Si(001). Although not included in this thesis, investigations of this system were published in [P3, P6]. Despite a systematic inspection of the configuration space of reasonable structure models, the stability of the nanowires could not be proven by means of straightforward grand-potential-chemical-potential phase diagrams. On the contrary, the width of the nanowires was found to be unlimited in that they would aggregate to a 2D film. The contradictory results were attributed to kinetic effects. Understanding the peritectic transition in the bulk phase diagrams might support the further elaboration of this issue. A further consequence of this work for the nanowire-RE@Si(001) system results from the finding that the stable structure models of the monolayer-Tb@Si(111) and nanowire-Tb@Si(557) systems obey the ZKB concept in a strict manner. Thus, it is likely that the nanowires on Si(001) obey the ZKB concept as well. Therefore, the structure models already found should be evaluated regarding this issue and further structure models could be set up based on this.

Outlook: Thin antimony layers on bismuth selenide

The findings on the Sb@Bi₂Se₃ heterostructure raise two further scientific questions. The first concerns the layer inversions, which introduce only small penalties into the

Sb chemical potentials. Since these are below $k_B T$ at room temperature, the omission of the lattice dynamics is certainly questionable. This point should be further investigated, e.g. by the frozen-phonon method.

The second question is about GW-corrected band structures. Since Bi_2Se_3 is a topological insulator, GW exerts a strong effect on the region around the Γ -point, which reduces the band gap and alters the Dirac cones of the clean surfaces of Bi_2Se_3 , Bi_2Te_3 and Sb_2Te_3 [163, 164, 170]. For this reason, GW effects on the bands of the $\text{Sb@Bi}_2\text{Se}_3$ heterostructures would be very interesting from a general point of view. Moreover, a corrected band structure would permit a quantitative comparison with ARPES, which could be very helpful for identifying layer inversions, e.g. by the slopes of TSS_{Sb} .

Appendix A

A.1 Mathematical identities

The Dirac notation

Dirac notation (discrete basis):

$$\begin{aligned}\sum_n |n\rangle\langle n| &= I && \text{Completeness} \\ \langle n|n'\rangle &= \delta_{nn'} && \text{Orthogonality} \\ |\Psi\rangle &= \sum_n |n\rangle\langle n|\Psi\rangle = \sum_n \Psi_n|n\rangle, \Psi_n = \langle n|\Psi\rangle && \text{Series expansion} \\ O_{nn'} &= \langle n|O|n'\rangle && \text{Matrix representation}\end{aligned}$$

Dirac notation (continuous basis):

$$\begin{aligned}\int dx |x\rangle\langle x| &= I && \text{Completeness} \\ \langle x|x'\rangle &= \delta(x-x') && \text{Orthogonality} \\ |\Psi\rangle &= \int dx |x\rangle\langle x|\Psi\rangle = \int dx \Psi(x)|x\rangle, \Psi(x) = \langle x|\Psi\rangle && \text{Series expansion} \\ O(x,x') &= \langle x|O|x'\rangle && \text{Matrix representation}\end{aligned}$$

The translation operator

The translation operator U_t is defined by its action on the real space distribution of a state, i.e. U_t shifts the expectation value of the position operator x for every $|\Psi\rangle \in \mathcal{H}$ by a constant t . Since translations do not change the scalar product, the translation operator has to be unitary.

$$\langle x\rangle = \langle \Psi|x|\Psi\rangle \Leftrightarrow \langle x+t\rangle = \langle \tilde{\Psi}|x|\tilde{\Psi}\rangle = \langle \Psi|U_t^{-1}xU_t|\Psi\rangle = \langle \Psi|x+t|\Psi\rangle$$

As this is, in particular, valid for the vectors of any basis, the condition can be summarised as a commutator equation.

$$U_t^{-1}xU_t = x + t \quad \Leftrightarrow \quad [U_t, x] = -tU_t \quad (*)$$

This can be solved by the following ansatz:

$$\begin{aligned}
 U_t &= \exp(it \cdot s) \quad \text{with} \quad [s, x] = c \in \mathbb{C} \\
 \Rightarrow [U_t, x] &= [\exp(it \cdot s), x] \stackrel{(A.93)}{=} it \exp(it \cdot s) [s, x] = it U_t [s, x] \\
 &\stackrel{(*)}{\Leftrightarrow} [s, x] = i
 \end{aligned}$$

As the position operator x and the momentum operator p hold the canonical commutation relation ($[-\frac{1}{\hbar}p, x] = i$), the solution for the translation operator U_t is:

$$U_t = \exp(-i\frac{1}{\hbar} t \cdot p) \quad (A.91)$$

The commutator of operator functions

Let A and B be linear operators acting on a Hilbert space \mathcal{H} . The commutator of A and B shall be a constant $c \in \mathbb{C}$. It then holds for $n \in \mathbb{N} \setminus 0$:

$$[A^n, B] = A^n B - B A^n = n A^{n-1} c \quad (A.92)$$

Proof. (A.92) will be proven by mathematical induction.

$$\begin{aligned}
 \forall n \in \mathbb{N} \setminus 0 : \quad & [A^n, B] = A^n B - B A^n = n A^{n-1} c & (IV) \\
 n = 1 : \quad & [A^1, B] = AB - BA = c \quad \Leftrightarrow \quad BA = AB - c & (IA) \\
 n \rightarrow n + 1 : \quad & [A^{n+1}, B] = A^{n+1} B - (BA) A^n = A^{n+1} B - (AB - c) A^n & (IS) \\
 & = A(A^n B - B A^n + c A^{n-1}) \stackrel{IV}{=} A(n A^{n-1} c + A^{n-1} c) \\
 & = (n + 1) A^n c
 \end{aligned}$$

□

A corollary is the generalisation to functions of operators which per definitionem have a converging power series:

$$f(A) = \sum_{k=0}^{\infty} f_k A^k \quad \Rightarrow \quad [f(A), B] = f(A)B - Bf(A) = f'(A)c \quad (A.93)$$

The Fourier series in multiple dimensions

Let $f : \mathbf{x} \rightarrow \mathbb{C}$ be a periodic function on a lattice \mathcal{R} with unit cell $C_{\mathcal{R}}$, reciprocal lattice \mathcal{G} , as defined in Sec. 2.2. Then f has the following Fourier series:

$$f(\mathbf{x}) \sim \sum_{\mathbf{G} \in \mathcal{G}} \exp(i\mathbf{x} \cdot \mathbf{G}) f_{\mathbf{G}} \quad (A.94a)$$

$$f_{\mathbf{G}} = \frac{1}{|C_{\mathcal{R}}|} \int_{C_{\mathcal{R}}} d\mathbf{x} \exp(-i\mathbf{x} \cdot \mathbf{G}) f(\mathbf{x}) \quad (A.94b)$$

If, in addition, $f \in \mathcal{H} = L^2(C_R)$, the Parseval theorem holds [174, pp. 145f]:

$$\sum_{\mathbf{G} \in \mathcal{G}} |f_{\mathbf{G}}|^2 = \frac{1}{|C_R|} \int_{C_R} dx |f(\mathbf{x})|^2 \quad (\text{A.95})$$

If, in addition, f is continuous and its derivative is piecewise continuous, then:

$$\sum_{\mathbf{G} \in \mathcal{G}} \mathbf{G} |f_{\mathbf{G}}|^2 = \frac{-i}{|C_R|} \int_{C_R} dx f^*(\mathbf{x}) \nabla_{\mathbf{x}'} f(\mathbf{x}') \Big|_{\mathbf{x}'=\mathbf{x}} \quad (\text{A.96})$$

Eq. (A.96) follows from the Parseval theorem applied on f and its gradient ∇f expressed as a Fourier series [174, pp. 148ff].

$$(\nabla f)_{\mathbf{G}} = i\mathbf{G} f_{\mathbf{G}}$$

A.2 The principle of minimal coupling

Let $H_0(\mathbf{p}, \mathbf{x})$ be the Hamilton operator of a free particle with charge q :

$$H_0(\mathbf{p}, \mathbf{x})|\Psi\rangle = E|\Psi\rangle$$

Then, the introduction of a vector potential $\mathbf{A}(\mathbf{x}, t)$ and a scalar potential $\varphi(\mathbf{x}, t)$ modifies the Hamiltonian as follows:

$$H_0(\mathbf{p} - q\mathbf{A}, \mathbf{x})|\Psi\rangle = (E - q\varphi)|\Psi\rangle \Leftrightarrow [H_0(\mathbf{p} - q\mathbf{A}, \mathbf{x}) + q\varphi]|\Psi\rangle = E|\Psi\rangle \quad (\text{A.97})$$

Eq. (A.97) can be motivated by the Hamiltonian for the classical problem. For this purpose, let H_0^c be the Hamiltonian for a classical charged particle moving in an electromagnetic field. The coupling of the electromagnetic potentials to the momentum and the energy yields the correct classical Lorentz force:

$$\begin{aligned} H_0^c &= \frac{(\mathbf{p} - q\mathbf{A})^2}{2m} + q\varphi \\ \dot{\mathbf{x}} &= \nabla_{\mathbf{p}} H_0^c = \frac{1}{m}(\mathbf{p} - q\mathbf{A}) \\ \dot{\mathbf{p}} &= -\nabla_{\mathbf{x}} H_0^c = -\frac{1}{2m} \nabla_{\mathbf{x}} (\mathbf{p} - q\mathbf{A})^2 - q\nabla_{\mathbf{x}} \varphi = q [(\dot{\mathbf{x}} \cdot \nabla_{\mathbf{x}}) \mathbf{A} + \dot{\mathbf{x}} \times (\nabla_{\mathbf{x}} \times \mathbf{A}) - \nabla_{\mathbf{x}} \varphi] \\ \frac{d\mathbf{A}}{dt} &= \frac{\partial \mathbf{A}}{\partial t} + \{\mathbf{A}, H_0^c\} = \frac{\partial \mathbf{A}}{\partial t} + (\dot{\mathbf{x}} \cdot \nabla_{\mathbf{x}}) \mathbf{A} \\ \Rightarrow m\dot{\mathbf{x}} &= \frac{d}{dt} (\mathbf{p} - q\mathbf{A}) = \dot{\mathbf{p}} - q \frac{d\mathbf{A}}{dt} = q \left[-\nabla_{\mathbf{x}} \varphi - \frac{\partial \mathbf{A}}{\partial t} \right] + q\dot{\mathbf{x}} \times (\nabla_{\mathbf{x}} \times \mathbf{A}) = q\mathbf{E} + q\mathbf{v} \times \mathbf{B} \end{aligned}$$

Eq. (A.97) follows from the correspondence principle by replacing the canonical variables \mathbf{p} and \mathbf{q} in H_0^c with the respective operators.

The proof for the meaningfulness of Eq. (A.97) consists in a test for gauge invariance. For this purpose, the solution $|\Psi\rangle$ is subjected to a $U(1)$ unitary transformation, i.e. for an arbitrary function $\chi(\mathbf{x}, t)$, the transformed states are:

$$|\tilde{\Psi}\rangle = U_\chi |\Psi\rangle = \exp(i\frac{q}{\hbar}\chi(\mathbf{x}, t)) |\Psi\rangle \quad (\text{A.98})$$

Consequently, the operators transform as follows:

$$\tilde{\mathbf{x}} = U_\chi \mathbf{x} U_\chi^{-1} = \mathbf{x} \quad (\text{A.99a})$$

$$\tilde{\mathbf{p}} = U_\chi \mathbf{p} U_\chi^{-1} = \exp(i\frac{q}{\hbar}\chi)(-i\hbar\nabla_x) \exp(-i\frac{q}{\hbar}\chi) = \mathbf{p} - q\nabla_x\chi \quad (\text{A.99b})$$

$$\tilde{E} = U_\chi E U_\chi^{-1} = \exp(i\frac{q}{\hbar}\chi)(i\hbar\frac{\partial}{\partial t}) \exp(-i\frac{q}{\hbar}\chi) = E + q\frac{\partial\chi}{\partial t} \quad (\text{A.99c})$$

With these relations, the full transformation of the differential equation Eq. (A.97) holds:

$$\begin{aligned} 0 &= [H_0(\mathbf{p} - q\mathbf{A}, \mathbf{x}) - (E - q\phi)] |\Psi\rangle \\ &= U_\chi [H_0(\mathbf{p} - q\mathbf{A}, \mathbf{x}) - (E - q\phi)] U_\chi^{-1} U_\chi |\Psi\rangle \\ &= \left[H_0(\mathbf{p} - q\nabla_x\chi - q\mathbf{A}, \mathbf{x}) - (E + q\frac{\partial\chi}{\partial t} - q\phi) \right] |\tilde{\Psi}\rangle \\ &= [H_0(\mathbf{p} - q\tilde{\mathbf{A}}, \mathbf{x}) - (E - q\tilde{\phi})] |\tilde{\Psi}\rangle \end{aligned} \quad (\text{A.100})$$

with

$$\tilde{\mathbf{A}} = \mathbf{A} + \nabla_x\chi, \quad \text{and} \quad \tilde{\phi} = \phi - \frac{\partial\chi}{\partial t} \quad (\text{A.101})$$

The transformed differential equation in Eq. (A.100) has the same structure as before, but different electromagnetic potentials. These are linked to the original ones by a gauge transformation according to Eq. (A.101). Therefore, the electromagnetic fields and, thus, the physics remain the same. The consistency between the phase shift applied to $|\Psi\rangle$ (Eq. (A.98)) and the gauge-transformed electromagnetic potentials (Eq. (A.101)) proves that the way of introducing electromagnetic potentials into the Hamilton operator is gauge invariant.

Eq. (A.97) is called *the principle of minimal coupling* since the electromagnetic potentials couple only via the charge q to the physics of the quantum particle. In other words, the effect of electromagnetic fields on the physics of a quantum particle is determined only by one scalar parameter and nothing else (like dipoles etc.). The principle of minimal coupling fulfils the physical prerequisite of gauge invariance. Moreover, it is a proof that the properties of electromagnetic fields arise naturally from the phase degree of freedom of the wavefunction $|\Psi\rangle$. The principle of minimal coupling can introduce electromagnetic fields into any differential equation of a free particle depending on energy and momentum operators, in particular the non-relativistic Schrödinger equation and the relativistic Dirac equation.

Appendix B

B.1 The terms and ionisation energies of the lanthanoids

Hund's second rule can be illustrated by the terms of the isolated, neutral Ln atoms. The divalent VEC of the first lanthanoid La ($4f^1 5d^0 6s^2$) is not stabilised by any exchange energy. Therefore, the electron leaves the 4f shell and occupies the 5d shell instead (actual VEC: $4f^0 5d^1 6s^2$, trivalent). For the second lanthanoid Ce, the exchange energy of two 4f electrons is too small to stabilise the divalent VEC wherefore, as in the case of La, one 4f electron is lifted to the 5d shell (actual VEC: $4f^1 5d^1 6s^2$, trivalent). For all subsequent lanthanoids of the first half-series, the divalent VEC is more stable than the trivalent one, ensured by the increasing exchange-related penalty on removing an electron from the 4f shell. The exchange penalty peaks in Eu, whose 4f shell is half-filled ($4f^7 5d^0 6s^2$). The first element of the second half-series Gd assumes the trivalent VEC ($4f^7 5d^1 6s^2$), because it would otherwise begin to fill the other spin component of the 4f shell without stabilising exchange energy. The next element Tb assumes the divalent VEC, unlike Ce, though, the trivalent VEC is less stable by only 0.04 eV. All subsequent lanthanoids of the second half-series assume the divalent VEC, analogously to the first half-series. The last lanthanoid, Lu, is trivalent, the only possible VEC due to exhaustion of the 4f shell [75].

Hund's rules manifest themselves also in the third ionisation energies. All Ln^{2+} ions assume the divalent VEC ($4f^n 5d^0 6s^0$), except La^{2+} , Gd^{2+} and Lu^{2+} , whose VECs are trivalent ($4f^0 5d^1 6s^0$, $4f^7 5d^1 6s^0$ and $4f^{14} 5d^0 6s^1$, respectively). However, the energy difference to the divalent state for La^{2+} and Gd^{2+} is small compared the ionisation energies. The peculiar dependence between the third ionisation energies and the atomic numbers can completely be explained by three contributions:

- 1) The exchange penalty, which increases the ionisation energy proportional to the number of 4f electrons with same spin. It is the most effective contribution and gives rise to the zigzag pattern with maxima at Eu and Yb.
- 2) The paring energy, which destabilises the second half shell and thus reduces the ionisation energies of the second half-series by a constant offset.
- 3) The orbital energy from the change in total angular momentum, which modulates the zigzag patterns by wavy slopes with inflexion points at quarter and three-quarters fillings of the 4f shell.

If all three contributions are subtracted, the residual of the third ionisation energies would follow a quite smooth curve with a positive slope, which accords with the increasing charge of the nucleus [75].

B.2 The RESi_{2-x} bulk phases

	a (Å)	b (Å)	c (Å)	c/a	V/N_{Er} (Å ³)	μ_{Er} (eV)	$\Delta\mu_{\text{Er}}$ (meV)
PBE							
ort- $\text{AlB}_2\text{-ErSi}_2$	4.24	3.84	3.91	0.923	56.8	-1.484	266
hex- $\text{AlB}_2\text{-ErSi}_{2-b}$	3.76		4.14	1.101	50.8	-1.750	0
tet- $\text{ThSi}_2\text{-ErSi}_2$	3.89	3.89	14.99	3.852	56.7	-1.500	251
ort- $\text{ThSi}_2\text{-ErSi}_{2-b}$ (1)	3.92	3.98	13.25	3.376	51.8	-1.708	43
ort- $\text{ThSi}_2\text{-ErSi}_{2-b}$ (2)	3.89	4.02	13.31	3.422	52.0	-1.658	92
PBEsol							
ort- $\text{AlB}_2\text{-ErSi}_2$	4.18	3.85	3.83	0.917	54.7	-1.739	259
hex- $\text{AlB}_2\text{-ErSi}_{2-b}$	3.72		4.10	1.102	49.0	-1.998	0
tet- $\text{ThSi}_2\text{-ErSi}_2$	3.85	3.85	14.79	3.838	54.9	-1.750	247
ort- $\text{ThSi}_2\text{-ErSi}_{2-b}$ (1)	3.86	3.95	13.09	3.393	49.8	-1.942	56
ort- $\text{ThSi}_2\text{-ErSi}_{2-b}$ (2)	3.83	3.98	13.18	3.444	50.1	-1.888	110
Exp. reference							
hex- $\text{AlB}_2\text{-ErSi}_{2-x}$	3.78		4.09	1.082	50.6		
ort- $\text{ThSi}_2\text{-ErSi}_{2-x}$	—	—	—	—	—		

Table B.1: Lattice parameters and relative Er chemical potentials of ErSi_{2-x} in the stoichiometric and the vacancy-populated AlB_2 and ThSi_2 phases. The unit cells were optimised by code-level relaxations with different xc-functionals. Experimental reference: [85]. TbSi_{2-x} : Tab. 4.6.

	d_a (Å)	d_b (Å)	d_c (Å)
PBE			
hex- $\text{AlB}_2\text{-TbSi}_2$	2.37 (mm)		
ort- $\text{AlB}_2\text{-TbSi}_2$	2.36/2.42 (mm)		
hex- $\text{AlB}_2\text{-TbSi}_{2-b}$	2.43 (mv)		
tet- $\text{ThSi}_2\text{-TbSi}_2$	2.36 (mm)	2.36 (mm)	2.43 (mm)
ort- $\text{ThSi}_2\text{-TbSi}_{2-b}$ (1)	2.49 (vv)	2.44 (mv)	2.36 (mm) 2.39 (mv)
ort- $\text{ThSi}_2\text{-TbSi}_{2-b}$ (2)	2.50 (vv)	2.47 (vv)	2.37 (mm) 2.37 (mv)
PBEsol			
ort- $\text{AlB}_2\text{-TbSi}_2$	2.34/2.39 (mm)		
hex- $\text{AlB}_2\text{-TbSi}_{2-b}$	2.42 (mv)		
tet- $\text{ThSi}_2\text{-TbSi}_2$	2.33 (mm)	2.33 (mm)	2.38 (mm)
ort- $\text{ThSi}_2\text{-TbSi}_{2-b}$ (1)	2.48 (vv)	2.44 (mv)	2.35 (mm) 2.38 (mv)
ort- $\text{ThSi}_2\text{-TbSi}_{2-b}$ (2)	2.49 (vv)	2.46 (vv)	2.36 (mm) 2.37 (mv)

Table B.2: Si-Si nearest neighbour distances in TbSi_{2-x} optimised with different xc-functionals. Complement to Tab. 4.7.

	d_a (Å)	d_b (Å)	d_c (Å)
PBE			
hex- $\text{AlB}_2\text{-ErSi}_2$	2.36 (mm)		
ort- $\text{AlB}_2\text{-ErSi}_2$	2.35/2.42 (mm)		
hex- $\text{AlB}_2\text{-ErSi}_{2-b}$	2.43 (mv)		
tet- $\text{ThSi}_2\text{-ErSi}_2$	2.35 (mm)	2.35 (mm)	2.42 (mm)
ort- $\text{ThSi}_2\text{-ErSi}_{2-b}$ (1)	2.51 (vv)	2.45 (mv)	2.36 (mm) 2.39 (mv)
ort- $\text{ThSi}_2\text{-ErSi}_{2-b}$ (2)	2.52 (vv)	2.48 (vv)	2.36 (mm) 2.37 (mv)
PBEsol			
ort- $\text{AlB}_2\text{-ErSi}_2$	2.39/2.34 (mm)		
hex- $\text{AlB}_2\text{-ErSi}_{2-b}$	2.42 (mv)		
tet- $\text{ThSi}_2\text{-ErSi}_2$	2.33 (mm)	2.33 (mm)	2.39 (mm)
ort- $\text{ThSi}_2\text{-ErSi}_{2-b}$ (1)	2.51 (vv)	2.44 (mv)	2.35 (mm) 2.38 (mv)
ort- $\text{ThSi}_2\text{-ErSi}_{2-b}$ (2)	2.51 (vv)	2.48 (vv)	2.35 (mm) 2.37 (mv)

Table B.3: Si-Si nearest neighbour distances in ErSi_{2-x} optimised with different xc-functionals. Complement to Tab. 4.7.

	a (Å)	c (Å)	V/N_{RE} (Å ³)	γ	d_a (Å)	$\Delta\mu_{\text{RE}}$ (meV)
TbSi ₂ , PBE						
ort- AlB_2	4.23 (3.88) ^a	4.00	58.3	124.7° (110.6°) ^a	2.36 (2.42) ^a	0
tr3- CaSi_2	3.78	5.56	63.4	103.6°	2.41	-30
tr6- CaSi_2	3.94	9.34	60.9	104.9°, 118.9°	2.49, 2.29	-67
TbSi ₂ , PBEsol						
ort- AlB_2	4.17 (3.88) ^a	3.92	56.2	124.0° (112.0°) ^a	2.34 (2.39) ^a	0
tr3- CaSi_2	3.75	5.50	61.6	103.2°	2.39	+54
tr6- CaSi_2	3.91	9.22	59.1	104.6°, 118.9°	2.47, 2.27	-34
ErSi ₂ , PBE						
ort- AlB_2	4.24 (3.84) ^a	3.91	56.8	125.4° (109.3°) ^a	2.35 (2.42) ^a	0
tr3- CaSi_2	3.75	5.48	61.4	103.0°	2.40	-140
tr6- CaSi_2	3.92	9.17	59.1	104.6°, 118.8°	2.48, 2.28	-100
ErSi ₂ , PBEsol						
ort- AlB_2	4.18 (3.85) ^a	3.83	54.7	124.6° (110.8°) ^a	2.34 (2.39) ^a	0
tr3- CaSi_2	3.72	5.42	59.7	102.6°	2.38	-63
tr6- CaSi_2	3.89	9.05	57.4	104.3°, 118.8°	2.46, 2.26	-70

Table B.4: Lattice parameters and relative RE chemical potentials of TbSi₂ and ErSi₂ in the stoichiometric AlB_2 and CaSi_2 phases. The unit cells were optimised by code-level relaxations with different xc-functionals. tr6- $\text{CaSi}_2\text{-RESi}_2$ has two independent M-star angles γ and Si-Si bond lengths d_a . ^aorthorhombic distortion. Complement to Tab. 4.8.

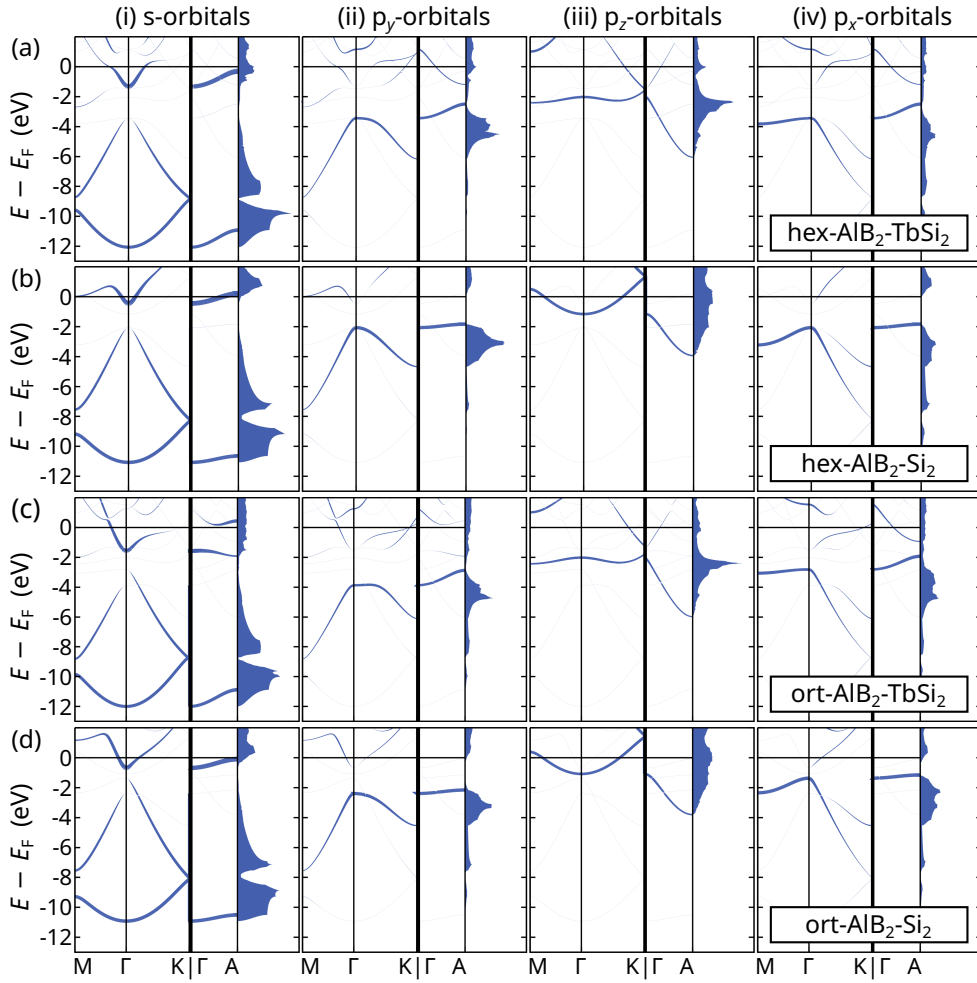


Figure B.1: Band structures of (a) hex- $\text{AlB}_2\text{-TbSi}_2$, (b) hex- $\text{AlB}_2\text{-Si}_2$, (c) ort- $\text{AlB}_2\text{-TbSi}_2$ and (d) ort- $\text{AlB}_2\text{-Si}_2$. The Si_2 structures are the respective TbSi_2 structures without the Tb atoms. The line width corresponds to the PAW projections of (i) the s orbitals, (ii) the p_y orbitals, (iii) the p_z orbitals and (iv) the p_x orbitals of the Si atoms.

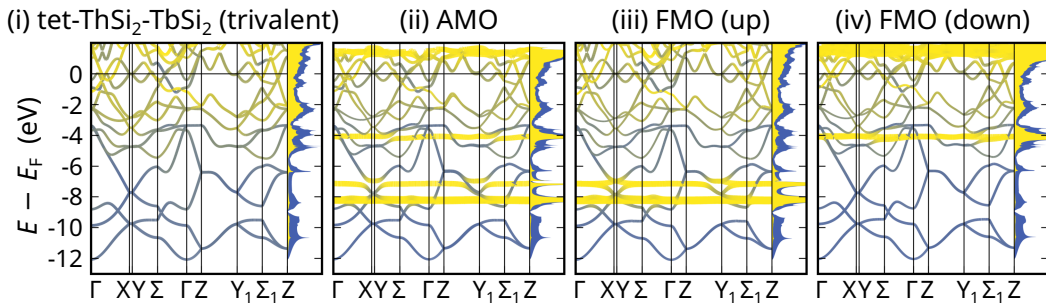


Figure B.2: Band structures of (i) trivalent and (ii) – (iv) f-valent tet- $\text{ThSi}_2\text{-TbSi}_2$. The plotting mode is analogous to Fig. 4.9 (b,i). Colour: yellow \rightarrow Tb, blue \rightarrow Si. AlB_2 structures: Fig. 4.11.

Appendix C

C.1 The geometric interpretation of the Aharonov-Bohm effect

As already mentioned, geometric phases become manifest in the Aharonov-Bohm effect, although not always recognised as such. Berry transferred his considerations to the ABE by a gedankenexperiment consisting in a thin solenoid like that in Sec. 7.1 and a particle with charge q confined to a box outside the magnetic field [127]. The origin of the box defines the three-dimensional parameter ξ , so a variation of ξ corresponds to a movement of the box. Unlike that in [127], the approach presented here works with the operator algebra, independently of the representation.

Let Ω be the space outside the solenoid and $W(\xi) \subset \Omega$ the box domain, a simply connected neighbourhood of ξ . Let $H_{\text{off}}(\mathbf{p}, \mathbf{x})$ be the Hamilton operator on W for the solenoid-off setup and $\xi = 0$. Let $|\Psi_{\text{off}}(0)\rangle$ be the eigenstate of the corresponding stationary Schrödinger equation.

$$H_{\text{off}}(\mathbf{p}, \mathbf{x})|\Psi_{\text{off}}(0)\rangle = E|\Psi_{\text{off}}(0)\rangle \quad (\text{C.102})$$

Without loss of generality, the expectation values of \mathbf{x} and \mathbf{p} may be 0, i.e. the particle is located at the box origin and does not move on average.

$$\langle \Psi_{\text{off}}(0) | \mathbf{x} | \Psi_{\text{off}}(0) \rangle = 0 \quad \wedge \quad \langle \Psi_{\text{off}}(0) | \mathbf{p} | \Psi_{\text{off}}(0) \rangle = 0 \quad (\text{C.103})$$

Now, two gauge transformations are being applied to the system: switching on the solenoid and moving the box. Since the box is simply connected and field-free, the solenoid field alters the wavefunction by a unitary transformation U_{D} , also called *Dirac factor* [127]. The movement of the box transforms implies the unitary transformation linked to the *translation group* U_{T} (vide appendicem, A.1).

$$\begin{aligned} U_{\text{T}} &= \exp(-i\frac{1}{\hbar} \xi \cdot \mathbf{p}) \quad (\text{Translation}) \\ U_{\text{D}} &= \exp(i\frac{q}{\hbar} \chi(\mathbf{x} | \xi)) \quad (\text{Dirac factor}) \end{aligned} \quad (\text{C.104})$$

with

$$\chi(\mathbf{x} | \xi) := \int_{\xi}^{\mathbf{x}} d\mathbf{x}' \cdot \mathbf{A}(\mathbf{x}') = \chi(\mathbf{x}) - \chi(\xi) \quad \Leftrightarrow \quad \mathbf{A}(\mathbf{x}) = \nabla_{\mathbf{x}} \chi(\mathbf{x} | \xi)$$

Nota bene, the Dirac factor depends on ξ , which is chosen to be the origin of the box. The entire integration path has to stay within the box so as to ensure the integrability of \mathbf{A} . The ξ -dependent term of χ must not be omitted, as it accommodates the pre-condition that χ is defined only locally. Omitting it would correspond to trying to find a global scalar potential for \mathbf{A} , which, of course, does not exist.

By means of the explicit representations of both unitary transformations, the stationary Schrödinger equation for the solenoid-on, boxed-moved setup, described by the Hamilton operator $H_{\text{on}}(\mathbf{p}, \mathbf{x} | \xi)$, can be solved.

$$\begin{aligned} U_D \mathbf{x} U_D^{-1} &= \mathbf{x}, & U_T \mathbf{x} U_T^{-1} &= \mathbf{x} + \xi \\ U_D \mathbf{p} U_D^{-1} &= \mathbf{p} - q\mathbf{A}(\mathbf{x}), & U_T \mathbf{p} U_T^{-1} &= \mathbf{p} \end{aligned} \quad (\text{C.105a})$$

$$\Rightarrow H_{\text{on}}(\mathbf{p}, \mathbf{x} | \xi) = U_T U_D H_{\text{off}}(\mathbf{p}, \mathbf{x}) U_D^{-1} U_T^{-1} = H_{\text{off}}(\mathbf{p} - q\mathbf{A}(\mathbf{x} + \xi), \mathbf{x} + \xi) \quad (\text{C.105b})$$

$$|\Psi_{\text{on}}(\xi)\rangle = U_T U_D |\Psi_{\text{off}}(0)\rangle = \exp(-i\frac{1}{\hbar}\xi \cdot \mathbf{p}) \exp(i\frac{q}{\hbar}\chi(\mathbf{x} | \xi)) |\Psi_{\text{off}}(0)\rangle \quad (\text{C.105c})$$

Inserting the transformed wavefunctions from Eq. (C.105c) into Eq. (7.55) yields the Berry connection \mathcal{A} . In the last step, Eq. (C.103) is used.

$$\begin{aligned} U_D^{-1} i\nabla_{\xi} U_D &= i\nabla_{\xi} + \frac{q}{\hbar}\mathbf{A}(\xi), & U_T^{-1} i\nabla_{\xi} U_T &= i\nabla_{\xi} + \frac{1}{\hbar}\mathbf{p} \\ \Rightarrow \mathcal{A}(\xi) &= i\langle \Psi_{\text{on}}(\xi) | \nabla_{\xi} | \Psi_{\text{on}}(\xi) \rangle = \langle \Psi_{\text{off}}(0) | U_D^{-1} U_T^{-1} i\nabla_{\xi} U_T U_D | \Psi_{\text{off}}(0) \rangle \\ &= \langle \Psi_{\text{off}}(0) | (i\nabla_{\xi} + \frac{q}{\hbar}\mathbf{A}(\xi) + \frac{1}{\hbar}(\mathbf{p} + q\mathbf{A}(\mathbf{x}))) | \Psi_{\text{off}}(0) \rangle \\ &= \frac{q}{\hbar}\mathbf{A}(\xi) + \frac{q}{\hbar}\mathbf{A}(0) \end{aligned} \quad (\text{C.106})$$

The Berry connection \mathcal{A} indeed equals the magnetic vector potential \mathbf{A} up to prefactors. Integrating it over a closed loop $\gamma : t \in [0, 1] \rightarrow \xi(t) \in \Omega$ returns the observable Berry phase χ^{B} :

$$\chi^{\text{B}} = \oint_{\gamma} \mathcal{A}(\xi) \cdot d\xi = \oint_{\gamma} \frac{q}{\hbar} \mathbf{A}(\xi) \cdot d\xi = N \frac{q}{\hbar} \Phi_0 \quad (\text{C.107})$$

where N is the winding number around the solenoid.

In conclusion, the treatment of the ABE within the Berry approach results in the same findings as those obtained in Sec. 7.1. The Berry phase in Eq. (C.107) equals the ABE phase in Eq. (7.52), both being proportional to the flux through the solenoid. The Berry approach confirms that the central origin of the ABE consists in the non-existence of a global gauge for \mathbf{A} on Ω . Like Berry phases from closed loops in general, the ABE is observable, although the box containing the particle has never penetrated the magnetic field inside the solenoid.

Moreover, Eq. (C.107) reveals an important property of geometric phases. Because the phase function $\exp(i\chi^{\text{B}})$ is periodic, it remains unchanged after the addition of integer multiples of 2π to χ^{B} . Consequently, a magnetic flux Φ_0 being integer multiples of the quantum flux $\frac{\hbar}{q}$ results in the same phase factor as the zero-flux configuration and, thus, in the same interference patterns. Therefore, the presence of a magnetic field permits the prediction of interference patterns, but the reverse, i.e.

the unambiguous deduction of the magnetic field from the interference patterns, is impossible. Only continuous flux changes allow the observer to count the number of circles passed and thus to determine the absolute magnetic flux difference from the interference patterns.

C.2 Proofs concerning the \mathbb{Z}_2 insulator

Gauge invariance of the electric polarisation under $U(\bar{n})$ transformations

The electric polarisation in terms of the Berry phase in Eq. (7.64) is invariant under $U(\bar{n})$ transformations, which mix the states of the occupied Bloch space.

Proof. Let $S(\xi)$ be a ξ -dependent, unitary $\mathbb{C}^{\bar{n} \times \bar{n}}$ -matrix rotating the occupied subspace spanned by the Bloch factors $\{|u_\alpha^\lambda(\mathbf{k})\rangle\}$. Then the Berry connection $\mathcal{A}(\xi)$ transforms as follows:

$$\begin{aligned}
 u(\xi) &:= \left(|u_1^{(\lambda)}(\mathbf{s})\rangle, \dots, |u_{\bar{n}}^{(\lambda)}(\mathbf{s})\rangle \right)^\top, & u^*(\xi) &:= \left(\langle u_1^{(\lambda)}(\mathbf{s})|, \dots, \langle u_{\bar{n}}^{(\lambda)}(\mathbf{s})| \right) \\
 \tilde{u}(\xi) &:= S(\xi)u(\xi) \\
 \tilde{\mathcal{A}}_i(\xi) &= \prod_{j \neq i} \left[\int_0^1 ds_j \right] \tilde{u}^*(\xi) i \nabla_\xi \tilde{u}(\xi) = \prod_{j \neq i} \left[\int_0^1 ds_j \right] u^*(\xi) S^*(\xi) i \nabla_\xi S(\xi) u(\xi) \\
 &= \prod_{j \neq i} \left[\int_0^1 ds_j \right] \sum_{k,l,m} u_k^*(\xi) S_{kl}^*(\xi) i \nabla_\xi S_{lm}(\xi) u_m(\xi) \\
 &= \left(\prod_{j \neq i} \left[\int_0^1 ds_j \right] u^*(\xi) i \nabla_\xi u(\xi) \right) + \sum_{k,l} S_{kl}^*(\xi) i \nabla_\xi S_{lk}(\xi) \\
 &= \mathcal{A}_i(\xi) + i \operatorname{tr}(S^*(\xi) \nabla_\xi S(\xi)) \stackrel{[128]}{=} \mathcal{A}_i(\xi) + i \nabla_\xi \ln(\det(S(\xi))) \\
 &= \mathcal{A}_i(\xi) - \nabla_\xi \theta(\xi)
 \end{aligned} \tag{C.108}$$

where $\theta(\xi)$ is the phase of the determinant of $S(\xi)$. Thus, also a more general $U(\bar{n})$ transformation basically reproduces Eq. (7.59), so band reordering within the occupied subspace during the parametric variation does not affect the results. \square

Nota bene, while band reordering within the occupied manifold is allowed, the conservation of the band gap separating the occupied subspace from its unoccupied complement is still obligatory for all values of ξ . In other words, the system strictly has to remain a band insulator for all λ .

Kramers link between the Berry connections of the components of a T-symmetric system

Eqs. (7.79) state that the Berry connections of the components of a T-symmetric Bloch system are linked by the Kramers symmetry. For the proof, it is crucial to keep track of the chain rule when dealing with the gradient of a function like $f(-\mathbf{k})$. This is facilitated by the following notation: $\nabla_k f(-\mathbf{k})$ means that the ∇ -operator has not yet been executed and acts on the exterior f and its argument $-\mathbf{k}$, the latter giving a minus sign. On the other hand, $(\nabla_k f)(-\mathbf{k})$ means that the gradient of f is *evaluated at* $-\mathbf{k}$. The difference between the two definitions is thus a minus sign.

By using the Kramers symmetry (Eq. (7.74)), the above remarks and the relations $\langle a | \nabla a \rangle = -\langle \nabla a | a \rangle$ and $\langle \Theta a | \Theta b \rangle = \langle b | a \rangle$, the Berry connection of component I evaluated at $-\mathbf{k}$ can be rewritten as follows:

$$\begin{aligned}
 \mathcal{A}_\alpha^I(-\mathbf{k}) &= i \langle u_\alpha^I(-\mathbf{k}) | (\nabla_k u_\alpha^I)(-\mathbf{k}) \rangle \\
 &= -i \langle u_\alpha^I(-\mathbf{k}) | \nabla_k | u_\alpha^I(-\mathbf{k}) \rangle \\
 &= -i \langle \Theta u_\alpha^{\text{II}}(\mathbf{k}) | \exp(-i\chi_\alpha(\mathbf{k})) \nabla_k \exp(i\chi_\alpha(\mathbf{k})) | \Theta u_\alpha^{\text{II}}(\mathbf{k}) \rangle \\
 &= +(\nabla_k \chi_\alpha)(\mathbf{k}) - i \langle \Theta u_\alpha^{\text{II}}(\mathbf{k}) | \Theta (\nabla_k u_\alpha^{\text{II}})(\mathbf{k}) \rangle \\
 &= +(\nabla_k \chi_\alpha)(\mathbf{k}) - i \langle (\nabla_k u_\alpha^{\text{II}})(\mathbf{k}) | u_\alpha^{\text{II}}(\mathbf{k}) \rangle \\
 &= +(\nabla_k \chi_\alpha)(\mathbf{k}) + i \langle u_\alpha^{\text{II}}(\mathbf{k}) | (\nabla_k u_\alpha^{\text{II}})(\mathbf{k}) \rangle \\
 &= +(\nabla_k \chi_\alpha)(\mathbf{k}) + \mathcal{A}_\alpha^{\text{II}}(\mathbf{k})
 \end{aligned} \tag{C.109a}$$

For the second component, a similar expression holds:

$$\begin{aligned}
 \mathcal{A}_\alpha^{\text{II}}(-\mathbf{k}) &= i \langle u_\alpha^{\text{II}}(-\mathbf{k}) | (\nabla_k u_\alpha^{\text{II}})(-\mathbf{k}) \rangle = -i \langle u_\alpha^{\text{II}}(-\mathbf{k}) | \nabla_k | u_\alpha^{\text{II}}(-\mathbf{k}) \rangle \\
 &= -i \langle \Theta u_\alpha^I(\mathbf{k}) | \exp(-i\chi_\alpha(-\mathbf{k})) \nabla_k \exp(i\chi_\alpha(-\mathbf{k})) | \Theta u_\alpha^I(\mathbf{k}) \rangle \\
 &= -(\nabla_k \chi_\alpha)(-\mathbf{k}) - i \langle \Theta u_\alpha^I(\mathbf{k}) | \Theta (\nabla_k u_\alpha^I)(\mathbf{k}) \rangle \\
 &= -(\nabla_k \chi_\alpha)(-\mathbf{k}) + i \langle u_\alpha^I(\mathbf{k}) | (\nabla_k u_\alpha^I)(\mathbf{k}) \rangle \\
 &= -(\nabla_k \chi_\alpha)(-\mathbf{k}) + \mathcal{A}_\alpha^I(\mathbf{k})
 \end{aligned} \tag{C.109b}$$

The sum and the difference between the partial connections of component I and II, defined as $\mathcal{A}^+(\mathbf{k})$ and $\mathcal{A}^-(\mathbf{k})$ in Eqs. (7.80a) and (7.81a), can be transformed into each other as follows:

$$\begin{aligned}
 &\mathcal{A}^-(\mathbf{k}) + \mathcal{A}^+(-\mathbf{k}) \\
 &\mathcal{A}^I(\mathbf{k}) - \mathcal{A}^{\text{II}}(\mathbf{k}) + \mathcal{A}^I(-\mathbf{k}) - \mathcal{A}^{\text{II}}(-\mathbf{k}) \\
 \stackrel{\text{Eqs. (C.109)}}{=} &\mathcal{A}^I(\mathbf{k}) + \mathcal{A}^{\text{II}}(\mathbf{k}) - \mathcal{A}^I(\mathbf{k}) - \mathcal{A}^{\text{II}}(\mathbf{k}) + \sum_\alpha (\nabla_k \chi_\alpha)(\mathbf{k}) + (\nabla_k \chi_\alpha)(-\mathbf{k}) \tag{C.110} \\
 &\mathcal{A}^+(\mathbf{k}) - \mathcal{A}^+(-\mathbf{k}) + \sum_\alpha (\nabla_k \chi_\alpha)(\mathbf{k}) + (\nabla_k \chi_\alpha)(-\mathbf{k})
 \end{aligned}$$

C.3 The antimony on bismuth selenide heterostructure

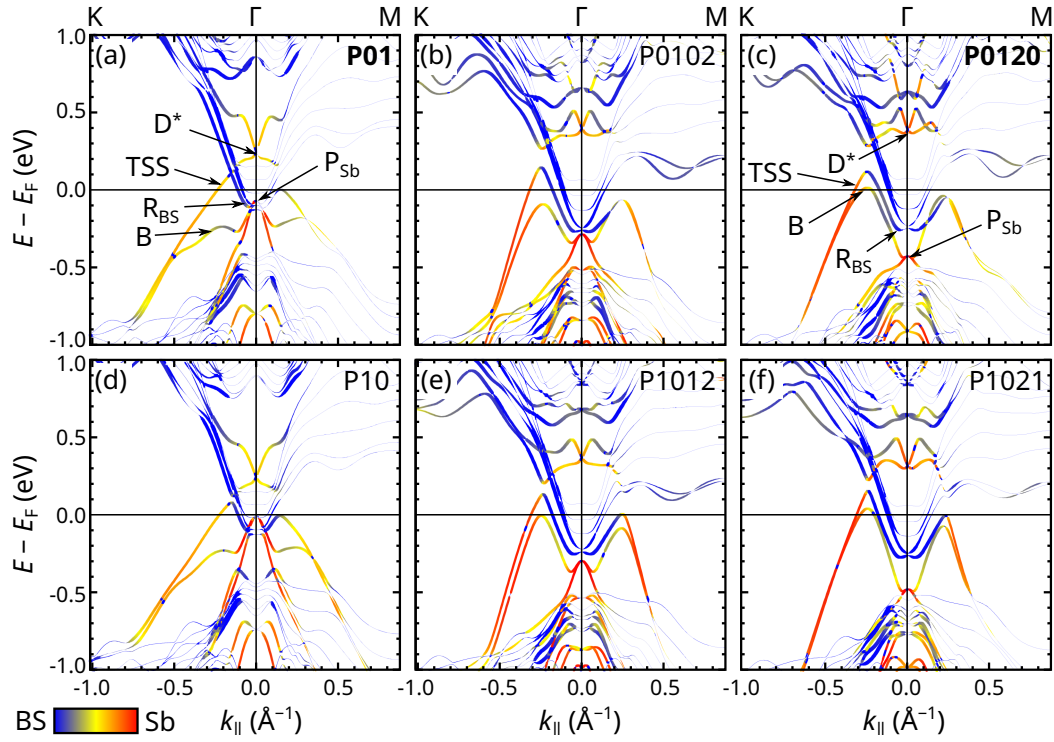


Figure C.1: Band structures of 1BL-Sb and 2BL-Sb structure models with different stacking optimised with DFT-D2+SOC. (a) **P01**, (b) P0102, (c) **P0120**, (d) P10, (e) P1012, (f) 1021. The line width, colouring and Fermi levels are analogous to Fig. 9.4. Arrows highlight special features. Stable structure models are highlighted bold. Reproduced from [P7].

Bibliography

- [1] M. M. Waldrop, *The chips are down for Moore's law*, Nature **530**, 144–147 (2016), DOI: 10.1038/530144a.
- [2] G. Kresse and J. Furthmüller, *Efficiency of ab-initio total energy calculations for metals and semiconductors using a plane-wave basis set*, Comput. Mater. Sci. **6**, 15–50 (1996), DOI: 10.1016/0927-0256(96)00008-0.
- [3] G. Kresse and J. Furthmüller, *Efficient iterative schemes for ab initio total-energy calculations using a plane-wave basis set*, Phys. Rev. B **54**, 11169–11186 (1996), DOI: 10.1103/PhysRevB.54.11169.
- [4] P. Giannozzi et al., *QUANTUM ESPRESSO: a modular and open-source software project for quantum simulations of materials*, J. Phys. Condens. Matter **21**, 395502 (2009), DOI: 10.1088/0953-8984/21/39/395502.
- [5] P. Giannozzi et al., *Advanced capabilities for materials modelling with Quantum ESPRESSO*, J. Phys. Condens. Matter **29**, 465901 (2017), DOI: 10.1088/1361-648X/aa8f79.
- [6] G. Czycholl, *Theoretische Festkörperphysik Band 1: Grundlagen: Phononen und Elektronen in Kristallen*, 4th ed. (Springer Spektrum, Berlin, Heidelberg, 2016), DOI: 10.1007/978-3-662-47141-8.
- [7] W. Kohn, *Nobel Lecture: Electronic structure of matter – wave functions and density functionals*, Rev. Mod. Phys. **71**, 1253–1266 (1999), DOI: 10.1103/RevModPhys.71.1253.
- [8] P. Hohenberg and W. Kohn, *Inhomogeneous Electron Gas*, Phys. Rev. **136**, B864–B871 (1964), DOI: 10.1103/PhysRev.136.B864.
- [9] W. Kohn and L. J. Sham, *Self-Consistent Equations Including Exchange and Correlation Effects*, Phys. Rev. **140**, A1133–A1138 (1965), DOI: 10.1103/PhysRev.140.A1133.
- [10] J. P. Perdew et al., *Generalized Gradient Approximation Made Simple*, Phys. Rev. Lett. **77**, 3865–3868 (1996), DOI: 10.1103/PhysRevLett.77.3865.
- [11] J. P. Perdew et al., *Restoring the Density-Gradient Expansion for Exchange in Solids and Surfaces*, Phys. Rev. Lett. **100**, 136406 (2008), DOI: 10.1103/PhysRevLett.100.136406.
- [12] D. Hobbs et al., *Fully unconstrained noncollinear magnetism within the projector augmented-wave method*, Phys. Rev. B - Condens. Matter Mater. Phys. **62**, 11556–11570 (2000), DOI: 10.1103/PhysRevB.62.11556.
- [13] M. Cococcioni, *The LDA+U Approach: A Simple Hubbard Correction for Correlated Ground States*, in *Correl. electrons model. simul.* Vol. 2, edited by E. Pavarini et al., 1st ed. (Verlag des Forschungszentrum Jülich, Jülich, 2012) Chap. 4, pp. 1–40.
- [14] S. L. Dudarev et al., *Electron-energy-loss spectra and the structural stability of nickel oxide: An LSDA+U study*, Phys. Rev. B **57**, 1505–1509 (1998), DOI: 10.1103/PhysRevB.57.1505.
- [15] A. Rohrbach et al., *Electronic correlation effects in transition-metal sulfides*, J. Phys. Condens. Matter **15**, 979–996 (2003), DOI: 10.1088/0953-8984/15/6/325.
- [16] A. I. Liechtenstein et al., *Density-functional theory and strong interactions: Orbital ordering in Mott-Hubbard insulators*, Phys. Rev. B **52**, R5467–R5470 (1995), DOI: 10.1103/PhysRevB.52.R5467.
- [17] A. F. Holleman et al., *Anorganische Chemie Band 1: Grundlagen und Hauptgruppenelemente*, 103rd ed. (De Gruyter, Berlin, Boston, 2016), DOI: 10.1515/9783110495850.

- [18] A. F. Holleman et al., *Anorganische Chemie Band 2: Nebengruppenelemente, Lanthanoide, Actinoide, Transactinoide*, 103rd ed. (De Gruyter, Berlin, Boston, 2016), DOI: 10.1515/9783110495904.
- [19] E. van Lenthe et al., *Relativistic regular two-component Hamiltonians*, J. Chem. Phys. **99**, 4597–4610 (1993), DOI: 10.1063/1.466059.
- [20] C. Chang et al., *Regular Two-Component Pauli-Like Effective Hamiltonians in Dirac Theory*, Phys. Scr. **34**, 394–404 (1986), DOI: 10.1088/0031-8949/34/5/007.
- [21] P. E. Blöchl, *Projector augmented-wave method*, Phys. Rev. B **50**, 17953–17979 (1994), DOI: 10.1103/PhysRevB.50.17953.
- [22] G. Kresse and D. Joubert, *From ultrasoft pseudopotentials to the projector augmented-wave method*, Phys. Rev. B **59**, 1758–1775 (1999), DOI: 10.1103/PhysRevB.59.1758.
- [23] S. Steiner et al., *Calculation of the magnetic anisotropy with projected-augmented-wave methodology and the case study of disordered $Fe_{1-x}Co_x$ alloys*, Phys. Rev. B **93**, 224425 (2016), DOI: 10.1103/PhysRevB.93.224425.
- [24] F. London, *Zur Theorie und Systematik der Molekularkräfte*, Zeitschrift für Phys. **63**, 245–279 (1930), DOI: 10.1007/BF01421741.
- [25] J. P. Wagner and P. R. Schreiner, *London'sche Dispersionswechselwirkungen in der Molekülchemie - eine Neubetrachtung sterischer Effekte*, Angew. Chemie **127**, 12446–12471 (2015), DOI: 10.1002/ange.201503476.
- [26] S. Grimme, *Semiempirical GGA-type density functional constructed with a long-range dispersion correction*, J. Comput. Chem. **27**, 1787–1799 (2006), DOI: 10.1002/jcc.20495.
- [27] S. Grimme et al., *A consistent and accurate ab initio parametrization of density functional dispersion correction (DFT-D) for the 94 elements H-Pu*, J. Chem. Phys. **132**, 154104 (2010), DOI: 10.1063/1.3382344.
- [28] S. Grimme et al., *Effect of the damping function in dispersion corrected density functional theory*, J. Comput. Chem. **32**, 1456–1465 (2011), DOI: 10.1002/jcc.21759.
- [29] A. Tkatchenko and M. Scheffler, *Accurate Molecular Van Der Waals Interactions from Ground-State Electron Density and Free-Atom Reference Data*, Phys. Rev. Lett. **102**, 073005 (2009), DOI: 10.1103/PhysRevLett.102.073005.
- [30] T. Bučko et al., *Improved Density Dependent Correction for the Description of London Dispersion Forces*, J. Chem. Theory Comput. **9**, 4293–4299 (2013), DOI: 10.1021/ct400694h.
- [31] T. Bučko et al., *Extending the applicability of the Tkatchenko-Scheffler dispersion correction via iterative Hirshfeld partitioning*, J. Chem. Phys. **141**, 034114 (2014), DOI: 10.1063/1.4890003.
- [32] K. N. Tu et al., *Low Schottky barrier of rare-earth silicide on n-Si*, Appl. Phys. Lett. **38**, 626–628 (1981), DOI: 10.1063/1.92457.
- [33] J. A. Knapp and S. T. Picraux, *Epitaxial growth of rare-earth silicides on (111) Si*, Appl. Phys. Lett. **48**, 466–468 (1986), DOI: 10.1063/1.96532.
- [34] P. Wetzel et al., *Experimental band structure and Fermi surface of a two-dimensional Er silicide on Si(111)*, Solid State Commun. **82**, 235–238 (1992), DOI: 10.1016/0038-1098(92)90633-K.
- [35] S. Vandr e et al., *Flatband Conditions Observed for Lanthanide-Silicide Monolayers on n-Type Si(111)*, Phys. Rev. Lett. **82**, 1927–1930 (1999), DOI: 10.1103/PhysRevLett.82.1927.
- [36] F. A. D'Avitaya et al., *Fabrication and structure of epitaxial Er silicide films on (111) Si*, Appl. Phys. Lett. **54**, 2198–2200 (1989), DOI: 10.1063/1.101517.
- [37] M. Lohmeier et al., *Interface structure of $Si(111)-(\sqrt{3}\times\sqrt{3})R30^\circ-ErSi_2-x$* , Surf. Sci. **345**, 247–260 (1996), DOI: 10.1016/0039-6028(95)00875-6.
- [38] P. Paki et al., *Growth of a two-dimensional Er silicide on Si(111)*, Phys. Rev. B **45**, 8490–8493 (1992), DOI: 10.1103/PhysRevB.45.8490.
- [39] L. Stauffer et al., *Electronic structure and interfacial geometry of epitaxial two-dimensional Er silicide on Si(111)*, Phys. Rev. B **47**, 10555–10562 (1993), DOI: 10.1103/PhysRevB.47.10555.

- [40] M. H. Tuilier et al., *Interfacial structure of two-dimensional epitaxial Er silicide on Si(111)*, Phys. Rev. B **50**, 2333–2338 (1994), DOI: 10.1103/PhysRevB.50.2333.
- [41] M. Lohmeier et al., *Atomic structure and thermal stability of two-dimensional Er silicide on Si(111)*, Phys. Rev. B - Condens. Matter Mater. Phys. **54**, 2004–2009 (1996), DOI: 10.1103/PhysRevB.54.2004.
- [42] T. Kalka et al., *STM study of epitaxial Dy silicides on Si(111) and Si(001) using ultra-sharp tips prepared by ion bombardment*, Appl. Phys. A Mater. Sci. Process. **66**, S1073–S1075 (1998), DOI: 10.1007/s003390051300.
- [43] D. J. Spence et al., *Medium-energy ion scattering studies of two-dimensional rare-earth silicides*, Phys. Rev. B **61**, 5707–5713 (2000), DOI: 10.1103/PhysRevB.61.5707.
- [44] S. Vandr e et al., *Conservation of flatband conditions for DySi₂ monolayers on n-type Si(111)*, Appl. Phys. Lett. **78**, 2012–2014 (2001), DOI: 10.1063/1.1360782.
- [45] H. Kitayama et al., *Structure analysis of two-dimensional Holmium silicide by low energy electron diffraction*, Surf. Sci. **482-485**, 1481–1486 (2001), DOI: 10.1016/S0039-6028(01)00859-7.
- [46] D. Spence et al., *Structural studies of two- and three-dimensional dysprosium silicides using medium-energy ion scattering*, Surf. Sci. **512**, 61–66 (2002), DOI: 10.1016/S0039-6028(02)01573-X.
- [47] C. Rogero et al., *Electronic structure and Fermi surface of two-dimensional rare-earth silicides epitaxially grown on Si(111)*, Phys. Rev. B **69**, 045312 (2004), DOI: 10.1103/PhysRevB.69.045312.
- [48] M. Tuilier et al., *Structure of clean and H-saturated epitaxial two-dimensional Er silicide on Si(111) studied by SEXAFS*, Surf. Sci. **555**, 94–100 (2004), DOI: 10.1016/j.susc.2004.02.023.
- [49] M. Wanke et al., *Energy surfaces of rare-earth silicide films on Si(111)*, Surf. Sci. **603**, 2808–2814 (2009), DOI: 10.1016/j.susc.2009.07.026.
- [50] I. Engelhardt et al., *Atomic structure of thin dysprosium-silicide layers on Si(111)*, Surf. Sci. **600**, 755–761 (2006), DOI: 10.1016/j.susc.2005.11.029.
- [51] M. Franz et al., *Terbium induced nanostructures on Si(111)*, Surf. Sci. **637-638**, 149–155 (2015), DOI: 10.1016/j.susc.2015.03.026.
- [52] M. Franz et al., *Growth and electronic properties of Tb silicide layers on Si(111)*, J. Vac. Sci. Technol. A Vacuum, Surfaces, Film. **34**, 061503 (2016), DOI: 10.1116/1.4964132.
- [53] S. Sanna et al., *Rare-earth silicide thin films on the Si(111) surface*, Phys. Rev. B **93**, 195407 (2016), DOI: 10.1103/PhysRevB.93.195407.
- [54] C. Preinesberger et al., *Formation of dysprosium silicide wires on Si(001)*, J. Phys. D. Appl. Phys. **31**, L43–L45 (1998), DOI: 10.1088/0022-3727/31/12/001.
- [55] Y. Chen et al., *Self-assembled growth of epitaxial erbium disilicide nanowires on silicon (001)*, Appl. Phys. Lett. **76**, 4004–4006 (2000), DOI: 10.1063/1.126848.
- [56] J. Nogami et al., *Self-assembled rare-earth silicide nanowires on Si(001)*, Phys. Rev. B **63**, 233305 (2001), DOI: 10.1103/PhysRevB.63.233305.
- [57] C. Preinesberger et al., *Structure of DySi₂ nanowires on Si(001)*, J. Appl. Phys. **91**, 1695–1697 (2002), DOI: 10.1063/1.1430540.
- [58] Y. Chen et al., *Growth and evolution of epitaxial erbium disilicide nanowires on Si(001)*, Appl. Phys. A Mater. Sci. Process. **75**, 353–361 (2002), DOI: 10.1007/s003390201315.
- [59] C. Preinesberger et al., *Structure and electronic properties of dysprosium-silicide nanowires on vicinal Si(001)*, Appl. Phys. Lett. **87**, 083107 (2005), DOI: 10.1063/1.2032620.
- [60] H. W. Yeom et al., *Robust One-Dimensional Metallic Band Structure of Silicide Nanowires*, Phys. Rev. Lett. **95**, 205504 (2005), DOI: 10.1103/PhysRevLett.95.205504.
- [61] T. Kobayashi, *Structural analysis of Er silicide nanowires on Si(001) using three-dimensional medium-energy ion scattering*, Phys. Rev. B - Condens. Matter Mater. Phys. **75**, 2–6 (2007), DOI: 10.1103/PhysRevB.75.125401.

- [62] C. Zeng et al., *Charge-order fluctuations in one-dimensional silicides*, Nat. Mater. **7**, 539–542 (2008), DOI: 10.1038/nmat2209.
- [63] M. Wanke et al., *Electronic properties of self-assembled rare-earth silicide nanowires on Si(001)*, Phys. Rev. B **83**, 205417 (2011), DOI: 10.1103/PhysRevB.83.205417.
- [64] M. Dähne and M. Wanke, *Metallic rare-earth silicide nanowires on silicon surfaces*, J. Phys. Condens. Matter **25**, 014012 (2012), DOI: 10.1088/0953-8984/25/1/014012.
- [65] S. Appelfeller et al., *Tb silicide nanowire growth on planar and vicinal Si(001) surfaces*, Surf. Sci. **641**, 180–190 (2015), DOI: 10.1016/j.susc.2015.07.001.
- [66] S. Appelfeller et al., *The electronic structure of Tb silicide nanowires on Si(001)*, New J. Phys. **18**, 113005 (2016), DOI: 10.1088/1367-2630/18/11/113005.
- [67] S. Appelfeller et al., *Refined structure model of rare earth silicide nanowires on Si(001)*, Appl. Phys. Lett. **114**, 093104 (2019), DOI: 10.1063/1.5086369.
- [68] M. Wanke et al., *Structural and electronic properties of rare earth silicide nanowires on Si(557)*, Phys. Rev. B **79**, 155428 (2009), DOI: 10.1103/PhysRevB.79.155428.
- [69] M. Wanke et al., *Electronic properties of dysprosium silicide nanowires on Si(557)*, J. Appl. Phys. **108**, 064304 (2010), DOI: 10.1063/1.3481456.
- [70] S. Appelfeller et al., *Growth and characterization of Tb silicide nanostructures on Si(hhk) substrates*, Phys. Rev. Mater. **3**, 126002 (2019), DOI: 10.1103/PhysRevMaterials.3.126002.
- [71] N. G. Connolly et al., *Nomenclature of Inorganic Chemistry* (Royal Society of Chemistry, Cambridge, 2005).
- [72] B. Zhou et al., *Global Potential of Rare Earth Resources and Rare Earth Demand from Clean Technologies*, Minerals **7**, 203 (2017), DOI: 10.3390/min7110203.
- [73] H. Sicius, *Seltenerdmetalle: Lanthanoide und dritte Nebengruppe*, in *Handb. der chem. elem.* (Springer Spektrum, Berlin, Heidelberg, 2019), pp. 1–116, DOI: 10.1007/978-3-662-55944-4_18-2.
- [74] A. J. Kenyon, *Erbium in silicon*, Semicond. Sci. Technol. **20**, R65–R84 (2005), DOI: 10.1088/0268-1242/20/12/R02.
- [75] P. F. Lang and B. C. Smith, *Ionization Energies of Lanthanides*, J. Chem. Educ. **87**, 875–881 (2010), DOI: 10.1021/ed100215q.
- [76] D. A. Johnson and P. G. Nelson, *Valencies of the lanthanides*, Found. Chem. **20**, 15–27 (2018), DOI: 10.1007/s10698-017-9291-6.
- [77] M. Luyckx et al., *Silicon and Plants: Current Knowledge and Technological Perspectives*, Front. Plant Sci. **8**, 1–8 (2017), DOI: 10.3389/fpls.2017.00411.
- [78] P. Treguer et al., *The Silica Balance in the World Ocean: A Reestimate*, Science (80-.) **268**, 375–379 (1995), DOI: 10.1126/science.268.5209.375.
- [79] K. S. Novoselov, *Electric Field Effect in Atomically Thin Carbon Films*, Science (80-.) **306**, 666–669 (2004), DOI: 10.1126/science.1102896.
- [80] H. Schäfer et al., *Zintl Phases: Transitions between Metallic and Ionic Bonding*, Angew. Chemie Int. Ed. English **12**, 694–712 (1973), DOI: 10.1002/anie.197306941.
- [81] J. A. Perri et al., *Rare Earth Metal “Disilicides”*, J. Phys. Chem. **63**, 616–619 (1959), DOI: 10.1021/j150574a041.
- [82] J. A. Perri et al., *Polymorphism of Rare Earth Disilicides*, J. Phys. Chem. **63**, 2073–2074 (1959), DOI: 10.1021/j150582a030.
- [83] I. P. Mayer et al., *Rare earth disilicides*, J. Phys. Chem. **66**, 693–696 (1962), DOI: 10.1021/j100810a028.
- [84] G. V. Samsonov, *The chemistry of the silicides of the rare-earth elements*, Russ. Chem. Rev. **31**, 702–712 (1962), DOI: 10.1070/RC1962v031n12ABEH001333.
- [85] I. Mayer et al., *Dimorphism of rare earth disilicides*, Inorg. Chem. **6**, 842–844 (1967), DOI: 10.1021/ic50050a043.

- [86] I. Shidlovsky and I. Mayer, *Mössbauer spectra of rare earth silicides and germanides*, J. Phys. Chem. Solids **30**, 1207–1213 (1969), DOI: 10.1016/0022-3697(69)90378-3.
- [87] A. Iandelli et al., *Valence fluctuations of ytterbium in silicon-rich compounds*, J. Less Common Met. **64**, 213–220 (1979), DOI: 10.1016/0022-5088(79)90172-3.
- [88] E. Houssay et al., *Metallurgical reinvestigation of rare earth silicides*, Appl. Surf. Sci. **38**, 156–161 (1989), DOI: 10.1016/0169-4332(89)90531-X.
- [89] P. Schobinger-Papamantellos et al., *Crystallographic and magnetic structure of $TbSi_{1.67}$ and $TbSi_{1.67-\delta}$* , J. Magn. Magn. Mater. **79**, 231–241 (1989), DOI: 10.1016/0304-8853(89)90102-9.
- [90] J. Pierre et al., *Magnetic structures of rare earth silicides RSi_{2-x} ($R = Nd, Ho, Dy$)*, J. Magn. Magn. Mater. **81**, 39–46 (1989), DOI: 10.1016/0304-8853(89)90226-6.
- [91] S. Auffret et al., *Crystallographic and magnetic structures of Er_3Si_5* , Phys. B Condens. Matter **162**, 271–280 (1990), DOI: 10.1016/0921-4526(90)90022-M.
- [92] J. Pierre et al., *Magnetic properties of rare earth silicide single crystals RSi_{2-x} ($R = Pr, Nd, Gd$)*, J. Magn. Magn. Mater. **89**, 86–96 (1990), DOI: 10.1016/0304-8853(90)90711-X.
- [93] S. Auffret et al., *Magnetic properties versus crystal structure in heavy rare-earth silicides RSi_{2-x}* , Phys. B Condens. Matter **173**, 265–276 (1991), DOI: 10.1016/0921-4526(91)90088-V.
- [94] L. Braicovich et al., *Valence photoelectron spectroscopy of Gd silicides*, Phys. Rev. B **41**, 3123–3127 (1990), DOI: 10.1103/PhysRevB.41.3123.
- [95] L. Magaud et al., *The effect of silicon vacancies on the electron structure of yttrium disilicide*, J. Phys. Condens. Matter **4**, 5399–5404 (1992), DOI: 10.1088/0953-8984/4/24/009.
- [96] L. Magaud et al., *Role of silicon vacancies in yttrium-disilicide compounds from ab initio calculations*, Phys. Rev. B **55**, 13479–13484 (1997), DOI: 10.1103/PhysRevB.55.13479.
- [97] J. Szade and M. Neumann, *Electronic structure investigation of Gd intermetallics*, J. Phys. Condens. Matter **11**, 3887–3896 (1999), DOI: 10.1088/0953-8984/11/19/308.
- [98] J. Yang et al., *Thermal expansion coefficients of rare earth metal disilicides and their influence on the growth of disilicide nanowires*, Appl. Phys. A **82**, 39–42 (2006), DOI: 10.1007/s00339-005-3336-8.
- [99] G. W. Peng et al., *Mechanisms of silicon diffusion in erbium silicide*, Phys. Rev. B **75**, 125319 (2007), DOI: 10.1103/PhysRevB.75.125319.
- [100] M. Zavala Aké et al., *First-principles calculations of the atomic and electronic properties of group IIIA disilicides in AlB_2 type structures*, Solid State Sci. **10**, 355–361 (2008), DOI: 10.1016/j.solidstatesciences.2007.10.002.
- [101] M. Nentwich et al., *Structure variations within RSi_2 and R_2TSi_3 silicides. Part I. Structure overview*, Acta Crystallogr. Sect. B Struct. Sci. Cryst. Eng. Mater. **76**, 177–200 (2020), DOI: 10.1107/S2052520620001043.
- [102] V. Eremenko et al., *Phase diagram of the holmium-silicon binary system and physical properties of holmium silicides up to 1050 °C*, J. Alloys Compd. **219**, 181–184 (1995), DOI: 10.1016/0925-8388(94)05035-X.
- [103] S. Luzan et al., *Phase diagram of the binary erbium-silicon system and physical properties of erbium silicides up to 1050 °C*, J. Alloys Compd. **239**, 77–82 (1996), DOI: 10.1016/0925-8388(95)01977-4.
- [104] S. P. Luzan et al., *Phase equilibria in the erbium-silicon system*, Powder Metall. Met. Ceram. **36**, 24–29 (1997), DOI: 10.1007/BF02684247.
- [105] M. Huang et al., *Experimental investigation and thermodynamic modeling of the Gd-Si system*, J. Alloys Compd. **441**, 94–100 (2007), DOI: 10.1016/j.jallcom.2006.09.068.
- [106] L. V. Goncharuk et al., *Thermodynamic properties of holmium silicides $HoSi_{1-x}$, Ho_5Si_4 , and Ho_5Si_3* , Powder Metall. Met. Ceram. **49**, 690–694 (2011), DOI: 10.1007/s11106-011-9289-x.
- [107] V. R. Sidorko and N. P. Gorbachuk, *Thermodynamic and thermochemical characteristics of erbium silicides*, Powder Metall. Met. Ceram. **51**, 93–101 (2012), DOI: 10.1007/s11106-012-9402-9.

- [108] F. Geenen et al., *On the formation and structural properties of hexagonal rare earth (Y, Gd, Dy, Er and Yb) disilicide thin films*, J. Alloys Compd. **611**, 149–156 (2014), DOI: 10.1016/j.jallcom.2014.04.142.
- [109] H. Okamoto, *Ho-Si (holmium-silicon)*, J. Phase Equilibria **17**, 370–371 (1996), DOI: 10.1007/BF02665570.
- [110] H. Okamoto, *Er-Si (erbium-silicon)*, J. Phase Equilibria **18**, 403–403 (1997), DOI: 10.1007/s11669-997-0073-z.
- [111] H. Okamoto, *Si-Tb (Silicon-Terbium)*, J. Phase Equilibria **21**, 500–500 (2000), DOI: 10.1361/105497100770339824.
- [112] H. Okamoto, *Gd-Si (Gadolinium-Silicon)*, J. Phase Equilibria Diffus. **30**, 213–214 (2009), DOI: 10.1007/s11669-009-9477-2.
- [113] J. Kim and I.-H. Jung, *Critical evaluation and thermodynamic optimisation of the Si-RE systems: Part II. Si-RE system (RE = Gd, Tb, Dy, Ho, Er, Tm, Lu and Y)*, J. Chem. Thermodyn. **81**, 273–297 (2015), DOI: 10.1016/j.jct.2014.08.014.
- [114] A. B. Gokhale and G. J. Abbaschian, *The Si-Sm (Silicon-Samarium) system*, Bull. Alloy Phase Diagrams **9**, 582–585 (1988), DOI: 10.1007/BF02881960.
- [115] A. B. Gokhale et al., *The Nd-Si (Neodymium-Silicon) system*, Bull. Alloy Phase Diagrams **10**, 246–251 (1989), DOI: 10.1007/BF02877504.
- [116] F. D. Murnaghan, *The Compressibility of Media under Extreme Pressures*, Proc. Natl. Acad. Sci. **30**, 244–247 (1944), DOI: 10.1073/pnas.30.9.244.
- [117] H. J. Monkhorst and J. D. Pack, *Special points for Brillouin-zone integrations*, Phys. Rev. B **13**, 5188–5192 (1976), DOI: 10.1103/PhysRevB.13.5188.
- [118] P. E. Blöchl et al., *Improved tetrahedron method for Brillouin-zone integrations*, Phys. Rev. B **49**, 16223–16233 (1994), DOI: 10.1103/PhysRevB.49.16223.
- [119] R. P. Feynman, *Forces in Molecules*, Phys. Rev. **56**, 340–343 (1939), DOI: 10.1103/PhysRev.56.340.
- [120] A. Kokalj, *Xcrysden – a new program for displaying crystalline structures and electron densities*, Journal of Molecular Graphics and Modelling **17**, 176–179 (1999), DOI: [https://doi.org/10.1016/S1093-3263\(99\)00028-5](https://doi.org/10.1016/S1093-3263(99)00028-5).
- [121] S. Fahy and D. R. Hamann, *Electronic and structural properties of CaSi₂*, Phys. Rev. B **41**, 7587–7592 (1990), DOI: 10.1103/PhysRevB.41.7587.
- [122] K. H. Janzon et al., *Notizen: Zur Struktur der Phase CaSi₂*, Zeitschrift für Naturforsch. B **23**, 1544–1544 (1968), DOI: 10.1515/znb-1968-1128.
- [123] W. Setyawan and S. Curtarolo, *High-throughput electronic band structure calculations: Challenges and tools*, Comput. Mater. Sci. **49**, 299–312 (2010), DOI: 10.1016/j.commatsci.2010.05.010.
- [124] S. G. Mayo et al., *Band unfolding made simple*, J. Phys. Condens. Matter **32**, 205902 (2020), DOI: 10.1088/1361-648X/ab6e8e.
- [125] K. von Klitzing et al., *New Method for High-Accuracy Determination of the Fine-Structure Constant Based on Quantized Hall Resistance*, Phys. Rev. Lett. **45**, 494–497 (1980), DOI: 10.1103/PhysRevLett.45.494.
- [126] K. von Klitzing, *The quantized Hall effect*, Rev. Mod. Phys. **58**, 519–531 (1986), DOI: 10.1103/RevModPhys.58.519.
- [127] M. V. Berry, *Quantal phase factors accompanying adiabatic changes*, Proc. R. Soc. London. A. Math. Phys. Sci. **392**, 45–57 (1984), DOI: 10.1098/rspa.1984.0023.
- [128] R. Resta, *Macroscopic polarization in crystalline dielectrics: the geometric phase approach*, Rev. Mod. Phys. **66**, 899–915 (1994), DOI: 10.1103/RevModPhys.66.899.
- [129] Y. Aharonov and D. Bohm, *Significance of Electromagnetic Potentials in the Quantum Theory*, Phys. Rev. **115**, 485–491 (1959), DOI: 10.1103/PhysRev.115.485.

- [130] Y. Aharonov and D. Bohm, *Further Considerations on Electromagnetic Potentials in the Quantum Theory*, Phys. Rev. **123**, 1511–1524 (1961), DOI: 10.1103/PhysRev.123.1511.
- [131] L. Vaidman, *Role of potentials in the Aharonov-Bohm effect*, Phys. Rev. A **86**, 040101 (2012), DOI: 10.1103/PhysRevA.86.040101.
- [132] Y. Aharonov et al., *Comment on “Role of potentials in the Aharonov-Bohm effect”*, Phys. Rev. A **92**, 026101 (2015), DOI: 10.1103/PhysRevA.92.026101.
- [133] L. Vaidman, *Reply to “Comment on ‘Role of potentials in the Aharonov-Bohm effect’”*, Phys. Rev. A **92**, 026102 (2015), DOI: 10.1103/PhysRevA.92.026102.
- [134] P. Pearle and A. Rizzi, *Quantum-mechanical inclusion of the source in the Aharonov-Bohm effects*, Phys. Rev. A **95**, 052123 (2017), DOI: 10.1103/PhysRevA.95.052123.
- [135] W. Franz, *Elektroneninterferenz im Magnetfeld*, in Verhandlungen der Deutschen Physikalischen Gesellschaft, Vol. 20 (1939).
- [136] W. Ehrenberg and R. E. Siday, *The Refractive Index in Electron Optics and the Principles of Dynamics*, Proc. Phys. Soc. Sect. B **62**, 8–21 (1949), DOI: 10.1088/0370-1301/62/1/303.
- [137] K.-H. Goldhorn and H.-P. Heinz, *Mathematik für Physiker 1: Grundlagen aus Analysis und Linearer Algebra*, 1st ed., Springer-Lehrbuch (Springer, Berlin, Heidelberg, 2007), DOI: 10.1007/978-3-540-48768-5.
- [138] G. Möllenstedt and W. Bayh, *Kontinuierliche Phasenschiebung von Elektronenwellen im kraftfeldfreien Raum durch das magnetische Vektorpotential eines Solenoids*, Phys. J. **18**, 299–305 (1962), DOI: 10.1002/phb1.19620180702.
- [139] A. Tonomura et al., *Evidence for Aharonov-Bohm effect with magnetic field completely shielded from electron wave*, Phys. Rev. Lett. **56**, 792–795 (1986), DOI: 10.1103/PhysRevLett.56.792.
- [140] R. M. Martin, *Comment on calculations of electric polarization in crystals*, Phys. Rev. B **9**, 1998–1999 (1974), DOI: 10.1103/PhysRevB.9.1998.
- [141] R. D. King-Smith and D. Vanderbilt, *Theory of polarization of crystalline solids*, Phys. Rev. B **47**, 1651–1654 (1993), DOI: 10.1103/PhysRevB.47.1651.
- [142] L. Fu and C. L. Kane, *Time reversal polarization and a Z_2 adiabatic spin pump*, Phys. Rev. B **74**, 195312 (2006), DOI: 10.1103/PhysRevB.74.195312.
- [143] D. J. Thouless et al., *Quantized Hall Conductance in a Two-Dimensional Periodic Potential*, Phys. Rev. Lett. **49**, 405–408 (1982), DOI: 10.1103/PhysRevLett.49.405.
- [144] C. L. Kane and E. J. Mele, *Z_2 Topological Order and the Quantum Spin Hall Effect*, Phys. Rev. Lett. **95**, 146802 (2005), DOI: 10.1103/PhysRevLett.95.146802.
- [145] F. D. M. Haldane, *Model for a Quantum Hall Effect without Landau Levels: Condensed-Matter Realization of the “Parity Anomaly”*, Phys. Rev. Lett. **61**, 2015–2018 (1988), DOI: 10.1103/PhysRevLett.61.2015.
- [146] X.-L. Qi et al., *Topological field theory of time-reversal invariant insulators*, Phys. Rev. B **78**, 195424 (2008), DOI: 10.1103/PhysRevB.78.195424.
- [147] L. Fu and C. L. Kane, *Topological insulators with inversion symmetry*, Phys. Rev. B **76**, 045302 (2007), DOI: 10.1103/PhysRevB.76.045302.
- [148] B. W. Roberts, *Three Myths about Time Reversal in Quantum Theory*, Philos. Sci. **84**, 315–334 (2017), DOI: 10.1086/690721.
- [149] P. de Marcillac et al., *Experimental detection of α -particles from the radioactive decay of natural bismuth*, Nature **422**, 876–878 (2003), DOI: 10.1038/nature01541.
- [150] H. Lind et al., *Structure and bonding properties of $(\text{Bi}_2\text{Se}_3)_m (\text{Bi}_2)_n$ stacks by first-principles density functional theory*, Phys. Rev. B **72**, 184101 (2005), DOI: 10.1103/PhysRevB.72.184101.
- [151] G. P. Voutsas et al., *The crystal structure of antimony selenide, Sb_2Se_3* , Zeitschrift für Krist. - Cryst. Mater. **171**, 261–268 (1985), DOI: 10.1524/zkri.1985.171.14.261.
- [152] A. C. Stergiou and P. J. Rentzeperis, *The crystal structure of arsenic selenide, As_2Se_3* , Zeitschrift für Krist. - Cryst. Mater. **173**, 185–192 (1985), DOI: 10.1524/zkri.1985.173.14.185.

- [153] S. Nakajima, *The crystal structure of $\text{Bi}_2\text{Te}_3 - x\text{Se}_x$* , J. Phys. Chem. Solids **24**, 479–485 (1963), DOI: 10.1016/0022-3697(63)90207-5.
- [154] H. Zhang et al., *Topological insulators in Bi_2Se_3 , Bi_2Te_3 and Sb_2Te_3 with a single Dirac cone on the surface*, Nat. Phys. **5**, 438–442 (2009), DOI: 10.1038/nphys1270.
- [155] O. Ü. Aktürk et al., *Single-layer crystalline phases of antimony: Antimonenes*, Phys. Rev. B **91**, 235446 (2015), DOI: 10.1103/PhysRevB.91.235446.
- [156] G. Wang et al., *Atomically Thin Group V Elemental Films: Theoretical Investigations of Antimonene Allotropes*, ACS Appl. Mater. Interfaces **7**, 11490–11496 (2015), DOI: 10.1021/acsami.5b02441.
- [157] R. Flammini et al., *Evidence of β -antimonene at the $\text{Sb}/\text{Bi}_2\text{Se}_3$ interface*, Nanotechnology **29**, 065704 (2018), DOI: 10.1088/1361-6528/aaa2c4.
- [158] C. S. Barrett et al., *The crystal structure of antimony at 4.2, 78 and 298 °K*, Acta Crystallogr. **16**, 451–453 (1963), DOI: 10.1107/S0365110X63001262.
- [159] J. C. Y. Teo et al., *Surface states and topological invariants in three-dimensional topological insulators: Application to $\text{Bi}_{1-x}\text{Sb}_x$* , Phys. Rev. B **78**, 045426 (2008), DOI: 10.1103/PhysRevB.78.045426.
- [160] P. Zhang et al., *Topological and electronic transitions in a $\text{Sb}(111)$ nanofilm: The interplay between quantum confinement and surface effect*, Phys. Rev. B **85**, 201410 (2012), DOI: 10.1103/PhysRevB.85.201410.
- [161] X. Luo et al., *First-principles investigations of the atomic, electronic, and thermoelectric properties of equilibrium and strained Bi_2Se_3 and Bi_2Te_3 including van der Waals interactions*, Phys. Rev. B **86**, 184111 (2012), DOI: 10.1103/PhysRevB.86.184111.
- [162] A. S. Hewitt et al., *Coexisting Bi and Se surface terminations of cleaved Bi_2Se_3 single crystals*, J. Vac. Sci. Technol. B, Nanotechnol. Microelectron. Mater. Process. Meas. Phenom. **32**, 04E103 (2014), DOI: 10.1116/1.4873689.
- [163] T. Förster et al., *Two-dimensional topological phases and electronic spectrum of Bi_2Se_3 thin films from GW calculations*, Phys. Rev. B **92**, 201404 (2015), DOI: 10.1103/PhysRevB.92.201404.
- [164] T. Förster et al., *GW calculations for Bi_2Te_3 and Sb_2Te_3 thin films: Electronic and topological properties*, Phys. Rev. B **93**, 205442 (2016), DOI: 10.1103/PhysRevB.93.205442.
- [165] E. Frantzeskakis et al., *Trigger of the Ubiquitous Surface Band Bending in 3D Topological Insulators*, Phys. Rev. X **7**, 041041 (2017), DOI: 10.1103/PhysRevX.7.041041.
- [166] S. H. Kim et al., *Atomically Abrupt Topological p-n Junction*, ACS Nano **11**, 9671–9677 (2017), DOI: 10.1021/acsnano.7b03880.
- [167] S. H. Kim et al., *Topological phase transition and quantum spin Hall edge states of antimony few layers*, Sci. Rep. **6**, 33193 (2016), DOI: 10.1038/srep33193.
- [168] K.-H. Jin et al., *Band structure engineering of topological insulator heterojunctions*, Phys. Rev. B **93**, 075308 (2016), DOI: 10.1103/PhysRevB.93.075308.
- [169] J. G. Analytis et al., *Bulk Fermi surface coexistence with Dirac surface state in Bi_2Se_3 : A comparison of photoemission*, Phys. Rev. B **81**, 205407 (2010), DOI: 10.1103/PhysRevB.81.205407.
- [170] I. Aguilera et al., *GW study of topological insulators Bi_2Se_3 , Bi_2Te_3 , and Sb_2Te_3 : Beyond the perturbative one-shot approach*, Phys. Rev. B **88**, 045206 (2013), DOI: 10.1103/PhysRevB.88.045206.
- [171] S. LaShell et al., *Spin Splitting of an $\text{Au}(111)$ Surface State Band Observed with Angle Resolved Photoelectron Spectroscopy*, Phys. Rev. Lett. **77**, 3419–3422 (1996), DOI: 10.1103/PhysRevLett.77.3419.
- [172] L. Fu, *Hexagonal Warping Effects in the Surface States of the Topological Insulator Bi_2Te_3* , Phys. Rev. Lett. **103**, 266801 (2009), DOI: 10.1103/PhysRevLett.103.266801.
- [173] J. Tersoff and D. R. Hamann, *Theory of the scanning tunneling microscope*, Phys. Rev. B **31**, 805–813 (1985), DOI: 10.1103/PhysRevB.31.805.

- [174] K.-H. Goldhorn and H.-P. Heinz, *Mathematik für Physiker 3: Partielle Differentialgleichungen - Orthogonalreihen - Integraltransformationen*, 1st ed., Springer-Lehrbuch (Springer, Berlin, Heidelberg, 2008), DOI: 10.1007/978-3-540-76334-5.

Webpages

- [W1] *Bald fahren autonome Fahrzeuge in Deutschland*, <https://www.faz.net/aktuell/wirtschaft/bald-fahren-autonome-fahrzeuge-auf-deutschen-strassen-17827948.html> (visited on 24/05/2022).
- [W2] *THE INVENTION OF THE COMPUTER*, <https://www.hnf.de/en/permanent-exhibition/exhibition-areas/the-invention-of-the-computer.html> (visited on 14/04/2022).
- [W3] *TIMELINE*, <https://www.computerhistory.org/siliconengine/timeline/> (visited on 15/04/2022).
- [W4] *All Nobel Prizes in Physics*, <https://www.nobelprize.org/prizes/lists/all-nobel-prizes-in-physics/> (visited on 04/03/2022).
- [W5] *22 nm process*, https://en.wikipedia.org/wiki/22_nm_process (visited on 18/04/2022).
- [W6] *5 nm process*, https://en.wikipedia.org/wiki/5_nm_process (visited on 18/04/2022).
- [W7] *Intel Now Packs 100 Million Transistors in Each Square Millimeter*, <https://spectrum.ieee.org/nanoclast/semiconductors/processors/intel-now-packs-100-million-transistors-in-each-square-millimeter> (visited on 18/04/2022).
- [W8] *Mit Höchstleistungsrechnern und Data Analytics gegen das Coronavirus*, <https://www.gesundheitsindustrie-bw.de/fachbeitrag/aktuell/mit-hoehchstleistungsrechnern-und-data-analytics-gegen-das-coronavirus> (visited on 13/04/2022).
- [W9] *Storage*, <https://home.cern/science/computing/storage> (visited on 13/04/2022).
- [W10] *PERFORMANCE DEVELOPMENT*, <https://top500.org/statistics/perfdevel/> (visited on 13/04/2022).
- [W11] *TOP500 Meanderings: Sluggish Performance Growth May Portend Slowing HPC Market*, <https://www.top500.org/news/top500-meanderings-sluggish-performance-growth-may-portend-slowing-hpc-market/> (visited on 13/04/2022).
- [W12] *TOP 10 Sites for November 2020*, <https://top500.org/lists/top500/2020/11/> (visited on 13/04/2022).
- [W13] *Stromverbrauch der privaten Haushalte nach Haushaltsgrößenklassen*, <https://www.destatis.de/DE/Themen/Gesellschaft-Umwelt/Umwelt/UGR/private-haushalte/Tabellen/stromverbrauch-haushalte.html> (visited on 24/05/2022).
- [W14] *Halbleiter-Knappheit – Wie der Chipmangel überwunden werden kann*, <https://www.faz.net/aktuell/wirtschaft/digitec/chipmangel-wie-das-problem-ueberwunden-werden-kann-17682182.html> (visited on 24/05/2022).
- [W15] *Ende der Chip-Engpässe könnte noch auf sich warten lassen*, <https://www.faz.net/agenturmeldungen/dpa/ende-der-chip-engpaesse-koennte-noch-auf-sich-warten-lassen-18027141.html> (visited on 24/05/2022).
- [W16] *HPE Apollo (Hawk)*, <https://www.hlrs.de/solutions/systems/hpe-apollo-hawk> (visited on 09/06/2022).
- [W17] *La Grande Arche de La Défense*, https://fr.wikipedia.org/wiki/Arche_de_la_D%C3%A9fense#/media/Fichier:Grande_Arche_F%C3%A9vrier_2020.jpeg (visited on 24/03/2022).
- [W18] *Heilen mit Antimon: Von der Chiematrie zur Chemotherapie*, <https://www.pharmazeutische-zeitung.de/inhalt-10-2000/titel-10-2000/> (visited on 21/05/2022).

Publication list

- [P1] S. Sanna, U. Gerstmann, E. Rauls, Y. Li, M. Landmann, A. Riefer, M. Rohrmüller, N. Vollmers, M. Witte, R. Hölscher, A. Lücke, C. Braun, S. Neufeld, K. Holtgrewe and W. G. Schmidt, *Surface Charge of Clean LiNbO₃ Z-Cut Surfaces*, in *High perform. comput. sci. eng.* '14 (Springer International Publishing, Cham, 2015), pp. 163–178, DOI: 10.1007/978-3-319-10810-0_12.
- [P2] A. Lücke, U. Gerstmann, S. Sanna, M. Landmann, A. Riefer, M. Rohrmüller, N. J. Vollmers, M. Witte, E. Rauls, R. Hölscher, C. Braun, S. Neufeld, K. Holtgrewe and W. G. Schmidt, *Solving the Scattering Problem for the P3HT On-Chain Charge Transport*, in *High perform. comput. sci. eng.* '15 (Springer International Publishing, Cham, 2016), pp. 155–170, DOI: 10.1007/978-3-319-24633-8_10.
- [P3] I. Miccoli, F. Edler, H. Pfnür, S. Appelfeller, M. Dähne, K. Holtgrewe, S. Sanna, W. G. Schmidt and C. Tegenkamp, *Atomic size effects studied by transport in single silicide nanowires*, *Phys. Rev. B* **93**, 125412 (2016), DOI: 10.1103/PhysRevB.93.125412.
- [P4] S. Sanna, C. Dues, U. Gerstmann, E. Rauls, D. Nozaki, A. Riefer, M. Landmann, M. Rohrmüller, N. J. Vollmers, R. Hölscher, A. Lücke, C. Braun, S. Neufeld, K. Holtgrewe and W. G. Schmidt, *Submonolayer Rare Earth Silicide Thin Films on the Si(111) Surface*, in *High perform. comput. sci. eng.* '16 (Springer International Publishing, Cham, 2017), pp. 163–175, DOI: 10.1007/978-3-319-47066-5_12.
- [P5] C. Hogan, K. Holtgrewe, F. Ronci, S. Colonna, S. Sanna, P. Moras, P. M. Sheverdyeva, S. Mahatha, M. Papagno, Z. S. Aliev, M. Babanly, E. V. Chulkov, C. Carbone and R. Flammini, *Temperature Driven Phase Transition at the Antimonene/Bi₂Se₃ van der Waals Heterostructure*, *ACS Nano* **13**, 10481–10489 (2019), DOI: 10.1021/acsnano.9b04377.
- [P6] K. Holtgrewe, S. Appelfeller, M. Franz, M. Dähne and S. Sanna, *Structure and one-dimensional metallicity of rare-earth silicide nanowires on Si(001)*, *Phys. Rev. B* **99**, 214104 (2019), DOI: 10.1103/PhysRevB.99.214104.
- [P7] K. Holtgrewe, S. K. Mahatha, P. M. Sheverdyeva, P. Moras, R. Flammini, S. Colonna, F. Ronci, M. Papagno, A. Barla, L. Petaccia, Z. S. Aliev, M. B. Babanly, E. V. Chulkov, S. Sanna, C. Hogan and C. Carbone, *Topologization of β -antimonene on Bi₂Se₃ via proximity effects*, *Sci. Rep.* **10**, 14619 (2020), DOI: 10.1038/s41598-020-71624-4.
- [P8] S. Appelfeller, K. Holtgrewe, M. Franz, L. Freter, C. Hassenstein, H.-F. Jirschik, S. Sanna and M. Dähne, *Continuous crossover from two-dimensional to one-dimensional electronic properties for metallic silicide nanowires*, *Phys. Rev. B* **102**, 115433 (2020), DOI: 10.1103/PhysRevB.102.115433.
- [P9] K. Holtgrewe, C. Hogan and S. Sanna, *Evolution of Topological Surface States Following Sb Layer Adsorption on Bi₂Se₃*, *Materials (Basel)*, **14**, 1763 (2021), DOI: 10.3390/ma14071763.
- [P10] C. Hogan, P. Lechiffart, S. Brozzesi, S. Voronovich-Solonevich, A. Melnikov, R. Flammini, S. Sanna and K. Holtgrewe, *Theoretical study of stability, epitaxial formation, and phase transformations of two-dimensional pnictogen allotropes*, *Phys. Rev. B* **104**, 245421 (2021), DOI: 10.1103/PhysRevB.104.245421.
- [P11] K. Holtgrewe, F. Ziese, J. Bilk, M. N. Pionteck, K. Eberheim, F. Bernhardt, C. Dues and S. Sanna, *Tuning the Conductivity of Metallic Nanowires by Hydrogen Adsorption*, in *High perform. comput. sci. eng.* '20 (Springer International Publishing, Cham, 2021), pp. 133–146, DOI: 10.1007/978-3-030-80602-6_9.
- [P12] S. Sanna, J. Plaickner, K. Holtgrewe, V. M. W Mittag, E. Speiser, S. Chandola and N. Esser, *Spectroscopic Analysis of Rare-Earth Silicide Structures on the Si(111) Surface*, *Materials (Basel)*, **14**, 4104 (2021), DOI: 10.3390/ma14154104.
- [P13] Z. Mamiyev, C. Fink, K. Holtgrewe, H. Pfnür and S. Sanna, *Enforced Long-Range Order in 1D Wires by Coupling to Higher Dimensions*, *Phys. Rev. Lett.* **126**, 106101 (2021), DOI: 10.1103/PhysRevLett.126.106101.
- [P14] C. Fink, F. A. Pfeiffer, K. Holtgrewe and S. Sanna, *Au adsorption on stepped Si(hhk)-Au surfaces*, *Surf. Sci.* **718**, 122010 (2022), DOI: 10.1016/j.susc.2021.122010.

Danksagung

Ich möchte mich hiermit bei all denjenigen bedanken, die mich auf meinem Wege bis zum Abschluss der Promotion begleitet haben.

Zuallererst gilt ein großer Dank meinem Doktorvater Prof. Simone Sanna, der mich immer kräftig unterstützt hat. Er hat sich nie davor gescheut, mir auch schwierige Aufgaben zu übertragen, und mir gleichzeitig den Freiraum gegeben, sie entsprechend gründlich zu bearbeiten. Insbesondere die Tatsache, dass er zum Beginn meiner Promotion den Ruf an die JLU bekommen und folglich mit mir und Dr. Christof Dues zusammen die Arbeitsgruppe gegründet hat, war eine Herausforderung, auch aus organisatorischer Sicht, die sich im Nachhinein als wertvolle Erfahrung erwiesen hat. Bei Christof möchte ich mich in diesem Zuge auch sehr herzlich bedanken, ebenso bei allen anderen Mitgliedern der AG Sanna, für gute fachliche Gespräche und ein hervorragendes Arbeitsklima, auch extra laborem.

Ich möchte mich sehr herzlich bei Prof. Wolf Gero Schmidt bedanken, der während meines Studiums an der Universität Paderborn mein Interesse an der theoretischen Materialphysik geweckt hat und mich bis zum Masterabschluss und darüber hinaus bestens unterstützt hat.

I want to thank Dr. Conor Hogan, who was my supervisor during my ERASMUS+ research internship at the university "Tor Vergata", Rome, Italy. The collaboration with him was very precious and fruitful. Furthermore, I want to thank all other collaborators with whom I worked on the RESi_2 nanowires and the antimony on Bi_2Se_3 heterostructures.

Ein ganz großer Dank gilt meinen Eltern, die schon früh mein Interesse an der Naturwissenschaft geweckt und mich in meinen Vorhaben immer unterstützt haben. Des Weiteren gilt mein Dank auch dem Rest meiner Familie und meinen Freunden dafür, dass sie mir immer Halt gegeben haben.

Ich möchte mich bei der Deutschen Forschungsgemeinschaft (DFG) für die finanzielle Unterstützung bedanken. Ferner möchte ich mich bei den HPC Einrichtungen bedanken, deren Rechenzeiten die Ergebnisse dieser Arbeit ermöglicht haben: das Hochschulrechenzentrum der JLU Gießen, das Hochschulrechenzentrum der TU Darmstadt und das Höchstleistungsrechenzentrum Stuttgart.

